FY-2015 FES Joint Research Target

Final Report for the period
October 1st, 2014 through September 30th, 2015

Prepared for the U.S. Department of Energy

U.S. DEPARTMENT OF ENERGY | Office of Science

by the JRT-15 Coordination Committee:

M. Podestà[1], *C. Holcomb*[2], *G. Wallace*[3],
S. P. Gerhardt[1], *S. D. Scott*[1], *W. Solomon*[1]
[1]PPPL, [2]LLNL, [3]MIT-PSFC

NSTX-U

Alcator C-Mod

DIII-D NATIONAL FUSION FACILITY SAN DIEGO

Annual JRT-15 Target:

Conduct experiments and analysis to quantify the impact of broadened current and pressure profiles on tokamak plasma confinement and stability. Broadened pressure profiles generally improve global stability but can also affect transport and confinement, while broadened current profiles can have both beneficial and adverse impacts on confinement and stability. This research will examine a variety of heating and current drive techniques in order to validate theoretical models of both the actuator performance and the transport and global stability response to varied heating and current drive deposition.

4th Quarter Milestone:

Complete the planned experiments and analysis. Prepare a joint report summarizing the impact of broadened current and pressure profiles on plasma confinement and stability and identifying important paths for future research.

List of Contributors:

A. Bhattacharjee, R. V. Budny, D. S. Darrow, L. Delgado-Aparicio, F. Ebrahimi, E. Fredrickson, M. Gorelenkova, N. Gorelenkov, B. A. Grierson, W. Guttenfelder, G. Kramer, S. Medley, D. Mueller, R. Nazikian, F. Poli, J. R. Wilson, R. B. White - *PPPL*

J. Berkery, J. Bialek, J. M. Hanson, S. A. Sabbagh, F. Turco – *Columbia University*

C. Collins, W. Heidbrink, D. Liu, G. Hao, E. Ruskov – *University of California Irvine*

N. Crocker, S. Kubota, T. Peebles, T. Rhodes – *University of California Los Angeles*

W. Boeglin, R. Perez – *Florida International University*

S. G. Baek, I. C. Faust, R. R. Parker, S. Shiraiwa, R. T. Mumgaard, B. L. LaBombard, D. Brunner, P. T. Bonoli, J. C. Wright, R. Granetz – *MIT PSFC*

L. Sugiyama – *MIT LNS*

J. R. Ferron, E. M. Bass, T. N. Carlstrom, X. Chen, A. M. Garofalo, R. J. La Haye, L. L. Lao, T. C. Luce, O. Meneghini, D. C. Pace, C. C. Petty, R. Prater, S. P. Smith, G. M. Staebler, E. J. Strait, M. A. Van Zeeland – *General Atomics*

S. Ding, X. Gong, G. Li, J. Qian, Q. Ren, B. Wan, G. Xu – *Institute of Plasma Physics, Chinese Academy of Sciences*

K. Kim, J. M. Park – *Oak Ridge National Laboratory*

G. McKee – *University of Wisconsin Madison*

M. Yoshida – *Japan Atomic Energy Agency*

Z. Taylor – *Oak Ridge Associated Universities*

E. Kolemen – *Princeton University*

R. Bravenec – *Fourth State Research*

F. Carpanese – *Politecnico di Milano, Dipartimento di Energia*

Table of Contents:

1.0 Executive summary 6
1.1: Current and pressure driven instabilities limiting tokamak performance 6
1.1.1: Unification of kinetic Resistive Wall Mode stabilization physics 6
1.1.2: C-Mod results on low-frequency MHD leading to disruptions 6
1.1.3: Suggested path for future research 6
1.2: Energetic particle driven instabilities limiting tokamak performance 7
1.2.1: Alfvénic modes reducing plasma performance 7
1.2.2: Suggested path for future research 7
1.3: Profile optimization for improved plasma performance 8
1.3.1: High-β_p scenarios with off-axis NB current drive 8
1.3.2: "Hybrid" scenarios with peaked profiles 8
1.3.3: Lower-Hybrid current drive for current profile optimization 9
1.3.4: Suggested path for future research 9
1.4: Role of impurities for plasma performance optimization 10
1.4.1: Impurity transport and effects on plasma performance 10
1.4.2: Suggested path for future research 10

2.0 DIII-D Contributions 11
2.2: Fast-ion transport in q_{min}>2, high-β steady-state scenarios on DIII-D 25
2.3 Measurements of Alfvén Eigenmode Induced Critical Gradient Transport of Fast-Ions 52
2.4: Suppression of Aflvén eigenmodes in high performance steady state discharges 55
2.5 Report on Confinement Optimization via q-profile Control 67
2.6: The High-β_N Hybrid Scenario for ITER and FNSF Steady-State Missions 69
2.7: Preliminary Results from Investigating Magnetic Flux Pumping in Hybrids 100
2.8: Impact of Central ECCD on Steady-State Hybrid Scenario in DIII-D 112

3.0 C-Mod Contributions 124
3.1: Improved numerical tools for LH current drive studies 124
3.1.1 Measurements of LH driven current on Alcator C-Mod 124
3.1.2 Summary of comparison between modeling and experiment 126
3.1.3 Discussion and implications 127
3.1.4 Impact of SOL Plasma Profiles on Lower Hybrid Current Drive: Experimental Evidence, Mitigation, and Modeling Approaches 132
3.1.5 Thick target bremsstrahlung measurements during LHCD 140
3.2: Impurity transport with off-axis current drive 141
3.2.1 Characterization of impurity transport in non-inductive LHCD scenarios 141
3.3: Exploration of accessible regimes through off-axis current drive 143
References 148

4.0 NSTX-U Contributions 149
4.1: Resistive Wall Mode physics and impact on plasma performance 150
4.1.1 Joint DIII-D and NSTX-U experimental activity 150
4.1.2: Comparison of NSTX and DIII-D kinetic RWM stabilization physics 156
4.1.3: Kinetic RWM marginal stability in NSTX and DIII-D – comparison of theoretical and experimental stability 160
4.2: Development of reduced models for fast ion transport 162
4.2.1: Critical Gradient Model (CGM) 162
4.2.2: Extension of the ORBIT code for mode saturation amplitude estimates 165

4.2.3: "Kick" model implementation in TRANSP/NUBEAM 165
4.3: Current drive and fast ion modeling in the presence of instabilities 166
4.3.1: Experimental scenarios and analysis procedure 167
4.3.2: Modifications of the fast ion distribution 168
4.3.3: Broadening of fast ion density and NB-driven current profiles 169
4.3.4: Implications for the assessment of NB current drive efficiency and power balance 170
4.4: Validation of LH-CD modeling through time-dependent simulations 172
4.4.1: C-Mod target scenario, diagnostics and modeling assumptions 172
4.4.2: Validation of LH-CD models against experiments 173
4.5 Characterization of impurity profiles and transport 177
4.5.1 Upgraded radiated power measurements on NSTX-U 177
4.5.2 Interpretation of impurity measurements including poloidal asymmetries 178
4.6: Characterization of the fast ion distribution function 180
4.6.1: FIDAsim modeling 180
4.6.2: Implementation of a new "3D Halo" model in TRANSP/NUBEAM 180
4.7: Diagnostics improvements on NSTX-U 181
4.7.1: Fast Ion D-Alpha and Neutral Particle Analyzers 181
4.7.2: Charged Fusion Product array 181
4.7.3: Internal measurements of fast ion driven instabilities 182
4.8: Experimental plans after machine re-commissioning 183
References 184

1.0 Executive summary

1.1: Current and pressure driven instabilities limiting tokamak performance

1.1.1: Unification of kinetic Resistive Wall Mode stabilization physics
Participating facilities: NSTX-U, DIII-D

- A dedicated experiment was run on DIII-D to test kinetic RWM stabilization physics proposed in several NSTX publications with the goal of unifying the physics understanding of kinetic RWM marginal stability conditions between devices. The experiment was successful in producing this understanding: kinetic RWM theory provides a sufficient breadth to understand the stabilization physics between the devices, which has an important complementarity, and experimental observations and kinetic RWM stability analysis between the devices shows good agreement between theory and experiment.
- The detailed experimental and analysis results show a unified understanding of kinetic RWM stabilization physics between the NSTX and DIII-D devices. Common analysis tools, (e.g the MISK code), were used to analyze the experimental results on both devices. Quantitative agreement was found between theory and experiment of kinetic RWM marginal stability points over a wide range of plasma rotation profile and speed.
- See Sec. 4.1 for more details.

1.1.2: C-Mod results on low-frequency MHD leading to disruptions
Participating facilities: C-Mod

- Analysis of data from previous run campaigns indicates deleterious low frequency MHD instability is possibly due to a 3/2 double tearing mode. The location of the q=1.5 rational surface is difficult to determine due to flatness of the q profile and size of error bars in these discharges.
- Dedicated experiments were planned on C-Mod to assess the feasibility of avoiding these MHD events using "pre-forming" techniques to avoid rational surfaces in flat regions of the q profile. Due to operational issues with the diagnostic neutral beam (needed for q profile measurements), these experiments are deferred to the 2016 fiscal year.

1.1.3: Suggested path for future research

Experiments are planned on NSTX-U to connect with DIII-D results at high-q_{min}, leveraging on the new capabilities enabled by the 2nd NB line. The combination of more tangential vs. perpendicular injection will provide scans of energetic particles' distribution (important for kinetic RWM stability) and of rotation profile.

1.2: Energetic particle driven instabilities limiting tokamak performance

1.2.1: Alfvénic modes reducing plasma performance

Participating facilities: DIII-D, NSTX-U

- DIII-D steady-state scenario plasmas with $q_{min}>2$ and $q_{95}<7$ (i.e. "standard high-q_{min}" as opposed to the high-b_P scenario) have been shown to have strong Alfvén eigenmode (AE) activity that redistributes or completely ejects fast ions from the plasma, resulting in poor normalized global energy confinement for an H-mode (i.e. $H_{89P}<2$). A key result is that a critical fast-ion gradient model seems to describe the onset of strong AE activity and enhanced fast-ion transport. State of the art fast-ion simulation codes were used to obtain quantitative agreement with measured neutron deficits, cf. sections 4.2-4.3. Detailed analysis of the linear AE-stability of these plasmas suggests additional broadening of the current profile via higher r_{qmin} and q_0 is a path forward for suppressing the fast-ion loss. See sections 2.2-2.4 for more details.
- New analysis and modeling suggests paths for future research in this area. On DIII-D, by increasing the radius of q_{min} and raising q_0, perhaps through faster current ramp-up, it may be possible to transiently suppress AEs and fast-ion loss. This works by moving the RSAEs to larger radius away from the region of large fast-ion pressure and by suppressing core AEs. This experiment is proposed for the FY16 campaign. If successful, additional off-axis current drive may be needed on DIII-D to achieve this regime in steady state conditions, and several new upgrades are planned starting in FY17 that should help: a 2nd off-axis neutral beam, more gyrotrons, and a helicon antenna. See sections 2.2-2.4.
- New analysis and modeling tools have been developed to assess the impact of Alvénic instabilities and associated fast ion transport on plasma performance. A "critical gradient" model has been tested on NSTX and DIII-D plasmas. The model computes the relaxed fast ion profile under the effects of AEs. An alternative approach has been developed to include a "transport probability" for fast ion transport by AEs in the NUBEAM module of TRANSP for time-dependent, integrated simulations. For both models, comparison with the experiments shows agreement with the measured neutron rate deficit when the unstable spectrum is correctly taken into account. Effects of AEs on broadening of fast ion and NB driven current profiles are being quantified for both devices. See sections 4.2-4.3 for more details.

1.2.2: Suggested path for future research

For NB heated scenarios, experiments are planned on NSTX-U to complement previous studies on DIII-D on the effects of broadened current profile on plasma performance. Experiments include a characterization of the 2nd NB line as a starting point, then a detailed investigation of

NB-CD efficiency vs. NBI parameters. In general, the interplay between q-profile, AE stability and fast ion transport needs to be investigated with the new set of analysis and simulation tools. Experiments are also planned on DIII-D to verify the prediction of AE suppression by moving q_{min} to larger radii and raising q_0 through faster current ramp assisted by off-axis NB-CD.

1.3: Profile optimization for improved plasma performance

1.3.1: High-β_p scenarios with off-axis NB current drive
Participating facilities: DIII-D, NSTX-U

- Using off-axis NBI and ECCD, DIII-D conducted experiments on two variations of a "high-β_P" steady-state scenario that clearly demonstrates several benefits of operation with broadened current and pressure profiles. At I_p=500-800 kA, partially self-organized plasmas dominated by bootstrap current (f_{BS}=0.6-0.8) are formed with an internal transport barrier at large radius. The relatively broad current profile and high-radius of the ITB result in good normalized confinement and classical fast-ion confinement. Very high q_{min}=3-5 helps to avoid low-order tearing modes. Normalized β is limited by the n=1 external kink mode. This limit has been increased by reducing the plasma-wall gap to increase coupling and wall stabilization.
- DIII-D studied ITBs in high-β_P scenario plasmas. Internal transport barriers in the density and temperature produce a steep pressure gradient at high radius (foot of ITB between ρ=0.6 and ρ=0.8). Analysis and modeling has shown a synergy between increasing the radius of the ITB and increasing β_N. When the Ohmic drive from the central solenoid is removed, the ITB is sustained even in the presence of large ELMs in fully non-inductive discharges with I_P=500-600 kA. But when I_p is feedback controlled at 800 kA, the ITB is transient, suffering from an n=1 mode located at the ITB radius. The reasons for the different stability properties are not yet known. These results show that realizing the possible benefits of broad current and pressure profiles with an ITB may require either greater profile control or sufficiently relaxed constraints for the plasma to self-organize, e.g. no direct I_p feedback control.
- The high-β_P scenario discharges can have either weak positive shear or strong negative central shear depending on the turn-on time of off-axis ECCD. A preliminary result from a July 2015 DIII-D experiment is that compared to positive or weak magnetic shear, negative shear alleviates the confinement reduction that usually happens with increased electron heating.
- See Sections 2.1, 2.2, and 2.5 for more details on high-β_p scenarios.

1.3.2: "Hybrid" scenarios with peaked profiles
Participating facilities: DIII-D

- On DIII-D, in FY15 new experiments and analysis were conducted on a scenario at the opposite end of the profile broadness spectrum compared to high q_{min}. The "hybrid" scenario has more peaked current and pressure profiles than high-q_{min} scenarios, but less peaked than standard sawtoothing H-modes. Anomalous current profile broadening via an n=2 or 3 tearing mode maintains $q_{min}>1$, prevents sawteeth, and increase the n=1 kink and tearing β_N limits above those of standard H-mode. This flux pumping effect eliminates the need for precise current profile control to reach steady state, and allows the use of high power on-axis current drive where it is most efficient. Flux pumping has been shown to persist under a variety of conditions, e.g. without ELMs, but there are limits to how much on-axis current drive can be used before the flux pumping ceases to maintain $q_{min}>1$. However, a small shift of ECCD deposition to higher radius has been shown to recover $q_{min}>1$ operation. This scenario is relatively insensitive to the use of off-axis NBI, which serves to broaden the pressure and raise the predicted ideal-wall n=1 kink β_N limit by ~10%, without any penalty in confinement.
- See sections 2.6-2.8 for more details.

1.3.3: Lower-Hybrid current drive for current profile optimization

Participating facilities: C-Mod, NSTX-U

- Significant effort was dedicated to improved understanding of LH wave physics through new experiments. Experiments were conducted to continue examining the role of the scrape-off-layer (SOL) in the propagation and absorption of LH waves. Power balance in the plasma edge/SOL will be featured in an upcoming invited talk by I.C. Faust at the 2015 APS DPP meeting.
- Computational models of LHCD continue to improve. Time dependent modeling with TRANSP has been updated to include the ray-tracking/Fokker-Planck package GENRAY/CQL3D, including SOL effects. The ray-tracking/Fokker-Planck approach is considerably more accurate compared to the adjoint method used by the LSC module previously included in TRANSP. Agreement between GENRAY/CQL3D and experiment has also improved with more realistic 2-D axisymmetric kinetic profiles in the SOL.
- See sections 3.1 and 4.4 for more details.

1.3.4: Suggested path for future research

For more confident use of high-β_P scenarios by future devices, next-step research is aimed at three goals, all while preserving steady-state operation: (1) Raising β_N/q_{95} and therefore projected fusion gain further by optimizing the plasma-wall coupling and applying additional off-axis external current drive as it becomes available, (2) Reducing injected torque to zero, and (3) eliminating large ELMs.

Results from "hybrid" scenarios on DIII-D suggest a path forward for future research by extending the operating parameters to values closer to ITER and FNSF. This involves exploration of a radiative divertor solution to handle the exhaust power and of regimes with $T_e/T_i \sim 1$ through additional electron heating.

1.4: Role of impurities for plasma performance optimization

1.4.1: Impurity transport and effects on plasma performance
Participating facilities: C-Mod, NSTX-U

- Synthetic diagnostics have been developed to facilitate the interpretation of 1D and 2D resolved measurements of impurity profiles. The new method enables more reliable data interpretation including the effects of poloidal asymmetries in the profiles induced, for example, by centrifugal forces.
- Experiments on C-Mod suggest that impurity transport and resulting profiles can be considerably different in scenarios with LHCD as compared to ohmic plasmas. Transport analysis of impurity traces through the laser blow-off system indicates a reduction of core impurity accumulation during LHCD. Preliminary analysis suggests that turbulent transport may be responsible for the observed differences.
- See sections 3.2 and 4.5 for more details.

1.4.2: Suggested path for future research

Perform experiments in C-Mod and NSTX-U to characterize impurity accumulation and its dependence on heating profiles and non-inductive current drive schemes. Assess impact of impurity accumulation on plasma performance, with the longer term goal of developing strategies for impurity accumulation reduction.

2.0 DIII-D Contributions

Experiments on DIII-D were conducted to explore the effects of current and pressure profile shape (i.e. more or less broad) on confinement, stability, and potential for steady-state operation. They focused on optimizing roughly three different operating scenarios. Taken as a set, these cover a broad range of current and pressure profiles. In this report the results are sequenced from most broad current and pressure to most peaked. Detailed descriptions of experiments conducted on DIII-D and analysis that satisfy this JRT milestone are given in the attached publication manuscripts submitted this fiscal year in Sections 2.2 and 2.6. Sections 2.1, 2.3, 2.4, 2.5, 2.7, and 2.8 contain reports describing recent experiments or preliminary analysis results. Here we briefly summarize the main results relevant to this JRT milestone deliverable.

Optimizing profiles for steady-state tokamak fusion requires balancing several trade-offs. Scenarios with broad current and pressure and high q_{min} have been sustained using off-axis NBI and ECCD. These are capable of supporting high β_N, high confinement, and high bootstrap current – all things needed in a power plant. But experiments on DIII-D have shown that achieving higher performance by broadening profiles is not straightforward because there are new challenges in this regime. As detailed in this report, some high-q_{min} scenarios suffer from enhanced fast-ion losses that result in low confinement. Thermal transport, including the formation and stability of internal transport barriers, is sensitive to the current profile and magnetic shear. Preliminary indications are that further profile broadening beyond what is presently achievable with existing tools may be needed to increase performance. However, not all future steady-state tokamaks will require extremely high fusion gain or bootstrap fraction with broad profiles. Near-term steady-state devices like ITER may meet their mission goals with more modest scenarios. Therefore work for this milestone also focused on a "hybrid" scenario with more peaked current and pressure profiles that do not rely on significant off-axis heating and current drive. Hybrids rely on anomalous current profile diffusion to maintain $q_{min}>1$ and avoid sawteeth. This year the conditions under which the anomalous current diffusion exits were better characterized, improving confidence in projections to burning plasmas.

The most convenient and widely used parameters for quantifying current profile and pressure profile shapes are internal inductance $\ell_i = (1/V)(\int B_P^2 dV)/((\mu_0 I_*/\int dl)|_a)^2$ and pressure peaking factor $f_p = p(0)/\langle p \rangle$, respectively. Peaked current profiles have high ℓ_i (e.g., greater than 1), and broad or hollow current profiles have low ℓ_i (e.g., ~0.5). Peaked pressure profiles have $f_P > \sim 3$, and broad pressure profiles have $f_P < \sim 3$. While convenient, these parameters only crudely characterize profile broadness. For example, they usually are insensitive to steep local gradients, such as an internal transport barrier (ITB) in the pressure, and global MHD stability and transport can be sensitive to such local features. Therefore, where appropriate this report discusses stability, transport, and current drive dependencies upon local profile features as well as the global 1-D

quantities like ℓ_i and f_P.

Future steady-state power plants will require a large bootstrap current fraction so several experiments have been done to explore this regime. The conference talks in Section 2.1 describe analysis of a scenario having ℓ_i=0.5-0.7 and f_P=2.5-3.3. This "high-β_P scenario" clearly demonstrates several benefits of operation with broadened current and pressure profiles. It uses off-axis NBI and ECCD and low I_p=500-600 kA (q_{95}=10-12) without inductive feedback control to produce a partially self-organized equilibrium dominated by bootstrap current (f_{BS}=0.7-0.8). Internal transport barriers in the density and temperature produce a steep pressure gradient at high radius (foot of ITB between ρ=0.6 and ρ=0.8). The relatively broad current profile and high-radius of the ITB result in good normalized confinement and classical fast-ion confinement. Very high q_{min}=3-5 helps to avoid low-order tearing modes. Normalized β is limited by the n=1 external kink mode. This limit has been increased by reducing the plasma-wall gap to increase coupling and wall stabilization. Analysis and modeling has shown a synergy between increasing the radius of the ITB and increasing β_N. Section 2.1 also compares high-β_P plasmas to a closely related inductive scenario with ~50% higher I_P regulated by feedback control. This scenario was tested in experiments in December 2014. While it still has a broad current profile and an internal transport barrier, the ITB is transient, suffering from an n=1 mode located at the ITB radius. These results show that realizing the possible benefits of broad current and pressure profiles with an ITB may require either greater profile control or sufficiently relaxed constraints for the plasma to self-organize, e.g. no direct I_p feedback control.

Plasmas with weak magnetic shear, q_{min}>2 and q_{95}<7, and off-axis NBI and ECCD have been studied as possible candidates for future burning plasma scenarios. These have ℓ_i and f_P in about the same ranges as the high-β_P scenario, but they do not have ITBs or locally steep gradients inside the H-mode pedestal. Also in contrast to the high-β_P scenario, these plasmas have lower density, higher electron temperature, and higher NBI power, so the fraction of the total pressure from fast-ions is greater. The Physics of Plasmas manuscript in Section 2.2 details how these conditions lead to strong Alfven eigenmode (AE) activity that redistributes or completely ejects fast ions from the plasma, resulting in poor normalized global energy confinement for an H-mode (e.g. H_{89P}<2). A key result, explored further in a July 2015 experiment described in Section 2.3, is that a critical fast-ion gradient model seems to describe the onset of strong AE activity and enhanced fast-ion transport. Therefore NBI-heated plasmas need to be controlled to stay below this gradient to avoid diminishing returns with more NBI power. Based on comparisons of the high-β_P and "standard high-q_{min}" scenarios, we predict that additional broadening of the heating and current drive profiles to reduce core AE activity and further optimize transport may help increase global confinement and β.

Predictive understanding of Alfven eigenmodes and fast-ion transport is needed to attain high plasma performance with broad current and pressure profiles in present and future devices.

Section 2.4 contains a report on applying AE and fast-ion transport codes to understand and predict these in DIII-D high-q_{min} plasmas. This work was started in December 2015 and strengthened by collaboration with NSTX-U staff. In summary, state of the art fast-ion simulation codes integrating NOVA-K, ORBIT, TRANSP and the Critical Gradient Model (CGM) were used to obtain quantitative agreement with the measured neutron deficit in DIII-D steady state plasmas. When the AEs are present the neutron yield, mainly from beam-plasma interactions, typically decreases 20% to 40% depending on the instabilities. Unstable core localized TAE, EAE, NAEs and RSAEs are identified in the NOVA-K analysis in the same frequency range (100-300 kHz) as the observed instabilities in DIII-D high-q_{min} plasmas. Inserting the NOVA eigenmodes into ORBIT/TRANSP yields a quantitative prediction of the fast-ion loss. Both the CGM and ORBIT analysis obtain ~20% fast-ion loss, consistent with most of the discharges. In a few discharges, up to 40% fast-ion loss is observed when additional (<100 kHz) modes are seen in the BAE gap, and ORBIT analysis confirms that such losses are consistent with the measured mode amplitudes. Detailed analysis of the linear stability of these plasmas suggest a path forward for suppressing the fast-ion loss. By increasing the radius of q_{min} and raising q_0, perhaps through faster current ramp-up, it may be possible to transiently suppress AEs and fast-ion loss. This works by moving the RSAEs to larger radius away from the region of large fast-ion pressure and by suppressing core AEs. This experiment is proposed for the FY16 campaign. If successful, additional current drive will be needed on DIII-D to achieve this regime in steady state conditions.

Thermal plasma confinement can also be optimized by controlling the hollowness of the current profile. Section 2.5 contains a preliminary report on a July 2015 experiment to investigate the role of magnetic shear on turbulence and thermal transport in high-q_{min} plasmas. This focused on using negative central magnetic shear to alleviate the confinement reduction that usually happens with increased electron heating in plasmas with positive or weak magnetic shear. Preliminary results are that under certain conditions making a more hollow current profile (i.e. negative central shear) improves confinement by reducing turbulence.

In FY15 new experiments and analysis were conducted on a scenario at the opposite end of the profile broadness spectrum compared to high q_{min}. The "hybrid" scenario discussed in Sections 2.6 (Physics of Plasmas manuscript), 2.7 and 2.8 (DIII-D Friday Science Meeting presentations) has a more peaked current profile with ℓ_i=0.7-0.8. For comparison, standard sawtoothing H-mode discharges typically have ℓ_i=0.9-0.95. This more peaked scenario is interesting because it offers an alternative steady-state operating mode, but it comes with a different set of challenges.

The hybrid scenario relies on anomalous current profile broadening via an n=2 or 3 tearing mode to increase the n=1 kink and tearing β_N limits above those of standard H-mode. This flux pumping effect eliminates the need for precise current profile control to reach steady state, and allows the use of high power on-axis current drive where it is most efficient. Recent results described in Sections 2.7 and 2.8 show that current profile broadening by flux pumping persists

under a variety of conditions, e.g. without ELMs, but there are limits to how much on-axis current drive can be used before the flux pumping ceases to maintain $q_{min}>1$. However, a small shift of ECCD deposition to higher radius has been shown to recover $q_{min}>1$ operation.

The hybrid has a relatively peaked pressure profile with f_P=3-4, but as detailed in Section 2.6, this does not seem to impose a severe penalty on the ideal-wall β_N limit, which modeling suggests is comparable with ideal limits of high-q_{min} discharges produced in DIII-D with existing tools. Using off-axis NBI in the hybrid scenario only reduces the pressure peaking factor and raises the predicted ideal-wall β_N limit by ~10%. Energy confinement, including fast-ion confinement, is generally good in hybrids.

In summary, based on the experimental observations, analysis, and modeling, some conclusions can be drawn about optimizing current and pressure profile broadness for steady-state operation. The moderately peaked hybrid scenario (weakly broadened current, relatively peaked pressure) has potential for use by more near term burning plasma devices like ITER or a possible fusion nuclear science experiment that do not require very high Q. The current and pressure profiles in hybrids are for the most part already optimized for such missions, and we are beginning to understand how current broadening via flux pumping depends on various conditions. Therefore future hybrid research will increasingly be directed towards testing the scenario in more reactor relevant conditions, such as higher T_e/T_i and lower torque. The most extreme high-q_{min} with very broad current and pressure have potential for achieving $\beta_N>4$, high bootstrap fraction, high confinement operation that is typically called for in steady-state DEMO or power plant studies. However there are still fundamental challenges to overcome. For both the high-β_p and standard high-q_{min} scenarios, we need to find ways to maintain or recover global energy confinement at least as good as in standard H-mode plasmas to enable access to higher β_N steady-state operation. For the high-β_p scenario this will require understanding how to maintain a high-radius ITB at higher I_p. The standard high-q_{min} scenario needs development to reduce fast-ion and thermal transport. Experiments and predictive modeling suggest that a path forward is to push to even broader current profiles than can be sustained with present tools. Higher ρ_{qmin} and possibly higher q_0-q_{min} may be beneficial for reducing fast-ion and thermal transport. New experiments in FY16 could demonstrate this transiently, and planned heating and current drive upgrades beyond FY16 will enable experiments to see if such profiles are compatible with steady-state operation.

Future advances in understanding profile broadness optimization and testing predictions and hypotheses made in this JRT milestone report will be enabled by planned DIII-D upgrades: (1) A second off-axis neutral beamline that will raise the maximum fraction of NBI power applied off-axis to 50%. When used with negative toroidal field direction these will drive substantial off-axis current for high-q_{min} studies, possibly with higher ρ_{qmin}. When used with positive toroidal field direction, the off-axis current will be minimized while still providing broad heating for high-ℓ_i studies. (2) Ability to inject all NBI in the co-I_p direction for maximum neutral beam current drive. This will allow tests of higher β_N fully non-inductive operation in all scenarios for future

fusion reactors. (3) Additional gyrotrons totaling up to ~9 MW of ECCD power will provide key further off-axis current drive and torque-free electron heating to test scalings towards burning plasma conditions. Flexible aiming enables precise current profile control and NTM control. (4) A prototype high-harmonic fast wave system that is predicted to have a high off-axis current drive efficiency, perhaps ~4x greater than that of ECCD. This would further expand the range of current profiles that can be tested on DIII-D and test a promising technique for future reactors.

2.1: High-β_P Scenarios

The following slides are excerpts from two presentations dealing with variants of the high-β_P scenario. The first presentation focusing on a 600 kA scenario was made at the 2015 US/EU Transport Task Force Workshop in Salem, MA, April 28-May 1. The second presentation focusing on an 800 kA version was made at the 5th Asia Pacific Transport Working Group International Conference, Dalian, China, June 9-12, 2015.

Confronting the Challenges of Integrated Transport, Neoclassical, and MHD Physics in the High β_p Regime

by

A.M. Garofalo

with

X. Gong, B.A. Grierson, C.T. Holcomb, O. Meneghini, Q. Ren, W.M. Solomon, S.P. Smith, G.M. Staebler, E.J. Strait, M.A. Van Zeeland, B. Wan, R. Bravenec, R.V. Budny, S. Ding, W. Guttenfelder, J.M. Hanson, W.W. Heidbrink, L.L. Lao, G. Li, C.C. Petty, J. Qian, and G. Xu

Presented at the

2015 US/EU Transport Task Force Workshop
Salem, MA

April 28th-May 1ST, 2015

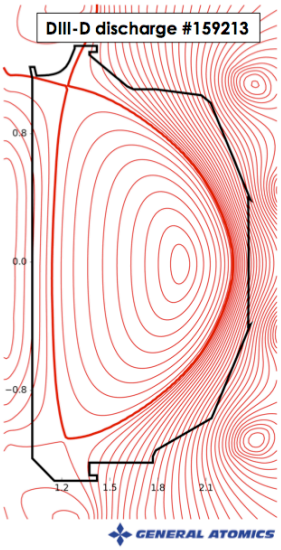

Joint EAST/DIII-D Experiment Developed Fully Non-inductive High β_P Scenario Under Relevant EAST Conditions

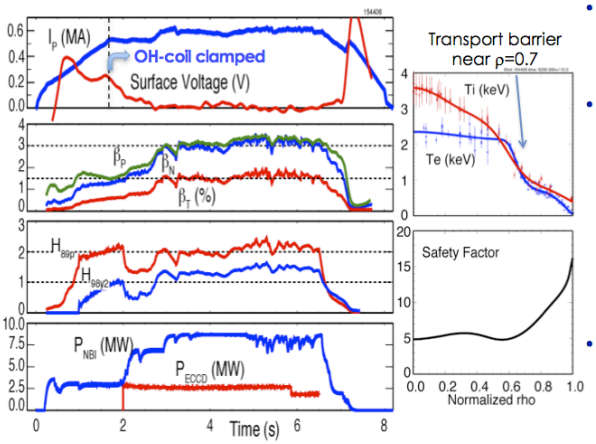

- **Builds on previous high β_P experiments**
  [Politzer et al., NF 2005]
- **I_p ramp rate consistent with superconductive EAST**
  - Similar plasma shape
  - I_P, B_T, P_{inj} consistent with upgraded EAST capabilities
- **Excellent energy confinement quality H_{98y2}~1.5 obtained also at reduced NBI torque**

"Relaxation Oscillations" Identified as Repetitive Buildup and Collapse of H-mode Pedestal

- **Previously believed to be caused by internal modes driven by ITB** [Politzer et al., NF 2005]

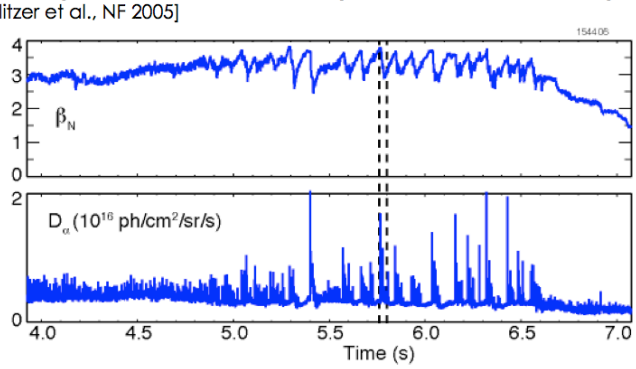

- **Strong impact of the oscillations on the β_N waveform**
- **Let's take a detailed look into one of these stored energy oscillations:**

Stored Energy Drop Caused by Bursts Of *n*=1 External Mode, Driven by Pedestal Gradients

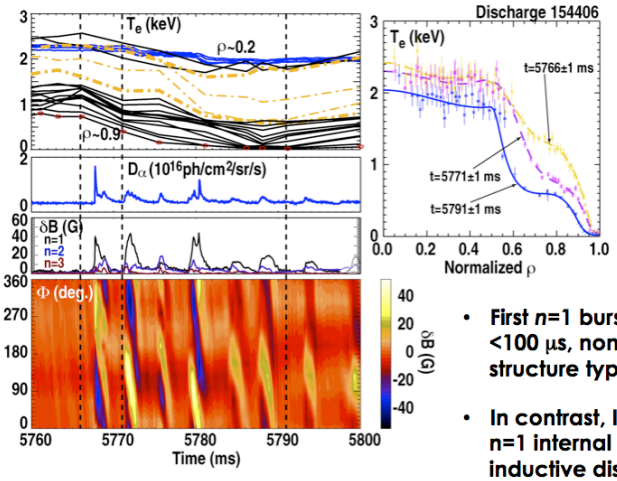

- **ITB maintained at large minor radius despite large ELMs**
- **First *n*=1 burst has growth time <100 μs, non-sinusoidal spatial structure typical of ELM**
- **In contrast, ITB terminated by n=1 internal mode in higher Ip, inductive discharges →**
  See Xu et al, today @ 16:00

At Maximum β_N these Discharges Operate Against the Kink Beta Limit with Ideal DIII-D Wall

- Mode becomes unstable for ideal wall at position of DIII-D wall
- Large plasma-wall separation (dictated by need to reduce wall heating by fast ion losses) reduces ideal-wall beta limit

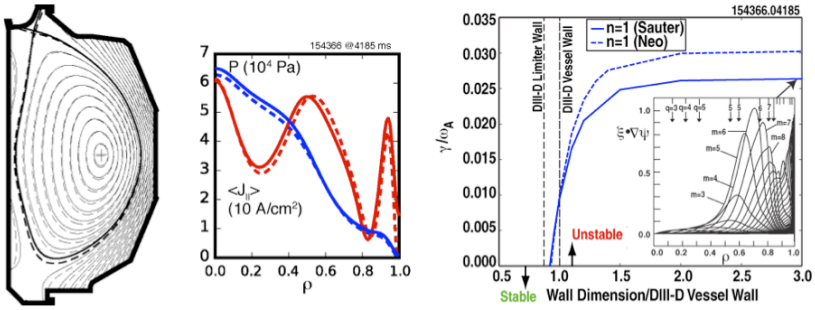

- ELMs can become particularly large as β_N is pushed against the ideal-wall kink limit because of amplification of the low-n components

Tailored Outer Gap Waveform Enables Higher Beta Without Unacceptable Levels of Wall Heating

- Outer gap is reduced as the density increases toward flattop
- Smaller outer gap increase the ideal-wall beta limit
- Measured growth time of limiting n=1 mode consistent with ideal-MHD mode driven through stability boundary
  [Callen, PoP 1999]

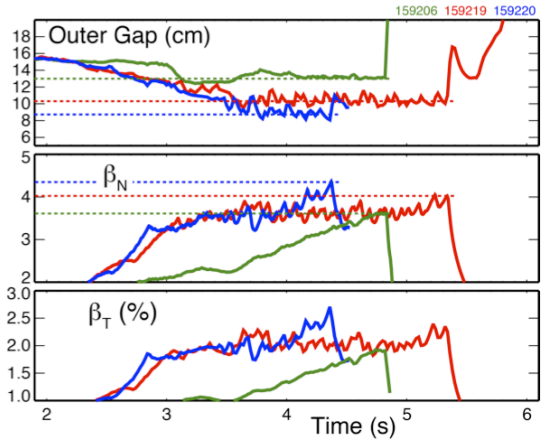

Record β Values Sustained with Strong ITBs

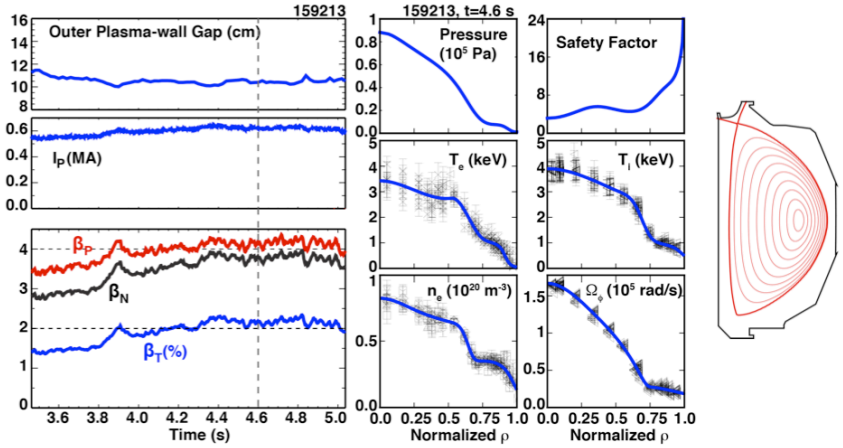

- High beta phase terminates due to NBI pulse length limitation

Emerging Synergy Between Increasing β_N and Expanding ITB

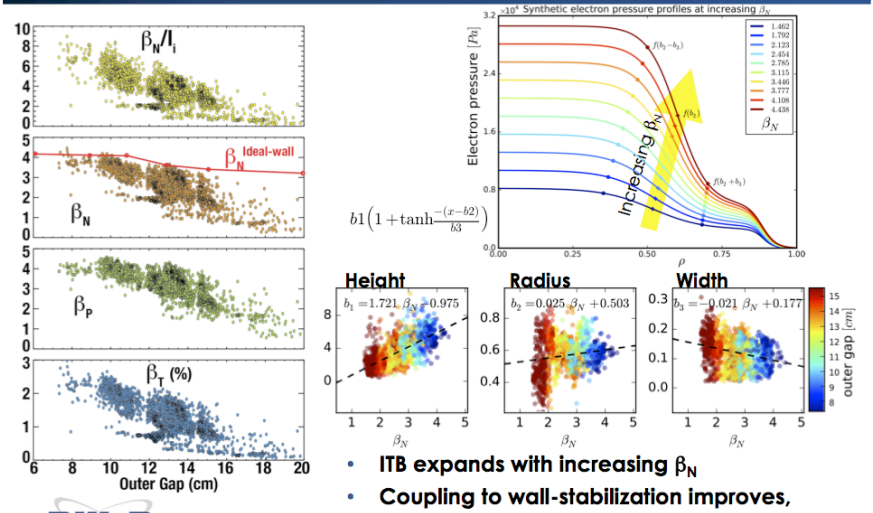

- ITB expands with increasing β_N
- Coupling to wall-stabilization improves, enabling higher β_N

Advances towards high performance low-torque $q_{min} > 2$ operations with large-radius ITB on DIII-D

G.S. Xu[1], W.M. Solomon[2], A.M. Garofalo[3], Q. Wang[1], S.Y. Ding[1], Y. Zhao[1], Z. Yan[4], G.R. McKee[4], J.R. Ferron[3], A.W. Hyatt[3], C.T. Holcomb[5], Q.L. Ren[1], G.Q. Li[1], J.P. Qian[1], H.Q. Wang[1], Q.Q. Yang[1], L. Wang[1], X.Z. Gong[1], B.N. Wan[1]

[1]Institute of Plasma Physics, Chinese Academy of Sciences, Hefei 230031, China
[2]Princeton Plasma Physics Laboratory, PO Box 451, Princeton, NJ 08543-0451, USA
[3]General Atomics, PO Box 85608, San Diego, CA 92186-5608, USA
[4]University of Wisconsin-Madison, Madison, Wisconsin 53706, USA
[5]Lawrence Livermore National Laboratory, 7000 East Ave, Livermore, CA 94550, USA

Email: gsxu@ipp.ac.cn

Second Joint DIII-D/EAST Experiment in December 2014 to extend $q_{min} > 2$ low-torque scenario to higher I_p (0.6 → 0.8 MA) for better performance

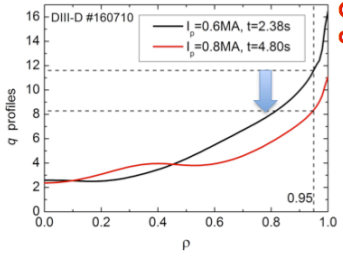

Optimized toward high fusion gain while keeping $q_{min} > 2$ and low torque, need to reduce q_{95}

Fusion gain	$G \propto \beta_T \tau_E \propto \beta_N H_{89P}/q_{95}^2$
Fusion power	$P_{fusion} \propto \beta_T^2 B^4 \propto \beta_N^2 B^4/q_{95}^2$
Steady-state	$f_{bootstrap} \propto \beta_P \varepsilon^{1/2} \propto \beta_N q_{min}$

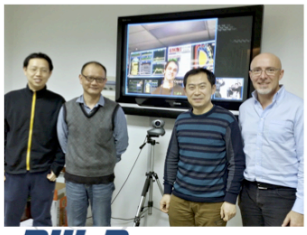

Relax the constraint of fully non-inductive. Allow some inductive current, but high $\beta_N q_{min}$, high bootstrap current fraction, thus still suitable for extension to long-pulse operation on EAST.

Given the RF-dominant heating schemes, limited beam torque and beam duration with balanced injection, and the strong off-axis current drive from LHCD and very little NBCD due to the nearly perpendicular injection, EAST plasmas are anticipated to operate at low torque and $q_{min}>2$.

Extremely high confinement (H_{89P} ~ 3.5, H_{98y2} ~ 2.1) achieved at I_p = 0.8 MA with an ITB at large-minor-radius (ρ = 0.6-0.7) mainly in the electron channel

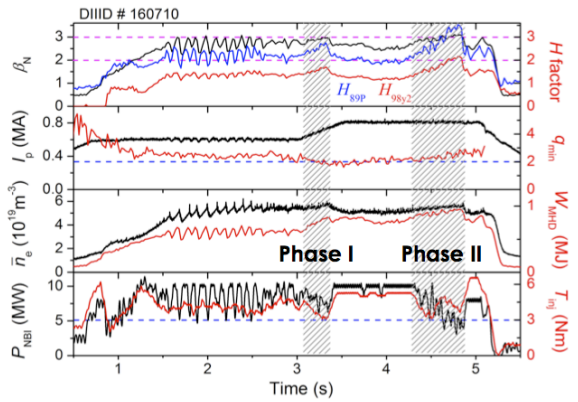

- Phase I : ITB triggered by I_p ramp up from 0.6 to 0.8 MA
- Phase II : ITB formed spontaneously at I_p = 0.8 MA
- β_N feedback control with target at 3.0
- $q_{min} \geq 2$ is achieved with B_T = 2.0 T
- W_{MHD} up to1MJ
- $G = H_{89P}\beta_N/q_{95}^2 = 0.16$

However, the high confinement state was sustained only for ~150 ms and the beam torque T_{inj} only down to ~ 3 Nm. We couldn't achieve even lower torque and rotation mainly due to reduced counter-beam power in order to avoid frequent photodiode trip-off. Further experiments with better beam availability are required.

11 DIII-D NATIONAL FUSION FACILITY SAN DIEGO

Phase I : formation of steep electron ITB (both in T_e and n_e, not in T_i) triggered by I_p ramp up

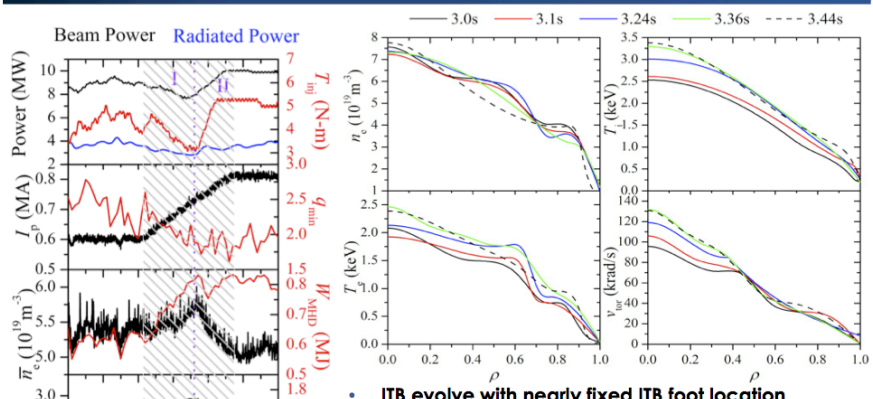

- ITB evolve with nearly fixed ITB foot location
- No obvious MHD modes trigger the ITB collapse
- ITB collapses perhaps as the pulse of the induced current travels to smaller minor radius, changing the q-profile in an unfavorable way.

12 DIII-D NATIONAL FUSION FACILITY SAN DIEGO

Why the high confinement state was not sustained?

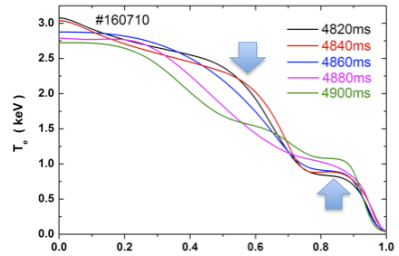

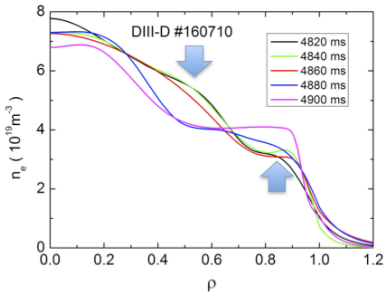

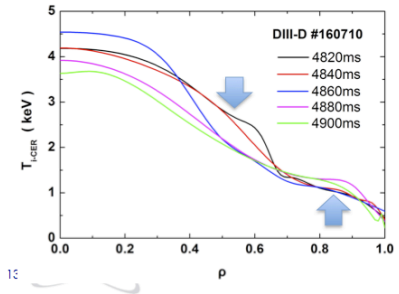

- In Phase II (I_p = 0.8 MA)
- ITB collapses without pedestal collapse.
- Pedestal is enhanced in n_e, T_e and T_i.

13

The ITB collapse is induced by n = 1 MHD modes at the ITB location (ρ ~ 0.6), which is triggered by ELMs

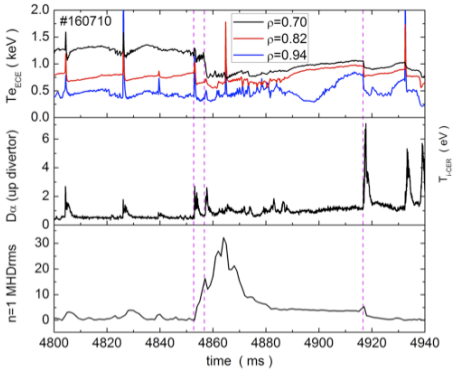

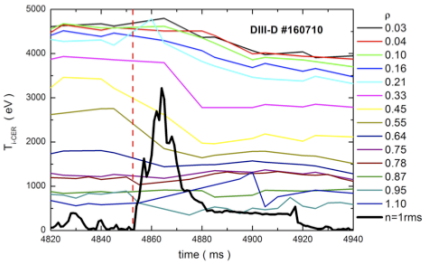

- n = 1 MHD mode is triggered by an ELM at 4853 ms.
- After 4-ms grow in mode amplitude, ITB collapse at 4857 ms.

CER T_i signals show the collapse starts from ρ ~ 0.6, which is roughly the ITB steep gradient region

14

Different from the low I_p (0.6 MA) fully non-inductive case, where the 'relaxation oscillation' identified as repetitive pedestal collapse triggered by n=1 external mode, while the ITBs were maintained.

"Relaxation Oscillations" Identified as Repetitive Buildup and Collapse of H-mode Pedestal

- Previously believed to be caused by internal modes driven by ITB [Politzer et al., NF 2005]

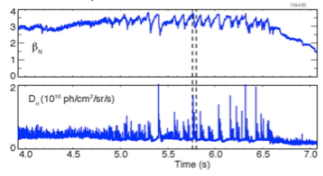

- Strong impact of the oscillations on the β_N waveform
- Let's take a detailed look into one of these stored energy oscillations:

32

Stored Energy Drop Caused by Bursts Of *n*=1 External Mode, Driven by Pedestal Gradients

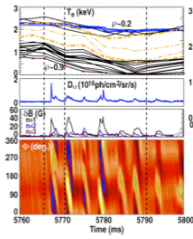

- ITB maintained at large minor radius despite large ELMs
- First *n*=1 burst has shorter growth time (<100 μs), more localized spatial structure (typical of ELM)
- Following bursts have longer growth time ≥200 μs, more sinusoidal (kink at ideal-wall limit

9

A.M. Garofalo/IAEA/Oct. 2014

One difference with the low I_p fully non-inductive discharges is the inductive fraction.

15

2.2: Fast-ion transport in $q_{min}>2$, high-β steady-state scenarios on DIII-D

The following manuscript was submitted to and accepted by Physics of Plasmas. The reference for the published article is C.T. Holcomb et al., Phys. Plasmas **22** 055904 (2015).

Fast-ion transport in $q_{min} > 2$, high-β steady-state scenarios on DIII-D

C. T. Holcomb,[1] W. W. Heidbrink,[2] J. R. Ferron,[3] M. A. Van Zeeland,[3] A. M. Garofalo,[3] W. M. Solomon,[4] X. Gong,[5] D. Mueller,[4] B. Grierson,[4] E. M. Bass,[3] C. Collins,[2]
J. M. Park,[6] K. Kim,[6] T. C. Luce,[3] F. Turco,[7] D. C. Pace,[3] Q. Ren,[5] and M. Podesta[4]

[1]*Lawrence Livermore National Laboratory, Livermore, California 94551, USA*

[2]*Department of Physics and Astronomy, University of California Irvine, Irvine, California 92697, USA*

[3]*General Atomics, P.O. Box 85608, San Diego, California 92186-5608, USA*

[4]*Princeton Plasma Physics Laboratory, P.O. Box 451, Princeton, New Jersey 05843, USA*

[5]*Chinese Academy of Sciences, Institute of Plasma Physics, Hefei, Anhui 230031, China*

[6]*Oak Ridge National Laboratory, P.O. Box 2008, Oak Ridge, Tennessee 37831, USA*

[7]*Columbia University, 2960 Broadway, New York, New York 10027, USA*

Abstract. Results from experiments on DIII-D [J.L. Luxon, *Fusion Sci. Technol*. **48**, 828 (2005)] aimed at developing high β steady-state operating scenarios with high-q_{min} confirm that fast-ion transport is a critical issue for advanced tokamak development using neutral beam injection current drive. In DIII-D, greater than 11 megawatts of neutral beam heating power is applied with the intent of maximizing β_N and the noninductive current drive. However, in scenarios with $q_{min} > 2$ that target the typical range of q_{95} = 5-7 used in next-step steady-state reactor models, Alfvén eigenmodes cause greater fast-ion transport than classical models predict. This enhanced transport reduces the absorbed neutral beam heating power and current drive and limits the achievable β_N. In contrast, similar plasmas except with q_{min} just above 1 have approximately classical fast-ion transport. Experiments that take $q_{min} > 3$ plasmas to higher β_P with q_{95}=11-12 for testing long pulse operation exhibit regimes of better than expected thermal confinement. Compared to the standard high-q_{min} scenario the high β_P cases have shorter slowing-down time and lower $\nabla\beta_{fast}$, and this reduces the drive for Alfvénic modes, yielding nearly classical fast-ion transport, high values of normalized confinement, β_N, and noninductive current fraction. These results suggest DIII-D might obtain better performance in lower-q_{95}, high-q_{min} plasmas using broader neutral beam heating profiles and increased direct electron heating power to lower the drive for Alfvén eigenmodes.

PACS Nos.: 52.25.Xz, 52.35.Bj, 52.55.Fa, 52.55.Pi

I. Introduction

Understanding superthermal fast-ion transport caused by interaction with Alfvén eigenmodes (AEs) is an important aspect of steady-state scenario development in existing tokamaks heated by neutral beam injection (NBI). The DIII-D program is testing a range of potential high-β, fully noninductive operating scenarios for next-step long pulse tokamaks leading up to the development of a fusion power plant. Primarily the shape of the current density profile distinguishes the scenarios from each other, and this ranges from strongly peaked to very hollow. Access to this range of profiles is provided by adjustable NBI and electron cyclotron heating (ECH) and current drive (ECCD).

Presently and for the near future the available NBI power on DIII-D is at least 3 times greater than the available ECH power, so most high-β scenario exploration is dominated by NBI power. In such cases the classically predicted β_{fast} can approach ~40% of β_{total}. Low-density operation is often chosen because this is expected to maximize the non-inductive current drive [1]. There are plans to increase both the NBI and ECH power, including more off-axis NBI. The classical fast-ion slowing down time on thermal electrons is proportional to $T_e^{3/2}/n_e$, where T_e is the electron temperature and n_e is the density [2]. If significant increases in NBI and ECH power were applied to future plasmas then the classical slowing-down time would increase, especially at low density, and the classically predicted fast-ion fraction $\beta_{fast}/\beta_{total}$ could increase. Such changes would increase the possibility for interaction between fast-ions and AEs. This may cause enhanced (i.e. higher than classical prediction) fast-ion transport that may take the form of redistribution to higher radius or loss to the wall. Enhanced fast-ion transport can reduce the power that would otherwise be absorbed by the thermal plasma, and it can reduce or redistribute

the NBI current drive [3]. Therefore, understanding how candidate steady-state operating scenarios can affect the drive and damping of fast-ion modes is essential.

The prototypical high-β steady-state scenario envisioned for many future devices uses an elevated q-profile. Various ITER steady state scenario models have $q_{\min} > 2$ with β_N near 2.5-3 [4,5]. A Fusion Nuclear Science Facility design (FNSF-AT) uses $q_{\min} > 1.4$ with strong negative central shear at $\beta_N = 3.7$ [6]. The ARIES-AT design uses $q_{\min} = 2.4$ and $\beta_N = 5.4$ [7]. All of these designs are based on several predicted advantages for steady-state operation at high $q_{\min}$. These include (i) a high ideal-wall kink mode β limit when the current density is sufficiently broad or hollow to produce strong coupling to a nearby conducting wall [8], (ii) a high bootstrap current fraction, which scales as β-poloidal (β_P) or $q\beta_N$ [9], (iii), avoidance of low-order tearing modes by exclusion of rational surfaces from the plasma, e.g. the $m/n = 2/1$ tearing mode when $q_{\min} > 2$ [10], and (iv) thermal confinement exceeding typical H-mode levels enabled by weak or negative magnetic shear [11].

Present experiments can test physics that goes into predictive models for next-step steady-state devices. For example, one can test if a proposed current profile is capable of sustaining the target value of β_N without encountering resistive tearing modes. Also of interest is whether or not the current profile is consistent with the expected transport and energy confinement.

Such questions motivated several experiments on DIII-D to identify β_N limits in steady-state scenario plasmas with $q_{\min}$ sustained above 2. The experiments identified unexpected 20%-30% differences in the normalized global energy confinement between two different regimes. Both regimes were tested with toroidal field 1.75-2.1 Tesla, and in double-null shapes. The “standard

high-q_{min}" regime has q_{min} = 2-2.5, q_{95} = 5-7, line-density = $3.5 - 4.5 \times 10^{19}$ m^{-3}, I_P = 0.8-1 MA, and Greenwald fraction [12] near 0.5. These conditions were chosen to target fully noninductive operation with a significant fraction of externally driven current, and projected fusion gain sufficient for next-step tokamaks like FNSF. In these plasmas β_N is usually limited to about 3 by the available power, and the normalized global energy confinement H_{89P} [13] is typically 1.6-1.8 [14]. A "high-β_P" regime developed for testing long-pulse operation on the EAST tokamak [15] has q_{min} = 3-5, q_{95} = 11-12, line-averaged density = $5 - 6.5 \times 10^{19}$ m^{-3}, I_P = 0.6-0.65 MA, and Greenwald fraction near 1. β_N is limited to about 4 by instability rather than by confinement, and H_{89P} = 2-3.

This paper discusses measurements and modeling that confirm that differences in AE stability and enhanced fast-ion transport account for the observed large variation in normalized confinement. To summarize, in standard high-q_{min} plasmas many AEs are unstable across a majority of the plasma radius, and these lead to fast-ion transport greater than that predicted by classical theory. This limits the absorbed heating power and limits the achievable β_N. Similar plasmas having q_{min} just above 1 have less AE activity and approximately classical fast-ion transport. A detailed paper on fast-ion measurements in these discharges was recently published [27]. High-β_P plasmas have better than expected total energy confinement because of the presence of either a high-radius transport barrier or a high pedestal pressure. In these cases the fast ion transport approaches the classical level. This is due to lower drive for AEs near the axis caused by a lower gradient in the fast ion pressure. These results suggest that increasing global confinement and β_N in high-q_{min} plasmas at lower q_{95} might be achieved by broadening the

NBI and ECH heating profiles to reduce core AE activity, and further optimization of thermal transport.

II. Comparison of high- and low-q_{min} discharges having q_{95} = 5-7

The current density or q-profile is a key attribute of the equilibrium that may be adjusted to optimize steady-state operation and projected fusion power gain. Most potential steady-state scenarios tested on DIII-D for use in a next-step reactor have q_{95} in the range of 5-7 during the high-β_N phase of the discharge when the inductive current fraction is minimized. By adjusting the L-to-H-mode transition time and the starting time of high-power NBI and ECH, $q_{\min}$ during the high-β_N phase can be set to a value between ~1 and ~2.5. At the low end of this range are scenarios like the "high-l_i" [16] and "steady-state hybrid" [17] that have potential applicability in next-step reactors. These tend to have good total energy confinement, i.e. $H_{89P} \geq 2$, and approximately classical fast-ion confinement. This paper focuses on fast-ion transport in high-$q_{\min}$ plasmas, but comparison of similar high- and low-$q_{\min}$ plasmas serves to elucidate many of the effects.

Figure 1(a) compares the q-profiles obtained during the high-β_N phases of a pair of consecutive discharges. During the time range t = 3.2-3.7 s the case with $q_{\min} \approx 1$ obtained $\beta_N = 2.9$ using 8 MW of NBI and 1.3 MW of ECH at $H_{89P} = 2.2$. During the same time period the case with $q_{\min} \approx 2$ obtained $\beta_N = 2.6$ using 9.4 MW of NBI and 1.3 MW of ECH at $H_{89P} = 1.8$. During the analysis time period, both discharges use the same boundary shape and have density profiles with the same shape, but the $q_{min} \approx 2$ case is about 10% lower density at all radii. The ion and electron temperature profiles outside ρ=0.5 are the same within 10%, but inside ρ=0.5 the $q_{min} \approx 2$ case has significantly lower temperature, i.e. 20% lower Te(0) and 25%

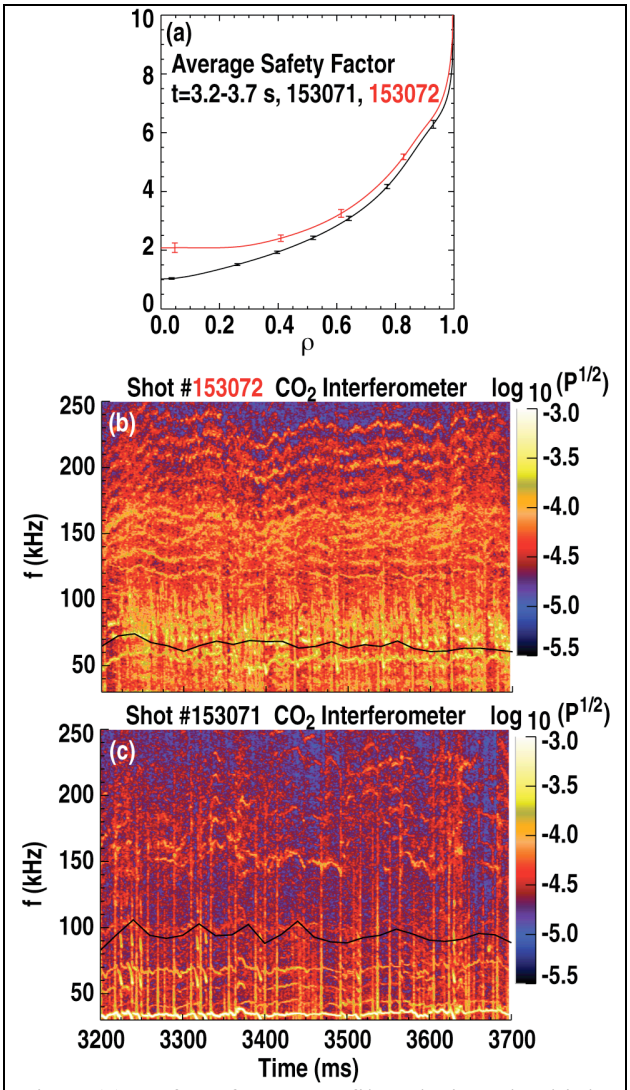

Fig. 1(a) Safety factor profiles during the high-β_N phase of two discharges. (b,c) Cross-power density fluctuation spectra vs time from CO_2 interferometer chords showing AEs for the (b) high-q_{min} case and (c) low-q_{min} case. The solid black lines denote the TAE frequency at the magnetic axis.

lower Ti(0). Due to these differences, the $q_{min}\approx 2$ case has about a 20% shorter classical fast-ion slowing-down time at the magnetic axis than the $q_{min}\approx 1$ case. While a shorter on-axis slowing-down time might be expected to result in lower Alfvénic activity, the observations show otherwise. The cross-power density-fluctuation spectra between the two most central interferometer chords shows significantly more toroidal Alfvén eigenmode (TAE) [19] activity in the plasma with $q_{\min} \approx 2$ than the plasma with $q_{\min} \approx 1$ [Fig. 1(b,c)]. To quantify this, the average amplitude of coherent modes with frequency in the TAE frequency band [27] is about four times higher in the high-$q_{\min}$ plasma. A plastic scintillator neutron counter measured a ~43% lower signal in the high-$q_{\min}$ case compared to the low $q_{\min}$-case.

The apparent correlation between higher AE activity, lower neutron rate, and lower normalized global energy confinement suggests that enhanced fast-ion transport could be a significant energy loss channel. All of the direct fast-ion loss detectors on DIII-D only work when $I_P > 0$ and $B_T < 0$ because this is the configuration used by most experiments. All experiments described in this paper use $I_P > 0$ and $B_T > 0$ to maximize the off-axis NBI current

drive that helps maintain elevated $q_{\min}$, and therefore no direct measurements of fast-ion loss exist. Instead, enhanced fast-ion transport above the classically predicted level is inferred by

comparing two ways to compute the plasma total stored energy. First, the EFIT code [20] is used for equilibrium reconstructions by fitting to magnetic measurements outside the plasma. This method accurately determines the total stored energy W_{EFIT} to better than 3% over the range of β_P obtained in this study. This is based on a Monte-Carlo statistical analysis of magnetic reconstructions with a 3% uncertainty in external magnetic measurements as described in section 3.2 of reference 20. The second method is to use the ONETWO transport code [21] to compute the total stored energy W_C, using the magnetic geometry, measured density and temperature profiles, and NBI power and injection angles as inputs. The NUBEAM Monte Carlo code [22] is used to compute the fast-ion distribution function assuming that the fast-ion transport is completely classical. NUBEAM does not account for possible neutral beam ionization in the scrape-off layer. This is estimated to be up to 3%-4% of the beam power depending on the scrape-off layer density. Figure 2 shows the values of W_{EFIT} and W_C determined from both approaches for the two discharges in Fig. 1. Figure 2(b) shows the percentage that W_C overestimates W_{EFIT} – a value that will be referred to as the "stored energy overestimate" throughout this paper. The plasma with $q_{\min} \approx 1$ has good agreement between the measured and computed total stored energies – the

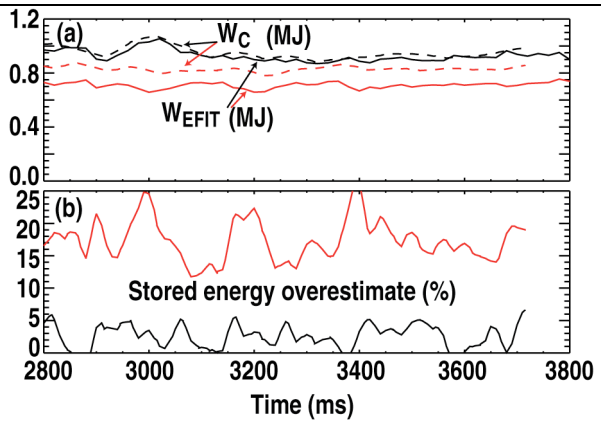

Fig. 2 (a) Comparison of W_C and W_{EFIT} vs time for the discharges shown in Fig. 1. (b) Stored energy overestimate defined as $\left(W_C - W_{\mathrm{EFIT}}\right)/W_{\mathrm{EFIT}}$.

average stored energy overestimate during the high β_N phase shown is 3%. Therefore, within the uncertainties, classical fast-ion transport is an accurate description for this plasma. In contrast the high-$q_{\min}$ case W_C overestimates W_{EFIT} by an average of 17%. This overestimate is interpreted as an indication of fast ion redistribution and/or loss.

Fast-ion D_α (FIDA) diagnostic measurements [23] confirm that high-$q_{\min}$ plasmas can have a deficit of fast ions compared to the level expected classically. Several FIDA views are available on DIII-D, but in steady-state scenario plasmas these do not routinely make useful measurements without careful design of the various NBI source waveforms. This must be done to provide background subtraction and temporally isolate "signal" beams the diagnostic is tuned to from "polluting" beams that it is not. This was done for the pair of discharges in Figs. 1 and 2.

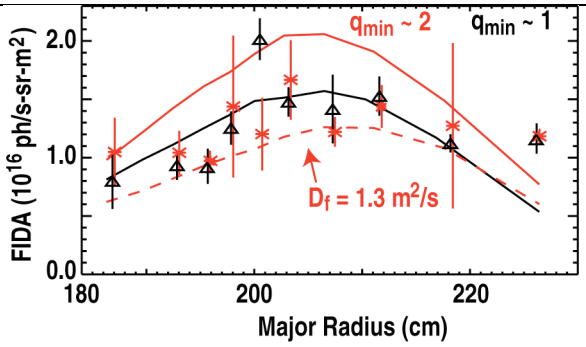

Fig. 3. Plot of fast-ion brightness (proportional to fast-ion density) vs major radius from the vertical FIDA views for the two discharges shown in Fig. 1. Solid lines: *FIDASIM* code predictions using classical fast-ion transport. Symbols: actual measurements. Dashed line: *FIDASIM* prediction for the high-$q_{\min}$ case after applying uniform fast-ion diffusion above the classical level. The FIDA spectra are summed over wavelengths of 650.5-652.7 nm, which corresponds to energies along the line-of-sight of 25-68 keV.

Figure 3 compares measurements from a vertical-viewing FIDA array with synthetic diagnostic predictions using the FIDASIM code [24]. The solid lines are the FIDASIM predictions for the high- and low-$q_{\min}$ cases using a classical fast-ion transport assumption. The classical prediction for the high-$q_{\min}$ case exceeds that of the low-$q_{\min}$ case. However, the FIDA measurements are at approximately the same level for both cases, so that the classical prediction roughly matches most measurements for $q_{\min} \approx 1$, but the classical prediction is higher than the measurements for

$q_{\min} \approx 2$. The dashed line is the FIDASIM prediction for the $q_{\min} \approx 2$ case after applying an ad-hoc uniform fast-ion diffusion profile. A value of 1.3 m^2/s was chosen because this makes the computed stored energy and neutron rate approximately match the experimental values. This value improves the match between prediction and experiment, although no attempt was made to find a fast-ion diffusion profile that might make a best fit to the FIDA data.

For the $q_{\min} \approx 2$ case, if only the inferred absorbed NBI power (i.e. what is left after applying an ad-hoc fast-ion diffusion) is included in the calculation, then H_{89P} rises from 1.8 to 2.2. This again implies that enhanced fast ion transport is the primary reason for lower normalized confinement at $q_{\min} > 2$. Power balance analysis with the inferred absorbed power finds that the thermal diffusivities do not differ significantly between the high- and low-$q_{\min}$ cases. Thus, under the presumption that NBI power is redistributed by Alfvénic modes this particular high-$q_{\min}$ plasma has thermal transport similar to the low-$q_{\min}$ case. It is possible that any expected increase in thermal transport with q is being offset by a decrease due to lower shear [25]. But without significantly improved thermal transport the $q_{\min} \approx 2$ case has $H_{89P} < 2$ because the fast-ions are not classically confined.

Degraded fast-ion confinement in the presence of enhanced AE activity is reproducibly observed by all fast-ion diagnostics that are sensitive to the co-passing portion of velocity space. Figure 4 compares classical and measured signals for the stored energy, volume-averaged neutron rate, and vertically-viewing FIDA diagnostic in several quasi-stationary discharges with q_{95} = 5-12. The classically predicted neutron signals are derived from a zero-dimensional prediction of the beam-plasma collision rate [26], and the FIDA data and the fast-ion stored

energy points are from the carefully analyzed discharges of Ref. 27. When there are many coherent AEs, the classical prediction overestimates the measured signals. The four discharges with a neutron overestimate greater than 100% are all at the lowest current (0.5-0.65 MA) in the group and they have quite strong AEs at ρ=0.6-0.7.

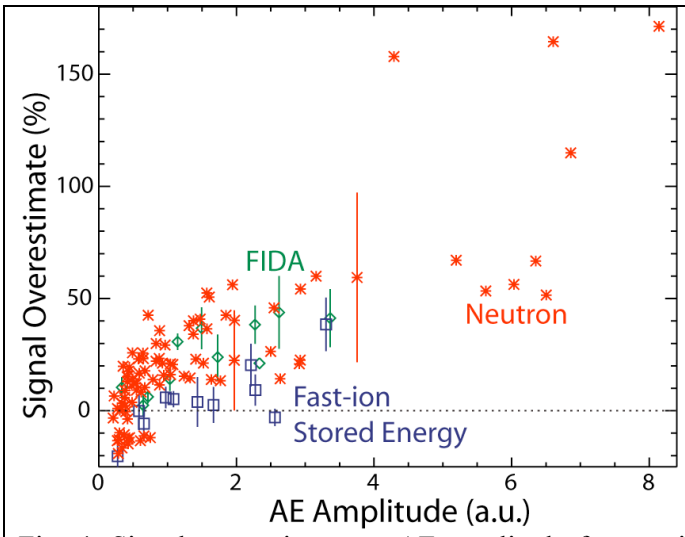

Fig. 4. Signal overestimate vs AE amplitude for quasi-stationary discharges from the 2013 and 2014 experimental campaigns. The overestimate is defined as (classical prediction – signal)/signal. The AE amplitude is the time average of coherent modes in the TAE band inferred from interferometer signals. Representative error bars associated with the 15% uncertainty in the absolute neutron calibration are shown.

Local fluctuation diagnostics show that the AE activity occurs throughout much of the plasma volume. Figure 5 shows electron cyclotron emission (ECE) [30] measurements of the AE profile for three coherent modes in a quasi-stationary discharge with $\beta_N = 2.8$, $q_{min} = 2.5$, $q_{95} = 6.9$, and $H_{89P} = 1.4$. The mode at 113 kHz is located near the q_{min} radius, which is at a normalized minor radius of $\rho = 0.37$ in this discharge; this is probably a reverse-shear AE [31]. The mode at 137 kHz is localized near the top of the H-mode pedestal. The mode at 153 kHz is a global mode, probably a TAE.

Both the MHD code NOVA-K [36,37] and the gyrokinetic code GYRO [32] predict AE instability for high-q_{min} plasmas. For example, GYRO was used to predict the eigenfunctions of AEs in the pair of discharges shown in Fig. 1. The calculations were performed in the range ρ = 0.2-0.8. The fast-ion pressure profiles supplied as inputs are those that result after any fast-ion diffusion needed to match the measured total stored energy is applied, i.e. for the high-q_{min}

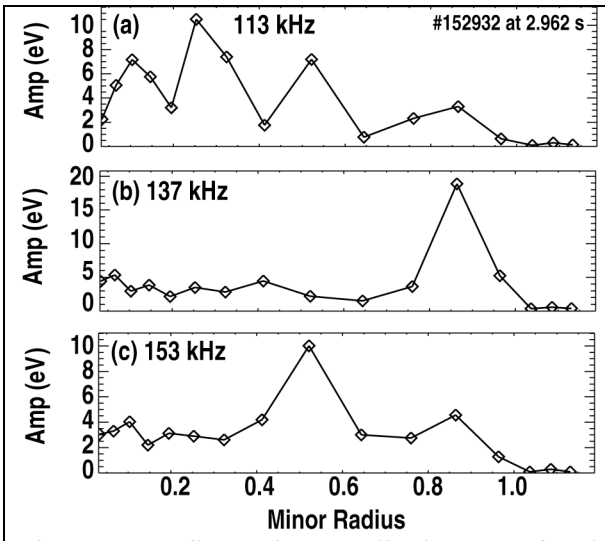

Fig. 5. ECE fluctuation amplitude vs ρ for three coherent modes in a discharge with degraded fast-ion and global confinement.

case the fast-ion pressure is lower than the classical prediction. Figure 6 compares the electrostatic potential of the most unstable eigenfunction for an $n = 4$ mode. The case with $q_{\min} = 2$ has the potential for AEs extending out to higher radius. Figure 6(b) compares the growth rates for a range of n. The high-$q_{\min}$ case has larger growth rate than the low-$q_{\min}$ case for n = 2-13. If the classically predicted fast ion pressure is used for the high-$q_{\min}$ case, then the predicted growth rates are significantly higher. (The low-$q_{\min}$ case fast ion pressure is already approximately classical).

Theoretically, the many modes cause fast-ion transport through resonance overlap [28,29]. Figure 7 illustrates this last point by comparing phase space diagrams for a pair of steady-state scenario plasmas at high- and low-$q_{\min}$. In both, the possible fast-ion orbits are gray symbols. Black symbols show where the NBI sources used in the discharge actually populate phase space with fast ions. Red symbols denote possible fast ion orbits that can resonate with the various AEs that were observed in the discharge. Where red and black

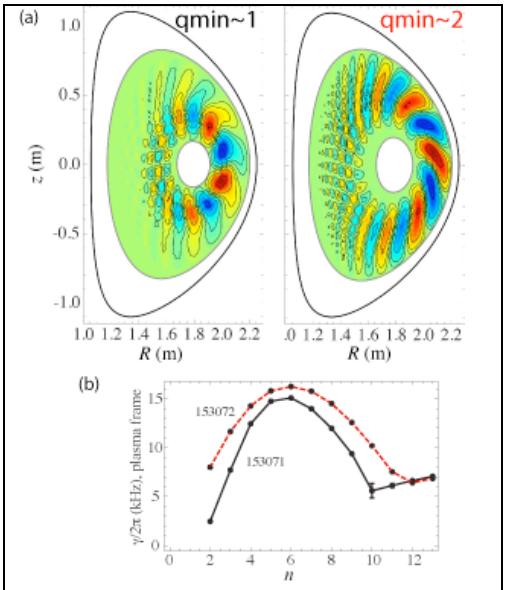

Fig. 6. GYRO eigenvalue solver code predictions for (a) the electrostatic potential of the most unstable eigenfunction for an $n = 4$ mode; and (b) growth rates for a range of toroidal mode numbers.

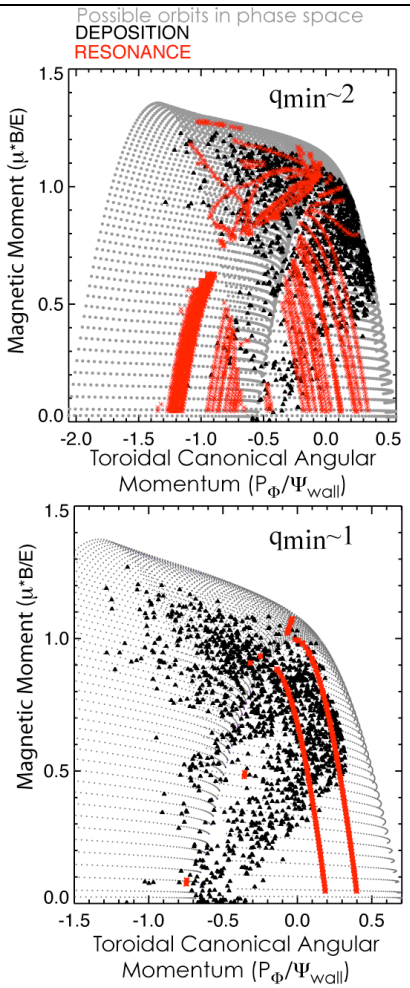

Fig. 7. Plots of possible fast-ion orbits in phase space for (a) a high-$q_{\min}$ discharge and (b) a low-$q_{\min}$ discharge. Gray points: all possible orbits. Black points: actual fast-ion orbits at the time of deposition produced by the NBI combinations used in the discharge. Red points: orbits computed to be resonant with observed AEs.

symbols overlap – i.e. where actual fast-ion orbits are capable of resonating with observed modes – there is the possibility for fast ion redistribution to other parts of phase space, including to loss orbits. While the case with $q_{\min} = 1$ has little overlap, the case with $q_{\min} = 2$ has substantial overlap.

In summary, the standard high-$q_{\min}$ steady-state scenario is observed to have lower than expected global energy confinement, substantial AE activity, and a deficit of confined fast ions compared to classical predictions. The negations of these statements are true for similar low-$q_{\min}$ plasmas. AE stability calculations confirm that the high-$q_{\min}$ plasmas have greater potential for instability and fast-ion transport than the low-$q_{\min}$ plasmas. This implies an important question: is high-$q_{\min}$ by itself necessarily bad for fast-ion transport and global energy confinement? Section III will show that the answer to this question is "no".

III. High q_{min} with high β_P

Very high $q_{\min}$ in the range of 3-5 has been sustained with $H_{89P} \geq 2$ in the DIII-D "High-β_P" regime [33–35] that is used to prepare for long-pulse operation on superconducting tokamaks like EAST. Fully noninductive plasmas sustained by 70%-80%

bootstrap current fraction and the 20%-30% NBI + ECCD have been produced in the following parameter ranges: β_N = 3-4, β_P = 3-4, β_T = 1.5%-2.5%, q_{95} = 11-12.5, I_P = 600-700 kA, and B_T = 2 Tesla. The line-density through the magnetic axis is typically in the range $5.5 - 6.5 \times 10^{19}$ m^{-3}. Successful shots with both thermal and total-energy confinement at or above levels expected for H-mode [18] (i.e. $H_{98P} \geq 1$ and $H_{89P} \geq 2$) have either a high radius ($\rho \approx 0.7$) transport barrier or infrequent edge localized modes (ELMs) and a high average pedestal pressure. Figure 8 shows time traces and profiles for an example High-β_P discharge.

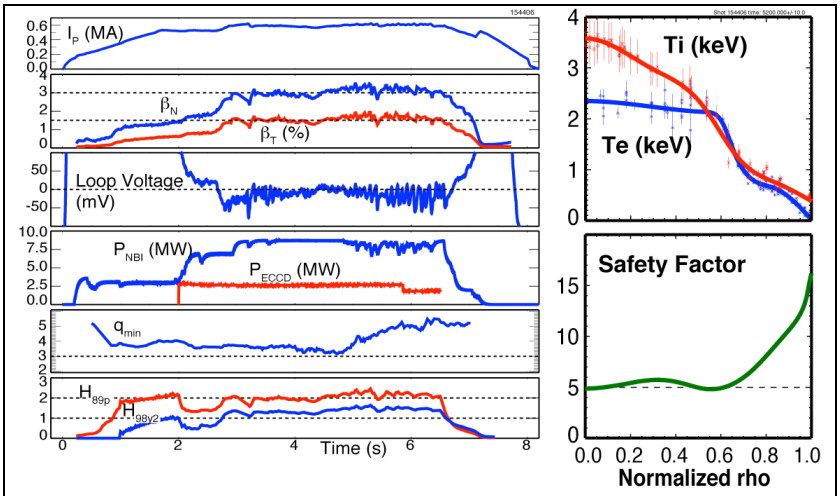

Fig. 8. Features of a high-β_P discharge. Left: time histories of (from top to bottom) I_P, β_N and β_T, surface loop voltage, NBI and ECCD power, q_{min}, H_{89P} and H_{98y2}. Right: radial profiles of electron and ion temperature and q at t = 5200 ms.

High-β_P plasmas with $H_{89P} \geq 2$ have inferred fast-ion transport near the classical level. Figure 9 compares a standard high-q_{min} case and a high-β_P case. Whereas the standard case has $q_{min} \approx 2.4$, $H_{89P} \approx 1.8$H, and a ~15% stored energy overestimate, the high-β_P case has $H_{89P} \approx 2.1$, and a stored energy overestimate of ~3% with almost double the value of q_{min}. Figure 10 shows the FIDA profile acquired between 3900-6000 ms during ELM-free phases in the same high-β_P discharge. (The absence of ELMs facilitates accurate FIDA measurements despite the relatively high density of this discharge.) Within experimental uncertainty, the FIDA, neutron, and stored energy measurements are all consistent with classical theory. The high-β_P

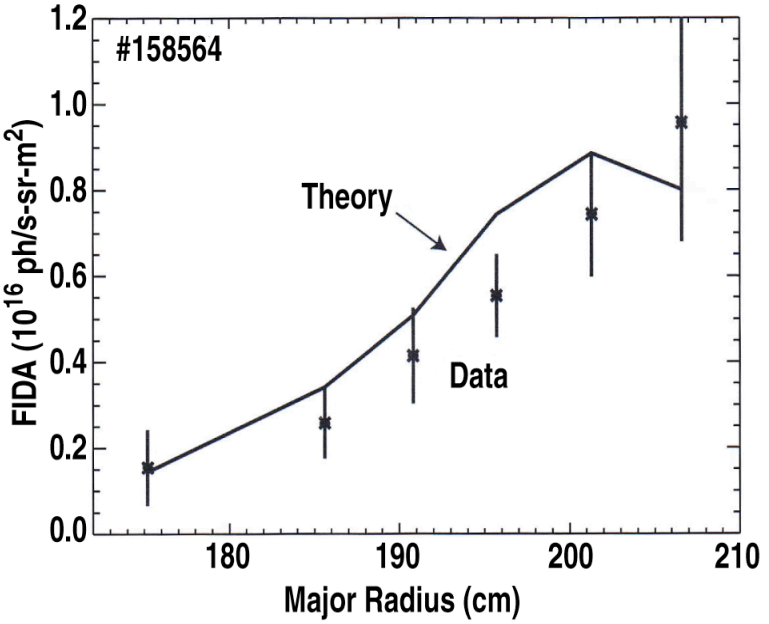

Fig. 9. Time traces of $q_{\min}$, H_{89P}, and stored energy overestimate for a standard high-$q_{\min}$ discharge and a high-β_P discharge.

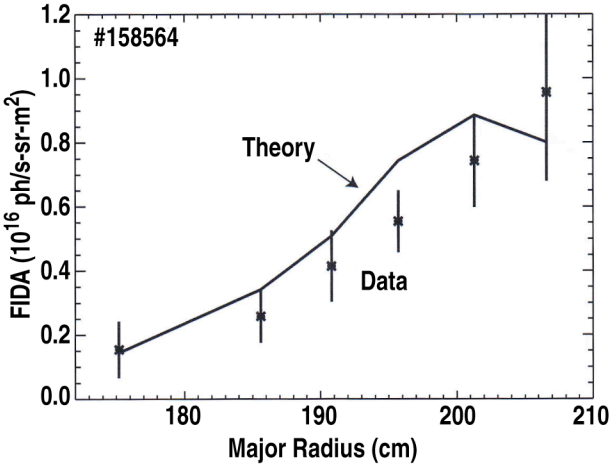

Fig. 10. FIDA profile from the oblique view that is sensitive to co-passing fast ions [C.M. Muscatello et al., Rev. Sci. Instrum. **81**, 10D316 (2010)]. The error bars represent the temporal variation of the ratio of experimental-to-theoretical values. The theoretical prediction assumes classical fast ions. The FIDA spectra are summed over wavelengths of 650.5-652.7 nm.

discharges demonstrate that very high values of $q_{\min}$ in the range of 3-5 do not invariably result in enhanced fast-ion transport or lower than expected global energy confinement. In both high-$q_{\min}$ regimes the strongest AEs observed are usually TAEs, and NOVA code [36,37] analysis (Fig. 11) of a pair of discharges finds that the core TAE gap structure inside of $\rho \approx 0.5$ is much wider for the standard high-$q_{\min}$ case than the high-β_P case. In the former case, NOVA predicts a plethora of radially-extended core TAEs that are minimally damped, while in the latter case the TAE gap only widens a similar amount outside of $\rho \approx 0.5$. Measurements of density and temperature fluctuations associated with TAEs are in qualitative agreement with these predictions. Figure 12 compares profiles of the electron temperature fluctuation frequency-spectrum measured by the electron cyclotron emission diagnostic. The standard high-$q_{\min}$ plasma has many more coherent modes

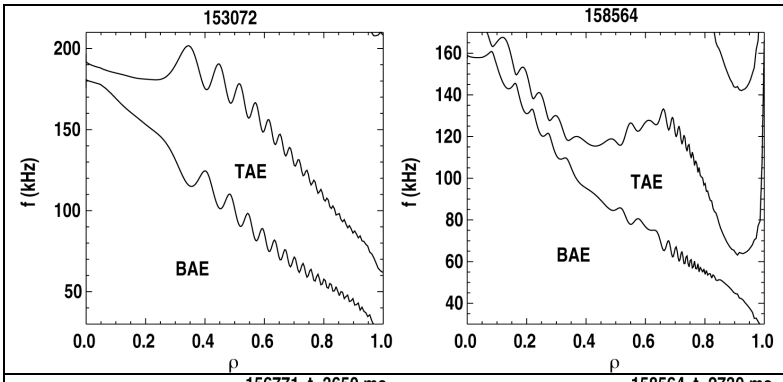

Fig. 11. *NOVA* code calculations of the TAE gap profiles for a standard high-$q_{\min}$ discharge (153072, left) and a high-β_P discharge (158564, right).

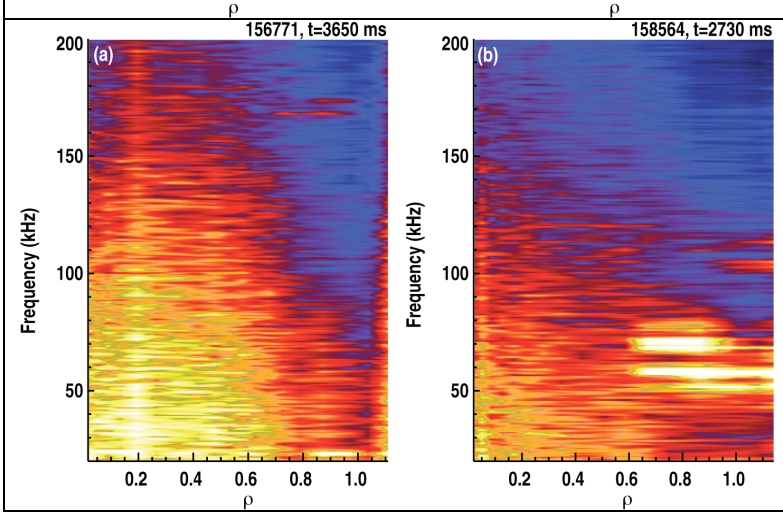

Fig. 12. Cross power spectra profiles of electron temperature fluctuations measured by the electron cyclotron emission diagnostic. Left: a standard high-$q_{\min}$ case. Right: a high-β_P case.

inside of $\rho \approx 0.5$ than the high-β_P case, which has strong modes around 60 and 70 kHz only outside of $\rho \approx 0.6$. Since in both cases the fast-ion profile is peaked on-axis, AEs near the magnetic axis are more likely to cause enhanced fast-ion transport than AEs at large radius.

The drive for core AEs is lower in high-β_P plasmas than in standard high-$q_{\min}$ plasmas because the former have a shorter slowing-down time and therefore a lower classically predicted $\nabla\beta_{fast}$ [Fig. 13(a,b)]. This is consistent with recent work [38] that suggests that the strength of

AE activity in L-mode, high-q_{min} plasmas has a critical-$\nabla\beta_{fast}$ dependence whereby the modes and fast-ion transport increase quickly above a certain value of $\nabla\beta_{fast}$. This produces stiff fast-ion transport and limits the actual fast-ion profile peaking (i.e. actual profiles show less peaking than classically predicted profiles). In the high-β_P cases, the shorter slowing-down times across the whole profile result from higher density and lower electron temperature. Profiles of these are

usually "step-like", i.e. relatively flat inside a transport barrier, rapidly changing at the barrier, and then flat again out to the H-mode pedestal barrier. Between the transport barriers, the very short slowing-down time should be more effective at thermalizing fast ions before they can be expelled from the plasma relative to plasmas without this feature.

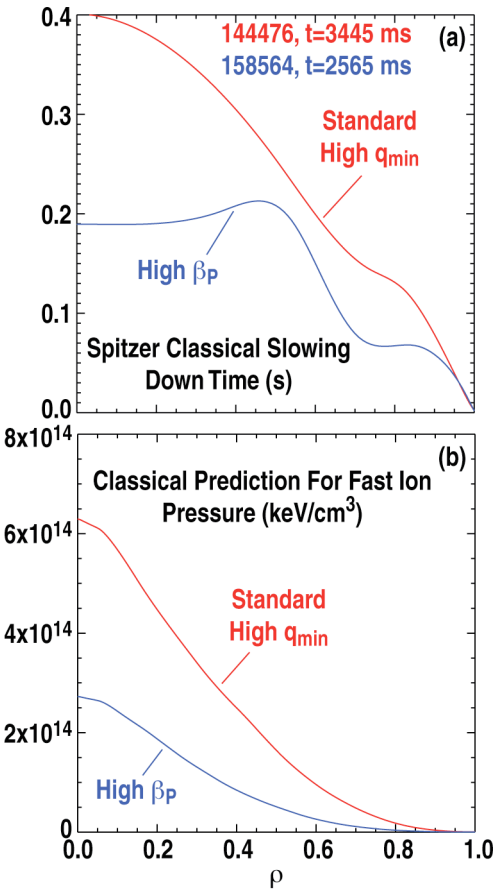

Fig. 13. (a) Profiles of the Spitzer classical slowing down time, and (b) the classically predicted fast-ion pressure.

Many observations made in high-β_P plasmas lead to the conclusion that these operate very close to a critical fast-ion gradient for enhanced transport. Reducing the density in these plasmas results in an increase in AE activity, lower confinement time and lower achievable β_N. In the example shown in Fig. 14, only the density is changed between two consecutive discharges, from a maximum of about 6.5×10^{19} m^{-3} to about 5×10^{19} m^{-3}. Lowering the density increased the slowing-down time, raised the maximum classically predicted fast-ion gradient by 50%-60%, increased the number and amplitude of AEs, and reduced H_{89P} to less than 2. Figure 15 shows another discharge in which the line-density was again about 5×10^{19} m^{-3}. As before, strong AE activity was observed. In the middle of the high-β_N phase, the total NBI power was stepped down by about 32%. After this change, the classically predicted maximum in $\nabla\beta_{fast}$ is reduced, the interferometer shows a reduction in AE amplitude, the stored energy overestimate falls from 5%-10% to close to 0 (i.e. the classical level), and remarkably, β_N remains approximately constant at

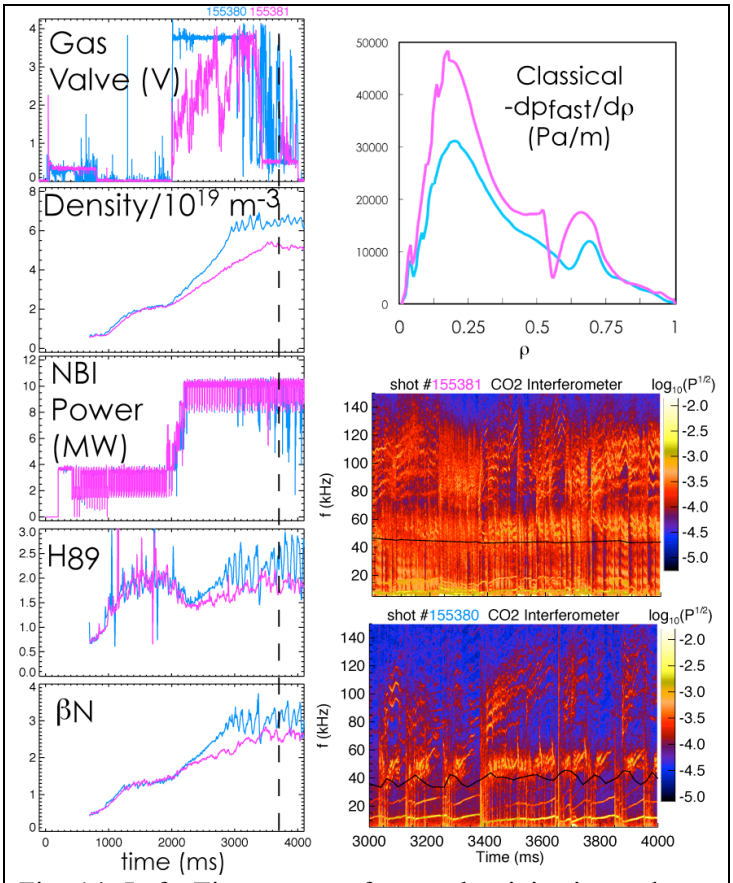

Fig. 14. Left: Time traces of gas valve injection voltage, density, NBI power, H_{89P}, and β_N for two high-β_P discharges. Right: profiles of the classically predicted fast-ion pressure gradient near t = 3700 ms, and time traces of cross-power density fluctuation spectra.

3. These observations are consistent with the NBI power reduction causing a relaxation of $\nabla\beta_{fast}$ to below a critical value and subsequently a reduction in fast-ion transport. Considering this case backwards in time (i.e. as if it were an NBI power step-up) shows that the effectiveness of NBI power to increase β_N falls rapidly once the critical gradient has been reached. Through variation of density and NBI power the classically predicted $\nabla\beta_{fast}$ can be varied. Figure 16 shows a compilation of data from different times in three high-β_P discharges. The AE amplitude and stored energy overestimate increase with increasing $\nabla\beta_{fast}$ while H_{89P} decreases. These observations are consistent with the picture of fast-ion transport increasing with $\nabla\beta_{fast}$.

The interplay between fast-ion transport and thermal transport is noteworthy for its complexity in high-β_P discharges. A correlation is observed between classical or nearly classical fast-ion confinement and the existence of either a transport barrier near $\rho = 0.7$ or a transport barrier near $\rho = 0.5$ with a higher pedestal pressure. Conversely, lower density discharges with enhanced fast-ion transport and lower H_{89P} do not have internal transport barriers or higher pedestals. Figures 17 and 18 compare pairs of discharges to illustrate these points. In Fig. 17,

both discharges had the same density feedback target waveform, but in one case more NBI power was used at early times resulting in an earlier L-to-H-mode transition time and higher $q_{\min}$. Once in H-mode, the density of both discharges followed the same trajectory until about $t = 3$ s when the higher-$q_{\min}$ case developed a transport barrier in all channels at $\rho = 0.7$. After this time the density and temperature inside the barrier rose to higher values than what was observed in the discharge without a barrier. But, the slowing-down-time profiles and classically predicted fast-ion pressure profiles did not change significantly. Thus the stored energy overestimate remained near 10% until after the NBI power was reduced at about t = 4.3 s. In this case the transport barrier apparently formed while the fast-ion transport was still higher than classical. The increase in thermal stored energy brought about by the barrier compensated for the enhanced fast-ion transport and achieved higher confinement and β_N than the case without a barrier.

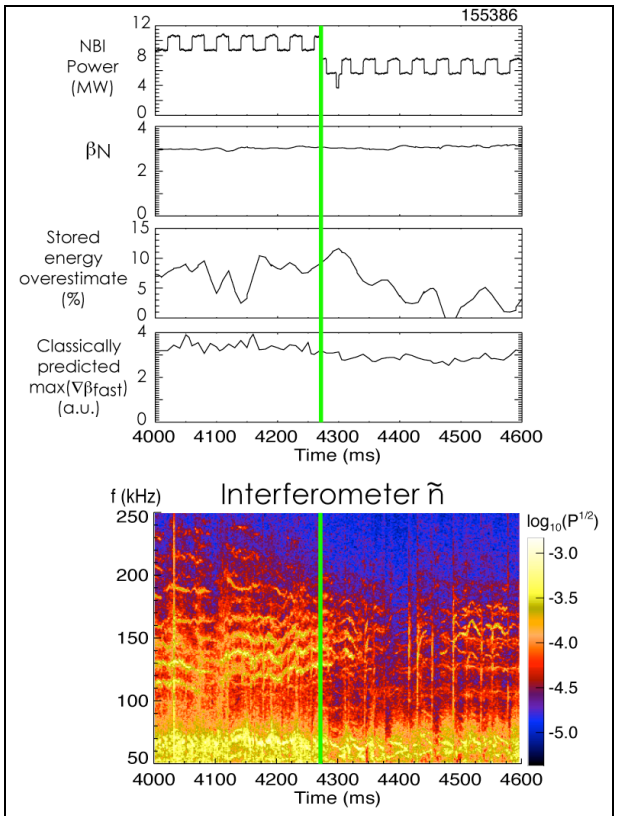

Fig. 15. High-β_P discharge time traces of NBI power, β_N, stored energy overestimate, maximum classically predicted gradient in β_{fast}, and density fluctuation spectra.

The example in Fig. 18 compares the low-H_{89P} discharge from Fig. 17 to a case programmed to have higher density for the entire discharge. The higher density case is inferred to have nearly classical fast-ion transport for the entire high-β_N phase of the discharge. After about t = 2.3 s this discharge obtains a higher average pedestal pressure, β_N, and H_{89P}. The higher average pedestal pressure is a result of an unsteady, but unusually long (~100-500 ms) ELM period. This

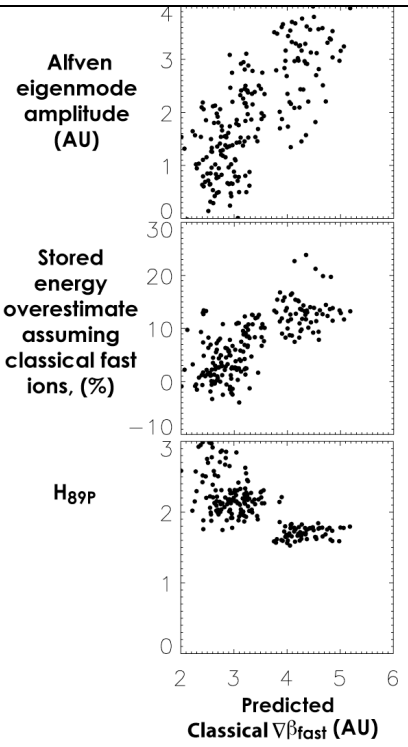

Fig. 16. From top to bottom: Average AE amplitude, stored energy overestimate, and H_{89P} versus classically predicted gradient in β_{fast}. Data is taken from three high-β_P discharges

coexists with a transport barrier near $\rho = 0.5$ that is somewhat narrower and shorter than the barriers observed at $\rho = 0.7$ in other discharges. In this case it appears that the attainment of nearly classical fast-ion confinement precedes, and possibly contributes to the formation of the high pedestal and internal transport barrier by more complete transfer of heat to the thermal plasma.

The comparisons in Figs 17 and 18 show improved thermal confinement can either push the global energy confinement time back up to expected H-mode levels (i.e. $H_{89P} \geq 2$) despite enhanced fast-ion transport, or a mode of better thermal confinement (e.g. internal transport barrier or higher pedestal) can result from having classical fast-ion transport. In either case, better thermal confinement reduces the required NBI power to obtain a target β_N, which helps to reduce the drive for AE modes.

In summary, the high-β_P operating scenario shows that high-q_{min} plasmas can have classical fast-ion confinement and good global energy confinement if $\nabla\beta_{fast}$ is kept low in the core to avoid strong AE activity there. This is caused by a relatively low and flat slowing-down time profile inside $\rho \sim 0.5$. There may be other ways to control the slowing-down time and fast-ion profiles to minimize AE activity and achieve good performance. These are discussed in Sec. IV.

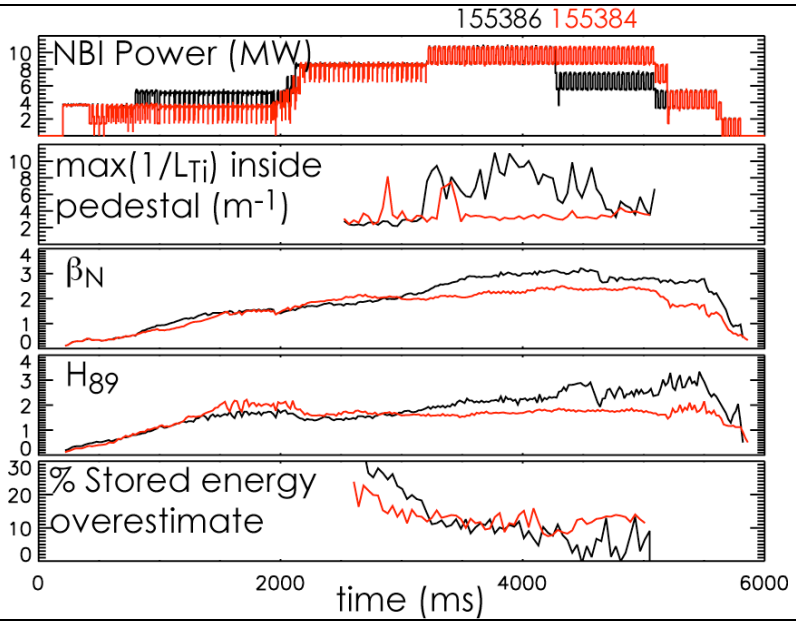

Fig. 17. Comparison of discharges showing the effects of an internal transport barrier. From top to bottom: NBI power, maximum inverse gradient scale length of the ion temperature inside the pedestal (large values indicate the presence of a barrier), β_N, H_{89P}, and stored energy overestimate versus time. The no-ITB case is in red and with-ITB case is in black.

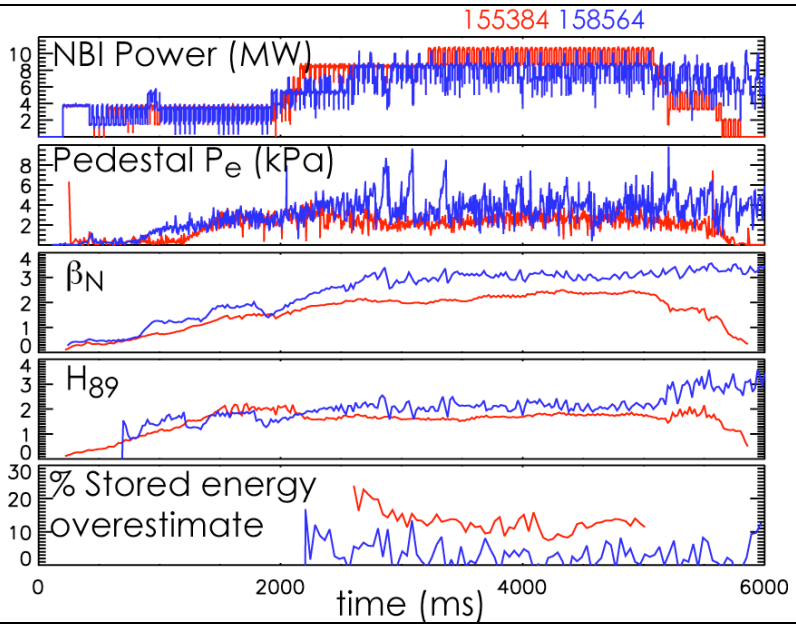

Fig. 18. Comparison of discharges showing the effects of a nearly classical fast-ion transport and higher average pedestal pressure. From top to bottom: NBI power, electron pedestal pressure, β_N, H_{89P}, and stored energy overestimate versus time.

IV. Future outlook

On DIII-D, achieving higher β_N in high-q_{min} plasmas with reactor-relevant q_{95} will require improved control of fast-ion modes. The L-mode studies in [38] showing that moving the same amount of NBI power from on- to off-axis reduces AE activity suggests that moving more NBI power from on- to off-axis may help in a high-q_{min}, high-β_N scenario. Presently ~1/3 of the co-I_P NBI power is injected off-axis in these scenarios, but a planned upgrade will increase this to ~2/3. This will enable further lowering of the fast-ion gradient near the axis, which will reduce the drive for AEs there. The high-β_P regime demonstrates cases where some mode of improved thermal confinement can either partially compensate for enhanced fast-ion transport, or permit classical fast-ion transport by lowering the NBI power requirement. In both cases the normalized confinement is at or above the expected level for an H-mode plasma. Therefore, future experiments should seek to identify and optimize potentially useful regimes of improved thermal confinement. The most likely modes to be compatible with high-q_{min} are a high-radius transport barrier or a "super-H-mode" pedestal [39].

A third lesson from the present experiments is that future experiments should seek to replace NBI heating with rf-electron heating. This will lower the drive for AEs and avoid the issue of reducing fast-ion confinement. This option is actually well aligned with future burning plasma reactors, which, unlike the experiments described here, will have chiefly electron heating, low input torque, and isotropic rather than anisotropic fast ions. To this end the DIII-D program has plans for a significant increase in ECH power and will test a novel high-harmonic fast wave or "helicon" system for off-axis heating and current drive. Lastly, in DIII-D and elsewhere there have been observations of direct impacts on reverse-shear AEs and TAEs by the careful application of ECH. For example, modulation between ECH on- and off-axis has been shown to

turn TAEs on and off at the same rate that is faster than a slowing down time [40]. These results are not fully understood and from low-β_N plasmas, but their existence encourages continued exploration of novel AE-control methods.

It was beyond the scope of the present paper to try to predict fast-ion confinement in next-generation steady state burning plasmas based on existing DIII-D results. But a few important dimensionless parameters can be compared to get some sense of how conditions will be different in ITER for example. Taking parameters from a model $q_{\min} > 2$ steady-state scenario for ITER [4] shows that it will have a mix of both more and less favorable conditions than DIII-D for fast-ion confinement. The analysis in this paper has focused mostly on the drive for AEs and resulting fast-ion transport. The quotient $\beta_{fast}/\beta_{thermal}$ serves as a proxy for the ratio of AE drive to damping. In the DIII-D high-$q_{\min}$ plasmas with q_{95} = 5-7 all having enhanced fast-ion transport, $\beta_{fast}/\beta_{thermal} = 0.2 - 0.4$. The high-$\beta_P$ plasmas having approximately classical fast-ion transport have $\beta_{fast}/\beta_{thermal} = 0.15 - 0.35$. The predicted ITER plasma from Ref. 4 would have $\beta_{fast}/\beta_{thermal} = 0.15$. This is at the low end of the DIII-D high-β_P range, and therefore this is favorable for ITER. Next, the much larger size of ITER compared to DIII-D means that the ratio of the fast-ion orbit to machine size ρ_{fast}/a is much lower in ITER: 0.015 for beam ions and 0.02 for alphas compared to 0.03-0.04 in the DIII-D experiments. Therefore the ability of AEs to move fast-ions all the way to the edge of the plasma is less in ITER. But ITER will have many more fast-ions that are capable of resonating with various AEs than DIII-D: the ratio of (on-axis) parallel fast-ion speed to Alfvén speed v_{fast}/v_A is 0.3-0.45 in DIII-D but about 0.64 for beam ions in ITER and over 1 for alpha particles. Thus additional experiments and modeling are needed to improve confidence in predictions of fast-ion confinement in high-$q_{\min}$ scenarios in ITER.

V. Summary

Recent DIII-D steady-state scenario experiments have shown the importance of optimizing the current density and fast-ion pressure profiles to minimize AE instability and fast-ion transport. High-β_N operation is dominated by co-I_P neutral beam injection heating, and therefore confined fast ions can make up a significant fraction of the total stored energy. Many experiments have had q_{95} in the range 5-7 because this corresponds to a value that would produce a reasonable level of fusion gain in a next-step reactor. Also, to maximize the externally driven noninductive current the line-density is often kept below ~$5x10^{19}$ m^{-3}. With these conditions, an increase of fast-ion transport above classically predicted levels occurs when $q_{\min}$ is raised from just above 1 to just above 2. This results in 20%-30% lower global energy confinement time at the higher value of $q_{\min}$. Taking the inferred lower absorbed NBI heating power into account, the thermal ion and electron diffusivities are found to be similar for both values of $q_{\min}$.

A high-β_P, high-$q_{\min}$ scenario developed in a different regime is useful for clarifying the physics underlying enhanced fast-ion transport, and also for demonstrating paths to recovering good global energy confinement. When higher q_{95} (i.e. lower I_P) and line-density above $\sim 5 \times 10^{19}$ m^{-3} are used, this results in high-β_P plasmas (β_P = 3-4) that have H_{89P}>2 and classical fast-ion transport. Classical fast-ion transport is evident even with q_{min}≈5 and ~8-10 MW of NBI power because higher density and lower temperature lead to shorter slowing-down times and a smaller fast-ion pressure gradient. Compared to standard high-$q_{\min}$ plasmas (q_{95} = 5-7), the high-β_P plasmas have a narrower TAE gap structure near the magnetic axis and observed AEs are usually only outside $\rho = 0.5$. Good high-β_P plasmas operate just below but close to a critical fast-ion gradient for increased AE activity. The thermal plasma has either a

high-radius transport barrier or a high average pedestal pressure, and these help to reduce the required NBI power and fast-ion gradient. These observations suggest that improved global energy confinement in standard high-$q_{\min}$ plasmas might be achieved by using planned heating and current drive upgrades to broaden the NBI heating profile and further optimize thermal transport at high radius.

Acknowledgment

This material is based upon work supported in part by the U.S. Department of Energy, Office of Science, Office of Fusion Energy Sciences, using the DIII-D National Fusion Facility, a DOE Office of Science user facility, under Awards DE-FC02-04ER54698, DE-AC52-07NA27344, SC-G903402, DE-AC02-09CH11466, DE-AC05-00OR22725, and DE-FG02-04ER54761. DIII-D data shown in this paper can be obtained in digital format by following the links at https://fusion.gat.com/global/D3D_DMP.

References

[1] M. Murakami, M. R. Wade, C. M. Greenfield, T. C. Luce, J. R. Ferron, H. E. St John, J. C. DeBoo, W. W. Heidbrink, Y. Luo, M. A. Makowski, T. H. Osborne, C. C. Petty, P. A. Politzer, S. L. Allen, M. E. Austin, K. H. Burrell, T. A. Casper, E. J. Doyle, A. M. Garofalo, P. Gohil, I. A. Gorelov, R. J. Groebner, A. W. Hyatt, R. J. Jayakumar, K. Kajiwara, C. E. Kessel, J. E. Kinsey, R. J. La Haye, L. L. Lao, A. W. Leonard, J. Lohr, T. W. Petrie, R. I. Pinsker, R. Prater, T. L. Rhodes, A. C. C. Sips, G. M. Staebler, T. S. Taylor, M. A. Van Zeeland, G. Wang, W. P. West, and L. Zeng, and the DIII-D Team, Phys. Plasmas **13**, 056106 (2006)

[2] ITER Physics Expert Group on Energetic Particles, Heating, and Current Drive and ITER Physics Basis Editors, Nucl. Fusion **39**, 2471 (1999).

[3] W. W. Heidbrink and G. J. Sadler, Nucl. Fusion **34**, 535 (1994).

[4] M. Murakami, J. M. Park, G. Giruzzi, J. Garcia, P. Bonoli, R. V. Budny, E. J. Doyle, A. Fukuyama, N. Hayashi, M. Honda, A. Hubbard, S. Ide, F. Imbeaux, E. F. Jaeger, T. C. Luce, Y.-S. Na, T. Oikawa, T. H. Osborne, V. Parail, A. Polevoi, R. Prater, A. C. C. Sips, J. Snipes, H. E. St. John, P. B. Snyder, I. Voitsekhovitch and ITPA/Integrated Operation Scenario Group, Nucl. Fusion **51**, 103006 (2011).

[5] F. M. Poli, C. E. Kessel, P. T. Bonoli, D. B. Batchelor, R. W. Harvey and P. B. Snyder, Nucl. Fusion **54**, 073007 (2014).

[6] A. M. Garofalo, V. S. Chan, J. M. Canik, M. E. Sawan, M. Choi, D. A. Humphreys, L. L.

Lao, R. Prater, P. C. Stangeby, H. E. St. John, T. S. Taylor, A. D. Turnbull and C. P. C. Wong, Nucl. Fusion **54**, 073015 (2014).

[7] C. E. Kessel, T. K. Mau, S. C. Jardin, F. Najmabadi, Fusion Eng. and Design **80**, 63 (2006).

[8] T. S. Taylor, H. St. John, A. D. Turnbull, Y. R. Lin-Liu, K. H. Burrell, V. Chan, M. S. Chu, J. R. Ferron, L. L. Lao, R. J. La Haye, E. A. Lazarus, R. L. Miller, P. A. Politzer, D. P. Schissel, E. J. Strait, Plasma Phys. Control. Fusion **36**, B229 (1994).

[9] T. C. Luce, Fusion Sci. and Technol. **48**, 1212 (2005).

[10] A. D. Turnbull, F. Yasseen, A. Roy, O. Sauter, W. A. Cooper, S. Nicli and F. Troyon, Nucl. Fusion **29**, 629 (1989).

[11] C. M. Greenfield, D. P. Schissel, B. W. Stallard, E. A. Lazarus, G. A. Navratil, K. H. Burrell, T. A. Casper, J. C. DeBoo, E. J. Doyle, R. J. Fonck, C. B. Forest, P. Gophil, R. J. Groebner, M. Jakubowski, L. L. Lao, M. Murakami, C. C. Petty, C. L. Rettig, T. L. Rhodes, B. W. Rice, H. E. St. John, G. M. Staebler, E. J. Strait, T. S. Taylor, A. D. Turnbull, K. L. Tritz, R. E. Waltz and DIII-D Team, Phys. Plasmas **4**, 1596 (1997).

[12] M. Greenwald, Plasma Phys. Control. Fusion **44**, R27 (2002).

[13] P. N. Yushmanov, T. Takizuka, K. S. Riedel, O. J. W. F. Karduan, J. G. Cordey, S. M. Kaye, and D. E. Post, Nucl. Fusion **30**, 1999 (1990).

[14] J. R. Ferron, C. T. Holcomb, T. C. Luce, J. M. Park, P. A. Politzer, F. Turco, W. W. Heidbrink, E. J. Doyle, J. M. Hanson, A. W. Hyatt, Y. In, R. J. La Haye, M. J. Lanctot, M. Okabayashi, T. W. Petrie, C. C. Petty, and L. Zeng, Phys. Plasmas **20**, 092504 (2013).

[15] Baonian Wan, Jiangang Li, Houyang Guo, Yunfeng Liang, Guosheng Xu and Xianzhu Gong for the EAST Team and International Collaborators, Nucl. Fusion **53**, 104006 (2013).

[16] E. J. Strait for the DIII-D Team, Nucl. Fusion **49**, 104008 (2009).

[17] C. C. Petty, *Proc. of the 25th IAEA Fusion Energy Conf., St. Petersburg, Russian Federation,* 2014, Paper PPC/P2-36 http://www-pub.iaea.org/iaeameetings/46091/25th-Fusion-Energy-Conference-FEC-2014 (in works)

[18] ITER Physics Groups on Confinement and Transport and Confinement Modeling and Database, ITER Physics Basis Editors and ITER EDA, Nucl. Fusion **39**, 2175 (1999).

[19] C. Z. Cheng and M. S. Chance, Phys. Fluids **29**, 3695 (1986).

[20] L. L. Lao, H. St. John, R.D. Stambaugh, A.G. Kellman, and W. Pfeiffer, Nucl. Fusion **25**, 1611 (1985).

[21] H. E. St. John, T. S. Taylor, Y. R. Lin-Liu, and A. D. Turnbull, in *Proceedings of the 15th Int. Conf. on Plasma Physics and Controlled Nuclear Research*, Seville, Spain, 1994 (IAEA, Vienna, 1995) Vol. 3, p. 603.

[22] A. Pankin, D. McCune, R. Andre, G. Bateman, and A. Kritz, Comput. Phys. Commun. **159**, 157 (2004).

[23] W. W. Heidbrink, Rev. Sci. Instrum. **81**, 10D727 (2010).

[24] W. W. Heidbrink, D. Liu, Y. Luo, E. Ruskov and B. Geiger, Commun. Comput. Phys. **10**, 716 (2011).

[25] C. C. Petty, T. C. Luce, D. R. Baker, B. Ballet, T. N. Carlstrom, J. G. Cordey, J. C. DeBoo, P. Gohil, R. J. Groebner, B. W. Rice, D. M. Thomas, M. R. Wade, and R. E. Waltz, Phys. Plasmas **5**, 1695 (1998).

[26] W. W. Heidbrink, P. L. Taylor, and J. A. Phillips, Rev. Sci. Instrm. **68**, 536 (1997).

[27] W. W. Heidbrink, J. R. Ferron, C. T. Holcomb, M. A. Van Zeeland, Xi Chen, C. M. Collins, A. Garofalo, X. Gong, B. A. Grierson, M. Podesta, L. Stagner, and Y. Zhu, Plasma Phys. Control. Fusion **56**, 095030 (2014).

[28] R. Nazikian, N. N. Gorelenkov, B. Alper, H. L. Berk, D. Borba, R. V. Budny, G. Y. Fu, W. W. Heidbrink, G. J. Kramer, M. A. Makowski, S. D. Pinches, S. E. Sharapov, W. M. Solomon, E. J. Strait, R. B. White, M. A. Van Zeeland, and JET-EFDA contributors, Phys. Plasmas **15**, 056107 (2008).

[29] M. A. Van Zeeland, W. W. Heidbrink, R. K. Fisher, M. García Muñoz, G. J. Kramer, D. C. Pace, R. B. White, S. Aekaeslompolo, M. E. Austin, J. E. Boom, I. G. J. Classen, S. da Graça, B. Geiger, M. Gorelenkova, N. N. Gorelenkov, A. W. Hyatt, N. Luhmann, M. Maraschek, G. R. McKee, R. A. Moyer, C. M. Muscatello, R. Nazikian, H. Park, S. Sharapov, W. Suttrop, G. Tardini, B. J. Tobias, Y. B. Zhu, and DIII-D and ASDEX Upgrade Teams, Phys. Plasmas **18**, 056114 (2011).

[30] M. E. Austin and J. Lohr, Rev. Sci. Instrum. **74**, 1457 (2003).

[31] Y. Kusama, H. Kimura, T. Ozeki, M. Saigusa, G. J. Kramer, T. Oikawa, S. Moriyama, M. Nemoto, T. Fujita, K. Tobita, G. Y. Fu, R. Nazikian, and C. Z. Cheng, Nucl. Fusion **38**, 1215 (1998).

[32] J. Candy and R. Waltz, J. Comput. Phys. **186**, 545 (2003).

[33] P. A. Politzer, A. W. Hyatt, T. C, Luce, F. W. Perkins, R. Prater, A. D. Turnbull, D. P. Brennan, J. R. Ferron, C. M. Greenfield, J. Jayakumar, R. J. La Haye, C. C. Petty and M. R. Wade, Nucl. Fusion **45**, 417 (2005).

[34] A. G. Garofalo, *Proc. of the 25th IAEA Fusion Energy Conf., St. Petersburg, Russian Federation,* 2014, Paper PPC/P2-31, http://www-pub.iaea.org/iaeameetings/46091/25th-Fusion-Energy-Conference-FEC-2014 (in works)

[35] X. Gong, *Proc. of the 25th IAEA Fusion Energy Conf., St. Petersburg, Russian Federation*, 2014, Paper EX/P2-39, http://www-pub.iaea.org/iaeameetings/46091/25th-Fusion-Energy-Conference-FEC-2014 (in works)

[36] C. Z. Cheng and M. S. Chance, J. Comput. Phys. **71**, 124 (1987).

[37] N. N. Gorelenkov, C. Z. Cheng, and G. Y. Fu, Phys. Plasmas **6**, 2802 (1999).

[38] W. W. Heidbrink, M. A. Van Zeeland, M. E. Austin, E. M. Bass, K. Ghantous, N. N. Gorelenkov, B. A. Grierson, D. A. Spong and B. J. Tobias, Nucl. Fusion **53**, 093006 (2013).

[39] W. M. Solomon, P. B. Snyder, K. H. Burrell, M. E. Fenstermacher, A. M. Garofalo, B. A. Grierson, A. Loarte, G. R. McKee, R. Nazikian, and T. H. Osborne, Phys. Rev. Lett. **113**, 135001 (2014).

[40] M. A. Van Zeeland, W. W. Heidbrink, R. Nazikian, M. E. Austin, C. Z. Cheng, M. S. Chu, N. N. Gorelenkov, C. T. Holcomb, A. W. Hyatt, G. J. Kramer, J. Lohr, G. R. McKee, C. C. Petty, R. Prater, W. M. Solomon and D. A. Spong, Nucl. Fusion **49**, 065003 (2009).

2.3 Measurements of Alfvén Eigenmode Induced Critical Gradient Transport of Fast-Ions

DIII-D experiments in July 2015 have shown the existence of a critical threshold for fast-ion transport in the presence of many, small-amplitude Alfvén eigenmodes (AE). Transport properties were measured under a variety of conditions in order to understand the underlying threshold physics for the sudden onset of AE induced fast-ion transport and facilitate comparisons with critical gradient models that are being developed to predict fast-ion profiles and losses. The observation of fast-ion critical gradient transport suggests that reduced models for fast-ion transport can effectively be used to predict fusion alpha and beam-ion profiles in ITER.

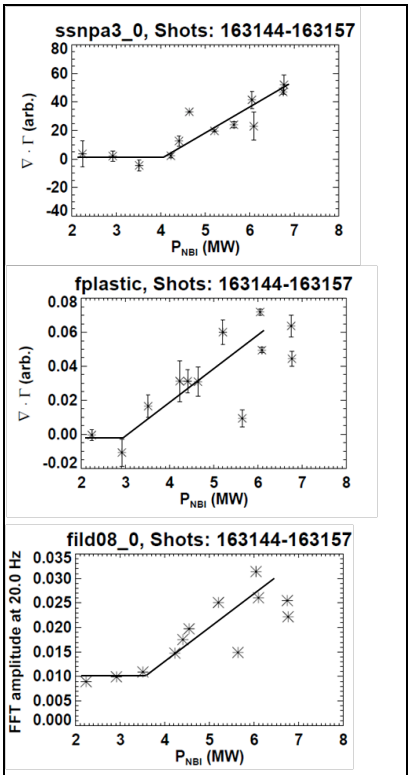

Fig. 1. A variety of fast-ion diagnostics were used to measure transport of the modulated test particles. The onset threshold differs as wave-particle resonance affect different parts of phase space.

Several approaches were used to change the amplitude, number, and types of AEs during the current ramp in L-mode plasmas, i.e. while q_{min} is high and the current profile broad. An off-axis source modulation technique was used to measure the divergence of fast-ion flux. The experiments have shown several key features consistent with critical gradient theory: fast-ion transport suddenly occurs at a critical threshold in the number of small-amplitude Alfvén eigenmodes (AE). The threshold is well above the AE linear stability limit, and the threshold differs between various fast-ion diagnostics, indicating a phase-space dependence of fast-ion transport (Figure 1). Above threshold, fast ion transport becomes stiff, resulting in virtually unchanged equilibrium fast-ion density profiles despite increased drive. In addition, stiff transport exhibits intermittent "spikes" in the fast-ion losses.

Transport properties were observed to change when the types of AEs were altered. A mix of RSAEs and TAEs were driven during an all-left beam power scan, and the scan was repeated with ECH near q_{min}, resulted in TAE dominant spectrum (Figure 2). When ECH was added, the transport measured by the ssNPA diagnostic (sensitive to the trapped particle population) was not strictly "stiff", and the fast-ion density profile did not appear to be clamped (Figure 3). Furthermore, the fast-ion loss detector showed largely reduced intermittent transport. Current modeling efforts aim to understand how different types of AEs and the amount of mode overlap affects the fast-ion distribution function and losses. In one approach, the AE mode structure is

modeled using the NOVA code (G. Kramer, N. Gorelenkov, PPPL) and mode amplitudes are scaled to match the experimental AE induced ECE temperature fluctuations. The ORBIT code (R. White, PPPL) is then used to evolve the fast-ion distribution function and calculate losses beyond the last closed flux surface, where the mode types and amplitude input can be varied. The FIDASIM code can then be used to compute the expected experimental FIDA spectrum. Preliminary results confirm that enhanced transport occurs when multiple modes cause many wave-particle resonances to overlap. Analysis of Doppler Backscattering (DBS) and Beam Emission Spectroscopy (BES) measurements will give an initial assessment on the microturbulence levels, which have been predicted to alter the critical gradient threshold level (R. Waltz & E. Bass, GA).

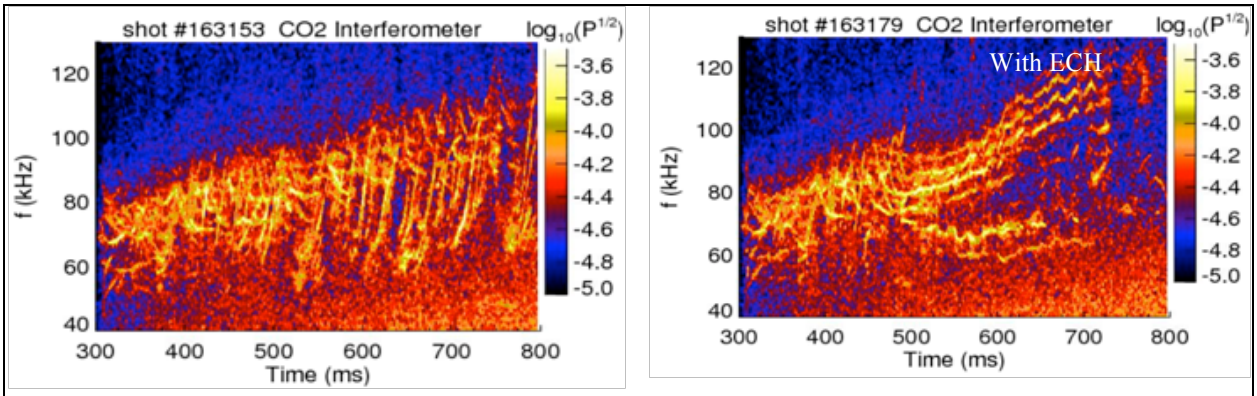

Fig. 2. (Left) Typical spectrum of mixed RSAEs and TAEs using all left neutral beams. (Right) TAE dominated ectrum produced with the same NBI drive, but with 3 MW ECH near q_{min}.

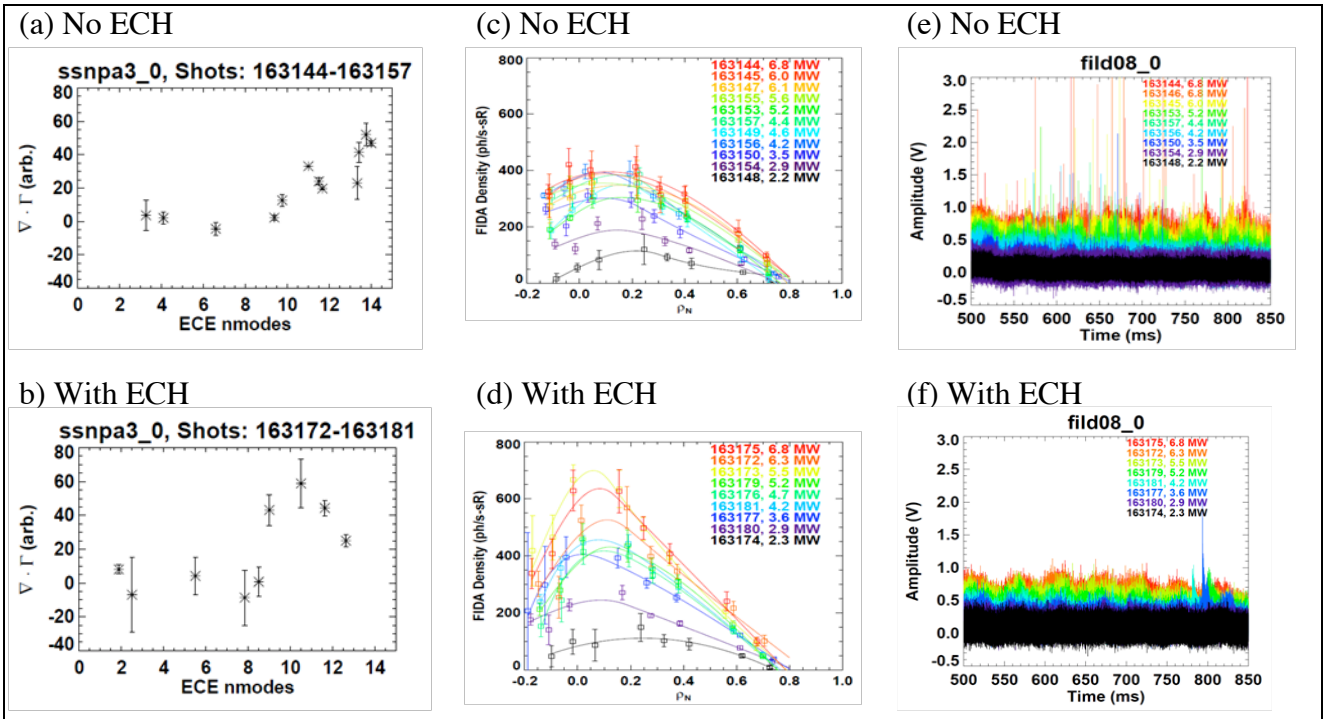

Fig. 3. In beam power scans, transport properties change when ECH is added. Comparing (a) and (b): transport of modulated trapped particles is not strictly stiff with ECH. Comparing (c) and (d): FIDA absolute density is larger and not clamped with ECH. Comparing (e) and (f): FILD records significantly fewer intermittent losses (spikes) with ECH.

2.4: Suppression of Aflvén eigenmodes in high performance steady state discharges

The following presentation was given at the DIII-D Friday Science Meeting, August 28, 2015.

Predictive understanding of fast-ion transport in high q_{min} steady state plasmas on DIII-D

G.J. Kramer

in collaboration with

M. Podesta, N.N. Gorelenkov,
M. van Zeeland, R. Nazikian,
W. Solomon, C. Holcomb,
B. Grierson

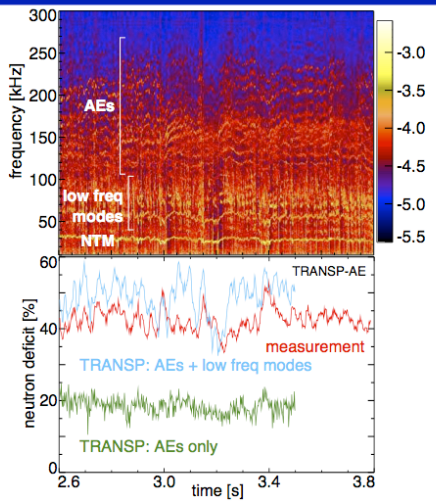

DIII-D NATIONAL FUSION FACILITY

PPPL PRINCETON PLASMA PHYSICS LABORATORY

Beam-ion losses reduce the performance of Steady-state discharges in DIII-D

- Steady-state high q_{min} discharges in DIII-D often suffer from high amounts of beam-ion losses that reduce performance
- A reduction of up to 40% can be observed on the neutron signal when it is compared to classical predictions
- A strong correlation has been found between the AE amplitude and the neutron deficit
- The correlation suggest that the AEs drive strong fast-ion transport

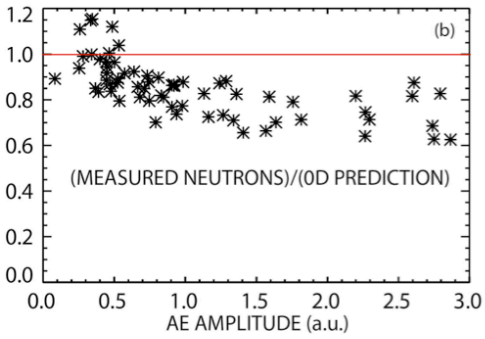

From: Heidbrink et al. PPCF 56 (2014) 095030

Understanding The AE activity in Steady-state discharges might lead to better performance

- Can we predict the neutron deficit from the observed AEs?
- Can we reshape the profiles to remove or render the AEs harmless?

- Optimize the absorbed beam power in DIIII-D:

  increase β and J_{bs}

- For future reactors:

  reduce alpha particle losses

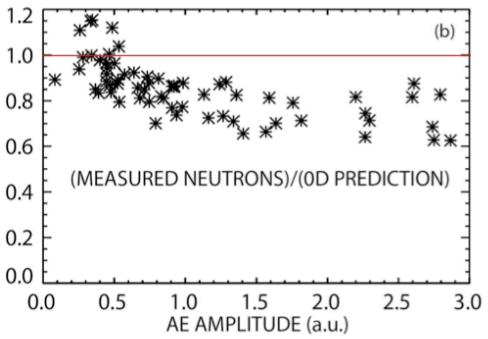

From: Heidbrink et al. PPCF 56 (2014) 095030

Two questions:

- Can we predict the neutron deficit from the observed AEs?
  - Model with the NOVA + ORBIT + TRANSP codes
- Can we reshape the profiles to remove or render the AEs harmless?

Strong AE activity is observed in plasmas with reversed shear and high q_{min}

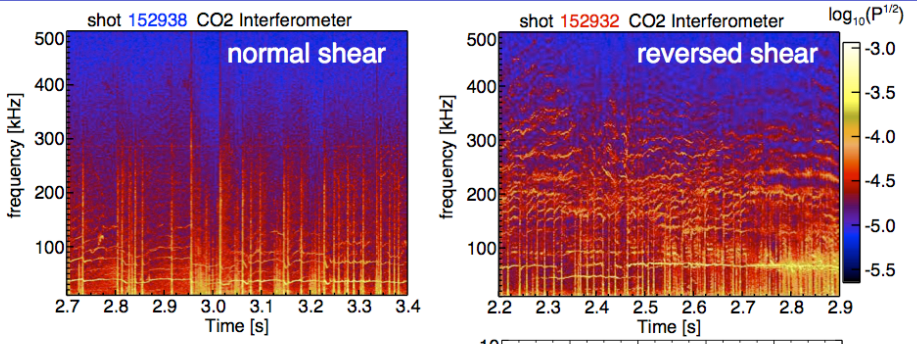

- In normal shear SS discharges:
  - weak AE activity
  - no neutron deficit
- In reversed shear SS discharges:
  - strong AE activity
  - significant neutron deficit

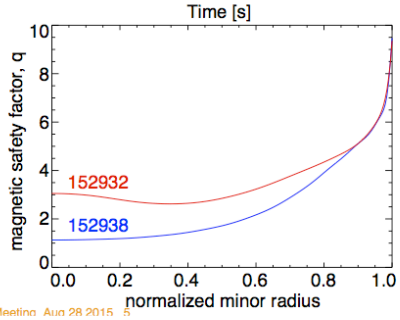

The radius of q_{min} is aligned well with the maximum of the fast-ion pressure gradient

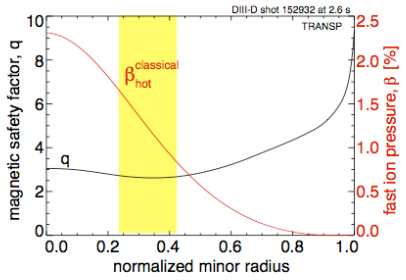

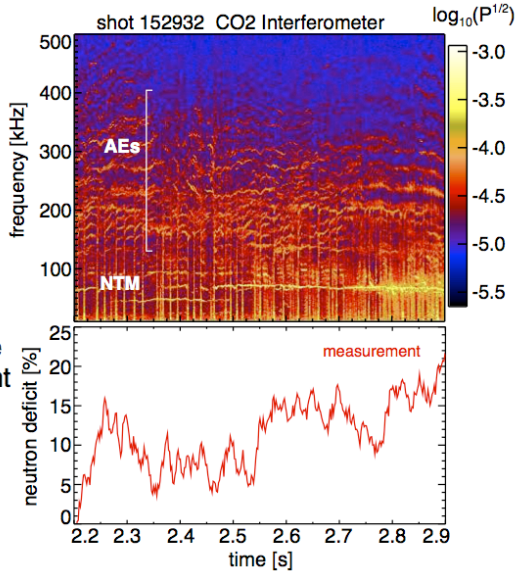

- The RSAEs are driven unstable by the fast-ion pressure gradient

Main plasma parameters:

B_T: 2.0 T	$n_e(0)$: 4.5 10^{19} m^3	q_0: 3.0
I_p: 0.95 MA	$T_e(0)$: 3.7 keV	q_{min}: 2.4
β_n: 2.6	$T_i(0)$: 6.2 keV	q_{95}: 5.6

NOVA finds a multitude of eigenmodes in agreement with the observations

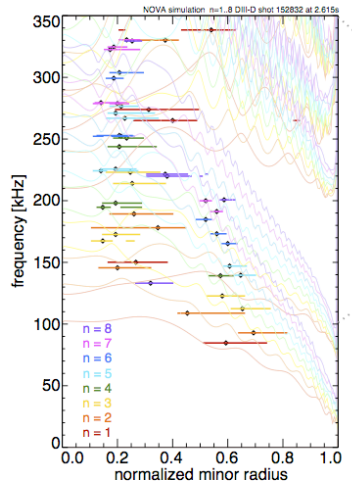

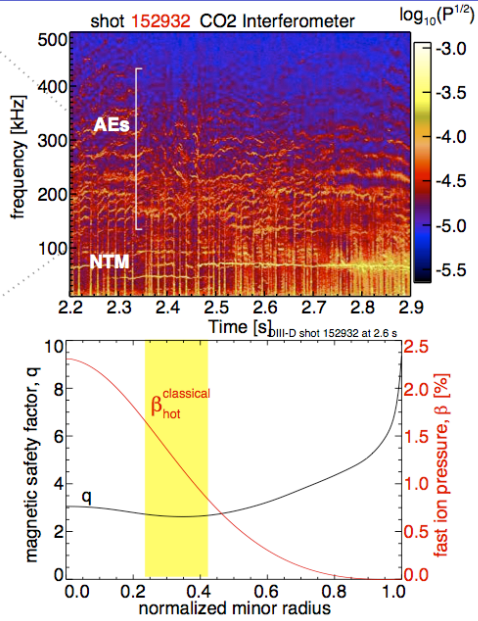

Main plasma parameters:

B_T: 2.0 T	$n_e(0)$: 4.5 10^{19} m^3	q_0: 3.0
I_p: 0.95 MA	$T_e(0)$: 3.7 keV	q_{min}: 2.4
β_n: 2.6	$T_i(0)$: 6.2 keV	q_{95}: 5.6

NOVA reproduces also the absence of core AEs in the normal shear discharge

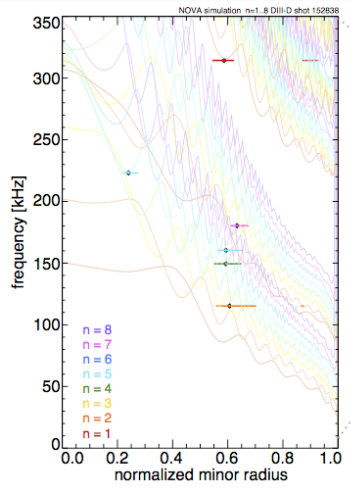

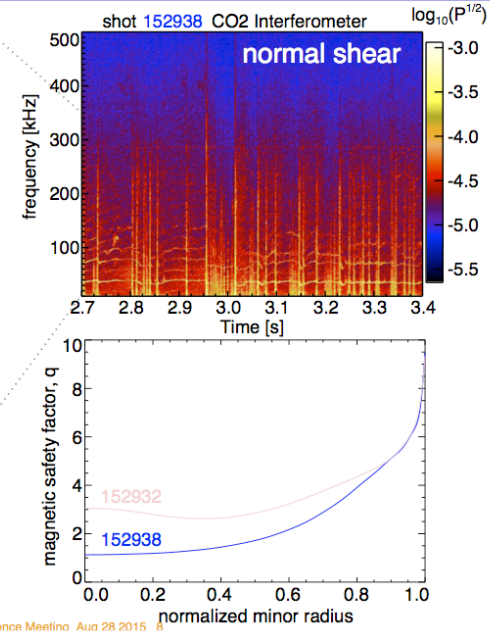

- NOVA confirms the observation that AEs do not exist in the core of the normal shear discharge

TRANSP integrates the results from NOVA + ORBIT to model the AE-induced fast-ion trasport

- Classical process: slowing-down and pitch-angle scattering
  - used to determine the neutron deficit
- Phase-space kick model: Enhanced fast-ion diffusion via correlated kicks in (P_ζ ,E)

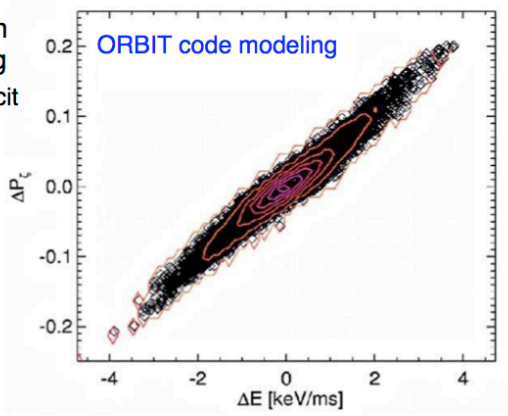

NOVA: eigenmodes
↓
ORBIT: (P_ζ ,E) kicks
↓
NUBEAM: Fast-ion evolution
↑ ↓
TRANSP

more details in: Podesta et al. PPCF 56 (2014) 055003

TRANSP-AE analysis reproduces the observed neutron deficit

- application of: NOVA + ORBIT + TRANSP around 2.6 s reproduces the the measured 15% deficit
- Used in the simulations:
  - NOVA eigenmodes
  - amplitudes from ECE
  - (P_ζ ,E) kicks from ORBIT
- Next step: Apply the TRANSP-AE analysis to the whole discharge
- However, higher neutron deficits are sometimes observed

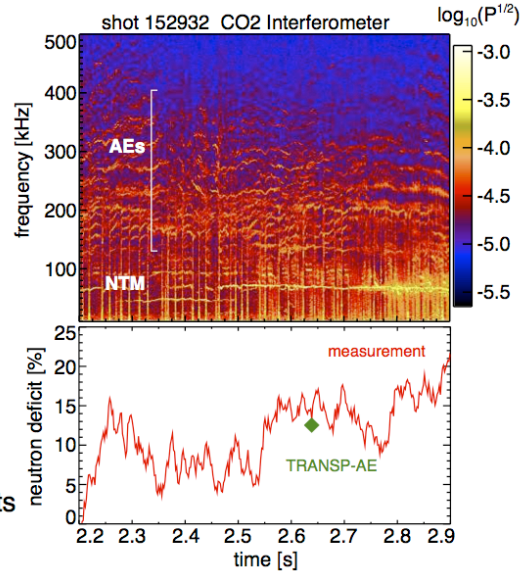

Low-frequency global modes in the BAE range can strongly enhance to the neutron deficit

- Up to 45% neutron deficit is observed
- Only half of the neutron deficit can be produced by AEs only

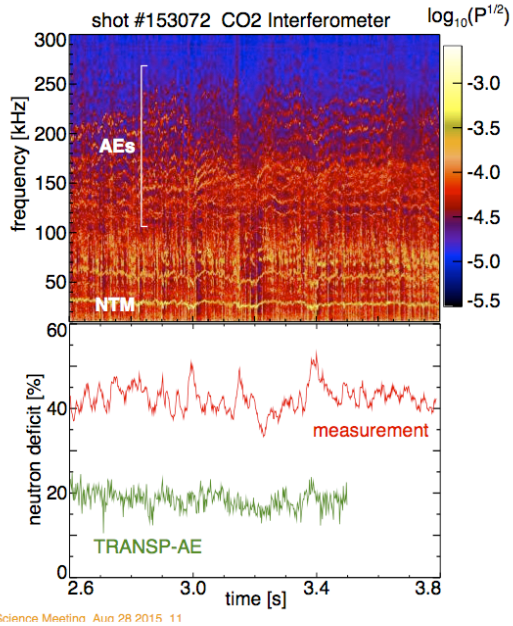

Main plasma parameters:

B_T: 1.7 T	$n_e(0)$: 3.5 10^{19} m^3	q_0: 2.4
I_p: 0.82 MA	$T_e(0)$: 2.7 keV	q_{min}: 2.2
β_n: 2.4	$T_i(0)$: 4.5 keV	q_{95}: 6.9

Low-frequency global modes in the BAE range can strongly enhance to the neutron deficit

- Up to 45% neutron deficit is observed
- Only half of the neutron deficit can be produced by AEs only
- The neutron deficit is recovered whith the low frequency modes
  - approximate structures
  - amplitudes, frequencies from ECE
- The nature of those modes is not yet clear: BAE? BAAE? EPM?
- Better theory needed for the low frequency modes

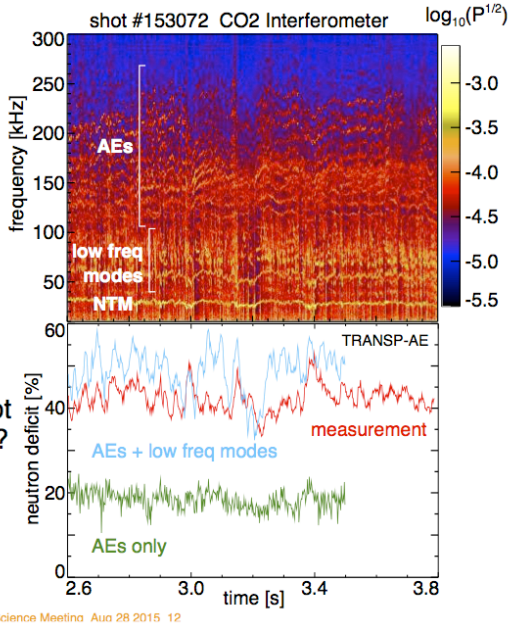

One question answered. One question left:

- We can model the neutron deficit from the observed AEs:
  - Model with the NOVA + ORBIT + TRANSP codes
  - Improved theory of low-frequency modes is needed
- Can we reshape the profiles to remove or render the AEs harmless?
  - Modify the equilibrium profiles to suppress AE activity

TAEs and EAEs are stabilized by increasing the 'normalized pressure gradient'

- TAEs and EAEs move into the continuum when the normalized pressure gradient:

$$\alpha = -\frac{R_0 q^2}{B_0^2}\frac{dP}{dr}$$

exceeds a critial value

- TAEs can be stabilized by increasing q(0)
- This is consistent with an increased off-axis current

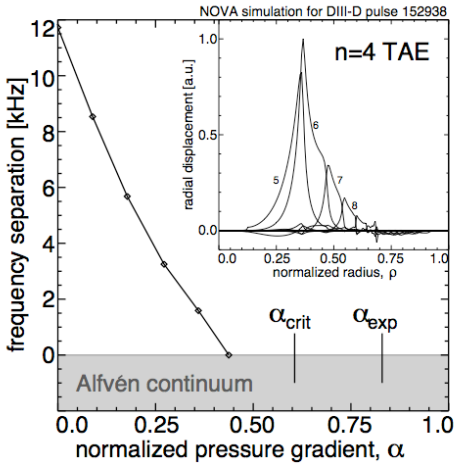

see also: G.Y. Fu PoP 2 (1995) 1029

However, RSAEs are destabilized by increasing the 'normalized pressure gradient'

- RSAEs emerge from the continuum when:

$$\alpha = -\frac{R_0 q^2}{B_0^2}\frac{dP}{dr}$$

exceeds a critial value

- Raising q_{min} leads the excitation of more modes
- Lowering q_{min} is not a solution for steady state scenarios

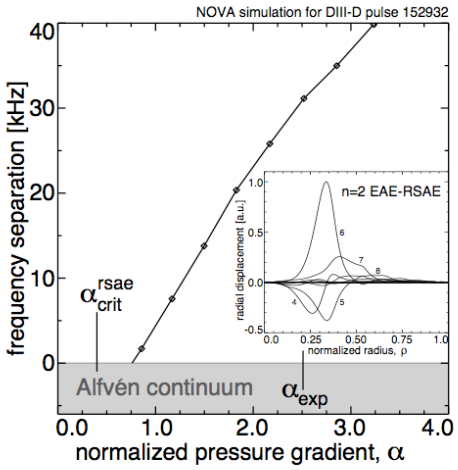

for more details: G.Y. Fu & H.L. Berk PoP 13 (2006) 052502
G.J. Kramer & G.Y. Fu PPCF 48 (2006) 1285

Move q_{min} to a larger radius can mitigate the effects of the RSAEs

- Reduce the RSAE fast-ion drive by moving q_{min} away from the steep fast-ion pressure gradient region
- This is consistent with a broad pressure profile and a high bootstrap current

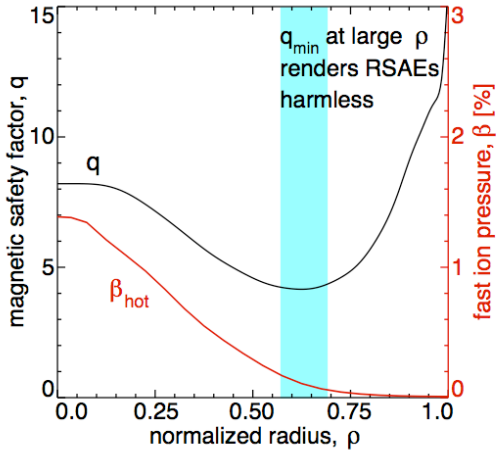

Move q_{min} to a larger radius can mitigate the effects of the RSAEs

- Reduce the RSAE fast-ion drive by moving q_{min} away from the steep fast-ion pressure gradient region
- This is consistent with a broad pressure profile and a high bootstrap current
- This is also favorable for TAE and EAE suppression in the plasma core
- Is there experimental evidence that this scenario can work?

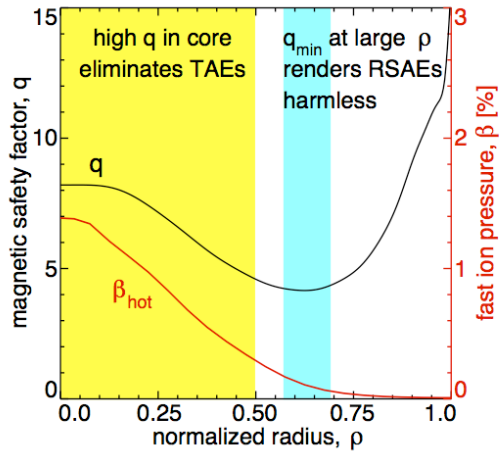

A good q profile for AE mitigation was obtained in a DIII-D EAST simultion high q_{min} high β_p discharge

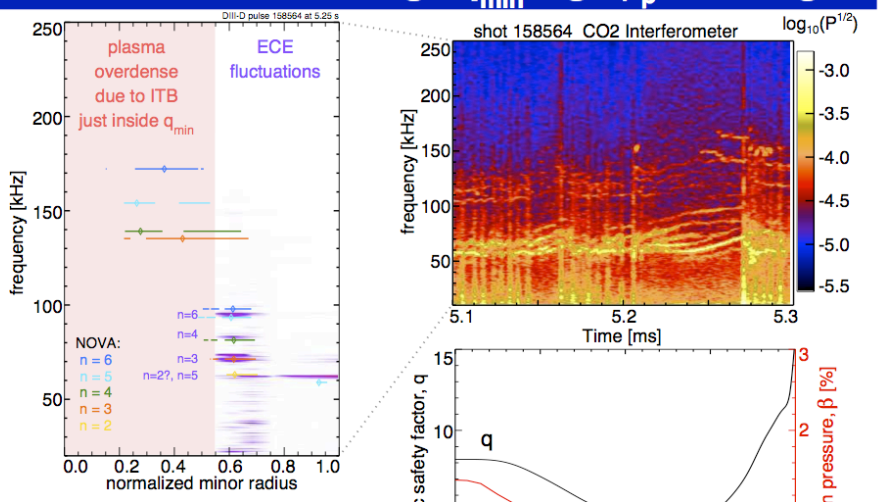

- NOVA reproduces the observed RSAEs very well

The neutron rate is classical in this DIII-D EAST simultion high q_{min} high β_p discharge

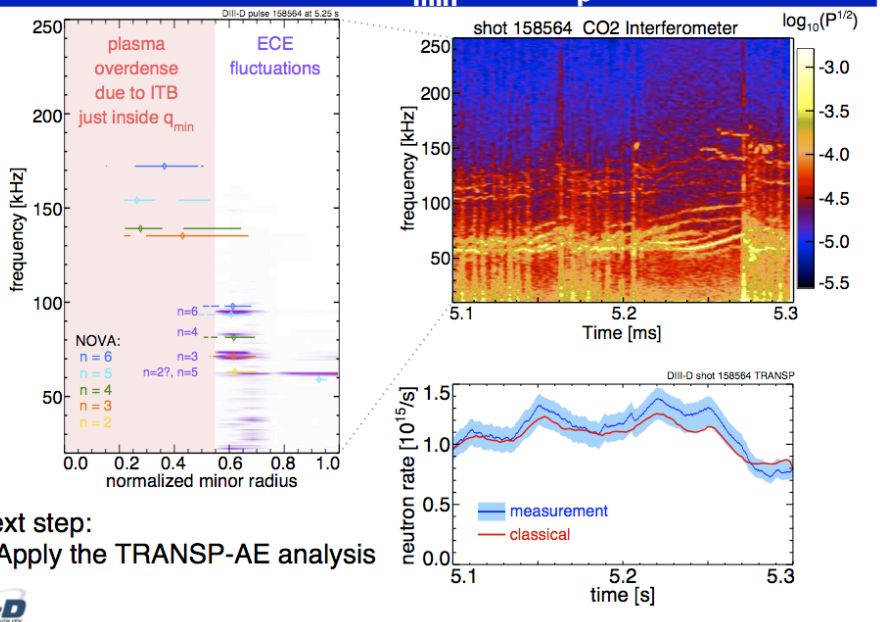

- Next step:
  Apply the TRANSP-AE analysis

Two answers:

- We can model the neutron deficit from the observed AEs:
  - Model with the NOVA + ORBIT + TRANSP codes
  - Improved theory of low-frequency modes is needed
- We can modify the discharge to render the AEs harmless:
  - Move q_{min} to large radius:
    - core TAEs and EAEs are mostly suppressed
    - RSAEs are outside the strong drive region

Future work:

- Experiment:
- Develop a high performance steady state discharge with:
  - Fast current ramp
  - Early beam injection
  - Off-axis ECH
- This might give access to higher β_{pol} and J_{BS}
- Sustained suppression may require additional off-axis current drive
  - Helicon wave
  - more ECCD

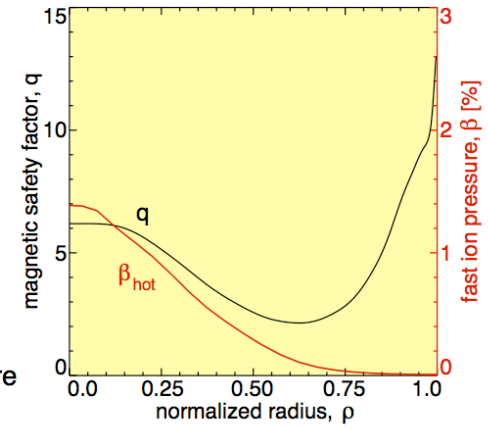

DIII-D NATIONAL FUSION FACILITY

PPPL PRINCETON PLASMA PHYSICS LABORATORY

2.5 Report on Confinement Optimization via q-profile Control

The dependence of transport, turbulence and confinement on central magnetic shear and the electron to ion temperature ratio was explored during a July 2015 experiment at DIII-D. A preliminary observation is that the energy confinement time decreased ~40% going from T_e/T_i ~1 to ~1.2 in positive shear plasmas, but in negative shear plasmas the decrease was only ~10%.

The experiment was motivated by JT-60U results demonstrating little or no confinement reduction with increasing T_e/T_i in negative central magnetic shear plasmas [M. Yoshida, IAEA-2014], and was proposed and led by Dr. Yoshida (JAEA). This experiment sought to understand the underlying turbulence and transport mechanisms behind this process in quasi-steady-state (non-inductive) high-beta-poloidal plasmas, developed through the EAST-DIII-D collaboration.

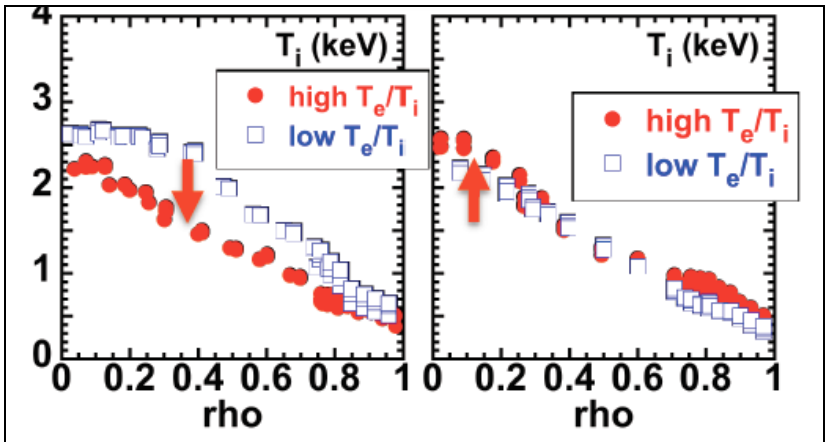

Fig. 1. Ion temperature measurement from CER diagnostic for low- and high-T_e/T_i cases in positive magnetic shear (left) and negative magnetic shear (right).

ECCD was employed to both drive off-axis current drive and increase the electron temperature. The q-profile was scanned inside of ρ~0.4 by varying the timing of neutral beam and ECCD injection during the I_P ramp-up phase. T_e/T_i was scanned from ~1 to ~1.2 across the profile using ECH/ECCD. In positive shear plasmas the electron density, ion temperature, and toroidal rotation decreased with T_e/T_i, while these quantities remained nearly constant with increasing T_e/T_i, as indicated in figure 1.

Comprehensive fluctuation measurements were obtained with BES, DBS, CECE, and PCI to help understand the mechanisms that cause the differing transport responses for different q-profiles as a function of T_e/T_i. Preliminary examination of BES fluctuation measurements near ρ=0.3 (Fig. 2), show nearly constant fluctuations with increasing T_e/T_i in positive shear, and a slight reduction in fluctuations with increasing T_e/T_i in negative shear, nominally consistent with transport trends.

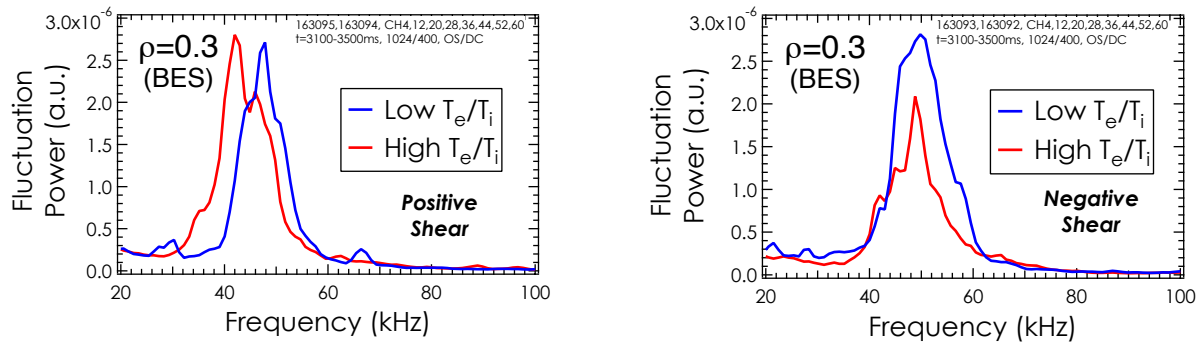

Fig. 2. BES fluctuation spectra.

These observations suggest that a relative improvement with reduced confinement degradation at high T_e/T_i can be made in steady-state regimes using negative shear.

2.6: The High-β_N Hybrid Scenario for ITER and FNSF Steady-State Missions

The following manuscript was submitted to and accepted by Physics of Plasmas. The reference for the published article is F. Turco et al., Phys. Plasmas **22**, 056113 (2015).

The High-β_N Hybrid Scenario for ITER and FNSF Steady-State Missions

F. Turco[1], C.C. Petty[2], T.C. Luce[2], T.N. Carlstrom[2], M.A. Van Zeeland[2], W. Heidbrink[3], F. Carpanese[4], W. Solomon[5], C.T. Holcomb[6], J.R. Ferron[2]

[1]*Columbia University, New York, New York USA*
[2]*General Atomics, P.O. Box 85608, San Diego, California 92186-5608 USA*
[3]*University of California, Irvine, Irvine, California USA*
[4]*Politecnico di Milano, Dipartimento di Energia, via Ponzio 34/3, I-20133 Milano, Italy*
[5]*Princeton Plasma Physics Laboratory, Princeton, New Jersey USA*
[6]*Lawrence Livermore National Laboratory, Livermore, California USA*

Abstract. New experiments on DIII-D have demonstrated the steady-state potential of the hybrid scenario, with 1 MA of plasma current driven fully non-inductively and β_N up to 3.7 sustained for ~3 s (~1.5 current diffusion time, τ_R, in DIII-D), providing the basis for an attractive option for steady-state operation in ITER and FNSF. Excellent confinement is achieved (H_{98y2}~1.6) without performance limiting tearing modes. The hybrid regime overcomes the need for off-axis current drive efficiency, taking advantage of poloidal magnetic flux pumping that is believed to be the result of a saturated 3/2 tearing mode. This allows for efficient current drive close to the axis, without deleterious sawtooth instabilities. In these experiments, the edge surface loop voltage is driven down to zero for >1 τ_R when the poloidal β is increased above 1.9 at a plasma current of 1.0 MA and the ECH power is increased to 3.2 MW. Stationary operation of hybrid plasmas with all on-axis current drive is sustained at pressures slightly above the ideal no-wall limit, while the calculated ideal with-wall MHD limit is β_N~4-4.5. Off-axis NBI power has been used to broaden the pressure and current profiles in this scenario, seeking to take advantage of higher predicted kink stability limits and lower values of the tearing stability index Δ', as calculated by the DCON and PEST3 codes. Results based on measured profiles predict ideal limits at β_N>4.5, 10% higher than the cases with on-axis NBI. A 0-D model, based on the present confinement, β_N and shape values of the DIII-D hybrid scenario, shows that these plasmas are consistent with the ITER 9 MA, Q=5 mission and the FNSF 6.7 MA scenario with Q=3.5. With collisionality and edge safety factor values comparable to those envisioned for ITER and FNSF, the high-β_N hybrid represents an attractive high performance option for the steady-state missions of these devices.

1. Introduction

The ITER and FNSF steady-state missions require plasmas with long duration and fully non-inductive conditions (f_{NI}=1) at fusion gain Q=5 and Q<=5 respectively. Extrapolation to these conditions from the current scenarios requires demonstration discharges in present machines and

validation of the models used for the extrapolation. In general, the plasma current (I_p) is composed of the ohmic current (J_{ohm}, inductive), the bootstrap current, and the non-inductive sources driven by Neutral Beam Injection (NBI), Electron Cyclotron (EC) waves, Ion Cyclotron (IC) waves, etc. The first two components are self-generated, while the other sources are generated externally by some part of the input power. Since the present means for NBI and EC current generation have fairly low efficiency, simultaneously meeting the constraints of high fusion gain and fully-noninductive CD entails the maximization of the bootstrap current fraction. However, a complex non-linear interaction links the bootstrap current J_{bs}, the safety factor (q) and the kinetic profiles (n_e, T_e, T_i, Z_{eff}, etc). The magnitude of the bootstrap current is proportional to the plasma pressure; therefore, operation at high-normalized pressure, β_N ($\beta_N = \beta(\%)\cdot a(m)\cdot B_T(T)/I_p(MA)$, where β is the ratio of the plasma pressure to the magnetic field pressure, a the plasma minor radius, B_T the toroidal magnetic field and I_P the plasma current), is required to maximize the bootstrap current generation. In general, the external current drive efficiencies are proportional to the local electron temperature, and inversely proportional to the density. All these quantities usually peak on-axis, and the external CD sources are most effective where T_e is higher. Therefore, high β_N is not only required to obtain a large enough fraction of bootstrap current (f_{BS}), but it is also a consequence of utilizing heating sources for a large amount of current drive (all the present heating sources also drive the non-inductive current mentioned so far).

In order to achieve fully-noninductive conditions, the sum of the non-inductive sources (external CD and bootstrap) have to align to the total current profile (J) that gives the q profile desired for the scenario. For this to be stationary, these conditions have to be achieved without Ohmic current (which is inherently transient), therefore, the non-inductive sources, in the final

desired condition, have to be positioned in a way that substitutes the Ohmic current over the whole radius. This usually requires a significant part of the current to be moved from the center to mid-radius, which has proven challenging and potentially power expensive.

The hybrid scenario, obtained in several machines [1-5], has the attractive characteristic of a self-organized current profile, which derives from a "flux pumping" mechanism transferring part of the central CD to an off-axis position. This is believed to be caused by the presence of a saturated, benign m=3/n=2 or m=4/n=3 tearing mode, located at ρ~0.25-0.4, which only slightly degrades the confinement, without creating a β_N or I_P collapse. For a more detailed discussion of the flux pumping mechanism we refer to [6,7]. For this reason, the issue of aligning the external current sources to the total current does not apply to the hybrid plasmas, which eliminates one of the challenges faced by the other candidates for steady-state operation. All the non-inductive current can be driven centrally around ρ~0, where T_e and T_i are large, and the CD efficiency is highest. Despite all the central current drive, the flux pumping mechanism produces a q profile that remains slightly above 1 for the duration of the discharges. This eliminates the m=1/n=1 internal kink mode, and no sawteeth appear even after several current diffusion times.

Throughout the paper we will compare the q_{min}~1 hybrid scenario to the higher $q_{min}\geq 1.5$ scenarios, from the perspective of performance and MHD stability. The latter is the more standard high-β_N scenario envisioned for steady-state operation in future machines. It is usually characterised by higher q_{min} (1.5<~q_{min}<~2.5), high normalized pressure and wall stabilization [8-10].

The hybrid discharges were designed to have reverse B_T direction with respect to the I_p direction, to take maximum advantage of the off-axis current [11], which places the $B \times \nabla B$ drift

direction towards the upper divertor. Both double-null (DN) and lower single-null (SN) discharges were studied. We will mainly report on the DN cases, biased upwards, downwards and roughly balanced. The full power of the co-injected neutral beam system was used, amounting to ~11 MW, with an additional ~4 MW of counter-injected power, as a first attempt to reduce the external torque. The ECCD power in these plasmas ranges between 2.4-3.2 MW, the injection is tangential with co-I_P driven current, and the deposition location is kept as close as possible to the plasma center (ρ~0.05-0.25), in a slightly broad shape to avoid excessive localized peaking of the profiles.

At high β_N, plasmas are usually closer to a stability limit, either resistive or ideal, or both. In steady state hybrids, the m=2/n=1 tearing mode appears more readily at high normalized pressure and, despite not causing disruptions, it degrades the confinement significantly, causing the loss of 20 to 50% of the plasma stored energy. Moreover, this mode perturbs the current profile in a way that is not recoverable with the available current sources. It has been shown [10, 12] that the tearing stability of a high β_N plasma is strongly correlated with its proximity to the ideal MHD with-wall limit. The tearing index Δ' shows a sharp increase to very large values when the equilibrium is approaching an ideal limit (figure 20 in reference 10), and under these conditions tearing modes are more susceptible to destabilization. Moreover, when the equilibrium is close to the ideal limit, the equilibrium is extremely sensitive to small perturbations, which may move the ideal limits slightly - in this steep region where Δ' increases rapidly, a small variation of the ideal limit causes large variations in Δ', and hence in the tearing stability. Since operating at lower β_N is typically not a viable option for steady-state scenarios, which require high f_{BS}, one approach is to modify the equilibrium to increase the ideal limit: pushing the ideal limit to higher β_N values allows us to have a high β_N scenario, while operating

in the region where Δ' varies slowly, has reduced values, and so is less sensitive to equilibrium perturbations.

It has been shown [8,10] that the ideal MHD limit increases with broader pressure and current profiles, for high q_{min} equilibria. Given the attractive characteristics of the hybrid scenario, it is crucial to investigate whether this approach can be beneficial also to the hybrid q_{min}~1 plasmas. The tilted, off-axis NBI line in DIII-D was designed to provide 4 MW of heating and current drive power deposited at ρ~0.4, and was utilized in the 2013-2014 hybrid campaign to broaden the pressure and current profiles of high-β_N hybrid plasmas. This means that roughly 35% of the NBI power is deposited at 40% of the minor radius, when one of the NB lines is tilted at the maximum angle. While applying this concept to the hybrid scenario may benefit the MHD stability, it is also important to verify how much the use of off-axis heating may degrade the confinement of these plasmas.

In the following sections we will present the comparison between on-axis and off-axis heating effects on hybrid confinement and performance (section 2), while in section 3 we will discuss the MHD activity present in moderate to high-β_N hybrid plasmas. The path to fully-noninductive conditions in high-β_N hybrid plasmas will be presented in section 4, and in section 5 we report on the ideal MHD and tearing limits of the scenario. We will present the extrapolation of the present plasmas to the ITER and FNSF relevant scenarios in section 6 and discussion of the particular needs and characteristics of the scenario for burning plasma devices are presented in the last section (7).

2. Performance of hybrid plasmas with on- and off-axis NBI

The use of off-axis NBI heating may cause a reduction in confinement and lower β_N levels for a given amount of NBI power, which would impact the bootstrap fraction and hinder the achievement of fully non-inductive conditions. In order to utilize the off-axis NBI system to enhance the MHD stability of the discharges, an assessment of the potential change in confinement associated with it is needed. An example of hybrid discharges with a slightly lower biased DN shape, off-axis NBI, high β_N=3.66 and surface loop voltage (V_{loop}) near zero for ~2 s is shown in figure 1. The discharges are stable to the 2/1 tearing mode, and their duration is limited by the energy available in the neutral beam system. The NBI power was optimized over 3 repeat shots to achieve the longest duration and maximized power yield on the β_N flattop (2.3 to 4.8 s), which in turn maximizes β_N and minimizes V_{loop}. The current diffusion time τ_R in these plasmas is τ_R~1.75 s, hence the high β_N and zero loop voltage duration of 2.5 s is equivalent to ~1.4×τ_R. The density was also optimized to obtain good confinement and to minimize the loop voltage. Lower density shots also yield slightly lower β_N~3.2-3.4 and slightly higher V_{loop}~5-10 mV. For reference, we show the comparison with the more standard high-q_{min} scenario typical time traces

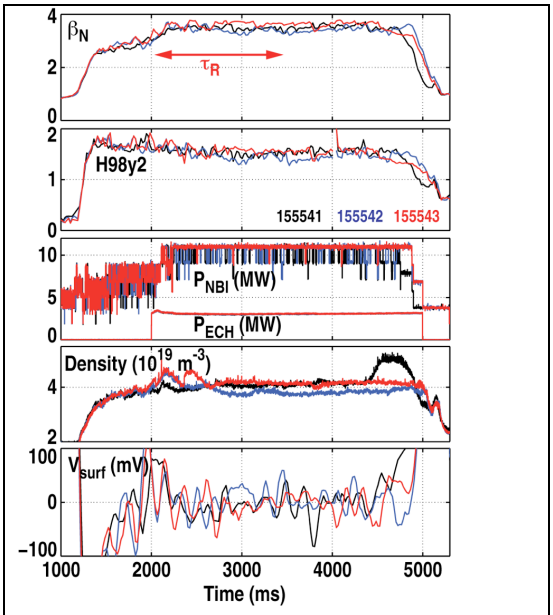

Fig. 1. Time evolution for β_N (a), H_{98y2} (b), NBI and ECH power (c), line averaged density (d) and surface loop voltage (e) for 3 hybrid discharges with off-axis NBI.

in figure 2: for comparable density and q_{95} values, the hybrid discharge (black traces) reaches the same β_N level as the high-q_{min} case (orange traces), while sustaining this β_N for ~1 s longer duration. The H_{98y2} and V_{loop} values are also reproduced by the hybrid plasma, while the lower q_{min}~1 is shown in the bottom part of the figure.

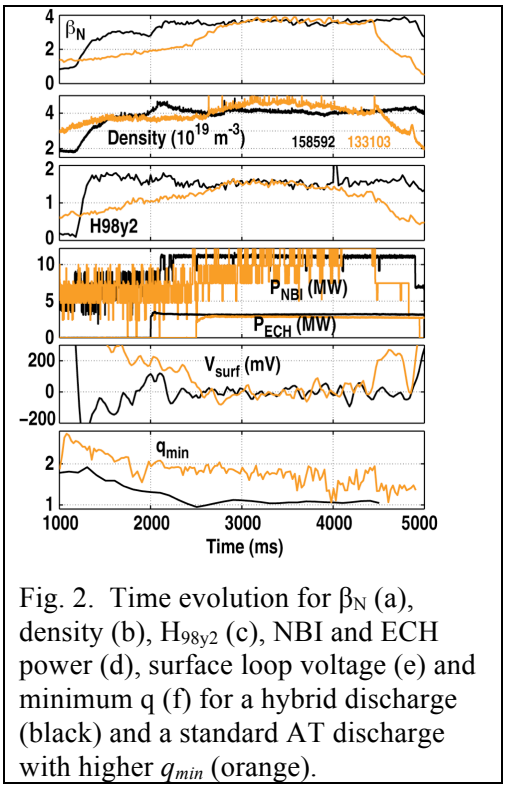

Fig. 2. Time evolution for β_N (a), density (b), H_{98y2} (c), NBI and ECH power (d), surface loop voltage (e) and minimum q (f) for a hybrid discharge (black) and a standard AT discharge with higher q_{min} (orange).

Since it was observed that higher density yields better confinement, a line averaged density scan was performed, in order to explore higher β_N levels, and investigate (i) at what density the positive effect on confinement stops, and (ii) what β_N level can be achieved. Increasing the density increases β_N, which in turn increases f_{BS}, but this may not be sufficient to counteract the decrease in CD efficiency with increased density. Therefore, the high density, higher β_N shots move away from fully non-inductive conditions, but they are useful to study the MHD stability closer to the ideal with-wall limit. In figure 3 we show the comparison between a $\tilde{n}_e$~4×10^{19} m^{-3} and the $\tilde{n}_e$~5×10^{19} m^{-3} case that yields the highest β_N achieved in DIII-D hybrids so far. The shots plotted in black and green have on-axis NBI, while the one plotted in red is sustained with ~4

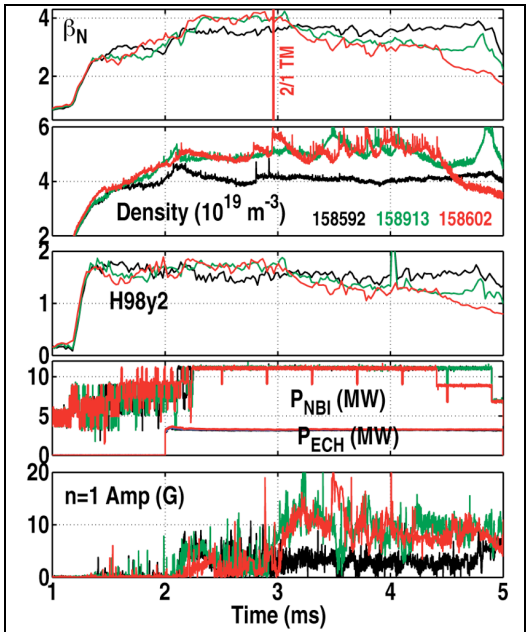

Fig. 3. Time evolution for β_N (a), density (b), H_{98y2} (c), NBI and ECH power (d) and perturbed n=1 field (e) for 3 hybrid discharges with on-axis NBI (black and green traces) and off-axis NBI (red traces).

MW of off-axis NBI. All cases have P_{NBI}~11 MW, P_{ECH}~3.2 MW with central CD injection at ρ~0.05-0.25. It is crucial to note that the plasma with ~36% of off-axis heating reaches exactly the same conditions and the same high β_N as the case with on-axis NBI. This shows that there is no confinement penalty for moving parts of the NBI power away from ρ=0, up to 40% of the normalised minor radius. On the other hand, when the density is increased by ~25% from $\tilde{n}_e$ ~4×10^{19} m^{-3}, the plasmas with $\tilde{n}_e$ ~5×10^{19} m^{-3} reach β_N ~4-4.2, a 10-15% increase from the β_N ~3.66 value. The H_{98y2} factor increases from ~1.55 to ~1.75, when β_N increases up to β_N ~4.2 just before a 2/1 tearing mode starts. This is true for both the on-axis and off-axis NBI cases.

3. MHD activity in high-β_N hybrids

Hybrid discharges with $\beta_N \geq 4$ are limited by MHD modes, while the confinement increases enough to allow for potentially higher β_N values, as suggested by the β_N=4.2 points. Before being terminated by the tearing instability, the β_N=4 cases have been sustained for ~800 ms on the flattop phase. The beneficial effect of increased density on the confinement saturates at $\tilde{n}_e$ ~5×10^{19} m^{-3}, i.e. the higher density discharges with $\tilde{n}_e$ ~6×10^{19} m^{-}3 reach β_N~4, without any further improvement. The m=3/n=2, m=4/n=3 modes are beneficial for the scenario and the deleterious m=2/n=1 modes can be avoided up to β_N~3.6 (the discharges are passively stable in

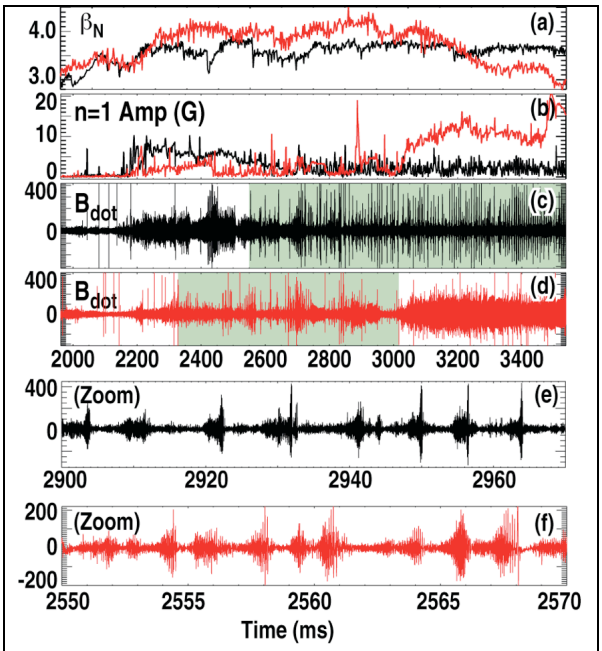

Fig. 4. Time evolution of β_N (a), continuous n=1 mode signal (b), time derivative of the radial field at the wall (c and d), and a zoom over the same traces (e and f) for two off-axis NBI hybrid discharges with β_N=3.7 (stable, black trace) and β_N=4 (unstable to a large n=1 rotating tearing mode at ~3.1 s, red traces). The green shaded area indicates the times with no large tearing modes and the presence of the fast bursting activity.

that case). However, bursts of MHD activity are present in several cases at this β_N level, appearing as fishbone-like events with higher frequency with respect to the 2/1 tearing modes (f_{bursts}~25-50 kHz, $f_{2/1}$~10-15 kHz). These modes, shown in figure 4, have a fairly fast growth time, τ_{bursts}~1 ms, compared to the tearing modes, which grow in τ_{TM}~10 ms. The radial field measurements (time derivative) from a magnetic probe array are shown in the two bottom boxes, with a zoom over the recurrent bursts. The burst pattern is similar to a fishbone type mode, with in some cases an abrupt decay of the oscillations (box f). Given the large fraction of fast ions generated by the NBI system and the low q_{min}~1, these modes would be consistent with fast-ion fishbones associated with the 1/1 surface. Nevertheless, the activity level does not decrease at higher density values, which is not consistent with expected fishbone behavior. When this type of activity ceases in the high-β_N flattop phase, the normalized pressure usually increases, indicating that the confinement was partially degraded during the bursting events.

Another aspect of the MHD activity found in these high power plasmas is the presence of Alfvén Eigenmodes (AEs), which develop at higher frequencies (f_A~200 kHz in these q_{min}~1 plasmas). The high-β_N hybrids appear to have a low level AE activity, consistent with the standard low-q_{min} plasmas. The amplitude of the AE activity decreases with increasing values of

toroidal field, while the use of off-axis NB power does not appear to reduce it. In figure 5 we show an example of the typical density fluctuation spectrogram in the AE frequency range, obtained by evaluating the cross-power of two line-averaged density chords of the CO2 system. The low frequency activity (50-75 kHz) in the higher β_N cases (boxes c and d) represents the previously discussed fishbone-like bursts, while the AE appear at a low level around and above the white dashed line, representing the AE frequency for those plasmas. The higher β_N cases are characterized by higher line averaged density and, of the two cases presented in boxes c and d, the discharge with off-axis NBI (box d) shows a slightly higher AE activity, before the 2/1 tearing mode is triggered (~3 s).

4. Pressure and current drive in hybrid plasmas with on- and off-axis NBI

The concept of broadening the pressure and current profiles to enhance the MHD stability has been applied to higher q_{min} scenarios with some success [8,10] The same amount of off-axis power (~4 MW) was used in DIII-D hybrid discharges to evaluate whether (i) the resulting profiles would be in fact broader, given the somewhat fixed central portion of the plasma, and (ii) the ideal and tearing MHD stability would be affected. The fast-ion pressure and density profiles are calculated by means of the NUBEAM code, tuned with an ad-hoc time-varying parameter representing a fast-ion diffusion coefficient so that the calculated stored energy matches the measured plasma stored energy values during the discharges. In figure 6 we

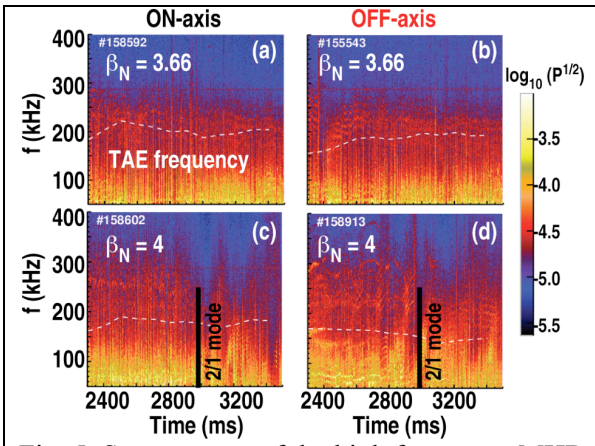

Fig. 5. Spectrogram of the high frequency MHD activity amplitude based on the density fluctuations measured by the CO2 system. Discharges with on-axis beams on the left column, with off-axis NBI on the right, β_N =3.66 on the top row, β_N =4 on the bottom row.

Figure 6 Fast-ion pressure profiles for on-axis (black) and off-axis NBI discharges (red), for β_N flattop of 3.6 (left box) and β_N =4 (right box).

compare the fast-ion pressure profiles of 2 set of discharges which reach β_N~3.6 (left box) and β_N=4 (right box) with and without off-axis power. In the β_N=3.6 case, the line averaged density is $\tilde{n}_e$~4x10^{19} m^{-}3 and the off-axis injection has a significant effect on the pressure profile (several profiles from the β_N flattop phase of both discharges are plotted to indicate the variability of the results). The fast ion content inside ρ~0.45 is significantly reduced in the case of off-axis NBI, and the central fast-ion pressure values are 2.5-3 times higher in the case of the on-axis NBI. In the right box the higher β_N set is shown, where the density is also higher ($\tilde{n}_e$~5x10^{19} m^{-3}), and the impact of the off-axis power is less pronounced. For the higher density cases the off-axis fast-ion pressure profiles appear only slightly less peaked, with a factor of ~1.6 between the central pressure of the on-axis NBI and the off-axis NBI cases. The fast-ion β_N is β_{fast}~19-26% for the on-axis NBI cases, while it's slightly lower, β_{fast}~18-24%, for the off-axis cases.

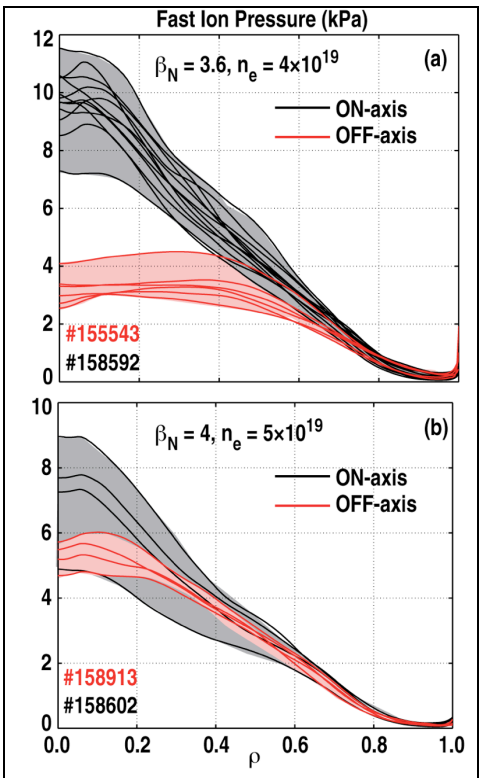

Fig. 6. Fast-ion pressure profiles for on-axis (black) and off-axis NBI discharges (red), for β_N flattop of 3.6 (left box) and β_N =4 (right box).

Since the thermal pressure changes in moving from

on-axis to off-axis NBI are very limited, the fast-ion effects have a small impact on the overall changes in the pressure peaking factor (f_p=$p_{(\rho=0)}$/<p>, where the brackets represent the volume averaged pressure) of the database. This is shown in figure 7, where the pressure peaking factors of all the discharges with (red squares) and without (black circles) off-axis NBI are plotted against the achieved β_N, for several time slices on their stationary β_N flattops. We separated the cases with a DN-biased upwards plasma shape (empty symbols) from the DN-biased downwards plasmas (full symbols) in the plot. The 3 discharges with upper-biased shape have line-averaged density of $\tilde{n}_e$ ~3.6x10^{19} m^{-3}, about 16% lower than the best lower-biased shots. The lower density yields slightly lower β_N values, and higher pressure peaking values for the off-axis NBI cases. Noting that the zero is suppressed in the plot, for comparable β_N values, the off-axis power reduces f_p by ~10%, although a few outliers are present in the database. It is interesting to note that, in the case of the higher q_{min} scenarios, the achieved β_N values span β_N~3-3.6, and the pressure peaking factors of those plasmas fall in a lower range, f_p~2.8-3.3. Despite having higher pressure peaking factors, which are usually associated with lower MHD limits [8-10], we will show that the hybrid regime is characterized by ideal and tearing limits comparable to those calculated for the high-q_{min} plasmas (section 5).

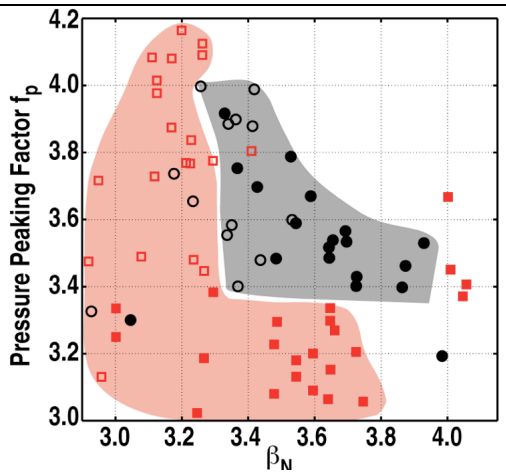

Fig. 7 Pressure peaking factor obtained on the β_N flattop of 8 hybrid discharges plotted against the corresponding β_N values. On-axis NBI cases in black, off axis in red.

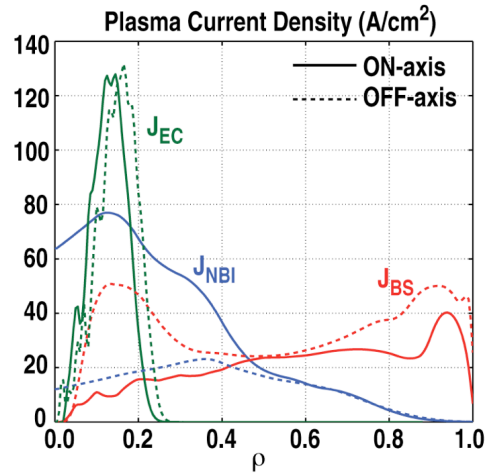

Fig. 8. Calculated EC (green), NBI (blue), bootstrap (red) current density profiles for an on-axis (full lines) and an off-axis NBI (dashed lines) fully-noninductive hybrid discharges.

The picture for the current profile is more complicated, because of the anomalous current diffusion typical of the hybrid scenario, and the non-linear dependencies between J_{BS}, q and the kinetic profiles introduced in the first section. An example of the non-inductive currents in an on-axis (full lines) and off-axis case (dashed lines), are presented in figure 8. The off-axis NBI case has much less NBI current (blue) in the centre, but this is compensated for by a significantly larger contribution from the bootstrap current (red), which shows a peak inside ρ~0.2, not present in the on-axis profiles. These differences are summarized in figure 9, where we compare the sum of all the non-inductive currents for the on- and off-axis case, compared to the total current profile as measured by the equilibrium reconstruction based on magnetics, MSE and kinetic profiles data. Evidence of the anomalous current diffusion mechanism is given by the large discrepancy between the central calculated and measured current, indicating clearly that part of the central poloidal flux is being transported outside of ρ~0.3. The usual location of the stationary, low amplitude 3/2 mode is given by the green shaded area. A more detailed picture of

the typical current density profiles that characterize the β_N flattop phase of these plasmas is in figure 10.

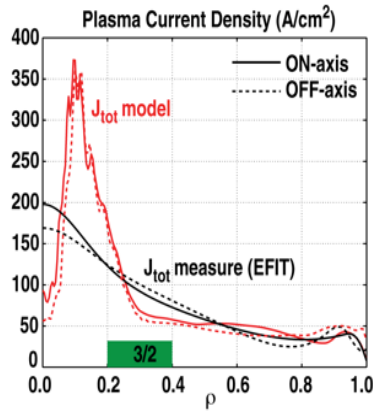

Fig. 9. Calculated plasma current density profile (red) and measured current density (black) for an on axis (full lines) and an off-axis NBI discharge (dashed lines). The radial localization of the m=3/n=2 saturated tearing mode is represented by the green shaded area.

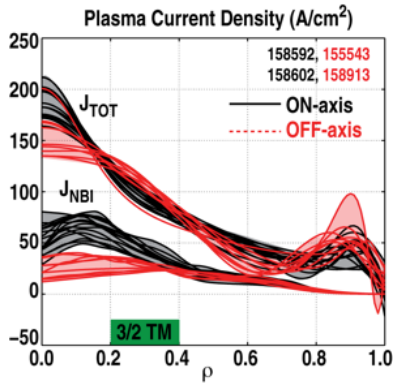

Fig. 10. Total current density profile (top traces) and NBI current density profiles (bottom traces) comparing on-axis (black) and off-axis NBI cases (red). All time slices are on the β_N flattop.

Several time slices at β_N~3.66 and β_N~4 are reported, in order to give an idea of the variability of the results. This confirms the description given previously, where the off-axis NBI mainly seems to reduce the central peak of the NBI current, while the total current density is more affected by the changes in the bootstrap current (red traces in figure 8). This is the cause of the larger amount of current at ρ~0.2-0.4, while the less peaked NBI current profile is the cause of the lower central current density in the off-axis cases. Some differences seem to appear also in the pedestal region; the pedestal profiles and MSE data are still under investigation, and will be deferred to a future paper.

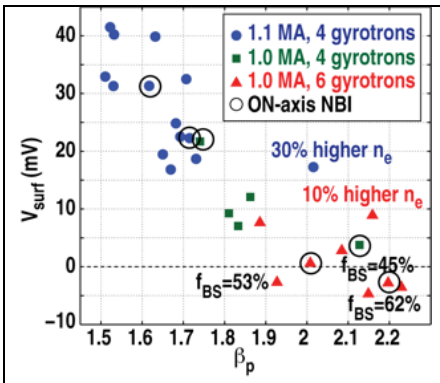

Fig. 11. Surface loop voltage represented against poloidal beta for all the shots in the SS-hybrid database. The blue circles represent the 1.1 MA cases, the green squares the 1.0 MA cases with 4 gyrotrons, the red triangles the 1.0 MA and 6 gyrotrons. The black circles isolate the on-axis NBI cases.

With the calculated current drive from the NB and EC systems and the self-generated bootstrap current, the total plasma current is completely non-inductively generated when 3 MW of ECCD power are used and the bootstrap fraction reaches ~>50-60% at q_{95}~5.5-6.5. The path to fully non-inductive conditions is shown in figure 11, where the measured surface loop voltage at the edge is represented against the values of poloidal β (β_p) for all discharges in the double-null, high q_{95} database. The loop voltage is driven to zero by decreasing the plasma current slightly from 1.1 MA to 1.0 MA and from there by increasing the ECH power by ~800 kW, from ~2.4 MW to 3.2 MW (equivalent of 2 extra gyrotrons used in the shots). We highlight two outliers in order to point out the hidden variable in the study: all the plasmas in the plot have line averaged densities of ~3.5-3.9x10^{19} m^{-3}, while the high β_p cases with V_{surf}≥10 mV have 10% and 30% higher density level, which drives the plasmas away from fully non-inductive conditions. If we isolate the cases with on-axis NBI (black circles), it is interesting to note that the best conditions for non-inductive drive occur for the same I_P, B_T values as for the off-axis cases. This indicates that the V_{loop} *vs* I_P,B_T landscape is not affected by the use of off-axis heating, so either on-axis and off-axis NBI can be chosen in the future, depending on the specific goals of the experiment, while maintaining the non-inductive conditions.

5. Ideal and tearing MHD limits of hybrid plasmas with on- and off-axis NBI

Together, the pressure and the current profile characteristics affect the ideal MHD and the tearing stability limits of a plasma. The DCON code [13] is used to calculate the ideal no-wall

and with-wall β_N limits, and it includes a smoothed model of the DIII-D vessel wall coordinates. The ideal limits are evaluated by progressively increasing the pressure of experimental equilibria in a self-similar fashion, keeping the q profile and the total plasma current fixed for all iterations. A sensitivity study showed that the choice of keeping the current profile fixed instead of the q profile leads to a difference in the calculated limits of ~5-10% in β_N. In figure 12, we report the results of the DCON calculations for a series of hybrid discharges with β_N~3.3-4.2, characterizing the ideal with-wall limit evolution during the β_N ramp and flattop phases. The blue traces show the β_N time evolution of several hybrid plasmas with similar characteristics, spanning the range of achieved β_N~3.3-4.1. On the top row we show the results for the lower biased discharges, on the bottom row those for the upper biased cases, which are characterized by slightly lower density, as described in the previous section. The left column contains the values for the β_N limit with an ideal wall, and on the right those without a wall (no-wall limits). The black circles represent the β_N limits for the plasmas with on-axis NBI, while the red squares are the limits for the corresponding off-axis plasmas. The variability in the results is represented by the various symbols for each time slice. Each discharge evolution has been analyzed by making different assumptions for the plasma density profile fits (e.g. reflectometry or Thomson measurements for the core and vice versa for the pedestal region), and by the presence of constraints on the value of the q profile at ρ=0 (e.g. no constraints, q_0=1.03, q_0=1.06).

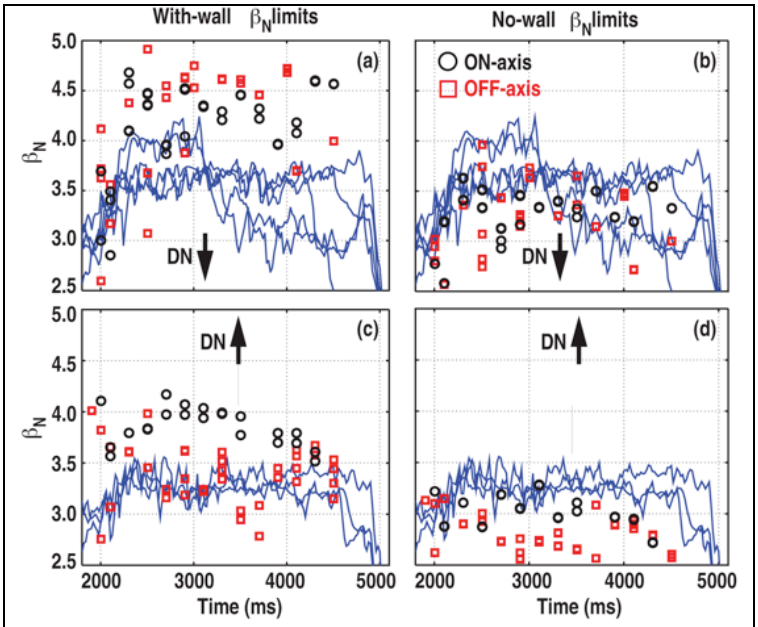

Fig. 12. Measured β_N traces (continuous blue lines) and calculated ideal with-wall (a, c) and no-wall limits (b, d) for 8 hybrid discharges with on-axis (black circles) and off-axis NBI (red squares). The top row contains DN, lower biased shots, while the bottom row the DN, upper biased cases.

Taking into account these variations in the equilibrium reconstructions, it is interesting to note that the upper biased cases are characterized by lower limits than the lower biased plasmas, in both the with-wall and the no-wall analysis. This could be due to a combination of the differences in the pedestal region for both the pressure and the current brought about by the lower density, and the difference in plasma shape (upper vs lower bias). Investigating the details of this difference is beyond the scope of this paper, and it will be addressed in future work focussed on comparing these plasmas and other steady-state hybrid discharges with the lower-single-null ITER shape. The ideal β_N limit without a wall (figure 12-b,d) ranges between β_N~2.5 and β_N~3.6, while the with-wall limit (figure 12-a) is β_N~4.0-4.8 for the lower biased cases, β_N~3.0-3.6 for the upper biased ones with off-axis NBI heating, and β_N~3.5-4.1 for the upper biased with full on-axis NBI heating. The upper biased, lower density cases have higher pressure peaking factor when the off-axis beams are used, and several smaller variations measured in the pedestal current, which seem to concur to make the limits for the on-axis NBI case higher than those of the off-axis plasmas. However, all discharges are operated at or 10-20% above the no-wall β_N limit. This is done with a fixed, standard error field correction algorithm, without the need for RWM feedback. This may be the results of the large toroidal rotation of these plasmas (sustained

with fully co-Ip injected NBI power) and non-resonant damping effects due to the large fraction of fast NBI-generated ions (this has been shown as possible for other DIII-D experiments and their modelling in [14]). When all the ideal with-wall limits for the hybrid database are brought together, it is clear that the limited decrease in the pressure peaking factor with off-axis NBI leads to a rather small increase in the ideal limits of the off-axis cases with respect to the plasmas with on-axis NBI. This is shown in figure 13, where the calculated ideal with-wall limits are plotted against the achieved β_N values for all the time slices on the β_N flattop of the hybrid database. For the higher achieved β_N>3.5, corresponding to the lower biased cases, the increase in the ideal limits for the off-axis cases, on average is ~10%, which brings the values from β_{lim}=4.1-4.7 to β_{lim}=4.5-5.2. At the lower β_N<3.5 values, the lower density, upper biased cases show slightly lower limits for the off-axis heated shots, even though they don't all achieve the same β_N in this case, which makes the comparison more difficult.

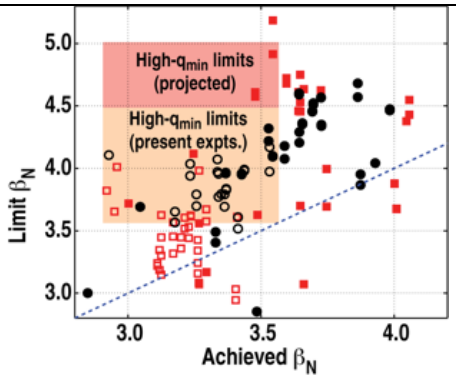

Fig. 13. Survey of with-wall β_N limit for 8 discharges in the SS-hybrid database, represented against the achieved β_N values. All points are on the β_N flattop. The red squares are the off-axis NBI cases, the black circles are the on-axis cases. The orange and red shaded areas represent the present with-wall limits for the standard higher q_{min} scenario and the projected limits for an optimized version of the high q_{min} scenario.

For comparison, we report the achieved and projected ideal limit range for the higher q_{min} scenario (orange shaded area in figure 13). This scenario, usually operated at q_{min}~1.5-2.5, is characterized by ideal with wall limits of β_{li}~3.5-4.2, for achieved β_N levels of β_N<3.6. Projected limits for further optmized higher q_{min} plasmas reach β_{lim}~5, as calculated in [15]. This indicates

that the presently achieved β_N limits of the hybrid scenario are comparable with the limits projected for the higher q_{min} AT plasmas.

The tearing stability of the equilibria can also be calculated, using the PEST3 code [16]. The tearing index Δ' represents the energy available for the plasma to tear, and it is useful to evaluate the first order effects on the tearing stability evolution. The values of the calculated Δ ' are very sensitive to small details of the current and pressure profiles in these high-β_N equilibria, so only the relative trends are meaningful for this kind of study. In figure 14, we show the Δ' evolution for a series of stable hybrid discharges, calculated for the same equilibrium reconstruction variations described for the ideal MHD limit study. Each square symbol reports the Δ' value associated with the plasma equilibrium for each time slice, also shown in the β_N and l_i traces on the same plot. In some cases, various Δ' values are reported, as calculated for slightly different equilibrium reconstructions of the same shot and time slice, to show the variability of the results in the database. Two discharges at higher β_N, where a large m=2/n=1 tearing mode sets in at t~3 s, are represented in figure 15, with the respective Δ' evolution. The Δ' values are evaluated for the m=2/n=1 surface, considering the m=2, m=3 and m=4 surfaces to be resonant and coupled. Despite the variability in Δ' values across the various discharges, the results suggest that the two unstable discharges are associated with increasing trends for the tearing index Δ' leading up to the mode. On the other hand, 3 of the 4 stable cases show a decreasing trend in Δ' all the way to the end of the shot, while the fourth case appears to have little variation in the Δ' values over the β_N flattop; the trend stays horizontal until the end of the shot. This is an indication that the higher β_N discharges are evolving towards a more unstable state, which is consistent with the triggering of the large 2/1 tearing mode in the experiment.

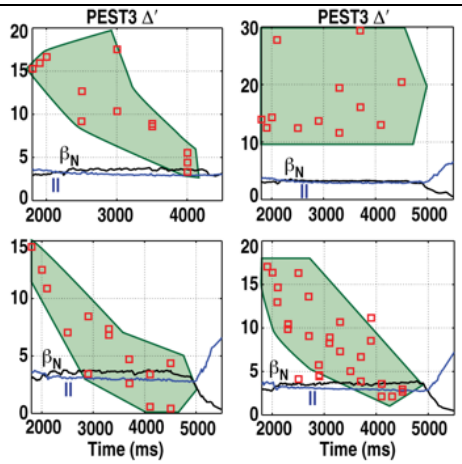

Fig. 14. Evolution of the calculated Δ' values for several equilibria leading up to and on the β_N flattop of 4 hybrid discharges that remain stable until the end. The β_N and li traces are also plotted for reference, and the shaded areas highlight the Δ' trends in time over the high-β_N phase.

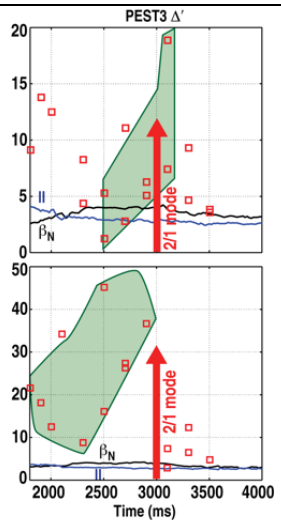

Fig. 15. Evolution of the calculated Δ' values for several equilibria leading up to and on the β_N flattop of 2 hybrid discharges that develop a 2/1 tearing mode at ~3 s. The β_N and li traces are also plotted for reference, and the shaded areas highlight the Δ' trends in time over the high-β_N phase.

6. Projecting the steady-state hybrid scenario to ITER and FNSF

The extrapolation of a scenario to future devices can be done with a 0-D model [17,18], to determine the feasibility of the hybrid scenario in burning plasma devices. The input parameters, such as the geometry, the density, B_T, I_P, are scaled up to the values of the desired machine. In this study we compare a ρ* scaling based on the present scenario density and a specified Greenwald fraction (f_{GW}) to obtain the input plasma density. The output parameters are determined self-consistently in the model, which yields the H_{98y2} factor, the temperature and the fusion, alpha and current drive power (P_{fus}, P_α and P_{CD} respectively). The profile shapes are specified, based on the experiment profiles parameters, and the β_N and q_{95} values are kept fixed at those in the present scenario. A realistic central current drive efficiency is evaluated from the

ITER physics basis [19], as a function of the plasma density, temperature and major radius, $\gamma_{CD}=I_{CD}n_{19}R/P_{CD}=2.5\times10^{19}$ A/m^{2}W at T_e=20 keV. We assume that 60% of the total plasma current is constituted by the bootstrap current, a fraction consistent with the values calculated for the best present hybrid discharges as reported in figure 11. This allows us to calculate the current drive power needed to sustain the external current source. The input operating parameters used for the steady-state hybrid scenario are reported in table 1, for a deuterium plasma in DIII-D and D-T plasmas in ITER and FNSF. To study the feasibility of the hybrid scenario in ITER we choose a lower density, lower β_N, LSN hybrid discharge, which is compatible with RMP ELM mitigation and has β_N~2.84 and line averaged density $\tilde{n}_e$ ~3.2x10^{19} m^{-3}. This lower β_N type of hybrid has been proven to reach fully non-inductive conditions, with a lower confinement quality (H_{98y2}=1.3). For the FNSF scaling, the DN hybrid scenario with β_N~3.66, $\tilde{n}_e$ ~4.1x10^{19} m^{-3} is used.

Inputs:	ITER	FNSF	DIII-D SN	DIII-D DN
R (m)	6.2	2.49	1.68	1.67
R/a	3.1	3.5	2.8	2.83
B_T (T)	5.3	6.0	1.9	1.9
I_P (MA)	9.0	6.7	1.0	1.0
f_{BS}	0.6	0.6	0.6	0.6
β_N	2.84	3.66	2.84	3.66
β_T	0.0235	0.031	0.0235	0.0315
T_0 (keV)	16	14	5.25	6.3

Table 1

Using the ρ* scaling for density and temperature $\tilde{n}_e$=B$^{4/3}$a$^{-1/3}$, T=B$^{2/3}$a$^{1/3}$ the projected ITER and FNSF densities are calculated, at fixed collisionality (ν^*), β_N and q. The new stored energy W is W=3nTV (where V is the plasma volume), and the powers are calculated with the *DS03*

scaling law [18], which has proven to best reflect the confinement scaling at high pressure in the tokamak databases. The details of the scalings are given in the formulas below:

$$\varsigma = 2.5\frac{T_0}{20Rn_0}$$

$$P_{CD} = I(1-f_{BS})/\varsigma$$

$$P_{HEATING} = \left(\frac{W}{0.0282 I_p^{0.831} B_T^{0.069} \tilde{n}_e^{0.488} R^{2.107} \varepsilon^{-0.3} H_{mass}^{0.14} \kappa^{0.75}}\right)^{1/0.45}$$

$$P_{BREM} = \frac{5.34\cdot 10^{-3} VZ\left(n_0/10\right)^2 \sqrt{T_0}}{1+2SN+0.5ST}$$

$$P_{FUSION} = 7.043\cdot 10^{15}\cdot 2V(fuel_{frac}\cdot n_0/10)^2 T_0^2 \cdot fus_{\text{int}}$$

$$fus_{\text{int}} = 1.64\cdot 10^{-19}(-0.455383+0.218998T_0 - 0.0089152T_0^2 + 0.000103742T_0^3)$$

$$P_\alpha = P_{FUSION}/5$$

$$\tau_E = \frac{W}{P_{HEATING}-P_{BREM}}$$

$$\tau_{98y2} = (P_{HEATING}-P_{BREM})^{-0.69}\cdot 0.144 I_p^{0.93} B_T^{0.15}\left(\tilde{n}_e/10\right)^{0.41} R^{1.97}\kappa^{0.78}\varepsilon^{-0.58} H_{mass}^{0.19}$$

$$H_{98y2} = \frac{\tau_E}{\tau_{98y2}}$$

$$Q = \frac{P_{FUSION}}{P_{HEATING}+P_{BREM}-P_\alpha}$$

where $SN=n_0/\tilde{n}_e$, ST=0.75 are profile shape factors describing the degree of peaking of the measured density and temperature profiles, f_{imp}=0.01, Z_{imp}=10, f_{He}=0.059 for the ITER case and f_{He}=0.018 for the FNSF case, $fuel_{frac}=1-2f_{He}-f_{imp}Z_{imp}$.

Taking into account the estimated bremsstrahlung radiation (P_{BREM}), these parameters allow us to estimate the auxiliary power needed to sustain the chosen W value ($P_{HEATING}$), the power needed to drive the external current in excess of $I_P \cdot f_{BS}$ (P_{CD}), the fusion and alpha powers (P_{FUSION} and P_α), and the resulting H_{98y2} factor and fusion energy gain Q. In table 2 the results of this scaling are reported for a DN FNSF scenario and a LSN ITER scenario. For the ITER Q=5 mission, the present temperature of 5.25 keV (averaged between T_e and T_i) scales to Q=5.6, with

auxiliary power P_{AUX}= 80 MW and an equivalent H_{98y2} factor of 1.46. This is encouraging from the point of view of the confinement - however, taking into account the alpha power, which drives minimal current, the power available for current drive is lower than the power necessary to drive all the current (P_{HEAT}-P_{α}<P_{CD}).

Inputs:	ITER	FNSF	DIII-D SN	DIII-D DN
R (m)	6.2	2.49	1.68	1.67
R/a	3.1	3.5	2.8	2.83
B_T (T)	5.3	6.0	1.9	1.9
I_P (MA)	9.0	6.7	1.0	1.0
f_{BS}	0.6	0.6	0.6	0.6
β_N	2.84	3.66	2.84	3.66
β_T	0.0235	0.031	0.0235	0.0315
T_0 (keV)	16	14	5.25	6.3

Table 2

At the current temperature and high Greenwald fraction (f_{GW}=1.17), there is no solution that yields P_{HEAT}-P_{α}=P_{CD}. In order to correct for the high Greenwald fraction and the low available power, the scenario can yield 71 MW of power for current drive (table 3), if the input temperature is increased by 15% (6 keV) and the Greenwald fraction reduced to 0.75. This requires a 3.5% increase in the H_{98y2} confinement factor of the scenario, and it would lead to a reduction of fusion gain to Q=3. In the case of the FNSF 6.7 MA scenario, the present DN discharges scale to Q=3.5, P_{AUX}=32 MW. The projected Greenwald fraction is low, but the power needed to reach fully non-inductive conditions is higher than the power available for current drive. To reach P_{HEAT}-P_{α}=P_{CD} in FNSF, the scenario requires and increase of 45% in temperature (9.1 keV), which could be achieved with an 11% increase in the H_{98y2} confinement factor. This would not decrease the fusion gain, but it would require a larger amount of auxiliary power (P_{AUX}=73). These examples show that the present hybrid scenario, in its SN and DN form, has achieved the required values of stored energy and fusion gain for both the ITER 9 MA and

Inputs:	ITER	FNSF	DIII-D SN	DIII-D DN
R (m)	6.2	2.49	1.68	1.67
R/a	3.1	3.5	2.8	2.83
B_T (T)	5.3	6.0	1.9	1.9
I_P (MA)	9.0	6.7	1.0	1.0
f_{BS}	0.6	0.6	0.6	0.6
β_N	2.84	3.66	2.84	3.66
β_T	0.0235	0.031	0.0235	0.0315
T_0 (keV)	16	14	5.25	6.3

Table 3: DIII-D SN T0=6 keV, DIII-D DN T0=9

the FNSF 6.7 MA missions. However, sustaining fully non-inductive conditions is more challenging, due to the low efficiency of the present current drive systems, and the scenario requires some modifications to be compatible with f_{NI}=1 in the projected cases.

It is important to note that these projections have been performed based on model hybrid discharges without counter-NBI injection, i.e. all co-Ip current and torque injection. This results in a high external torque of ~8.8 Nm. It is expected that ITER may have much lower external input torque values, due to its larger volume; therefore, it will be necessary to extend the all-co-NBI steady-state hybrid scenario to low torque conditions. Some results on this, applied to lower pressure, inductive hybrid plasmas are described in [20]. Work has started to extend the high-β_N, steady-state hybrid scenario to lower values of external torque by utilizing the neutral beam line injecting current and torque in the direction opposite to the plasma current. This method provides 4 MW of extra NB power, and ~3.2 Nm torque in the counter-I_P direction. By adding the counter-I_P NBI source to an existing high-β_N hybrid discharge, the external torque is reduced by ~35%, from ~8.8 Nm to ~5.6 Nm, while the total injected power reaches ~19 MW. However, the counter-NBI system is detrimental to the discharge confinement time τ_E, which decreases by ~18%, and the confinement factor H_{98y2}, which decreases by 22%. With the additional 35% of

auxiliary power, the discharge reaches the same β_N flattop value as the co-injected case, hence, the confinement decreases.

From the perspective of the scaling work presented in this section, the effects of this choice are limited: as shown in the equations above, the projected temperature and stored energy W are based on the measured T_e and T_i, which are the same for the all-co-NBI discharges and the corresponding counter-NBI cases. This is used to evaluate $P_{HEATING}$, and therefore τ_E, τ_{98y2} and H_{98y2}. The temperature and density profiles appear similar for the co-NBI cases and the counter-NBI injection case available, and this is consistent with the fact that the higher power, lower torque case reaches the same β_N as the co-injected cases. Since the heating power for the scaled scenario is not projected from the presently used input power, but instead from the presently achieved W and T, the projected H_{98y2} and Q values do not change significantly for the lower torque cases. However, this is a consequence of the type of scaling method, and since a lower confinement factor and a lower confinement time is observed in the present counter-injected discharges, it is reasonable to expect that this may project to the ITER and FNSF scenarios, which could potentially require more auxiliary power ($P_{HEATING}$ in this study) to reach the projected W. Therefore, operating the hybrid scenario at low torque may entail obtaining lower confinement factor and Q values than those extrapolated from the present high-torque plasmas.

7. Discussion and conclusions

Steady-state hybrid plasmas have been obtained in DIII-D with a DN plasma shape, $\beta_N \geq 3.5$ and zero surface loop voltage for ~1.5 τ_R, being limited only by the available NB system energy. These plasmas are characterized by a flat q profile, at q_{95}=5.5-6.5, and are generally stable to deleterious 2/1 tearing modes. Although the central current is theoretically overdriven by the use of efficient NB and EC current drive close to the axis, an anomalous current diffusion

mechanism, believed to stem from a small saturated 3/2 tearing mode, maintains q_{min} above 1, avoiding sawtooth instabilities. The discharges exceed the ideal no-wall β_N limit and reach 80-90% of the calculated with-wall limit. The confinement quality of these plasmas is excellent (H_{98y2}=1.6) and appears to increase with density, up to line averaged densities of $\tilde{n}_e$ ~5x10^{19} m^{-3}. The highest β_N cases, obtained with $\tilde{n}_e$ ~5x10^{19} m^{-3}, exceed β_N=4 and reach 80-90% of the calculated ideal wall β_N limit. These cases are sustained for ~800 ms in the β_N flattop, before a growing 2/1 mode is triggered. The TAE activity level of these discharges is consistent with the usual TAE amplitudes characterizing low q_{min} plasmas. The use of ~35% of off-axis NB heating increases the calculated ideal limits by ~10%, without any confinement penalty.

On the other hand, adding 4 MW of counter-injected NBI power decreases the confinement time and the confinement factor by ~20%, and does not lead to higher β_N values. The cause of this apparent loss of confinement associated with counter-Ip NBI injection is still under investigation for several DIII-D scenarios. However, this is the first step toward operating the steady-state hybrid scenario at lower injected torque values, which is among the requirements for future burning plasma devices. Furthermore, in order for the hybrid scenario to be considered compatible with future machine operation, it is necessary to extend it in several directions, besides low torque operation, such as an ELM suppressed regime, integration with a radiating divertor, and electron heating schemes. Encouraging results have been obtained in the former, with a lower β_N steady-state version of the hybrid scenario. In these lower pressure hybrids, an n=3 RMP technique has successfully suppressed ELMs at β_N=2.4, and mitigated them at β_N=2.9. This has been achieved in a LSN plasma shape and at lower density ($\tilde{n}_e$ ~3x10^{19} m^{-3}). Both the DN and the LSN shaped cases lead to fusion gain values compatible with operation in ITER and

FNSF at the desired values of Q. However, the current drive efficiency of the present heating systems remains low and requires high values of current drive power in the scaled scenarios.

It is interesting to note that, in the case of these future devices, a fundamental difference will be the presence of the α-heating power, which increases with β_N, and drives minimal current. In the present machines, where the auxiliary power also drives part of the plasma current, the operating point where f_{NI}=1 occurs in virtually all cases with a bootstrap fraction that does not exceed 60%, including for the standard higher q_{min} scenarios [8-10,15]. An exception may be the case of plasmas with a strong internal temperature or density gradient, such as an ITB, which will increase the bootstrap fraction for the given β_N level. Under these conditions f_{BS} may reach 60-70% and the external current drive needed for f_{NI}=1 will be reduced. In the case of a burning plasma device, the β_N level needed to obtain the desired output power will be sustained in part by the α-heating, which limits the amount of external power capable of driving the plasma current. This is where the more efficient central current drive, which can be used in the hybrid scenario without overdriving the center of the plasma current density profile, is likely to be a very attractive feature. The solution for f_{NI}=1 can be achieved with lower β_N values than those needed for f_{NI}=1 in a higher-q_{min} scenario, which entail lower f_{BS} values, since the CD efficiency is higher for the central hybrid injection. This makes up for the lower bootstrap current, and for the presence of the α-heating, which supplies part of the auxiliary power available to sustain the chosen β_N value. The scaling study presented in section 7 confirms this scenario.

Nevertheless, more work is necessary to extend the steady-state hybrid scenario to operating parameters required for ITER and FNSF. Besides the progress made for the low torque and ELM suppression direction, a radiating divertor solution needs to be explored, and prove to be compatible with the high core performance of these plasmas. The next steps also involve

increasing the electron heating power to reach T_e/T_i~1, which will also go in the direction of reducing the externally injected torque.

Finally, the mechanism that allows for a flat q profile without sawteeth, despite the theoretical current overdrive in the plasma center, is not yet completely understood, and no theory has been put forward to explain it in detail. This is an important point that needs to be addressed, in order to be able to scale this anomalous current diffusion effect to future machines, and prove that the q_{min}~1 hybrid conditions can indeed be reproduced in burning plasma devices.

ACKNOWLEDGEMENTS

This material is based upon work supported by the U.S. Department of Energy, Office of Science, Office of Fusion Energy Sciences, using the DIII-D National Fusion Facility, a DOE Office of Science user facility, under Awards DE-FG02-04ER54761, DE-FC02-04ER54698, DE-AC52-07NA27344, SC-G903402, and DE-AC02-09CH11466. DIII-D data shown in this paper can be obtained in digital format by following the links at https://fusion.gat.com/global/D3D_DMP.

REFERENCES

[1] T.C. Luce, C.D. Challis, S. Ide, E. Joffrin, Y. Kamada, P.A. Politzer, J. Schweinzer, A.C.C. Sips, J. Stober, G. Giruzzi, C.E. Kessel, M. Murakami, Y.-S. Na, J.M. Park, A.R. Polevoi, R.V. Budny, J. Citrin, J. Garcia, N. Hayashi, J. Hobirk, B.F. Hudson, F. Imbeaux, A. Isayama, D.C. Mc Donald, T. Nakano, N. Oyama, V.V. Parail, T.W. Petrie, C.C. Petty, T. Suzuki, M.R. Wade, the ITPA Integrated Operation Scenario Topical Group Members, the ASDEX-Upgrade Team, the DIII-D Team, JET EFDA Contributors and the JT-60U Team, 2014 Nucl. Fusion **54** 013015

[2] A.C.C. Sips, R. Arslanbekov, C. Atanasiu, W. Becker, G. Becker, K. Behler, K. Behringer, A. Bergmann, R. Bilato, D. Bolshukhin, K. Borrass, B. Braams, M. Brambilla, F. Braun, A. Buhler, G. Conway, D. Coster, R. Drube, R. Dux, S. Egorov, T. Eich, K. Engelhardt, H.-U. Fahrbach, U. Fantz, H. Faugel, M. Foley, K.B. Fournier, P. Franzen, J.C. Fuchs, J. Gafert, G. Gantenbein, O. Gehre, A. Geier, J. Gernhardt, O. Gruber, A. Gude, S. Günter, G. Haas, D. Hartmann, B. Heger, B. Heinemann, A. Herrmann, J. Hobirk, F. Hofmeister, H. Hohenöcker, L. Horton, V. Igochine, D. Jacobi, M. Jakobi, F. Jenko, A. Kallenbach, O. Kardaun, M. Kaufmann, A. Keller, A. Kendl, J.-W. Kim, K. Kirov, R. Kochergov,

H. Kollotzek, W. Kraus, K. Krieger, B. Kurzan, P.T. Lang, P. Lauber, M. Laux, F. Leuterer, A. Lohs, A. Lorenz, C. Maggi, H. Maier, K. Mank, M.-E. Manso, M. Maraschek, K. F. Mast, P. McCarthy, D. Meisel, H. Meister, F. Meo, R. Merkel, D. Merkl, V. Mertens, F. Monaco, A. Mück, H.W. Müller, M. Münich, H. Murmann, Y.-S. Na, G. Neu, R. Neu, J. Neuhauser, J.-M. Noterdaeme, I. Nunes, G. Pautasso, A.G. Peeters, G. Pereverzev, S. Pinches, E. Poli, M. Proschek, R. Pugno, E. Quigley, G. Raupp, T. Ribeiro, R. Riedl, S. Riondato, V. Rohde, J. Roth, F. Ryter, S. Saarelma, W. Sandmann, S. Schade, H.-B. Schilling, W. Schneider, G. Schramm, S. Schweizer, B. Scott, U. Seidel, F. Serra, S. Sesnic, C. Sihler, A. Silva, E. Speth, A. Stäbler, K.-H. Steuer, J. Stober, B. Streibl, E. Strumberger, W. Suttrop, A. Tabasso, A Tanga, G. Tardini, C. Tichmann, W. Treutterer, M. Troppmann, P. Varela, O. Vollmer, D. Wagner, U. Wenzel, F. Wesner, R. Wolf, E. Wolfrum, E. Würsching, Q. Yu, D. Zasche, T. Zehetbauer, H.-P. Zehrfeld and H. Zohm, 2002 Plasma Phys. Control. Fusion **44** B69.

[3] E. Joffrin, A.C.C. Sips, J.F Artaud, A. Becoulet, L. Bertalot, R. Budny, P. Buratti, P. Belo, C. D Challis, F. Crisanti, M. de Baar, P. de Vries, C. Gormezano, C. Giroud, O. Gruber, G. T.A Huysmans, F. Imbeaux, A. Isayama, X. Litaudon, P.J. Lomas, D.C. McDonald, Y. S Na, S.D. Pinches, A. Staebler, T. Tala, A. Tuccillo, K.-D. Zastrow and JET-EFDA Contributors to the Work Programme 2005 Nucl. Fusion **45** 626.

[4] A. Isayama, Y. Kamada, N. Hayashi, T. Suzuki, T. Oikawa, T. Fujita, T. Fukuda, S. Ide, H. Takenaga, K. Ushigusa, T. Ozeki, Y. Ikeda, N. Umeda, H. Yamada1, M. Isobe1, Y. Narushima1, K. Ikeda1, S. Sakakibara1, K. Yamazaki1, K. Nagasaki and the JT-60 Team, 2003 Nucl. Fusion **43** 1272.

[5] T.C. Luce, M.R. Wade, P.A. Politzer, S.L. Allen, M.E. Austin, D.R. Baker, B. Bray, D.P. Brennan, K.H. Burrell, T.A. Casper, M.S. Chu, J.C. DeBoo, E.J. Doyle, J.R. Ferron, A.M. Garofalo, P. Gohil, I.A. Gorelov, C.M. Greenfield, R.J. Groebner, W.W. Heidbrink, C.-L. Hsieh, A.W. Hyatt, R. Jayakumar, J.E. Kinsey, R.J. La Haye, L.L. Lao, C.J. Lasnier, E.A. Lazarus, A.W. Leonard, Y.R. Lin-Liu, J. Lohr, M.A. Mahdavi, M.A. Makowski, M. Murakami, C.C. Petty, R.I. Pinsker, R. Prater, C.L. Rettig, T.L. Rhodes, B.W. Rice, E.J. Strait, T.S. Taylor, D.M. Thomas, A.D. Turnbull, J.G. Watkins, W.P. West and K.-L. Wong, 2001 Nucl. Fusion **41** 1585.

[6] M.R. Wade, T.C. Luce, R.J. Jayakumar, P.A. Politzer, A.W. Hyatt, J.R. Ferron, C.M. Greenfield, M. Murakami, C.C. Petty, R. Prater, J.C. DeBoo, R.J. La Haye, P. Gohil and T.L. Rhodes, 2005 Nucl. Fusion **45** 407.

[7] C.C. Petty, M.E. Austin, C.T. Holcomb, R.J. Jayakumar, R.J. La Haye, T.C. Luce, M. A. Makowski, P.A. Politzer, and M.R. Wade, 2009 Phys. Rev. Lett. 102 045005.

[8] A.D. Turnbull, T.S. Taylor, M.S. Chu, R.L. Miller and Y.R. Lin-Liu, Nucl. Fusion **38**, 1467 (1998).

[9] A. D. Turnbull, T. S. Taylor, Y. R. Lin-Liu, and H. St. John, Phys. Rev. Lett. 74, 718 1995.

[10] F. Turco, C.T. Holcomb , J.R. Ferron , T.C. Luce , P.A. Politzer , J.M. Park, A.E. White, D.P. Brennan, A.D. Turnbull, J.M. Hanson , M. Okabayashi , and Y. In, Phys. Plasmas **19**, 122506 (2012).

[11] J.M. Park, M. Murakami, C.C. Petty, W.W. Heidbrink, M.A. Van Zeeland, D.C. Pace, R. Prater, J.R. Ferron, T.H. Osborne, C.T. Holcomb, G.J. Jackson, T.W. Petrie, B.A. Grierson, C.J. Murphy and T. Suzuki, IAEA conference paper.

[12] D.P. Brennanb, A.D. Turnbull, M.S. Chu, R.J. La Haye, L.L. Lao, and T.H. Osborne, S.A. Galkin, Phys, Plasmas **14**, 056108 2007.

[13] A.H. Glasser and M.S. Chance, Bull. Am. Phys. Soc. **42**, (1997) 1848.
[14] F. Turco, A.D. Turnbull, J.M. Hanson, G.A. Navratil, Phys. Plasmas **22** 022503 (2015)
[15] J.R. Ferron, C.T. Holcomb, T.C. Luce, J.M. Park, P.A. Politzer, F. Turco, W. W. Heidbrink, E. J. Doyle, J. M. Hanson, A. W. Hyatt, Y. In, R. J. La Haye, M. J. Lanctot, M. Okabayashi, T. W. Petrie, C. C. Petty and L. Zeng, Phys. Plasmas **20**, (2013) 092504.
[16] A. Pletzer, A. Bondeson, and R. L. Dewar, J. Comput. Phys. **115**, 530 (1994).
[17] V.S. Chan, R.D. Stambaugh, A.M. Garofalo, M.S. Chu, R.K. Fisher, C.M. Greenfield, D.A. Humphreys, L.L. Lao, J.A. Leuer, T.W. Petrie, R. Prater, G.M. Staebler, P. B. Snyder, H.E. St. John, A.D. Turnbull, C.P.C. Wong, M.A. Van Zeeland, Fusion Science and Technology **57** (2010) 66
[18] T.C Luce, C.C Petty and J.G. Cordey, Plasma Phys. Control. Fusion **50** (2008) 043001
[19] ITER Physics Basis Editors, ITER Physics Expert Group Chairs and Co-Chairs and ITER Joint Central Team and Physics Integration Unit, Nucl. Fusion **39** (1999) 2137.
[20] W.M. Solomon, P.A. Politzer, R.J. Buttery, C.T. Holcomb, J.R. Ferron, A.M. Garofalo, B.A. Grierson, J.M. Hanson, Y. In, G.L. Jackson, J.E. Kinsey, R.J. La Haye, M.J. Lanctot, T.C. Luce, M. Okabayashi, C. C. Petty, F. Turco and A. S. Welander, Nucl. Fusion **53** 093033 (2013)

2.7: Preliminary Results from Investigating Magnetic Flux Pumping in Hybrids

The following presentation on MP2015-22-02 was made at the DIII-D Friday Science Meeting on July 31, 2015.

Preliminary Results from Investigating Magnetic Flux Pumping in hybrids MP2015-22-02

by
Zane Taylor, ORAU

R.J. La Haye, T.C. Luce, C.C. Petty, R. Nazikian

Presented at the
DIII-D Friday Science Meeting
General Atomics, San Diego

July 31, 2015

Outline

- Hybrid scenario in DIII-D
  - Characteristics of a hybrid discharge
  - Flux pumping broadens current profile, inhibits sawteeth
- Evaluation of Flux states used to track poloidal flux consumption
  - Flux states to investigate/evaluate flux pumping
- Preliminary results
  - ECCD for 3/2 NTM mode control
  - n=3 RMP ELM suppression
  - β_N / β_p fluxpumping scaling?
- Conclusion
  - Next steps

MHD Activity is an Integral Part of Hybrid Operation

The effect of the ~stationary NTM:

- **is to broaden the current profile**
  - **raises q_0**
  - **sawteeth are reduced (for q_{95} <4)**
  - **or eliminated (for q_{95} >4)**
  - **better confinement**
  - **removes one trigger for the 2/1 NTM**
- **increases stability of 2/1 mode**
- **with only a modest confinement reduction est. $\Delta\tau_E/\tau_E \approx$ -6-15% (4/3 or 3/2) depending on q_{95}, rotation**
- **leading to high β operation; up to $\beta_N \sim 4\ell_i$ (~ no-wall limit)**

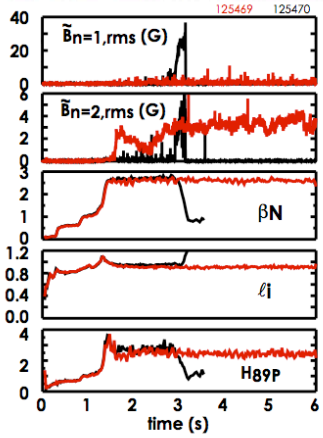

- **Without a 3/2 (or 4/3) mode, the discharge evolves to an unstable 2/1 tearing mode**

Flux Pumping is Dependent on NTM Amplitude (Here 3/2 Controlled by ECCD)

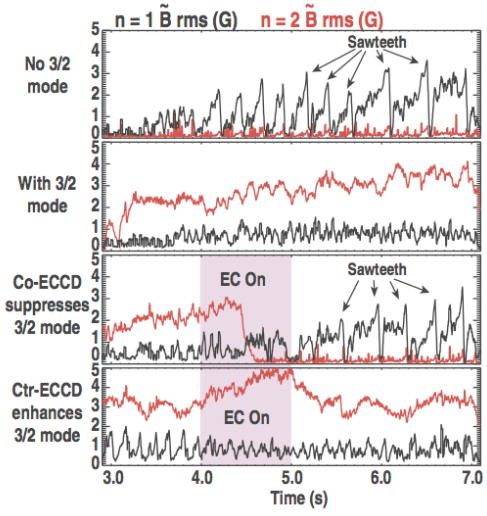

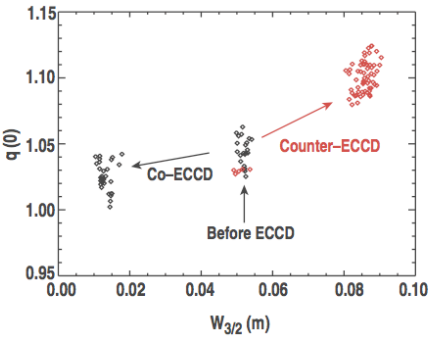

- **3/2 NTM Amplitude is key to avoid sawteeth**

M.R. Wade IAEA 2004

Hybrid scenario summary

- **Presence of stationary NTM mode (usually m/n=3/2) modifies the current profile**
- **broadened current profile raises q0 above one —> no sawteeth. Detrimental 2/1 tearing mode not triggered**
- **No definitive identification of flux pumping mechanism**
  - ~~Direct current drive by the 3/2 mode~~
  - ~~Broadening of the fast ion spatial profile by the 3/2 mode~~
  - Dynamo, conversion of kinetic to magnetic energy via <vXb>?
  - **Modulation of the NTM amplitude by ELMs**
  - other…

5 DIII-D NATIONAL FUSION FACILITY

Change in Flux States track poloidal flux usage

$\Psi_{kin} I_p = W_{kin}$ = Work done by the electric field within the plasma. Amount of poloidal magnetic energy being converted to kinetic energy in the plasma.

$\Psi_c I_p = W_{coil}$ = Energy provided by poloidal coils coupling with the plasma. Mutual inductance between coils and the plasma

$$\Psi_{kin} = \frac{1}{I_p}\int \mathrm{d}R\mathrm{d}z J_\phi \psi \qquad \Psi_c = \frac{1}{I_p}\int \mathrm{d}R\mathrm{d}z J_\phi \psi_c$$

- J_ϕ & ψ - obtained from E-fit, ψ_c - obtained from poloidal coil currents
- T.C. Luce Nucl. Fusion paper: Vary I_p ramp rate to find optimum flux usage in DIII-D.

6 DIII-D NATIONAL FUSION FACILITY

Change in Flux States track poloidal flux usage

- Surplus and deficit in the first two intervals can be explained by the change in stored energy in the plasma.

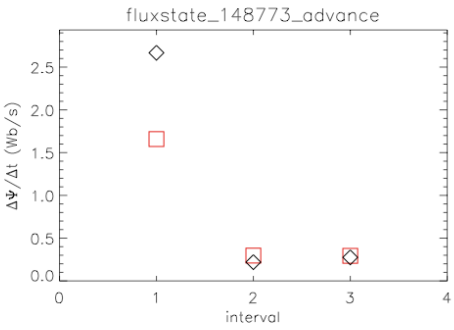

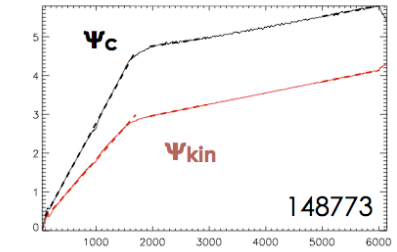

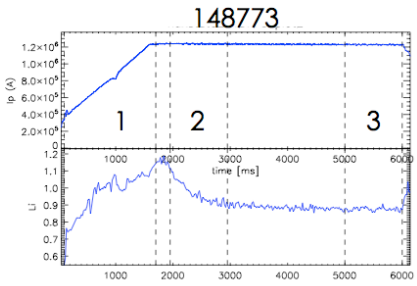

7

Deficit in Rate of Change in Flux States in Hybrid discharges

late in discharge (~middle to end of I_p flat top):

$$\Delta\Psi_c < \Delta\Psi_{kin} \longrightarrow$$

Deficit in poloidal flux. More poloidal flux being converted to kinetic energy than being provided by the coils

Explanations for unexpected deficit:

- **Stored magnetic energy in plasma being removed. Decrease in internal and external inductance (no evidence for this)**
- **Cyclic behavior of MHD instabilities —> convert toroidal flux to poloidal flux**

8

2015-22-02: Investigating Magnetic Flux Pumping in hybrids

Background:

- In the Hybrid Scenario a beneficial tearing mode facilitates the transport of poloidal flux (Flux pumping).
- Physics of this process not well understood

Experimental Goals:

- Use flux consumption deficit to measure flux pumping
- Use ECCD control 3/2 TM amplitude
- RMP to effect ELM amplitude/activity
- Measure flux pumping at two different q_{95}

Intervals in Hybrid Discharges Where the 3/2 Mode is Absent or Suppressed

162873: no 3/2 mode

162893: co-ECCD 3/2 mode suppression

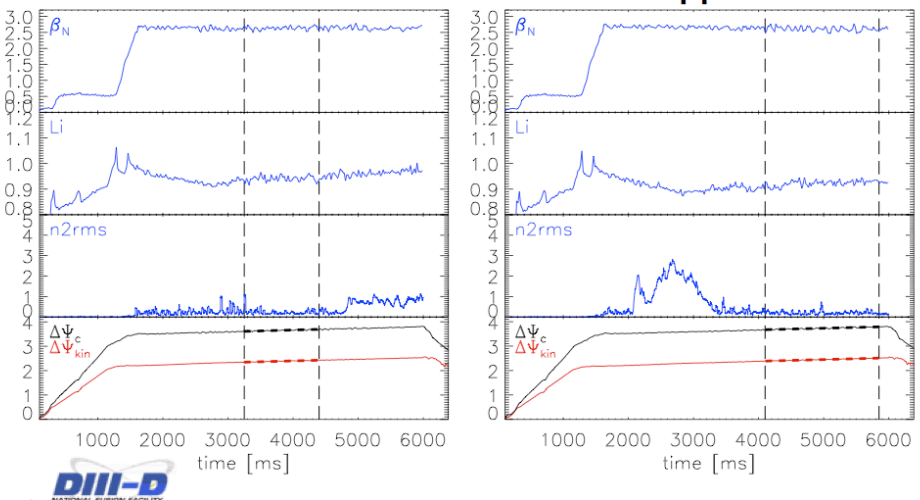

Intervals in Hybrid Discharges Where the 3/2 Mode is Present or Destabilized

162894: counter-ECCD 3/2 mode destabilization

162896: ECH at q = 3/2 surface

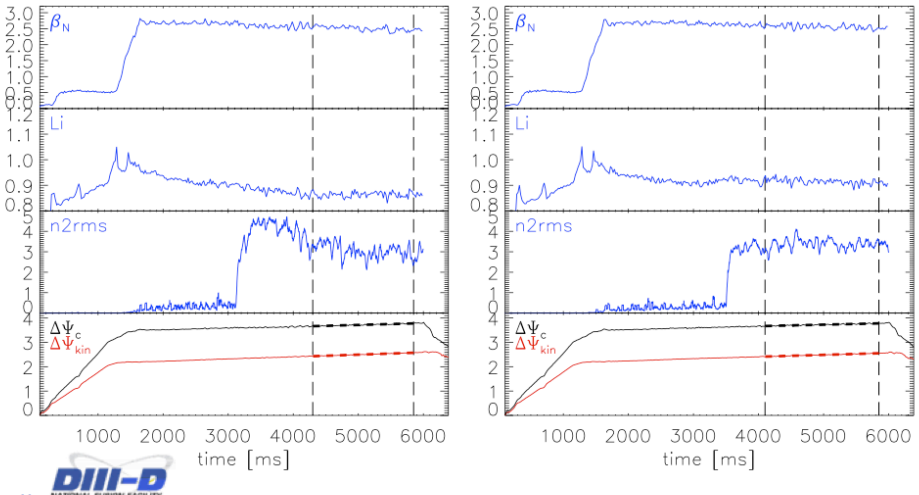

11

Difference in Flux states much Larger in Cases With a 3/2 mode

- **Observed deficit in shots where the 3/2 NTM is present.**
- **Little or no deficit in shots where the mode is suppressed/ absent**

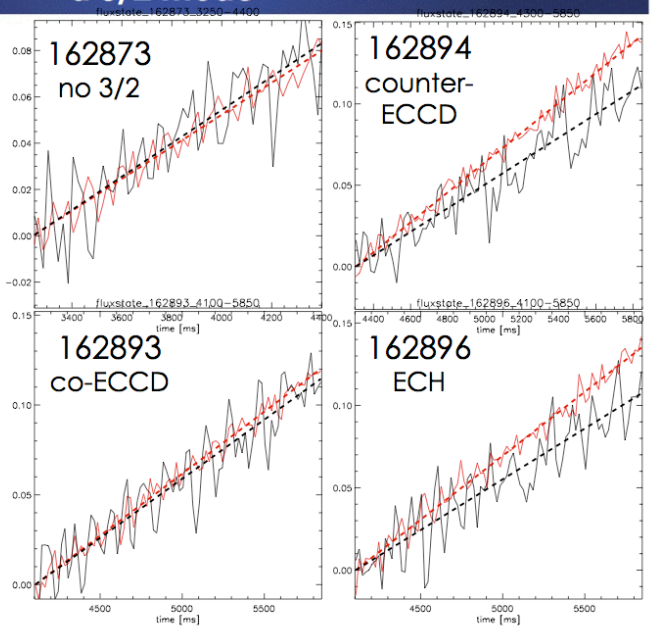

12

Difference in Flux states much Larger in Cases With a 3/2 mode

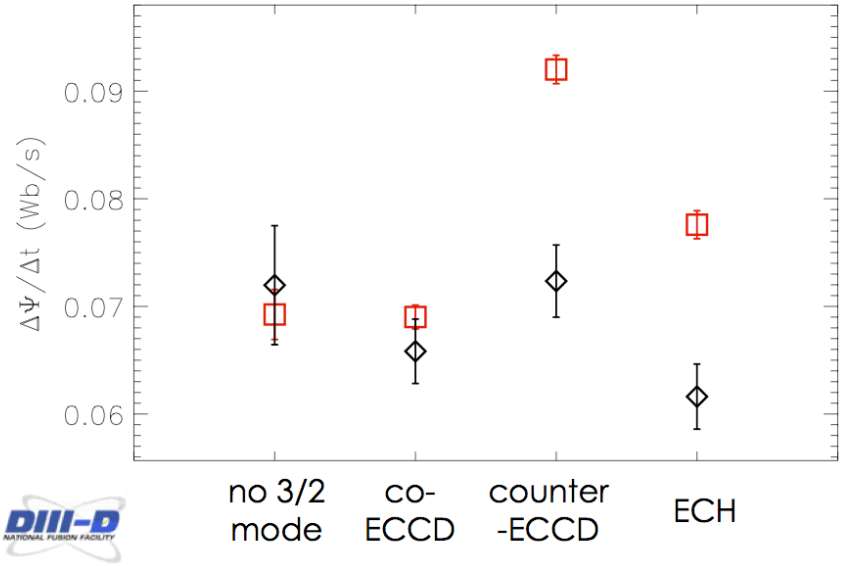

13

Survey of Hybrid Shots from the Experiment Shows the Flux State Deficit Dependent on 3/2 mode

- **A 3/2 Tearing mode is present in all shots with a flux state deficit**
- **Experiment enforces correlation between Flux state deficit and flux pumping.**

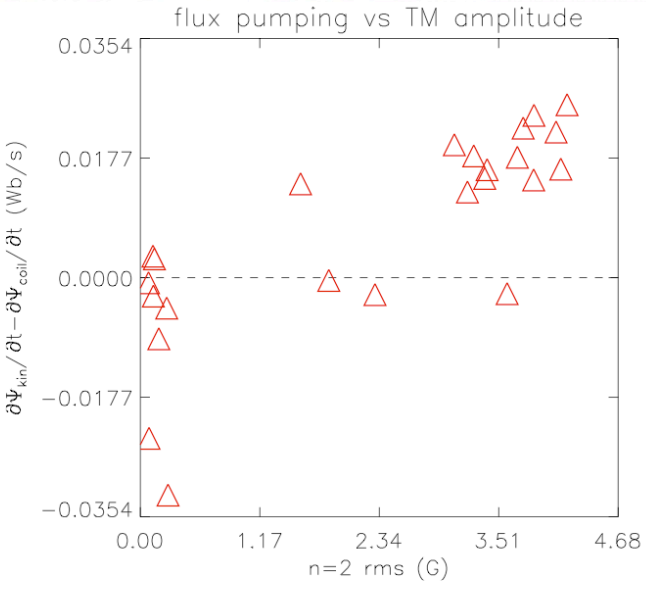

14

n=3 RMP ELM suppression/mitigation not effective

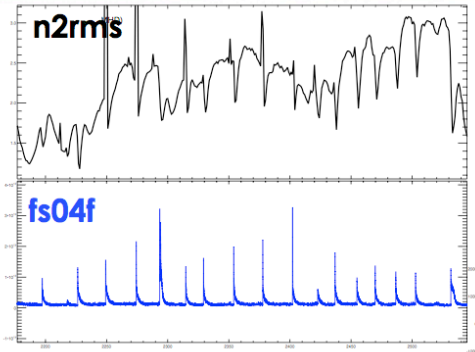

- Modulation of the 3/2 NTM amplitude by ELMs observed.

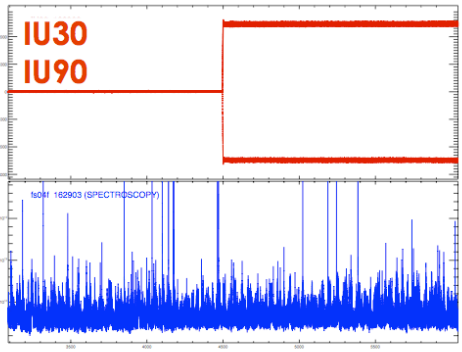

- RMP not effective in changing ELM behavior

15

Flux state deficit disappears when β_N is lowered: 2.8 —> 2.0

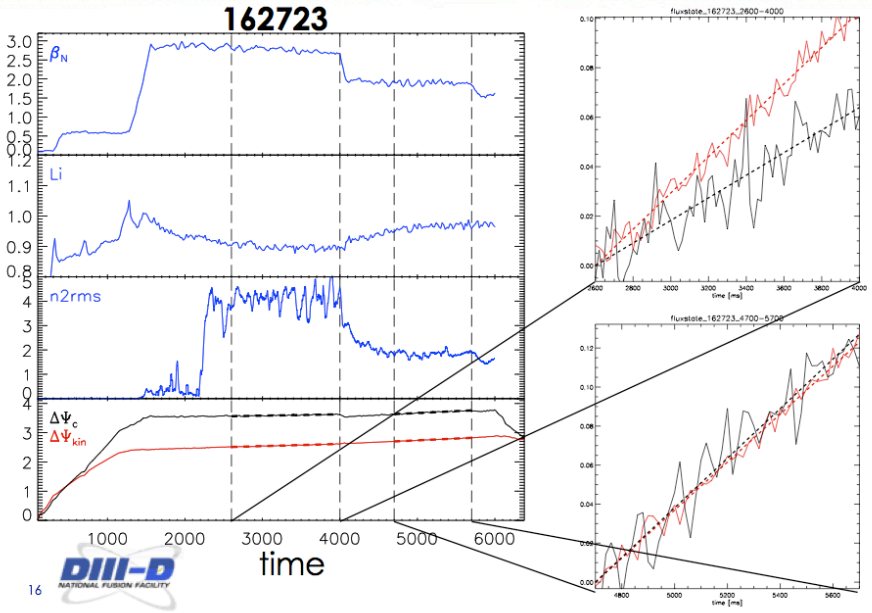

16

Old hybrid q_{95} scan: I_p=1.21, β_N=2.5, B_T = 1.52–>2.13

126182: Bt=2.13

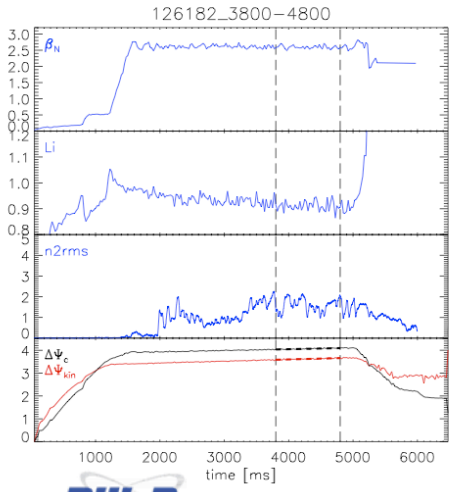

126185: Bt=1.93

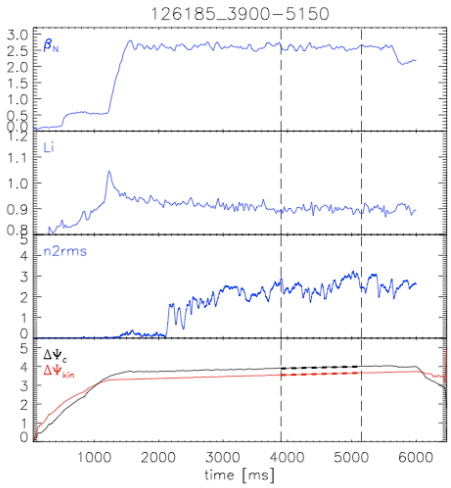

17

Old Hybrid q_{95} scan: I_p=1.21, β_N=2.5, B_T = 1.52–>2.13

126173: Bt=1.78

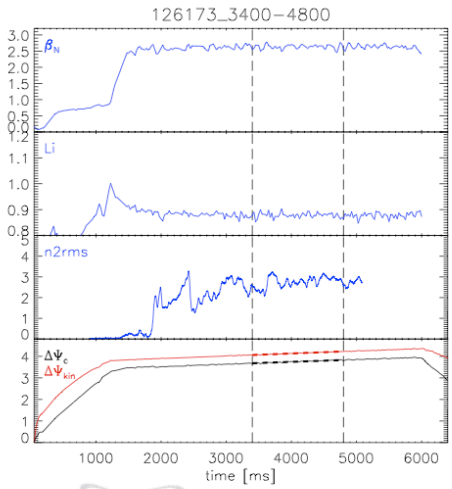

126189: Bt=1.52

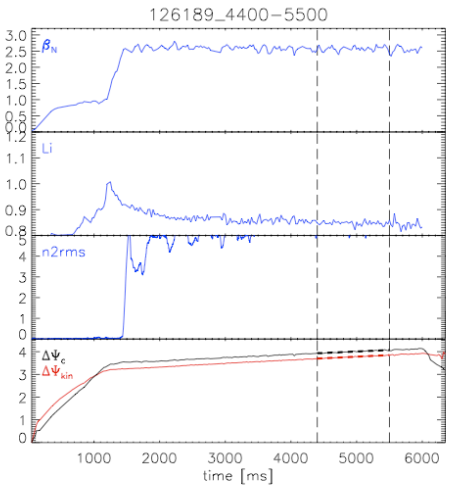

18

Hybrid q_{95} scan: I_p=1.21, β_N=2.5, B_T = 1.52-2.13

- 3/2 mode present in all four shots Observed deficit in all four shots
- Deficit slightly larger in higher q_{95} shots

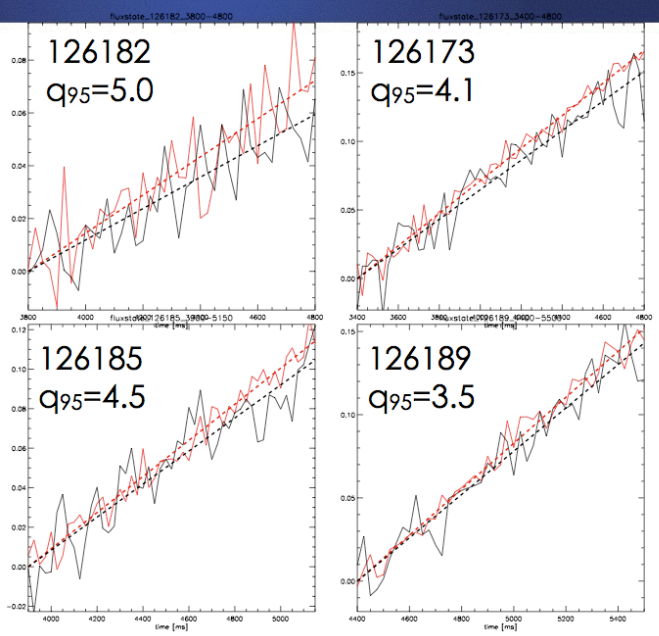

19 DIII-D NATIONAL FUSION FACILITY

Old Hybrid q_{95} scan: I_p=1.21, β_N=2.5, B_T = 1.52-2.13

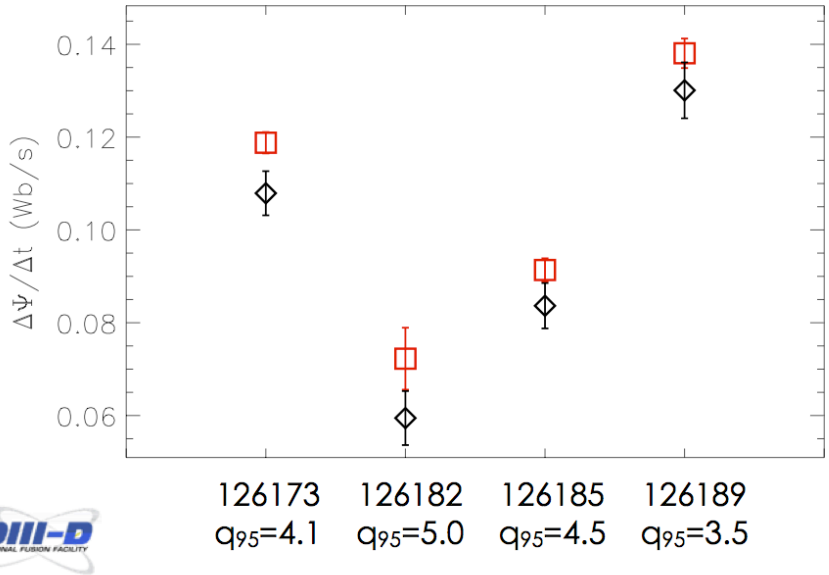

20 DIII-D NATIONAL FUSION FACILITY

Hybrid q_{95} scan: Flux pumping Scales with β_p?

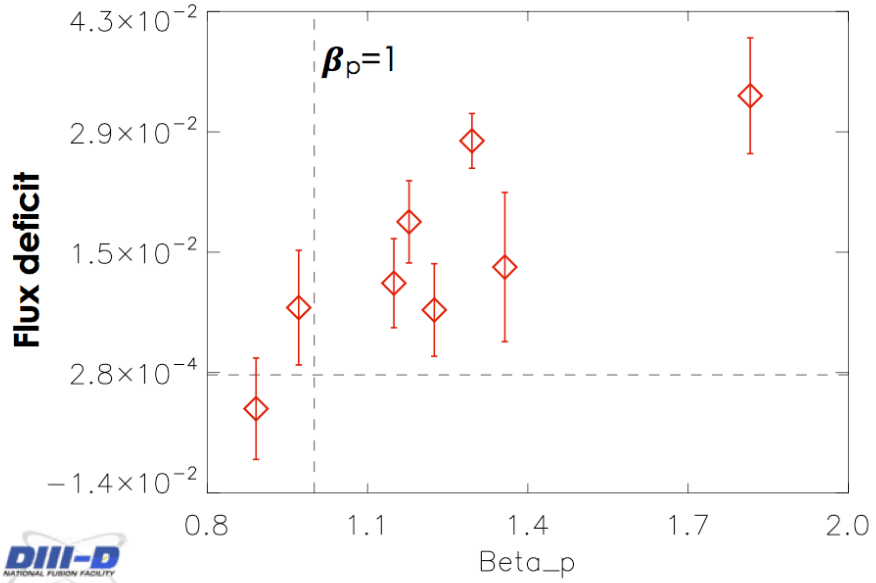

Conclusion

- **ECCD successful in controlling NTM amplitude**
  - mode fully suppressed and enlarged at q_{95}=4.5
  - not fully suppressed at q_{95}=6.5
- **n=3 RMP not successful in effecting ELMs**
  - upper/lower single row
  - even/odd parity
  - Further experiments in LSN?
- **Evaluation of flux states used to track poloidal flux consumption**
  - Flux deficit present in hybrids with a 3/2 mode and high Beta
  - Deficit not present when no 3/2 mode or at lower Beta
  - Deficit indicates that there could be a conversion of toroidal flux to poloidal flux
  - Flux pumping scales with β_p?

2.8: Impact of Central ECCD on Steady-State Hybrid Scenario in DIII-D

The following presentation was made at the DIII-D Friday Science Meeting on May 1, 2015.

Impact of Central ECCD on Steady-State Hybrid Scenario in DIII-D

by
C.C. Petty

In collaboration with
R. Nazikian, M.A. Van Zeeland, D.C. Pace, B.A. Grierson, Xi Chen, E. Kolemen, G.R. McKee, R. Prater and F. Turco

Presented at the
Friday Science Meeting

May 1, 2015

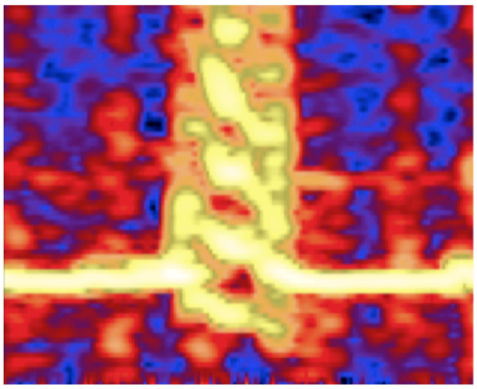

Hybrid With Central ECCD and NBCD Sustains Up to 1.0 MA Fully Non-Inductively With β_N Up to 3.7

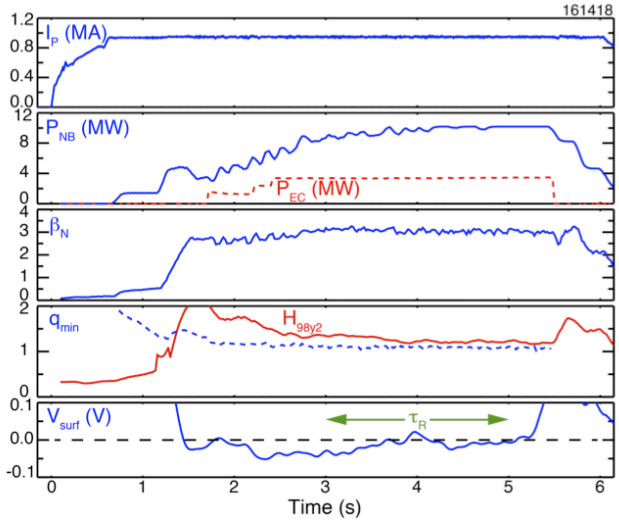

- Promising scenario for steady-state device with Q_{fus}~5
- Compatible with RMP ELM stabilization
- Pulse length limited by NBI duration
- q_{95} = 6
- Reproducible zero loop voltage

I. Current Drive Analysis

EC Heating & Current Drive (3.5 MW) is Crucial to Achieving 100% Non-Inductive Current

- **Central ECH has ~3 times the current drive efficiency of NBI**

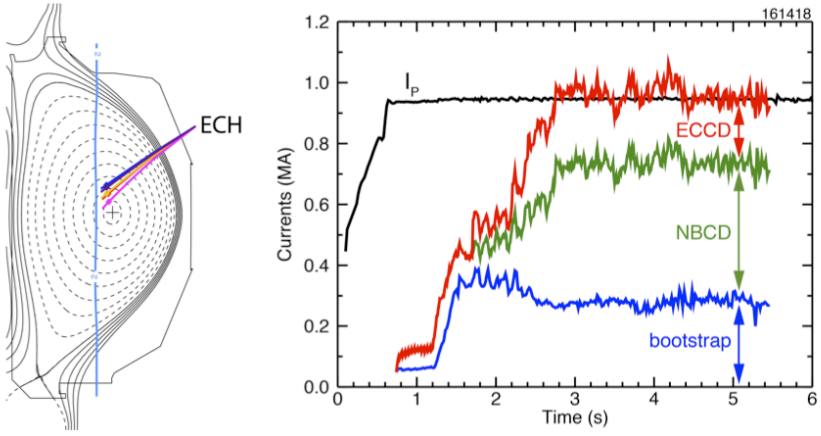

Safety Factor Profile Anomamously Remains >1 in Steady-State Hybrids ➔ Poloidal Flux Pumping

- Adding central ECCD does push safety factor minimum closer to 1
- TRANSP modeling confirms current profile is anomalously broad ➔ q_{min} should drop well below 1

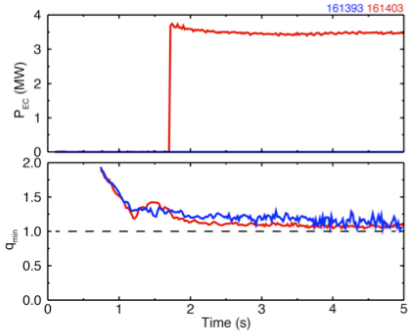

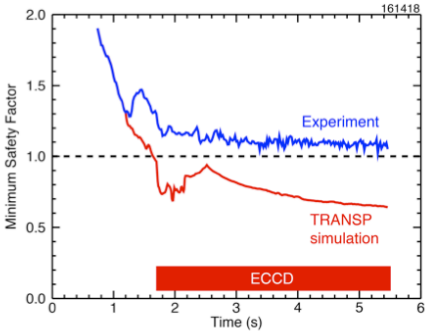

Experimental Non-Inductive Current Fraction Matches TRANSP Modeling

$$I_{NI} = I_P - I_{\text{ohm}}$$

- Ohmic current found from measured loop voltage profile using MSE-constrained EFITs

$$I_{\text{ohm}} = \int \sigma \frac{V_{\text{loop}}}{R_0} \rho d\rho$$

$$V_{\text{loop}} = -2\pi \frac{\partial \psi}{\partial t}$$

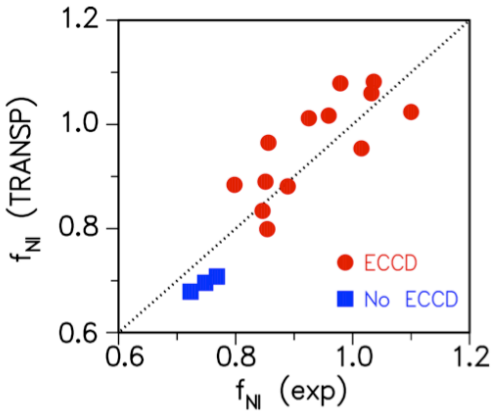

II. Sawtooth Activity

Electron Cyclotron Current Density is Varied to Test Effect on MHD Activity and Safety Factor Profile

- **ECCD power scan at fixed deposition**
- **ECCD deposition scan at fixed power**

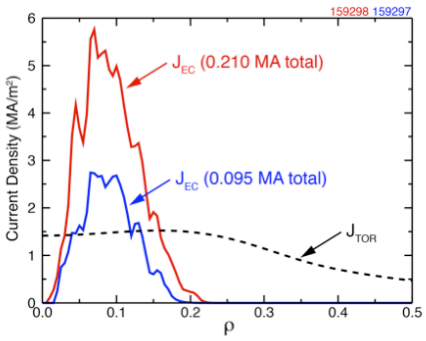

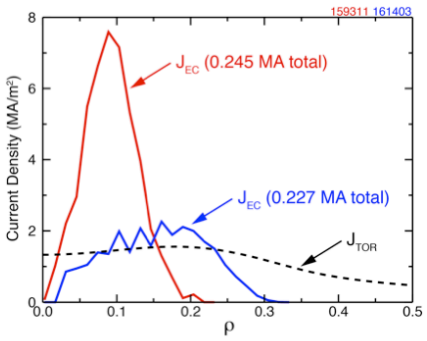

Higher EC Power With Fixed Narrow Profile Gives Significant Increase in Sawtooth Activity

- For P_{EC}=1.5 MW, n=1 mode and sawteeth are extremely weak
- For P_{EC}=3.2 MW, q_{min} is pushed down to 1 and sawteeth are seen

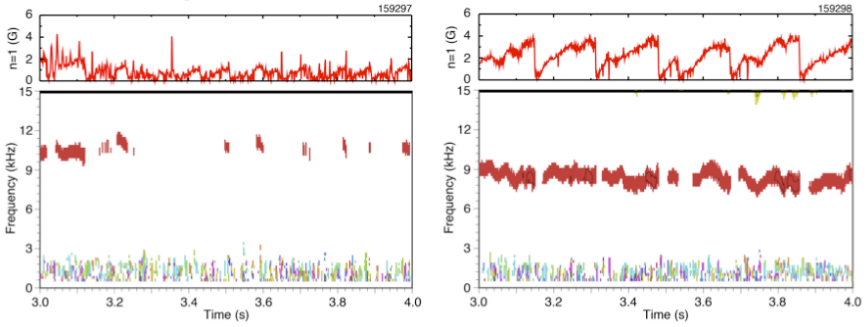

Intense central ECCD "overwhelms" poloidal flux pumping mechanism that keeps q_{min} > 1

Broadening ECCD Profile Can Lessen Sawtooth Activity

- Broadened ECCD profile (P_{EC}=3.5 MW) weakens n=1 mode and essentially eliminates sawteeth
- Narrow ECCD profile (P_{EC}= 3.2 MW) strengthens n=1 mode and generates well-formed sawteeth

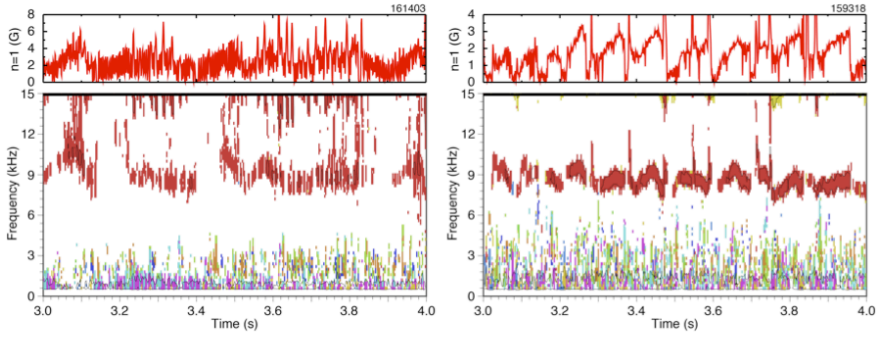

III. AEs and Fast Ion Transport

Plasmas With ECCD Exhibit Much Weaker Core MHD Than Similar Plasmas Without ECCD

- **Cross-amplitude spectrum from CO_2 interferometer**
- **Top plot shows large number of modes (8-10) excited in case without ECCD**
  - Combination of low frequency NTM and (likely) TAE/EAE
- **Bottom plot shows high frequency AEs disappear in case with ECCD**

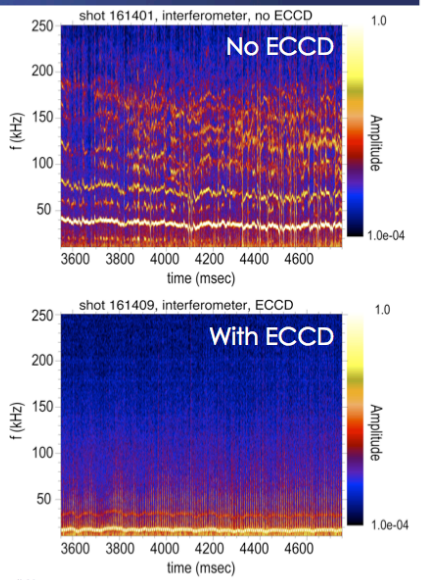

Without ECCD, Large Beam Ion Diffusion is Needed in TRANSP to Match Experimental Neutron Rate

- **Without ECCD**
- **With ECCD**

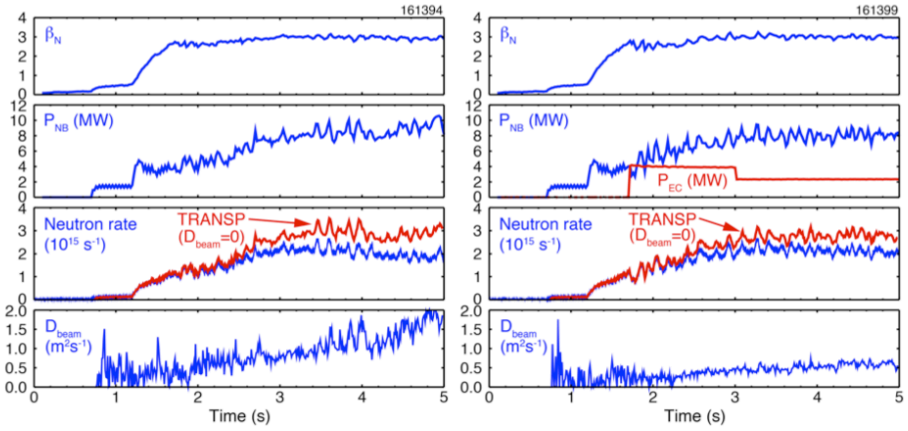

Increasing Beam Ion Diffusion Over Time is Correlated With Higher TAE/EAE Activity

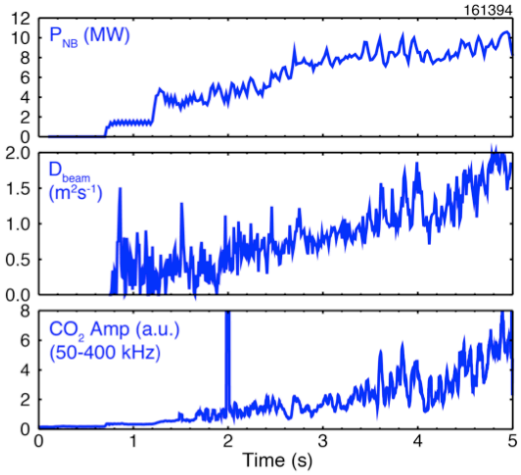

- **CO_2 density fluctuations are integrated above 50 kHz to avoid tearing mode activity**

Deduced Beam Ion Transport From Neutron Rate Increases With Stronger Activity in the TAE/EAE Band

- ECCD seen to be effective at reducing TAE/EAE amplitude
- D_{beam} dependence on AE mode amplitude suggests a critical-gradient-like threshold

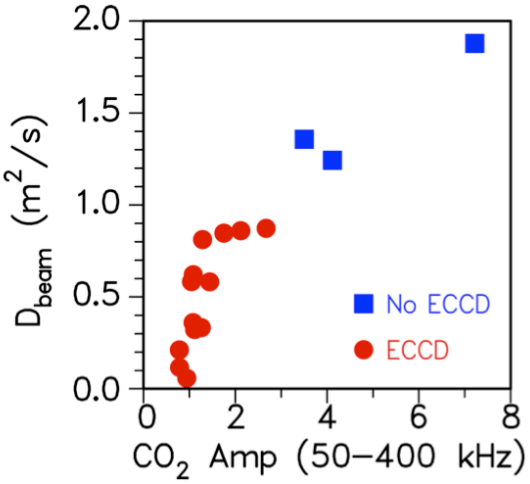

IV. Thermal Transport

Central Electron Heating With ECH Has Significant Effect on All Plasma Profiles

- **ITB seen in NBI-only plasma (especially in T_i and Ω_{tor}) is not present in plasmas with ECH**
- **ECH is effective at bringing T_e and T_i closer together**
  - Above 2 MW of ECH power the changes in the plasma profiles "saturate"

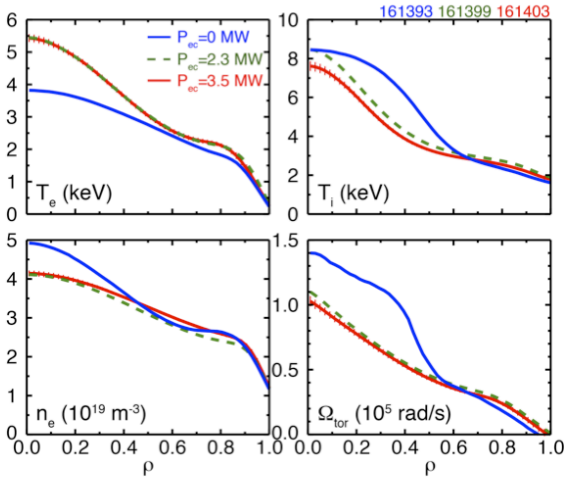

Thermal Diffusivities Increase Systematically With ECH Power, With Ions Having the Largest Increase

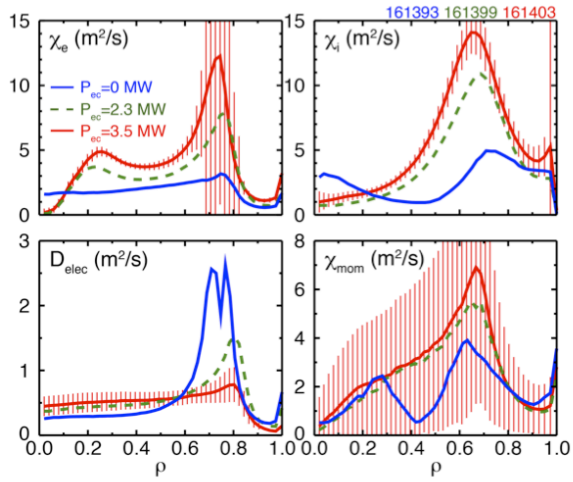

- **Since $\chi_e \approx \chi_i$, using equal amounts of electron and ion heating will naturally give $T_e \approx T_i$**
- **Flattening of D_{elec} profile during ECH causes density profile to broaden**

Central Electron Heating Rapidly Increases Electron and Ion Thermal Diffusivities

- Transport coefficients take into account the time varying beam ion transport
- Diffusivities are nearly constant with time (except when ECH power changes)
- Compared to thermal diffusivities, particle diffusivity has weak dependence on ECH

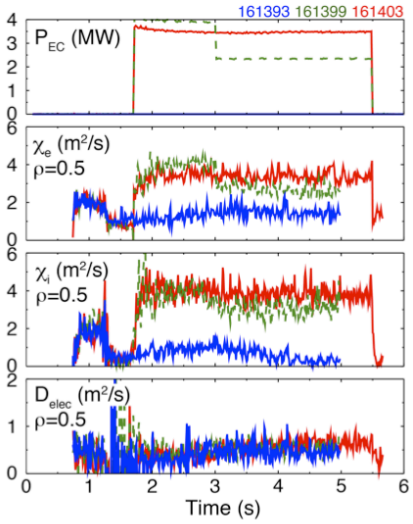

Beam Ion Transport from MHD Activity is Main Reason Why Global Confinement Decreases Over Time

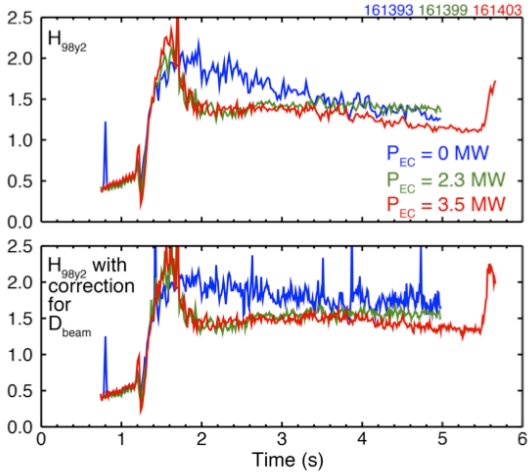

- Beam ion transport lowers H_{98y2} since it reduces NBI heating effectiveness
- After correcting for the increase in fast ion transport, H_{98y2} becomes fairly constant over time
- Higher thermal transport during ECH is mostly offset by improved fast ion transport

Summary

- **Current profile in steady-state hybrids remains anomalously broad with $q_{min} \geq 1$ despite strong central ECCD**
- **High EC current density can "overwhelm" flux pumping mechanism and create sawteeth, but spreading out ECCD deposition lessens or even eliminates sawteeth**
- **During ECCD, TAE/EAE modes are replaced by a more benign 1/1 fishbone-like mode**
  - TRANSP modeling of neutron rate indicates D_{beam} increases with high frequency MHD activity, and may have a critical-gradient-like threshold
- **Electron and ion thermal diffusivities increase rapidly with ECH, but improved fast ion transport mitigates any decrease in H_{98y2}**

3.0 C-Mod Contributions

3.1: Improved numerical tools for LH current drive studies

Sections 3.1.1-3.1.3 are derived from the PhD thesis of Robert T. Mumgaard (copyright MIT 2015). The text and figures are taken verbatim from the thesis sections 7.11 and 8.7-8.8 with changes only to the formatting for the purposes of this report. The thesis was defended in June 2015, with the majority of the analysis for this chapter conducted early in FY2015. Additional detail on these studies can be found by consulting the original thesis, available as PSFC internal report PSFC/RR-15-6.
Section 3.1.4 consists of Syun'ichi Shiraiwa's study of ray tracing with improved SOL profiles, titled "Impact of SOL Plasma Profiles on Lower Hybrid Current Drive: Experimental Evidence, Mitigation and Modeling Approaches". This work was presented in April 2015 at the 21st Topical Conference on Radiofrequency Power in Plasmas in Lake Arrowhead, CA. The work has been submitted to the proceedings of the conference and is available as PSFC internal report PSFC/JA-15-50. The full text of the report is included as section 3.1.4.
Section 4.4 contains additional model validation work on C-Mod LHCD discharges by Francesca Poli of PPPL.

3.1.1 Measurements of LH driven current on Alcator C-Mod

The first systematic measurements of the current profile were performed on Alcator C-Mod using the upgraded MSE system and the HXR camera. This study is the first published study across many different parameter ranges at the field, frequency, and density envisioned for a reactor in a diverted geometry. The measured current profile has the expected time dynamics, settling into an equilibrium within 0.3 seconds while the HXR profile is prompt and self-similar.
Database studies indicated parameter ranges of interest for detailed studies in parameter scans. The strongest dependence identified was due to plasma current with broader LHCD-driven current and HXR profiles and more efficient current drive occurring at higher plasma current in a manner also observed on other tokamaks at lower density and field. There is current drive across the entire plasma minor-radius at all plasma currents including near the edge of the plasma. The current drive in the outer r/a ~ 0.3 increases at increased plasma current and is apparent even at modest (< 500kW) LHCD power. However, at nominal low current operating conditions (< 900kA) the LHCD-driven current remains centrally peaked. The current profile broadens from that observed during

Ohmic drive but does not typically create an off-axis peak (except in plasmas with an internal transport barrier, not discussed here). q_0 is raised in these plasmas but does not typically reach values as high as 2. These results are consistent with temperature profiles remaining peaked on-axis, MHD observations, and the appearance and cessation of sawteeth. Additional comparisons to the polarimetry system installed on C-Mod using a MK-EFIT-driven synthetic diagnostic show consistent results in all three chords [CMOD-1], adding confidence that the current profile is correctly represented by the reconstructions.

The driven current profile and HXR profiles are self-similar across large ranges of LHCD power with a linear dependence of HXR emission on power. The LHCD current profiles and current drive efficiency are independent of the residual parallel electric field, consistent with previous results on C-Mod and results on other tokamaks operating at high density.

Database studies were conducted on global indicators of current drive efficiency as a function of the launched $n_{||}$. It was found that the current drive efficiency is generally a weak function of this parameter in the last several campaigns. A very well controlled dedicated experiment was conducted which indicated that the current drive efficiency was independent of launched $n_{||}$ as were the current and HXR profiles. Other experimental scans confirm this in the operating range of interest on C-Mod. However, a previous experiment conducted seven years ago with a previous lower hybrid launcher in a similar regime on C-Mod showed a strong dependence that could not be reproduced. Resolving this apparent contradiction may provide insight into some aspects of LHCD that could be important for future experiments.

Experiments were conducted to determine the dependence of the current drive profiles on plasma density in the regime where the current drive efficiency rapidly degrades with increasing density. The driven current profile may become slightly broader as the density is raised but generally does not show significant dependence on the plasma density—there is no major shift in any of the profiles, the current drive just goes away. When the plasma becomes inner wall limited the current drive is recovered, consistent with previous observations, and the current profile is indeed significantly modified.

Generally it is observed that the LHCD acts mostly to replace the Ohmic driven current with a similar current profile. The large changes in MSE pitch angle and current profile with the accompanying MHD activity seen in other tokamaks with current profiles peaked off-axis are not typically observed on C-Mod. The central electron temperature also typically peaks or stays the same in these discharges despite replacing the Ohmic heating with LHCD heating. The shape of the LHCD current profile is also robust, always producing self-similar HXR and LHCD contributions to the current profile—except as a function of plasma current.

It is as if the lower hybrid waves simply find the hottest part of the plasma—the core in these plasmas—and mostly damp there. At higher current this hotter part of the plasma is broader, possibly explaining differences as a function of current. The upgraded multispectral MSE system will enable profile measurements in plasmas with extensive ICRF heating, a regime where the MSE diagnostic was blinded by background light and the HXR diagnostic has contamination from fusion neutrons. Previous experiments have indicated that increasing the temperature may increase the current drive efficiency and these will be revisited with this enhanced measurement capability to determine profiles. It may be interesting to determine if the LHCD driven current profile can be broadened in low current discharges using auxiliary heating or if the current profile can be made off axis using off-axis heating.

Previous work has highlighted the role of the sol and edge parameters on the lower hybrid current drive at high densities when the device operates in the multi-pass regime. However, the work reported here was conducted at lower densities where good current drive efficiencies, in agreement with theory, are typically achieved. However, these discharges are still in the multi-pass regime. The lack of a LHCD current profile and HXR profile dependence on parameters such as launched $n_{||}$ and density, which are important in the wave propagation and damping, could hint that something besides traditional lower hybrid wave physics is influencing the current drive even at these low densities similar to what has been studied at higher densities. Thus selected scans will be compared to simulation in the next chapter. One could speculate that the role of the sol and reflections is important even in this density regime. Perhaps the edge modifies the wave power or $n_{||}$ prior to absorption or the wave makes many passes, filing the tokamak until it damps in the hottest region, leading to peaked profiles and the lack of any strong dependency besides the current dependence—an important parameter for the sol profiles. Future experiments such as $n_{||}$ scans into limited discharges (where the sol profiles are significantly different than diverted discharges) would be illuminating, particularly if dependencies could be observed that are not observed in limited discharges.

3.1.2 Summary of comparison between modeling and experiment

The experimental and simulation observations are summarized in Table 3.1. Overall the experimental results are very robust and insensitive to the details of the experimental setup. The fast electrons appear to be on-axis leading to bell-shaped HXR profiles and central current drive. The only significant profile shape change is due to changes in total plasma current.

The GENRAY/CQL3D simulated current and HXR profiles show considerable variability in their fine structure (e.g., the radial location and magnitude of off-axis current spikes) even when input profiles are changed only modestly, but always drive

most of the current far off-axis leading to flat-top HXR profiles. This general behavior is observed in other ray-tracing Fokker-Planck codes applied to C-Mod data and is apparent in previous simulations by other code users [CMOD-2]. The observed lack of dependency on launched $n_{\|}$ is reproduced by the simulations as are the shifts at higher plasma current. Changes in density cause large shape changes. The total current is generally well predicted except at high loop voltage and high LHCD power, where slide-aways are present in the simulation leading to an overprediction.

3.1.3 Discussion and implications

The simulation/experiment comparison described in this work raises important questions about the validity of using GENRAY/CQL3D (and likely other similar codes) for C-Mod tokamak plasmas even in conditions where efficient current drive is observed. While the simulation predicts reasonable total currents and HXR count rates, it fails to correctly predict any of the important details of the LHCD profiles. The simulation is much more sensitive to perturbations than the experiment and misses important 0-D trends in parameters. Something important appears to be missing.
At a high level, these results suggest a robust physics mechanism that leads to damping of the waves in the center of the plasma is required to explain the simulation results. It appears that this mechanism must lead to upshifts in $n_{\|}$~3−4 to damp waves at the 2−3 keV core plasma. This is often referred to as the spectral gap problem [CMOD-3]. This upshift must occur without concomitant large losses in power.

Table 3.1: Summary of the comparison between measurements and GENRAY/CQL3D.

Character	Experimental observation	GENRAY/CQL3D simulation result
0D current	NA	Usually predicted within 30 percent except in cases with a large synergy term (high power, high loop voltage, low density)
LHCD current profile shape	Broadened from Ohmic but always peaked on-axis.	Large spike at $0.4 < r/a < 0.8$, rarely significant LHCD current on-axis.
HXR profile shape	Always bell-shaped, rarely flat-top and never with significant "ears" (except the active divertor emission). Self-similar at all points in the discharge.	Usually has "ears", rarely peaked on axis.
Sensitivity on n_e and T_e profiles	Both current density and HXR profiles are very reproducible, robust, and stationary.	Both profiles are sensitive to small changes in the inputs, particularly in density profile shape and magnitude. Spikes in current profile move around $\Delta r/a \sim 0.1$ and HXR ears appear and disappear. Less dependence on temperature profile. 0D current prediction sensitive at ±20 percent level.
LHCD power dependence	Small changes in current profile—decreasing central current density by 30 percent between fully-inductive and non-inductive. HXR profile shape very self-similar and count rate linear in power.	Current profile shifts from on-axis peak to far off-axis peak with 80 percent changes in on-axis current density. HXR profile shifts from centrally peaked to having ears. 0D current sometimes under predicted as fully non-inductive current drive is approached.
Launched $n_{//}$ dependence	Very little $n_{//}$ dependence in the current drive, current profile, HXR profile shape, or HXR count rates.	Some dependence in LHCD current location, significant variability in the HXR profile shape and count rates. Total current prediction independent of $n_{//}$ but is too high with a large synergy component.
Ip dependence	Current profile and HXR profile broadens with increasing current. Current drive efficiency increases at higher current.	Spike in off-axis current moves outward and HXR profile broadens at higher current. Total count rate not well ordered. Total current prediction too high with a large synergy term at high current and high power. Current drive efficiency (due to LHCD acting alone) is fairly constant.
Density dependence	Smoothly decreasing LHCD profiles as density is increased. Self-similar HXR profiles at all densities (perhaps slightly broader at higher densities), rapidly decreasing current drive efficiency and HXR count rates at increased density.	Profile details very sensitive to details in density, shifting spike location and changing profile shapes with little correlation. Significant shape changes in HXR profiles and over prediction of count rates at highest density. Total current drive prediction fairly accurate across density range.

The upshift must occur but not be so large as to damp the waves in the colder regions as indicated by the large spike in the edge observed in the GENRAY/CQL3D simulations. Potential mechanisms that could generate a sufficient $n_{||}$ upshift without unacceptable power loss, and other mechanisms that might reconcile the simulations to the experimental measurements are discussed in the speculative sections below.

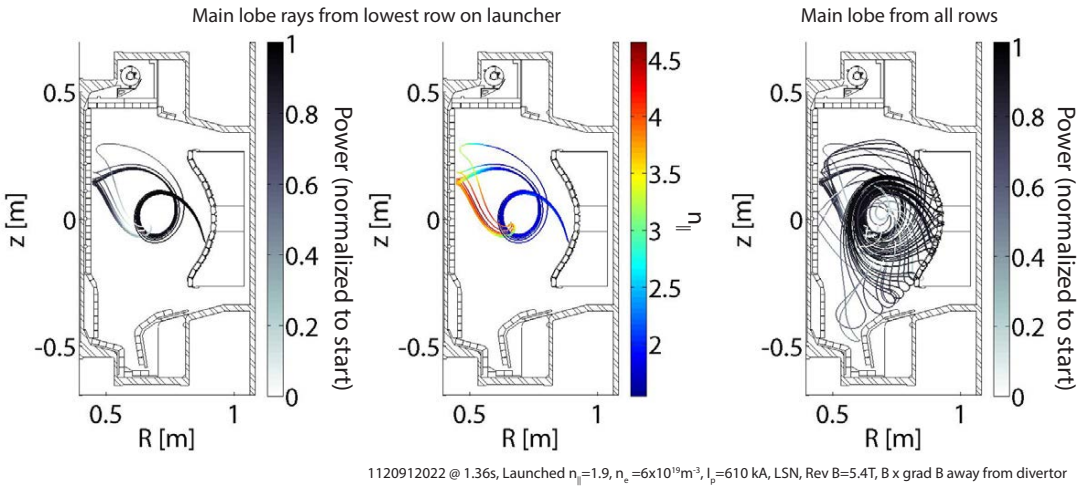

Fig. 3.1: The trajectory of a bundle of rays traversing the plasma prior to damping indicating the normalized power left in the ray (left). The $n_{||}$ of these rays (center). All the main $n_{||}$-lobe rays from the launcher making many bounces (right). This is from a discharge analyzed as part of the $n_{||}$ scan.

Unlike much of the previous LHCD work on C-Mod, this work was conducted in the low-density regime where the current drive efficiency is high and the plasma responds well to current drive. Unlike what occurs at higher density, the simulated rays make just a few bounces in the plasma prior to damping, but still traverse the central part of the plasma. An example of the ray-trajectories is shown in Figure 3.1. The left figure shows the power in a single main $n_{||}$-lobe ray from the lowest launcher row as it propagates into and out of the plasma, making a reflection on the inner wall prior to damping at mid-radius. The $n_{||}$ upshift in this bundle of rays occurs near the reflection on the inner wall (center). All of the main-lobe rays make similar bounces around the boundary of the tokamak prior to damping (right).

Since the change of trajectory of the rays results in the upshift which leads to damping, the model is sensitive to the details of the ray trajectories, likely creating the sensitivity to the details of the density and density profile (and to an extent the launched $n_{||}$) as this affects the trajectories and where the rays eventually bounce. Reference [CMOD-4] Figure 5-26 shows that at these low densities (5×10^{19} m^{-3}), the rays only make a few bounces prior to damping. Cutting the ray off after 1 reflection significantly changes the HXR production from the fully damped case (2 orders of magnitude) whereas cutting the ray off after 2 reflections only degrades the HXR production by a small amount (this work was done with a separatrix that is perfectly reflecting). These low density plasmas have little collisional absorption (< 100kW) predicted by the simulations.

Radial diffusion was invoked to try to smooth the profiles. However, this also leads to significant fast-electron loss from the plasma, lowering the predicted total current. Thus

different levels of fast-electron diffusion would be required in different plasma conditions to match the total current. Diffusion also has a difficult time creating centrally peaked profiles from a source of fast electrons off-axis. Inward advection would help this. Small levels of inward advection 0.05 m/s was also used in the simulation to reconcile the profile discrepancies and was found to not significantly change the profiles. Previous experiments bounded the advection in C-Mod to < |0.5|m/s [CMOD-5].

Full-wave codes have been developed to explore the multi-pass regime where diffraction and interference of the LHCD wave could potentially be important. A full-wave code named LHEAF was used previously to simulate C-Mod plasmas including a low-density plasma similar to that studied in this work. The results can be found in [CMOD-6] with the relevant portions shown in Figure 129.

The simulated current profile remains peaked very far off-axis in this simulation which is at 800kA with $V_{loop} = 0.2$ V[1]. The HXR profiles show the same ears as the GENRAY/CQL3D simulations and only under significant fast electron diffusion (~ 5× that observed in experiments) does the HXR profile begin to match that observed in the experiment. This result hints that the full-wave approach is not significantly different from GENRAY/CQL3D in this low-density few-pass regime.

An alternate hypothesis is that the launched wave is affected due to interactions immediately in the front of the launcher. This could spread the launched $n_{||}$, allowing the spectral gap to be bridged on the first pass into the plasma. This conjecture was explored computationally by the group from CEA [CMOD-7]. In addition to launching a main $n_{||}$ lobe, many lower-power lobes were launched at higher $n_{||}$. These lobes contained approximately half the power and are conjectured to arise from an as-yet unobserved edge fluctuation. The initial results of this model are promising as the the simulations better matched the measured HXR profiles on tore supra during LHCD, and the sensitivity of the ray-tracing models to input profiles was significantly decreased.

GENRAY/CQL3D was adapted to explore the effects from wave scattering from density fluctuations in the edge of the plasma on Alcator C-Mod in the density range of $6 \times 10^{19} m^{-3}$ [CMOD-8]. The results showed that scattering alters the deposited LHCD power with the power deposition profile still being strongly peaked off-axis at r/a~0.4 − 0.7 (implying it also did not change the current profile). However, the results did show a broader peak with scattering than the case with no scattering.

[1] The experiment had a $V_{loop} = 0.4$V and no MSE making quantitative comparison between experiment and simulation difficult for this result.

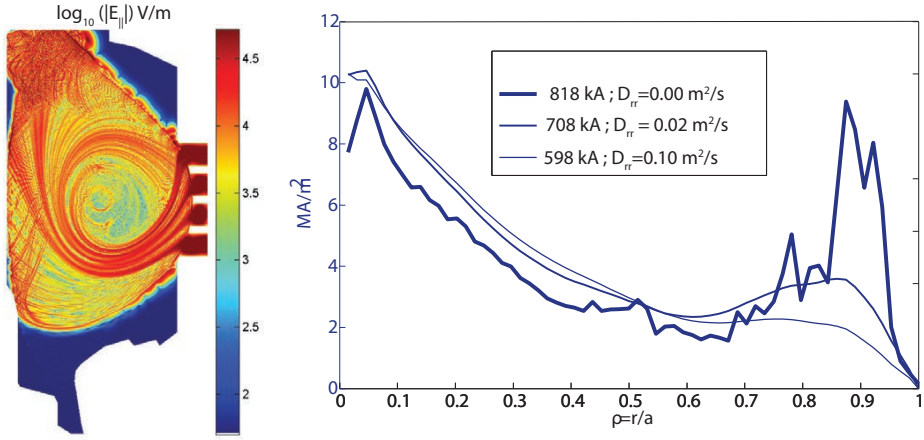

Fig 7-5 in Meneghini thesis

Fig 7-6 in Meneghini thesis

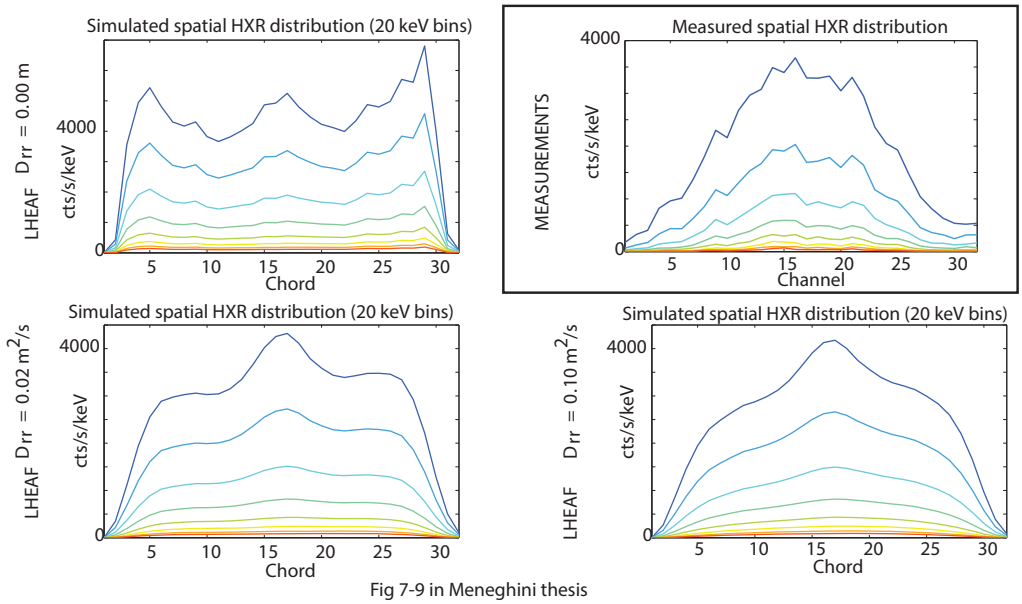

Fig 7-9 in Meneghini thesis

1080429007 @ 0.84s, n_e=7x10^{19}m^{-3} P_{LH}=560kW, P_{SOL}=6kW, $n_{||}$=1.9, Z_{eff}=2.0, V_{loop} (sim) = 0.2V, V_{loop} (exp) = 0.4V, I_p= 800kA

Fig. 3.2: Full-wave simulations of a plasma similar to that used in this study. The wave fields and current profile are shown along with the HXR profile under various assumptions of fast-electron diffusion. Adapted from [CMOD6].

3.1.4 Impact of SOL Plasma Profiles on Lower Hybrid Current Drive: Experimental Evidence, Mitigation, and Modeling Approaches

The following is the full text of PSFC internal report PSFC/JA-15-50. This paper has been submitted for publication in the *Proceedings of the 21st Topical Conference on RF Power in Plasmas*. References are listed at the end of this section.

Impact of SOL Plasma Profiles on Lower Hybrid Current Drive: Experimental Evidence, Mitigation and Modeling Approaches

S. Shiraiwa[a], S. G. Baek[a], I. Faust[a], G. Wallace[a], P. Bonoli[a], O. Meneghini[a1], R. Mumgaard[a], R. Parker[a], S. Scott[b], R. W. Harvey[c], B. J. Ding[d], M. H. Li[d], S. Y. Lin[d], and C. Yang[d]

[a]Plasma Science Fusion Center, MIT, MA 02139, USA
[b]Princeton Plasma Physics Laboratory, Princeton, NJ 08543, USA
[c]CompX, Del Mar, CA 92014, USA
[d]Institute of Plasma Physics, Chinese Academy of Sciences, China

Abstract. Recent progress in understanding and mitigating parasitic wave absorption in edge plasmas is presented. Experimental observations collected on Alcator C-Mod suggest multiple physics mechanisms are involved in such losses. Localized measurement of parametric decay instabilities (PDIs) has been performed using RF Langmuir probes. The divertor heat flux due to LH and ionization power loss have been evaluated quantitatively. We observe that the LHCD efficiency can be recovered when the SOL density profile is controlled by operating the tokamak at high current. The experimental progresses motivated a re-examination of the LHCD simulation model based on the ray-tracing/Fokker-Planck code (GENRAY/CQL3D). The effect of introducing a relatively small wave number broadening in the launched power spectrum and using 2D SOL density and temperature profiles was investigated. Comparison with C-Mod experiment indicates that the new model can explain the experimental trend over a wider density range including the density regime where disagreement was seen previously, suggesting that including realistic SOL geometry is a key to improve the simulation accuracy.

Keyword: LHCD, SOL, ray-tracing
PACS: 52.35.Hr

INTRODUCTION

Understanding and mitigating parasitic wave absorption in edge plasmas has been a major issue of lower hybrid current drive (LHCD) research. A loss of current drive has been observed in tokamak since 1980's, and is termed as "critical density" or "(lower hybrid) density limit"[1]. Various physics processes have been considered theoretically to explain such a loss. In particular, the wave energy loss due to transferring injected RF power to high parallel wave number ($n_{//}$) daughter waves by parametric decay instabilities (PDIs) has been examined in great detail [2]. The work was followed by the experimental observation showing such a process indeed occurs in plasma when the density approaches the critical density [3]. However, despite dedicated experimental and theoretical efforts in past decades, the root cause of the loss has not yet been identified nor has the method to mitigate the loss been established.

[1] Present address: General Atomics, San Diego, CA 92186, USA

This long-standing issue gained more attention recently following experiments on Alcator C-Mod [4], which reported that current drive degradation was worse in diverted configurations. The C-Mod experiment suggests that better understanding this loss mechanism is needed to predict the LHCD performance on a reactor. Experimentally, the loss of current drive is observed most clearly in a rapid decrease of non-thermal hard X-ray emission as the density is increased. Since the standard LHCD modeling based on the ray-tracing/FokkerPlanck code was found to overpredict the current drive, we sought for physics processes to add in order to reproduce this experimental trend [4, 5]. We first extended the computational domain to include the SOL plasma. Since the SOL plasma tends to be more collisional compared to the core, this can effectively reduce the RF power absorbed by electron Landau damping. Later we used the LHEAF full wave code [6]. The full wave code can predict wave number spectrum spreading in plasma more accurately, which tends to be broader than what is predicted with WKB approximation [7]. This may increase the power absorbed in colder region, and thereby reduces the overall current drive efficiency. Interestingly, however, although adding the SOL model and using the full wave code improve the agreement with the experimental observations, the predictions nonetheless deviate from the experimental trend at a high density $n_e > 1x10^{20}m^{-3}$ [8], where n_e is the line averaged density.

Our recent experimental efforts to understand the loss of current drive efficiency at high density focused on 1) measuring where and how the wave propagates in plasma and if the wave propagation changes when density becomes high; and 2) establishing a method to improve the LHCD performance at the high density. The new experiments provided guidance on how to improve the LHCD numerical model. Section 2 of this paper describes recent experimental results obtained on Alcator C-Mod. Section 3 will describe our approach to improve the LHCD modeling. Section 4 compares the new model with experiment, followed by a discussion and a summary.

EXPERIMENTAL PROGRESSES TO IMPROVE LHCD AT HIGH DENSITY

To determine where the LH waves propagate, we measured LH wave frequency spectrum using several electrostatic RF probes positioned at various locations around the tokamak plasma. Two key questions to address are: 1) how much of the LH power propagates to the high field side (HFS) at high density; and 2) if the wave frequency spectrum change when loss of current drive occurs. The first question is important because the present day LH experiments are performed in a weak single pass absorption regime, by contrast in a reactor, the LH wave is expected to be absorbed strongly during the first pass. So, although a loss of current drive is observed universally today, it may not occur on a reactor unless the loss is caused by a phenomena

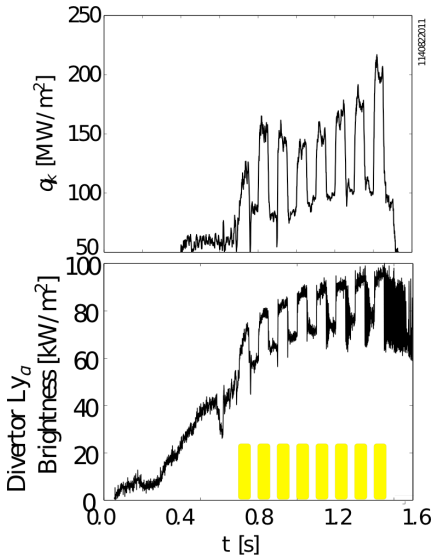

FIGURE 1. Modulation of parallel heat flux measured on a divertor tile (top) and Lyman-α emission from active X-point (bottom). LH power modulation is indicated by the yellow boxes.

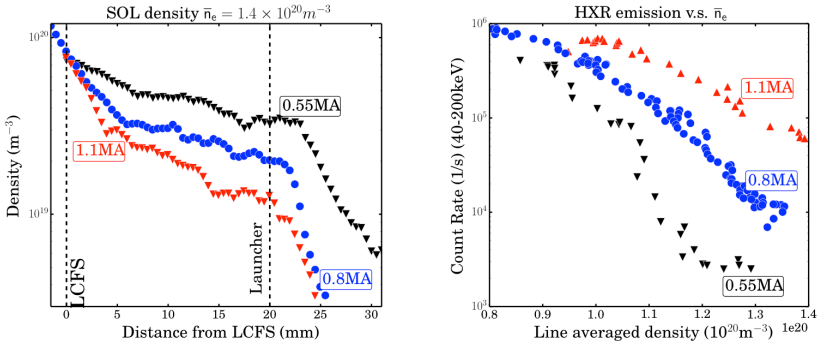

FIGURE 2. SOL density profiles (left) and total HXR emission for I_p = 0.55, 0.8 and 1.1MA. SOL profiles are measured by a scanning probe, when the line averaged density (n_e) is $1.4x10^{20}m^{-3}$ [14]

occurring immediately in front of the launcher. The LH power measurement at the HFS of tokamak may indicate if something peculiar occurs during the first pass. The change of the LH wave frequency spectrum indicates an excitation of non-linear wave-wave interaction, which may explain why the deviation of the numerical prediction from the experimental trend occurs beyond a certain density threshold.

Results of the RF probe experiments are shown in several publications [9-11]. In short, we indeed observe that the wave power reaches the HFS when density is low, but gradually decreases when the density exceeds approximately $1x10^{20}m^{-3}$, i.e. the same density at which the reduction of HXR emission occurs. Spontaneous excitation of various PDIs is observed, including a unique PDI locally excited and strongly absorbed at HFS of torus, when density exceeds around $1x10^{20}m^{-3}$. However, the PDI excitation has a unique magnetic field configuration dependence that is not observed on the HXR emission. In addition, while the HFS ion-cyclotron PDI tends to be observed locally on the HFS, the low field side (LFS) one tends to be observed more uniformly. Excitation of an ion-sound PDI did not always correlate well with changing the magnetic configuration from limited to diverted.

Customary indications of LH fast electron generation including HXR emission and non-thermal ECE are lost at high density. Therefore, we looked at prompt change of heat flux to divertor tiles measured by fast surface thermo-couples and Lyman-α emission profile during modulated LHCD [12] as shown in FIGURE 1. We found that a significant fraction of power is deposited near the last closed flux surface at high density. Moreover, the loss is not toroidally localized and the lost fraction appears to increase as the density increases. These results may provide a hint about the nature of physical mechanisms that might be included in the simulation model to improve fidelity to the experimental measurements.

Developing a technique to mitigate the loss of current drive is equally important. Previously, we reported that the LHCD performance recovered by using a limited magnetic configuration in Ref. [13]. An alternate approach to recover the current drive in a diverted configuration was discovered last year when we measured the dependency of CD efficiency in a wide range of plasma current [14]. FIGURE 2 compares the SOL density profile and the density dependence of HXR emission at three different plasma currents. The SOL density profiles are measured near the midplane LFS, when the line averaged density is $1.4x10^{20}m^{-3}$, showing that

the scale length becomes shorter at high current, while the HXR emission becomes an order of magnitude stronger.

LHCD NUMERICAL MODEL IMPROVEMENTS

A major issue in modeling is to understand and reduce the discrepancy between the experiment and our simulation models above $n_e \sim 1.0\text{x}10^{20}\text{m}^{-3}$. Another issue is to improve the accuracy of P_{LH} and J_{LH} profile prediction when the power absorption is weak. We investigated the effectiveness of various physics model modifications in our simulation. Here, we report the effect of spreading initial LH launcher spectrum and the impact of including more realistic SOL density and temperature profiles.

Modification of launched LH wave spectrum could happen even in a reactor where the LHCD single pass absorption is strong. Therefore, it is interesting to see if such a modification could improve the simulations universally. We evaluated the effect of spectrum spreading originally using EAST experiment (FIGURE 3), finding that a relocation of 10% of total LH power to modestly high $N_{\|}$ (~2.7) reproduce best the experimental HXR emission profile shape. We applied the spectrum spreading on one C-Mod simulation too. In this case, we found that even smaller spectrum spreading, only 4% of LH power, is sufficient to change a hollow power deposition profile into a centrally peaked profile.

The effect of modifying launched LH wave spectrum in LHCD numerical models has already been studied previously by several authors. In Ref 15, parametric decay instabilities in JET effectively shifted the injected LH power toward higher $N_{\|}$, resulting in better agreement with experimental measurement. Interestingly, however, the fraction of power we found necessary to relocate toward high $N_{\|}$ is much smaller than what was found in previous studies. For example, the same author relocated 50 % of injected LH power in high $N_{\|}$ components in Ref 16. In the last RF conference, J. Decker studied spectrum spreading on Tore Supra and concluded that shifting approximately the half of the injected power yield a robust agreement with experiment [17]. The reason why we need significantly smaller fractions is not known yet. It could be caused by subtle differences in the implementation of ray-tracing/Fokker-Planck model, and we are working closely with the Tore Supra group to resolve this issue.

The correlation between observed change of SOL plasma profiles and the concomitant improvement in current drive motivated us to include more realistic SOL plasma profiles in the numerical model. Previously when we extended the computation domain of GENRAY [18] to include SOL plasmas [4], the SOL plasma density and temperature profiles were assumed to be an

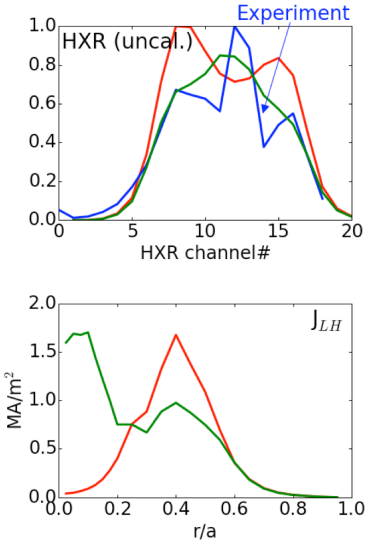

FIGURE 3. Comparison of HXR emission profile and current profile prediction and HXR emission profiles, obtained in experiment (blue), simulation without spectrum spreading (red) and with spreading (green) (EAST #48888 at 5.5s.)

exponential function (FIGURE 5 (left)). Although the scale length of the exponential function was selected to match the profile measured at outboard mid-plane, it did not incorporate the actual SOL plasma geometry, such as divertor X-point. It also tended to restrict the high collision frequency region to be near the last closed flux surface.

To investigate the importance of SOL geometry, we have added a new SOL model in our LHCD simulation using GENRAY/CQL3D [19]. The model uses a measurement of T_e and n_e on the midplane and T_e on divertor tiles ("two point model"), and computes the density and temperature elsewhere along the field line based on the pressure conservation along the field line and classical Spitzer parallel heat conduction. As shown in FIGURE 5 (right), the new profile is significantly different near the divertor region. This new SOL profile reconstruction was incorporated in our GENRAY/CQL3D simulation workflow built on πScope [20].

Using this new SOL model, we find that GENRAY/CQL3D predicts HXR emission intensity that is much more consistent with measured HXR intensity at high density. In FIGURE 5, the prediction of HXR emission at $n_e = 1.3\text{x}10^{20}\text{m}^{-3}$ is compared with the previously published result. Evidently, using the new SOL profile the code predicts considerably less intense HXR emission relative to the previous simulation. This is caused by an increase of collisional losses of LH power in the SOL region. At this density, about 83% of injected forward lobe power is predicted to be lost before being absorbed by electron Landau damping (ELD), while in the old model about the half of the forward lobe power was absorbed by ELD.

We also ran GENRAY/CQL3D using the new 2D SOL for the experiment shown in FIGURE. 2. The result, shown in FIGURE 6, is quite encouraging: while the code predicts the order of magnitude decrease of HXR emission for the low current case, it predicts a much smaller decrease for the high current case. The agreement with experiment indicates that the change is SOL profile shown in FIGURE 2 is indeed the key to improve LHCD at high density. It is also noteworthy that even in the high current case, about 40% of forward lobe power is lost

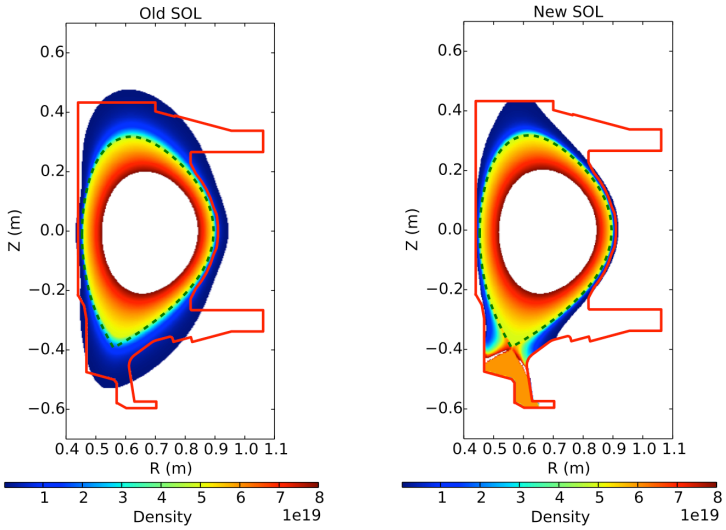

FIGURE 4. Comparison of density profiles used in previous publications (left) and reconstructed based on two-point models (right)

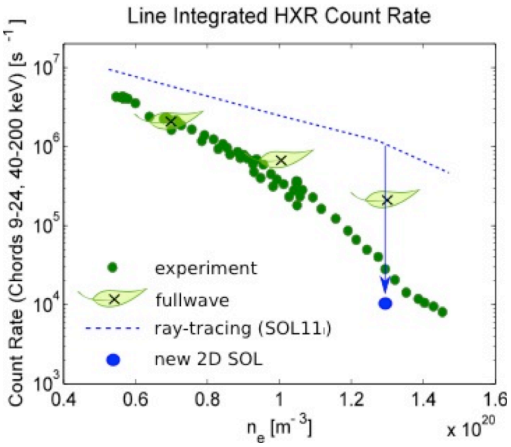

FIGURE 5. GENRAY/CQL3D prediction of HXR emission intensity when 2D realistic SOL is used (blue). Other simulation data are based on Ref. 5 and 8.

before being absorbed by ELD, suggesting a possibility of further improving the efficiency by additional narrowing SOL width.

FIGURE 7 compares ray-trajectories for low and high density cases. Each ray is colored based on the normalized ray power. It can be seen that at high density, ray power is lost when a ray enters SOL region, changing the color from red to blue quickly. The HFS electrostatic RF probe (indicated by arrows in the Figure) showed that the LH power reached to the HFS decreases by a factor of 10, when density is raised from 0,9 to $1.3 \times 10^{20} m^{-3}$ (See Figure 16 in Ref. 14). To make a quantitative comparison with the observation, we estimated the LH power by the sum of ray power propagating near the probe location. By "propagating near the probe", we selected the rays passing through the region between 5cm below and above the probe position. The ray data shown in FIGURE 7 suggests a drop of LH power by 70%. This looks close enough to the observation, given the ambiguity of ray selection, suggesting that the observed decrease of LH power measured at the HFS could be explained by the power loss during the first pass and change of ray propagation due to the increased density.

DISCUSSION

As shown in the previous section, the new 2D SOL model can reproduce the experimental trend over a wide density range, even at high density, where the previous agreement with the experiment was relatively poor. Originally the disagreement at high density motivated us to look for non-linear wave interactions. However, depending on experimental conditions, PDI activities on C-Mod occur at different locations, with different localization, and potentially by different mode coupling (i.e. parallel coupling vs. perpendicular coupling). If PDIs are the main loss mechanism, one would imagine qualitatively that the loss of CD efficiency would change depending on experimental conditions. The lack of such dependency

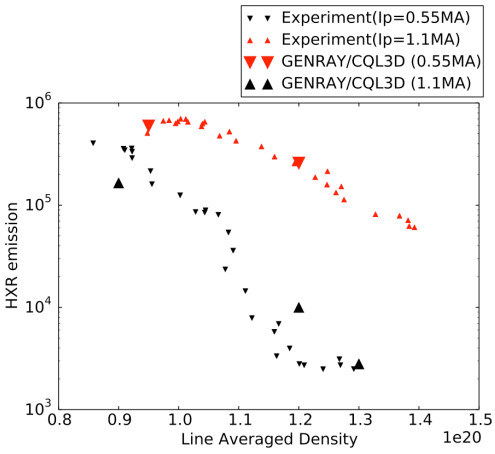

FIGURE 6. Prediction of HXR emission by GENRAY/CQL3D using the new SOL profiles for low (0.55MA) and high (1.1MA) current cases shown in FIG 2.

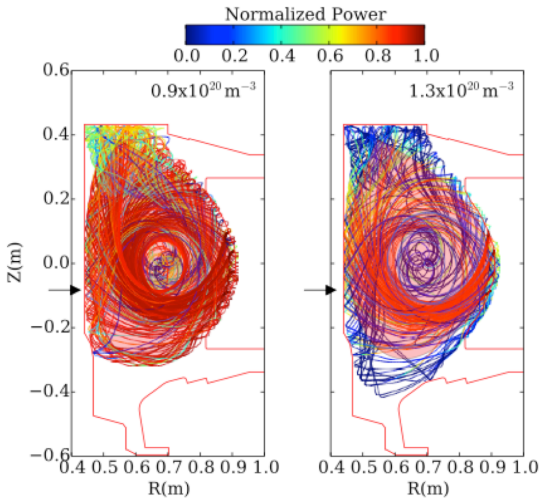

FIGURE 7. Comparison of ray trajectories on poloidal crosssection at low density case (left) and high density case (right)

suggests that it is not the case, or at least the model to explain the loss of current drive should include SOL profiles as detailed as what we used in this paper, so that one can predict what type of non-linear interactions are unstable. On the other hand, the success of the model with rather simple linear collisional absorption presented here suggests the possibility of explaining this on much simpler physics model. Either way, it is critical to cooperate SOL plasmas into the LHCD simulation model.

The approach to reconstruct 2D SOL profile we used in GENRAY/CQL3D is quite similar to the approach used previously in the LHEAF code [6]. In this regard, it is interesting to understand why LHEAF predicted much smaller collisional absorption. This might be due to the fact that the previous full wave code analysis was made in a single toroidal mode analysis. In a single mode analysis, the wave power tends to propagate relatively narrower region in the poloidal crosssection. This might have resulted in overestimating RF quasi-linear diffusion operator, and therefore the power absorbed via ELD. This should be studied further by running a full wave code using multiple toroidal modes.

In the future, we will further investigate the possibility of mitigating the current drive loss via SOL profile control. Previously we saw a recovery of LHCD efficiency at 1.2MA up to $1.5x10^{20}m^{-3}$. However, at that time several experimental conditions were changed simultaneously and so it is difficult to determine the root cause of recovery [8]. We plan to revisit and extend the experiment even higher current up to 1.5MA in FY15.

SUMMARY

Significant progress in understanding and mitigating parasitic wave absorption in edge plasmas on a reactor relevant diverted tokamak has been made on Alcator C-Mod. The power loss near the last closed flux surface was directly measured by an LH power modulation technique and was shown to increase as the density increases. LH wave propagation, and in particular PDI activities, which are long suspected as a physics mechanism to cause such a loss, were measured by electrostatic RF probe distributed around tokamak plasma. We observed a variety of PDI activities excited above the density threshold around $1x10^{20}m^{-3}$. However, the PDIs on C-Mod have a complicated dependency on experimental conditions, in contrast to the loss of current drive with increasing density, which is a rather robust trend as seen on HXR emission. Spectrum spreading was examined and it was found that including even a small spectrum spreading could improve the simulation accuracy. A new 2D realistic SOL model has been incorporated in our GENRAY/CQL3D simulation workflow. The SOL model is fully

determined by experimental data, and was found to improved the agreement with the experiments at high density where the discrepancy was large in previous works, implying that the loss of current drive is caused by the wave propagation in a cold dense peripheral region of diverted tokamak. This result implies that observed PDIs should be looked as a symptom indicating that the LH wave is propagating in such a cold region rather than the cause of losses.

ACKNOWLEDGEMENTS

This work was conducted on the Alcator C-Mod tokamak, a DoE Office of Science user facility, and is supported by USDoE awards DE-FC02-99ER54512, DE-AC02-09CH11466, and DoE Grant DE-SC0010492.

REFERENCES

[1] *"Non-Inductive Current Drive in Tokamaks"*, Proceeding of IAEA technical committee meeting (1983)
[2] M. Porkolab, Phys. Fluids 20, 2058 (1977)
[3] Y. Takase, M. Porkolab, J. J. Schuss, R. L. Watterson, et. al., Phys. Fluids 28, 983 (1985)
[4] G.M. Wallace, R.R. Parker, P.T. Bonoli, et. al., Physics of Plasmas **17**, 082508 (2010)
[5] G.M. Wallace, I. C. Faust, O. Meneghini, et. al., Phys. Plasmas **19**, 062505 (2012)
[6] O. Meneghini, *"Full-wave modeling of lower hybrid waves on Alcator C-Mod*", Ph. D thesis (2012).
[7] S Shiraiwa, J Ko, O Meneghini, R Parker, et al.,Physics of Plasmas **18**, 080705 (2011)
[8] S. Shiraiwa, G. Baek, P.T. Bonoli, I.C. Faust, et. al., Nucl. Fusion **53** 113028 (2013)
[9] S.G. Baek, R.R. Parker, S. Shiraiwa, G.M. Wallace, et. al., Plasma Physics and Controlled Fusion **55**, 052001 (2013)
[10] S. G. Baek, R. R. Parker, S. Shiraiwa, et. al., Physics of Plasmas, 21, 061511 (2014)
[11] S.G.Baek, S.Shiraiwa, R.R.Parker, C.Lau,and G.M.Wallace, Plasma and Fusion Research 7, 2402031 (2012)
[12] I. Faust, D Brunner, B. LaBombard, R.R. Parker, et. al., *"Measurment of LHCD edge power deposition through modulation technique on Alcator C-Mod" (at this conference)*
[13] G.M. Wallace, A.E. Hubbard, P.T. Bonoli, et. al., Nuclear Fusion **51**, 083032 (2011)
[14] S.G. Baek, R.R. Parker, P.T. Bonoli, S. Shiraiwa, G.M. Wallace, B. LaBombard, I.C. Faust, M. Porkolab, D.G. Whyte, Nucl. Fusion **55** 043009 (2015)
[15] R. Cesario, A. Cardinali, C. Castaldo, F. Paoletti, and D. Mazon, Phys. Rev. Lett. **92**, 175002 (2004).
[16] R. Cesario, L. Amicucci, A. Cardinali, C. Castaldo, et. al., Nucl. Fusion **54** 043002 (2014)
[17] J. Decker, Y. Peysson, J.-F. Artaud, E. Nilsson, A. Ekedahl, M. Goniche, J. Hillairet and D. Mazon, Phys. Plasmas **21**, 092504 (2014)
[18] A. P. Smirnov and R. Harvey, Bull. Am. Phys. Soc. 40, 1837 (1995).
[19] R. W. Harvey and M. McCoy, in Proc. of the IAEA TCM on Simulation and Modeling of Thermonuclear Plasmas, Montreal, 1992, pp. 489–526.
[20] S Shiraiwa, T Fredian, J Hillairet, J Stillerman, *"πScope: python based scientific workbench with MDSplus data visualization tool"*, to be accepted in Fusion Engineering and Design

3.1.5 Thick target bremsstrahlung measurements during LHCD

Computer modeling of current drive in Alcator C-Mod has faced difficulties in reproducing the radial distribution of fast electrons. These profiles are determined from the emission of high energy bremsstrahlung and are measured using the hard X-ray diagnostic. Synthetic hard X-ray emission profiles determined by ray-tracing and full wave simulations were narrower than what was observed in the experiment. The broad experimental fast-electron profile is more likely to diffuse fast-electrons into the scrape-off-layer (SOL) of Alcator C-Mod. Understanding the loss of electrons at the edge can improve models of LHCD in diverted plasmas and can inform on LHCD efficiency in high temperature tokamak plasmas.

A low elongation equilibrium with a high inner divertor strike point was developed in order to measure the sensitive thick-target bremsstrahlung emission from the inner divertor using the HXR. Measurements of X-ray emission at the strike point and in the core were made at various densities. Modulation of the RF power was used in order to isolate the RF effects, this follows procedures used extensively for the characterization RF power deposition. It was found that in all cases that the emission from the strike point location was several times higher than that of the core emission.

The emission of thick target bremsstrahlung is significantly higher in reversed field, this is due to the intrinsic nature of LHCD. Current is generated by LHCD through the formation of an assymetry in the electron distribution. A larger population of fast electrons is created which travels counter-current with a substantially smaller population that travels co-current. By extension, fast electrons which are lost to the SOL are more likely to be traveling in the counter-current direction. With the fixed helicity of Alcator C-Mod, fast electrons predominantly hit the outer divertor in forward field, and the inner divertor in reversed field. The electrons generated by LHCD are passing and have low collisionality, are predominantly travel directly to the divertor. Initial characterization finds that the emission from reversed field plasmas are 100 times the core value, while in forward field the emission is 3-5 times that of the core

Edge losses of fast electrons have been theorized to cause the LHCD density limit in diverted discharges. However, the lack of thick target bremsstrahlung at very high density (when no current is driven) suggests that the loss of current drive is not simply due to edge fast electron loss. A significant loss of power in fast electrons would be shown through massive thick-target emission or via non-thermal character in the SOL at the highest densities.

3.2: Impurity transport with off-axis current drive

C-Mod provides a unique platform for the study of impurity transport with off-axis current drive. The laser blow-off impurity injector can provide an impulse-like source of a wide range of possible impurities (Ca, F, Mo, W, etc). Preliminary experiments in 2012 did not result in clean data due to diagnostic issues. These conditions will be revisited to obtain detailed measurements of mid- to high-Z impurity transport in nearly non-inductive discharges. Preliminary results are summarized below. Additional details on the analysis of impurity transport with off-axis current drive in C-Mod can be found in Section 4.5.

3.2.1 Characterization of impurity transport in non-inductive LHCD scenarios

Impurity accumulation leads to plasma dilution and an overall degradation of plasma performance. Understanding the mechanisms leading to large impurity fractions in the core plasma is the first, necessary step to avoid those negative effects. In collaboration with C-Mod, studies have focused on transport of medium to high-Z impurities such as Ca, Fe, Mo and W. On C-Mod, a laser blow-off system [CMOD-9] is used as impulse-like, well controlled source of impurities at the plasma edge. The evolution of impurities is then monitored and transport coefficients inferred from forward-modeling of the experimental data.

A dedicated experiment has focused on Ca transport for ohmic and LHCD scenarios. The C-Mod Soft X-ray system provides time-dependent, 2D profiles of Ca emissivity, from which diffusion/convection coefficients are inferred. For the ohmic case, a scan in plasma current from I_p=0.6 MA to I_p=1.2 MA was performed. Transport analysis of the Ca tracer

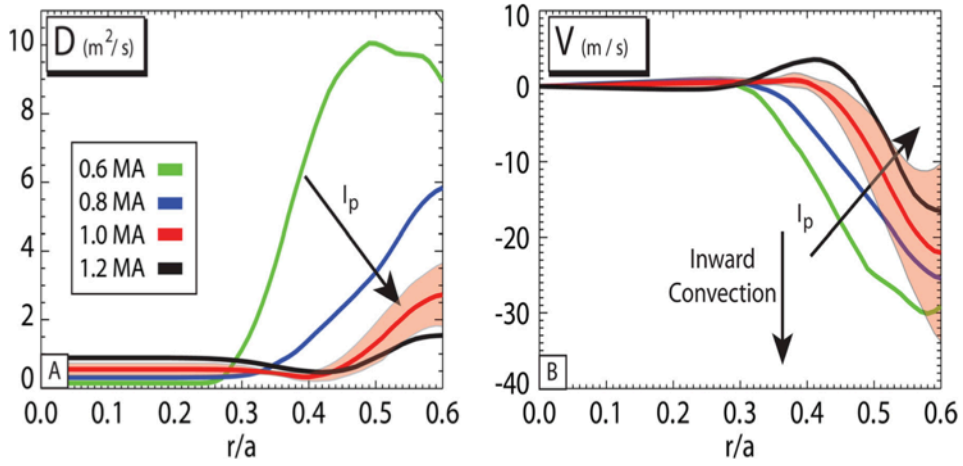

Fig. 3.3: Diffusion and convection coefficients computed for Ca from laser blow-off during a ohmic current scan on C-Mod.

impurity shows a strong dependence on I_p, with a decrease in the inferred diffusivity and inward convection as the current is increased (see Fig. 3.3).
When LHCD is added to the ohmic scenario, a clear difference in impurity transport is observed. Figure 3.4 shows an example of Ca emissivity measured 5 and 10ms after laser blow-off injection of Ca into both ohmic and LHCD plasmas. Emissivity profiles indicate core accumulation of Ca for the ohmic case, which is not observed (or much reduced) during the LHCD phase. Analysis is under way to explain these results. A possible explanation is related to turbulent transport of impurities by underlying TEM or ITG turbulence. Three terms are being considered, which can affect the pinch of impurities: B-field curvature, thermodiffusion and parallel compressibility. Preliminary estimates indicate parallel compressibility from TEM turbulence as a viable candidate.

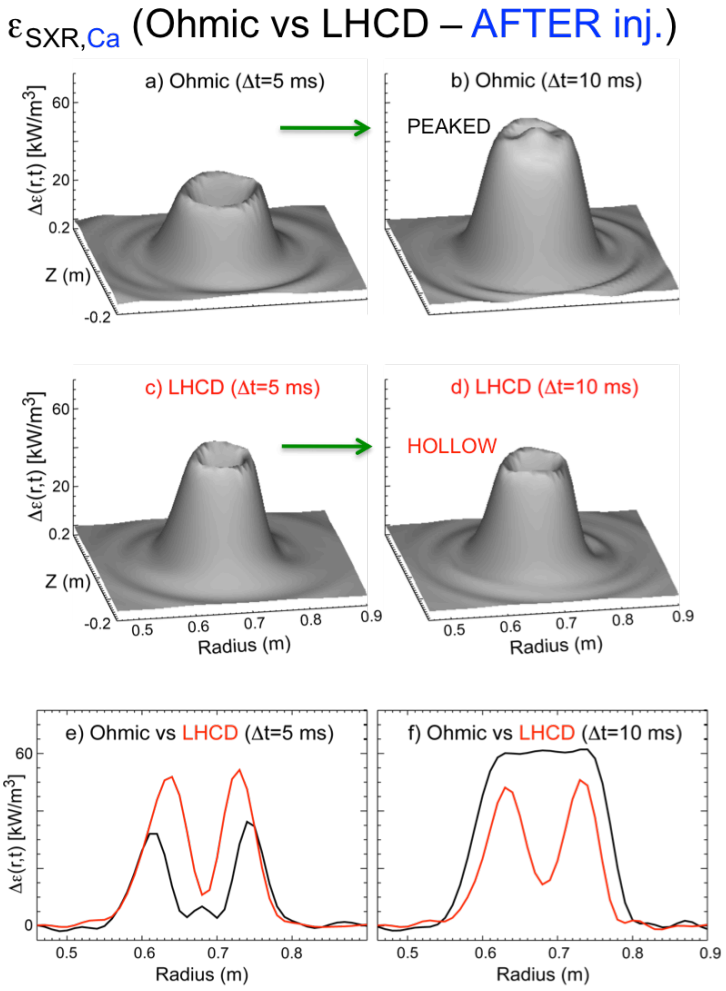

Fig. 3.4: (a-d) 2D emissivity profiles at two times after laser blow-off Ca injection during ohmic and LHCD phases. (e,f) Midplane projections of the emissivity.

3.3: Exploration of accessible regimes through off-axis current drive

C-Mod discharges with strong off-axis current drive ($\Delta v/v>0.5$) sometimes develop MHD instabilities as the current profile evolves. These instabilities can be benign, but often result in loss of current drive efficiency and degraded transport [CMOD-10]. Figures 3.5 and 3.6 show an example of a discharge with MHD instability developing around 1.15 s.

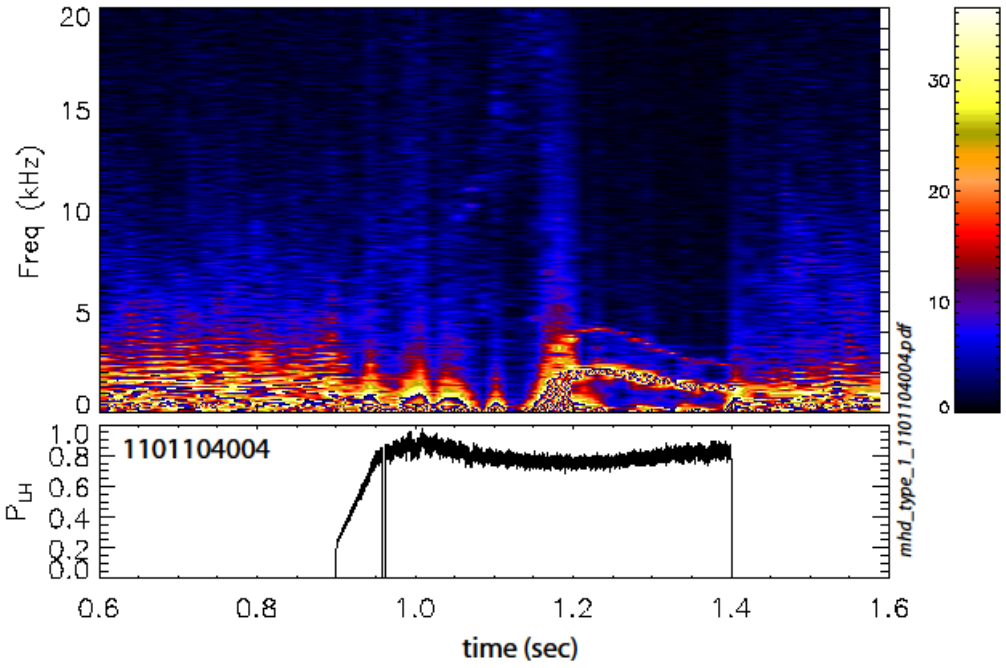

Figure 3.5: Low-frequency MHD is sometimes observed during high-power Lower Hybrid current drive in Alcator C-Mod.

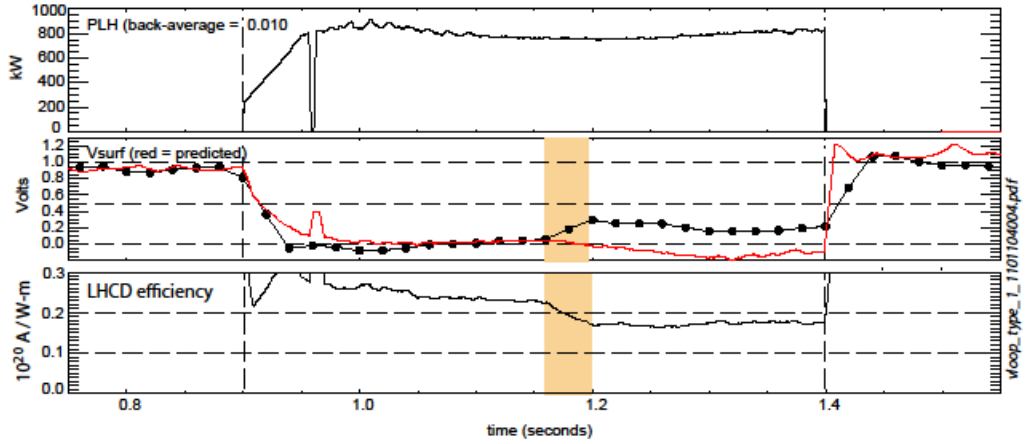

Figure 3.6: Low-frequency MHD sometimes, but not always, results in a reduction in LH current-drive efficiency.

A database of existing discharges with lower hybrid current drive (LHCD) has been created. The database includes information on net LH power, launched $n_{||}$, plasma current, loop voltage, electron density and temperature, Z_{eff}, driven current, 0-D LHCD efficiency, and the presence of deleterious MHD instabilities. The range of parameters for which MHD is problematic is shown in Figure 3.7. MHD instabilities also appear to be responsible for termination of T_e ITBs in reverse shear discharges [CMOD-11] (see Figures 3.8-3.9). Although the MHD activity typically causes a decrease in current drive efficiency, some discharges with MHD continue to show good current drive efficiency as shown in Figure 3.10.

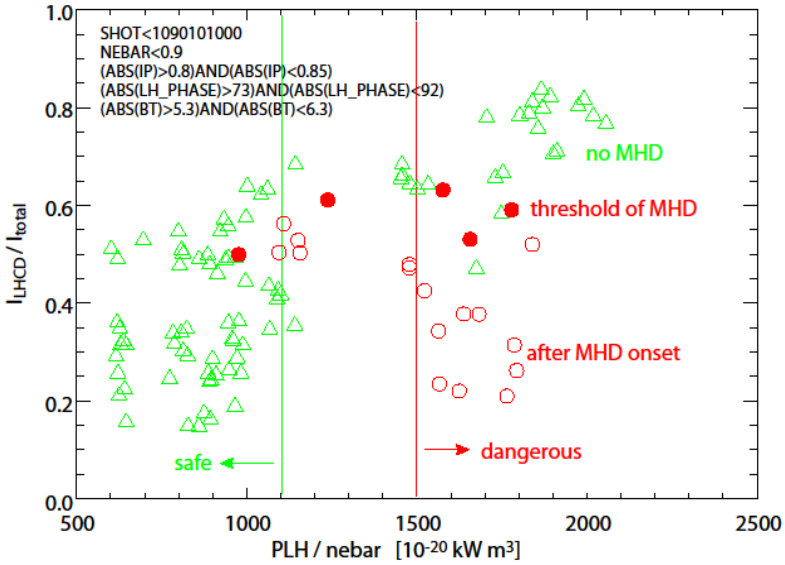

Figure 3.7: The probability of deleterious MHD generally increases as the plasma becomes more non-inductive.

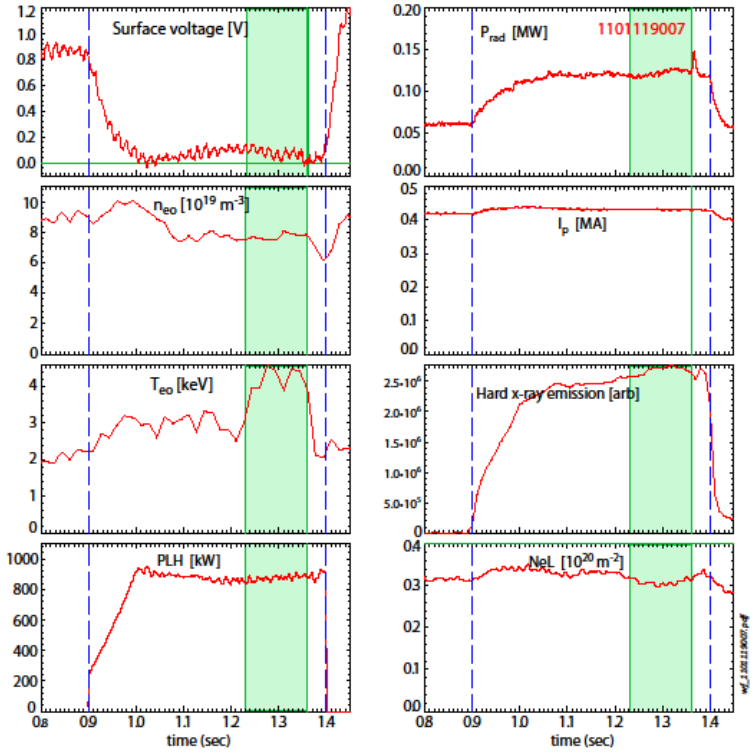

Figure 3.8: Internal transport barriers (eITBs) sometimes develop during LHCD which result in steep electron temperature gradients but little change in density gradient.

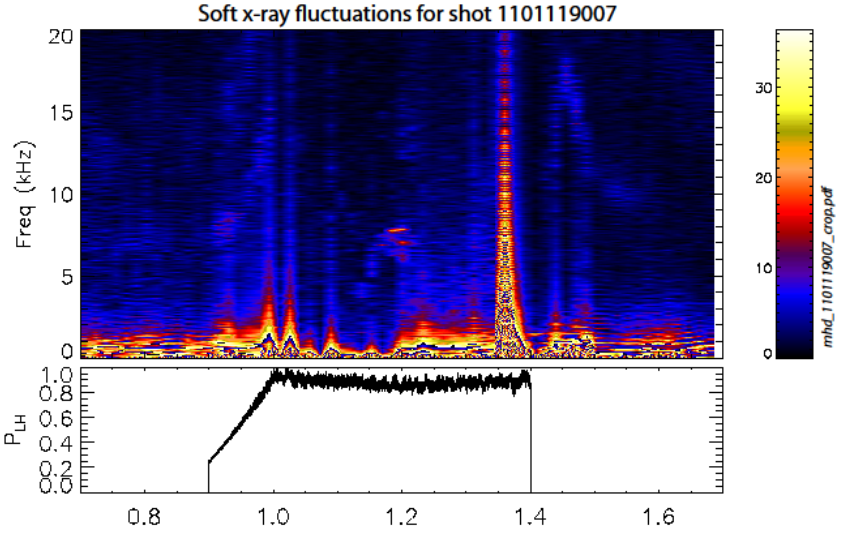

Figure 3.9: The duration of eITBs is often terminated by MHD.

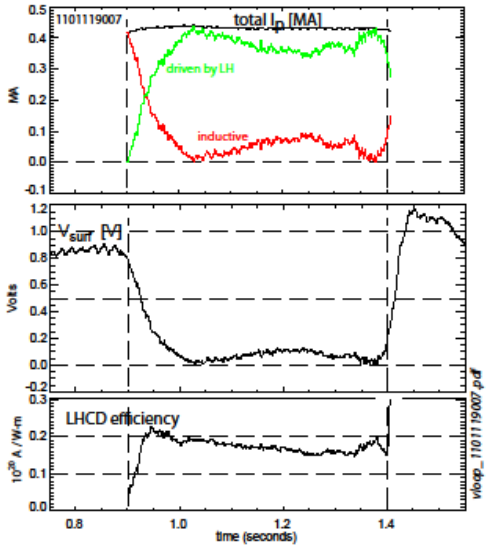

Figure 3.10: Interestingly, the LH current drive efficiency is not reduced when MHD terminates the eITB, despite a significant reduction in electron temperature. This suggests that the radial location of the LH-driven current is largely outside the radial location of the MHD.

Analysis of experimental data from 2012 with the NIMROD code shows that MHD instability may be due to an m = 3, n = 2 mode at the q = 1.5 surface. Uncertainty within the MSE constrained EFIT reconstructions allows for either a single q = 1.5 surface, or two q = 1.5 surfaces with q_{min} ~1.1, as shown in Figure 3.11.

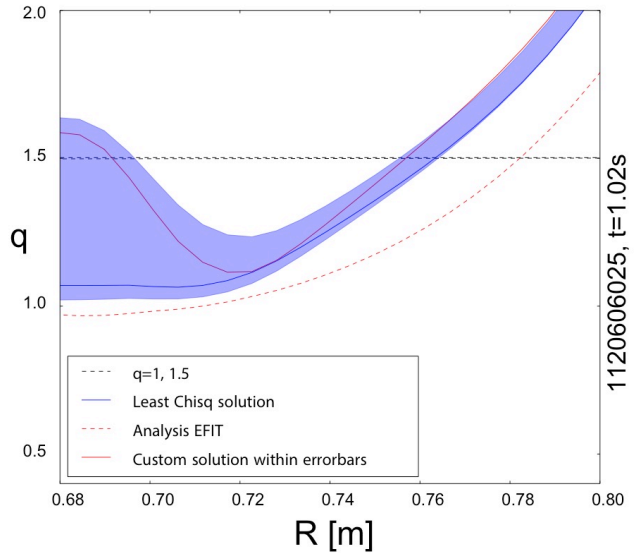

Figure 3.11: MSE constrained EFIT reconstructions of discharges with deleterious MHD show the possible of a single q = 1.5 surface, or two q = 1.5 surfaces with reverse shear and q_{min} ~ 1.1. The solid blue line indicates the least χ^2 solution, the solid red indicates another possible q profile exhibiting two q = 1.5 surfaces, and the horizontal dashed line indicates q = 1.5.

Upgrades to the motional stark effect (MSE) diagnostic will improve accuracy and time resolution of current profile reconstructions for 2015 [CMOD-12] for input to MHD stability calculations. The upgraded MSE diagnosted was assumed for planning of experiments in FY2015. Miniproposal 787 was approved by the C-Mod Experimental Program Committee (EPC) and scheduled several times during the FY2015 run campaign, however experiments on this topic were delayed to FY2016 due to failure of the diagnostic neutral beam (DNB) needed for MSE measurements.

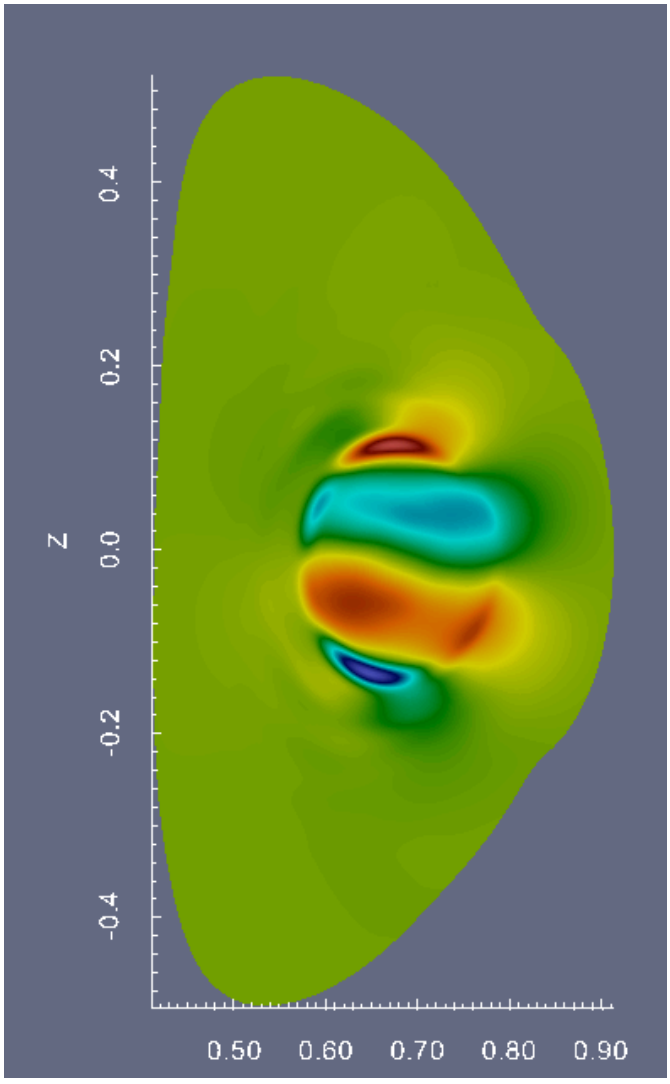

Figure 3.12: Radial magnetic field perturbation - Core MHD mode structure obtained from the linear simulations using NIMROD for shot 1120606025 at t=1.12s. For this case, q is above 1 with no shear reversal. This is the mode structure for n=1 core mode. The poloidal cross section shows m=2 and m=3 structures.

References

[CMOD-1] P. Xu. *Polarimetry measurements of current density profile and fluctuation changes during lower hybrid experiments on Alcator C-Mod*. Thesis, Massachusetts Institute of Technology, 2013.
[CMOD-2] A. E. W. Schmidt. *Measurements and modeling of Lower Hybrid Driven fast electrons on Alcator C-Mod*. PhD, 2011.
[CMOD-3] P. T. Bonoli and R. C. Englade, Phys. Fluids **29** (1986) 2937.
[CMOD-4] G. M. Wallace. *Behavior of lower hybrid waves in the scrape off layer of a diverted tokamak*. Thesis, Massachusetts Institute of Technology, 2010.
[CMOD-5] A. Schmidt et al., Phys. Plasmas **18** (2011) 056122
[CMOD-6] O. Meneghini. *Full-wave modeling of lower hybrid waves on Alcator C-Mod*. Thesis, Massachusetts Institute of Technology, 2012.
[CMOD-7] J. Decker et al., Phys. Plasmas **21** (2014) 092504.
[CMOD-8] N. Bertelli et al., Plasma Phys. Control. Fusion **55** (2013) 074003.
[CMOD-9] N. T. Howard et al., Rev. Sci. Instrum. **82** (2011) 033512
[CMOD-10] S. D. Scott et al. "Scaling of Global LHCD Efficiency in Alcator C-Mod." Bull. Amer. Physical Soc. Vol. 1. 2014.
[CMOD-11] S. Shiraiwa et al., Nucl, Fusion **53** (2013) 113028.
[CMOD-12] R. T. Mumgaard and S. D. Steven, "Design and construction of a multi-spectral MSE system for Alcator C-Mod." Bull. Amer. Physical Soc. Vol. 1. 2014.

4.0 NSTX-U Contributions

NSTX-U supported the FY-15 Joint Research Target by leading and coordinating research activities on the DIII-D, C-Mod and NSTX-U facilities. Preparation for the JRT-15 started in late CY-2013 with two meetings at PPPL. Potential goals and contributions from NSTX-U were discussed in a first meeting, based on previous brainstorming sessions of the NSTX-U Topical Science Groups. Initial ideas and a tentative plan for the JRT-15 were then discussed in a joint NSTX-U/DIII-D meeting, in which opportunities and priorities for collaborative research were presented. From these initial meetings, joint work on the physics of steady-state scenarios sustained by Neutral Beam current drive emerged as the highest priority for NSTX-U and DIII-D to address the JRT-15 goals. Once C-Mod operations were also confirmed for FY-15, the experimental plans have been naturally extended to include lower-hybrid current drive as a means to alter the current profile and improve plasma stability and performance.
The initial scoping activities to identify possible experiments and analysis tasks resulted in the definition of the 4 Quarterly Milestones in early FY-14, followed by teleconferences of the Coordination Committee and by Team meetings at the three facilities throughout FY-15 to assess progress and future plans. Plans for specific experiments on NSTX-U and DIII-D were discussed at Research Forums during the Second Quarter and finalized in the following months. C-Mod plans were defined throughout the FY-15. Fig. 4.1 shows an overview of the JRT-15 calendar.
In general, the goals for the 4 Quarters transitioned from organization/planning to experimental activities and analysis with all 3 facilities expected to contribute with experimental results. However, an hardware failure during NSTX-U re-commissioning in the 3rd Quarter led to a revision of the NSTX-U plans for the remainder of FY-15. The delay in machine start-up motivated a shift of activities towards modeling work, targeting specific areas of overlap with experiments conducted on the other two facilities. Achievements for joint modeling activities are discussed in the next Sections.

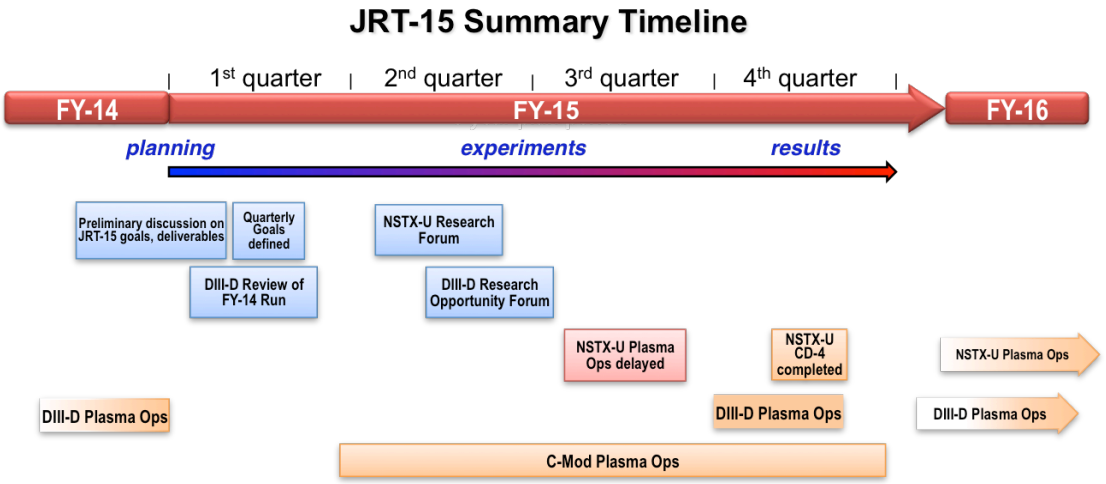

Fig. 4.1: Summary timeline of JRT-15 related activities on the 3 facilities during FY-15.

4.1: Resistive Wall Mode physics and impact on plasma performance

4.1.1 Joint DIII-D and NSTX-U experimental activity

A dedicated experiment was run on DIII-D (S.A. Sabbagh, J.W. Berkery, J.M Hanson, C. Holcomb, et al. "*MP2014-22-07: Testing kinetic RWM stabilization theory at marginal stability in high beta, tearing mode stabilized plasmas*") to test kinetic Resistive Wall Mode (RWM) stabilization physics proposed in several NSTX publications [NSTXU-1 - NSTXU-5] with the goal of unifying the physics understanding of kinetic RWM marginal stability conditions between devices. After comparison with previous results from NSTX, the experiment was successful in producing this understanding:

1. Kinetic RWM theory provides a sufficient breadth to understand the stabilization physics between the two devices, which have an important complementarity.
2. Experimental observations and kinetic RWM stability analysis between the two devices show good agreement between theory and experiment.

Prior experiments have shown that unstable RWMs cause disruptions – full current quenches that terminate the plasma, and major thermal quenches that rapidly drop the plasma stored energy by 50 – 80%. Such disruptions observed in this experiment, caused by rapidly growing RWM activity, appear to be at points of RWM marginally stability (full analysis for all representative cases are summarized in the final section below on this topic, see Sec. 4.1.3). RWM instability doesn't occur when significant tearing modes (TM) appear, and so the present experiment was designed to create significant periods during which the plasma was stable to large tearing modes that would otherwise preclude RWM destabilization. As tearing modes are foreseen to be stabilized in ITER and future tokamaks, one must be concerned with what instabilities limit plasma performance when TMs are avoided or controlled. Another important observation in this experiment is that RWM activity can itself trigger tearing modes. A unification of the underlying kinetic RWM stability physics between NSTX and DIII-D gives the greatest confidence to confidently extrapolate results to future devices for disruption avoidance.

High β_N, q_{min} plasmas were chosen to study kinetic RWM stability characteristics in the DIII-D experiment for several reasons. These plasmas are candidates for steady-state, high β_N operation and are therefore important to the DIII-D program and future tokamak operation. These plasmas can also operate at high $q_{min}>2$, which eliminates the 2/1 rational surface and therefore precludes destabilization of the significant 2/1 tearing mode. In this condition, 3/1 tearing modes were observed to be destabilized, but ECCD control was used to successfully suppress this mode, allowing an investigation of the

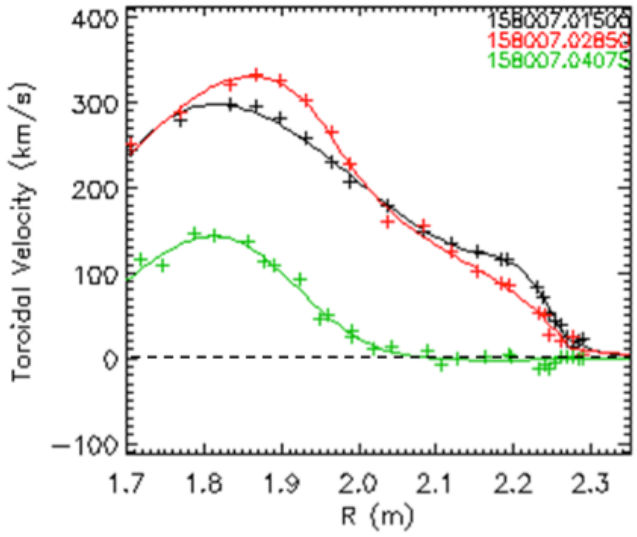

Fig. 4.2: Rotation profiles in DIII-D near different RWM marginal stability conditions.

RWM marginal stability point over a wide range of plasma rotation profiles. RWM marginal stability crossings were found for three different rotation profiles and plasma conditions:

1. *Induced by profile peaking at moderate β_N and high rotation*
2. *Found at high β_N and low rotation*
3. *Found at high β_N and high rotation*

Plasma rotation profiles representing these conditions are shown in Fig. 4.2. The unique 1 ms Charge Exchange Recombination (CER) spectroscopy capability in DIII-D and magnetics showed that "radially extended Edge Localized Modes (ELMs)" (also named "global bursting MHD events" because the modes are not edge localized) sometimes correlate with crossing the RWM marginal stability point - either moving toward instability or toward stability - but a trigger that initiates RWM growth was sometimes not found. The high time-resolution CER shows that the thermal and rotation collapses presently appear to be caused by RWM mode growth rather than a loss in rotational torque balance.

Representative detail of approaching and crossing the RWM marginal stability point were produced in the three different rotation profile and β_N conditions mentioned above. Here, we examine just one condition in detail for the sake of brevity. Figure 4.3 illustrates a 50% thermal collapse during RWM activity. The lower right-hand side magnetic spectrogram shows that a 3/1 tearing mode stabilizes before the large thermal collapse (time period highlighted in yellow). This stabilization of the tearing mode - not mode locking - is confirmed by the ECE and MIR diagnostics. During the next time interval (highlighted in green), the frequency of ELMs decreases and β_N rises, even though NBI

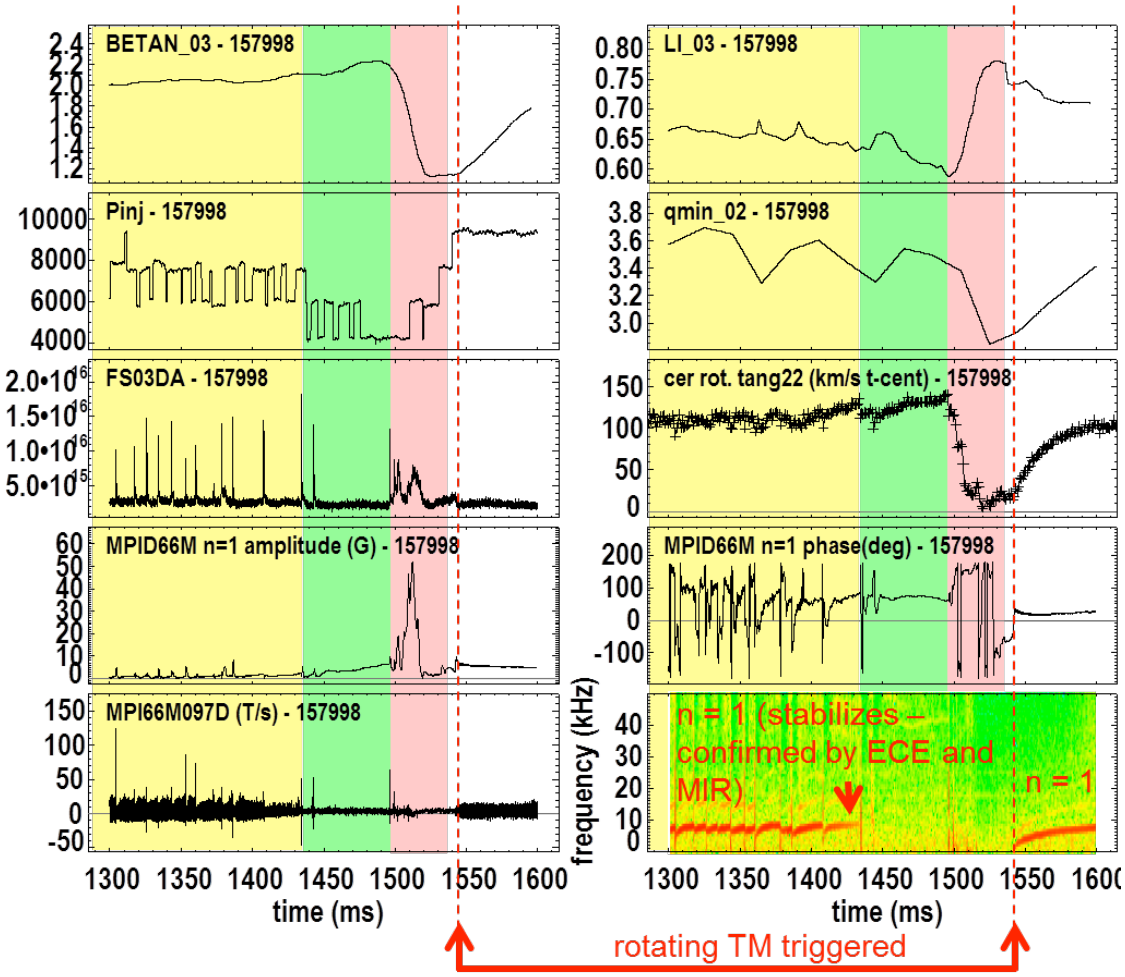

Fig. 4.3: Illustrative plasma parameter waveforms approaching an RWM marginal stability point in DIII-D.

power has been automatically decreased via real-time β_N control. The *n=1* RWM sensor amplitude then begins to rise during this period of approximately 60 ms, indicating resonant field amplification of the stable *n=1* RWM field perturbation rising to about 5G. After this point, there is a strong increase in the *n=1* RWM field perturbation. The detail of this increase is shown in Fig. 4.4, which shows a zoomed-in view of the time period highlighted in red in Fig. 4.3. Three bursts are observed in the D_a signal (upper left frame in the figure) which would generically be classified as ELMs. However, this is literally a misnomer, as these events are found to be radially extended modes, and are therefore not "edge localized". They otherwise share common characteristics with ELMs, including toroidal and poloidal localization. The 3D magnetics arrays in DIII-D show the mode to be ballooning, as the mode amplitude is observed to increase as the mode propagates through the device midplane. These characteristics, especially the radially extended eigenfunction, suggest that these events are closer to "X-Events" in DIII-D [NSTXU-6], or "3D ballooning modes" in TFTR [NSTXU-7], but the presently observed radially

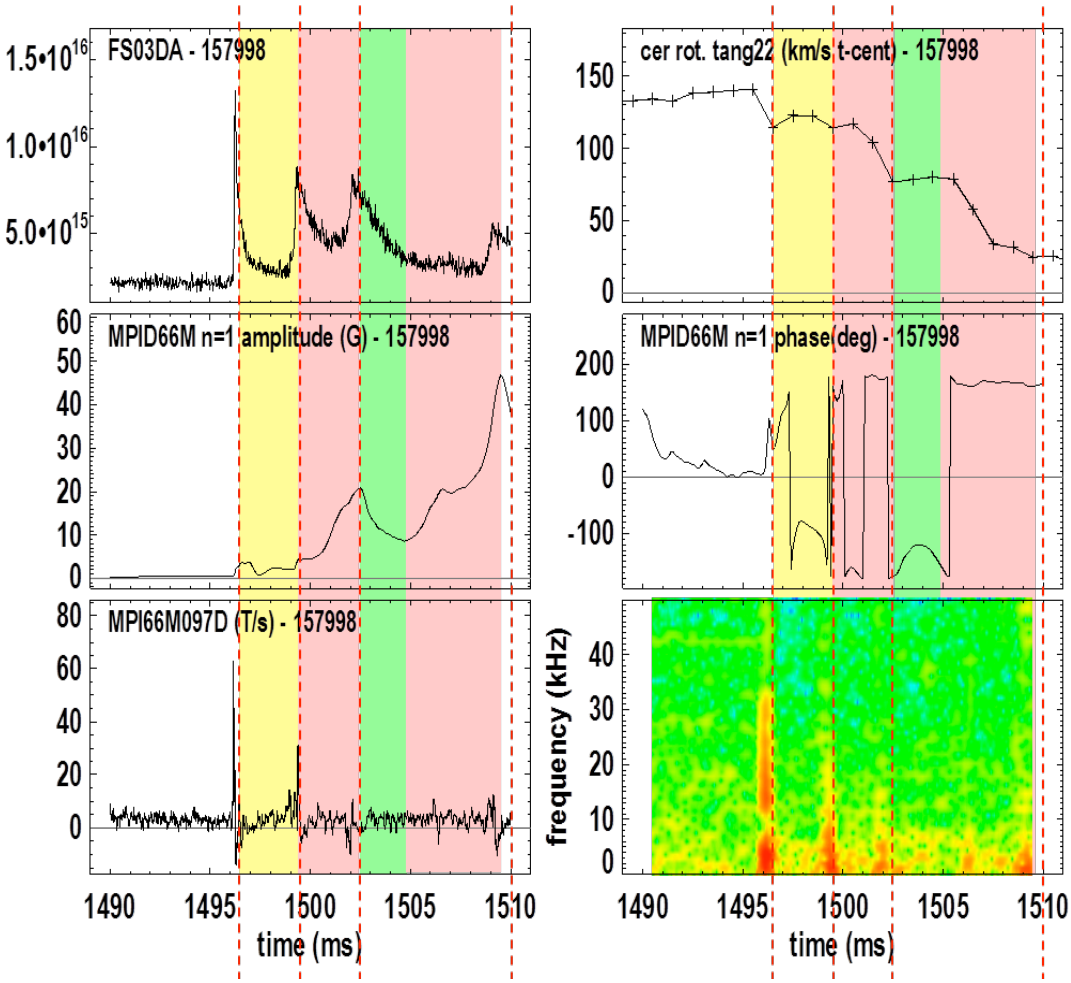

Fig. 4.4: Illustrative plasma parameter waveforms approaching an RWM marginal stability point in DIII-D (zoomed in view of Fig. 4.3).

extended MHD bursts are significantly less perturbative to the plasma than either. The toroidal and poloidal mode spectrum for a toroidally/poloidally localized mode is expected to be broad, which is measured, but these spectra vary significantly when comparing different instances of these events. The 1 ms CER diagnostic data shows an orderly decrease of the plasma toroidal rotation as the strong n=1 RWM that causes the strong β_N collapse unfolds. The middle two frames of Fig. 4.4 show the n=1 RWM amplitude and phase. During the initial drop in rotation apparently caused by the first bursting event (yellow highlight), the n=1 amplitude changes a small bit, but doesn't show strong growth, the RWM apparently rotates in the co-NBI direction, and the plasma rotation itself partially recovers within 3 ms. The next bursting event (red highlight) shows a strong increase in the $n=1$ amplitude in a short period ~2 ms which is near the expected RWM growth time. This strong increase in n=1 amplitude leads to a strong decrease in plasma toroidal rotation, which would be caused by neoclassical toroidal viscosity (NTV) if, as expected, the observed global perturbation is ideal. The next period

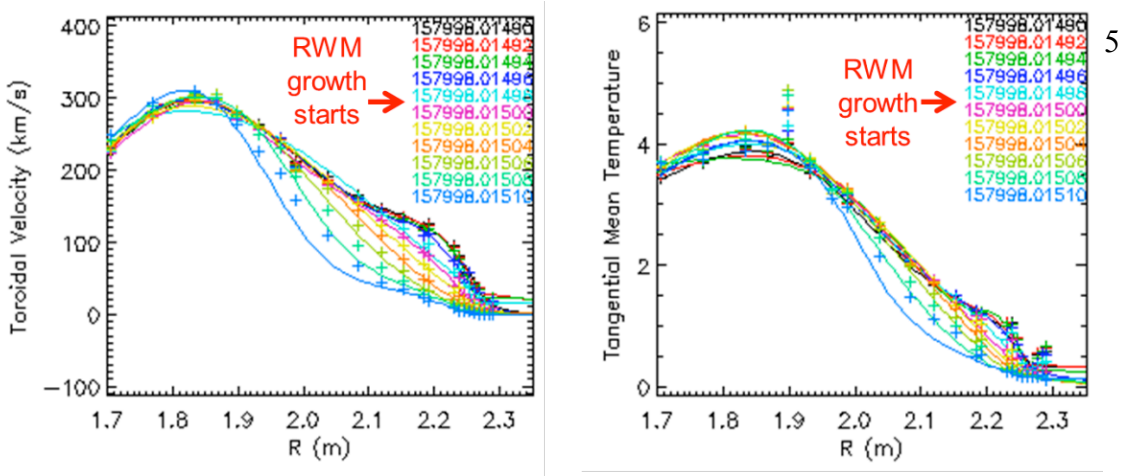

Fig. 4.5: High time-resolution CER data showing profiles of plasma rotation and ion temperature during the n = 1 RWM growth, showing a peaking of both profiles.

(highlighted by green) interestingly shows damping of the *n=1* RWM amplitude after a smaller MHD burst. Finally, strong RWM growth occurs during the time of the second red highlighted region, without an obvious trigger.

The 1 ms CER data indicate that RWM instability is caused by peaking of both the ion temperature and plasma toroidal rotation during this time interval (Fig. 4.5). The kinetic RWM stability analysis of these and similar discharges used to design the experiment has been completed, and are shown in the final section in kinetic RWM marginal stability below, see Sec. 4.1.3.

This especially illustrative example yields two new hypotheses to potentially explain the dynamic shown in the last few figures. First, a simple model of kinetic RWM stabilization has been long proposed by A. Boozer [NSTXU-8] and can qualitatively explain the detail shown. Details of this hypothesis are exemplified by Fig. 4.6. The figure shows a contour plot of RWM sensor signals (toroidal angle vs. time), also showing the field perturbation (in Gauss) in the upper frame for *n*=1, 2 and 3 field components. Time intervals highlighted by yellow, red and green correspond to time intervals similarly highlighted in Fig. 4.4. In the Boozer theory, the RWM is stabilized by the differential rotation between the plasma rotation and the RWM rotation, with a difference symbolized by a parameter α. Higher α signifies a higher differential rotation between mode and plasma rotation, which increases stability, with the opposite being true for lower α. When the plasma is at RWM marginal stability, small changes in the α parameter can bring the equilibrium across the marginal point. We then notice a drop in α in Fig. 4.6 as the plasma enters the following time interval highlighted in red. This is because the RWM phase decreases during this period, meaning that the mode is spinning with the plasma rotation at a faster pace, and therefore decreasing the differential rotation with the plasma. This could change the RWM stability from stable to unstable, since the plasma is expected to be at marginal stability in the yellow highlighted time interval. In

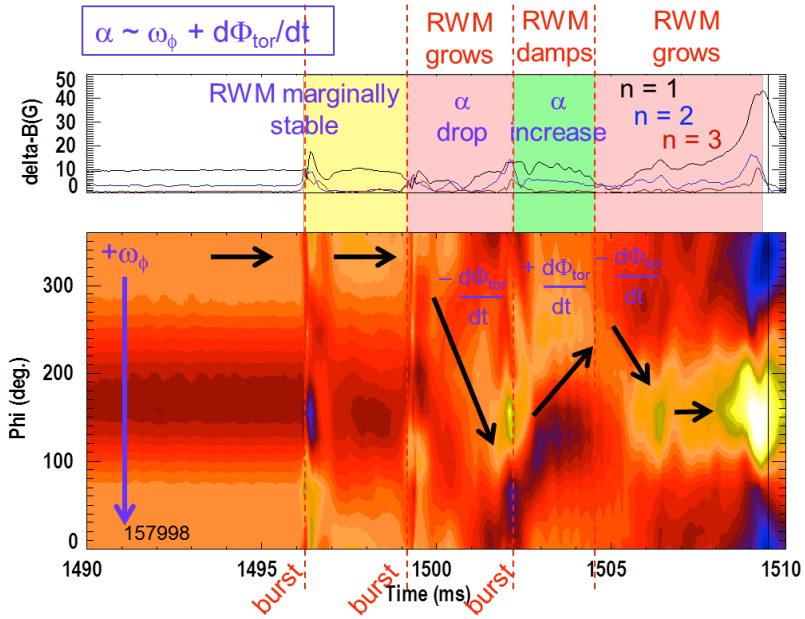

Fig. 4.6: Contour plot of RWM sensor signals (toroidal angle vs. time), showing the δB perturbation (in Gauss) in the upper frame for n=1, 2 and 3 field components. Time intervals highlighted by yellow, red and green correspond to intervals similarly highlighted in Fig. 4.4.

the next time interval highlighted in green, there is an observed temporary reversal in the sign of the change in the RWM phase. This indicates an increase in α (i.e. increased stability), which correlates with the hypothesis that the plasma has now moved back over the marginal point to – again - become RWM stable. In the next time interval, again highlighted in red, there is another reversal in sign of the RWM phase change vs. time, which again means a drop in α and theoretically reduced stability. This correlates with a RWM growth observed in the experiment.

A second new and provocative hypothesis arises from these observations – that the plasma is becoming non-linearly destabilized by the bursting MHD events that occur. The following qualitative explanation follows from work of Bagaipo, et al. on the non-linear destabilization of MHD interchange modes [NSTXU-9]. Again, consider the illustration in Fig. 4.6 and examine the highly simplified qualitative illustration of non-linear MHD interchange destabilization shown in Fig. 4.7. Following the same progression through the highlighted time intervals in Fig. 4.4 as done in the prior paragraph, before the yellow highlighted region (before the first MHD burst), we expect we are near the RWM linear stability boundary, but we are still linearly stable (see Fig. 4.7 – we are in the "RWM stable" region). Since an MHD burst has not occurred yet, the blue region in this figure labeled "RWM non-linearly unstable" does not exist. Then, after the first MHD burst in Fig. 4.4, a region of RWM non-linear instability exists, but the mode is not growing strongly, showing that the plasma does not cross into the RWM non-linearly unstable region. Note that the size of the RWM non-linear unstable region scales in theory with the amplitude of the field perturbation generated by the bursting MHD event that is superposed in time and space with the RWM activity. Therefore, as the field perturbation generated by the bursting MHD event dies away on a fast timescale

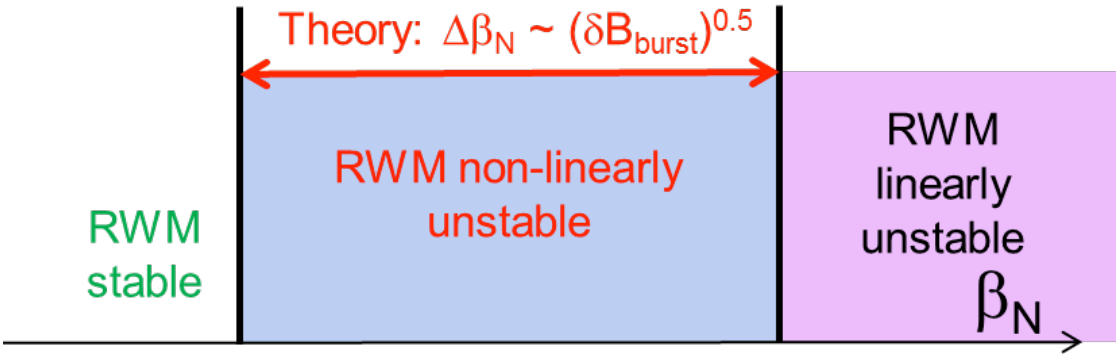

Fig. 4.7: Simple qualitative illustration of non-linear RWM destabilization hypothesis.

(magnetics and other diagnostics indicate the timescale to be ~ 1 ms), the non-linearly destabilized region also reduces to zero. By the time of the next highlighted time interval (first red interval in Fig. 4.4), the plasma rotation and ion temperature profiles have now increased in peakedness to bring us closer to RWM linearly unstable point, and when the second MHD burst occurs, the observation of the strongly growing RWM is consistent with the amplitude of the MHD burst moving the plasma into the RWM non-linearly unstable region. Further supporting evidence of this hypothesis is shown in Fig. 4.4 as it appears that the growth rate of the unstable RWM may be decreasing as the green highlighted time interval is approached, correlated to the field perturbation generated by the second bursting MHD event dying away and the related vanishing of the non-linear unstable region. Then, as the green highlighted time interval is reached, the third bursting event observed apparently not have sufficient field perturbation amplitude to create a significant RWM non-linear unstable region. By the time of the second red highlighted time interval, the plasma finally crosses into the linearly unstable RWM region, and the mode strongly grows continually.

4.1.2: Comparison of NSTX and DIII-D kinetic RWM stabilization physics

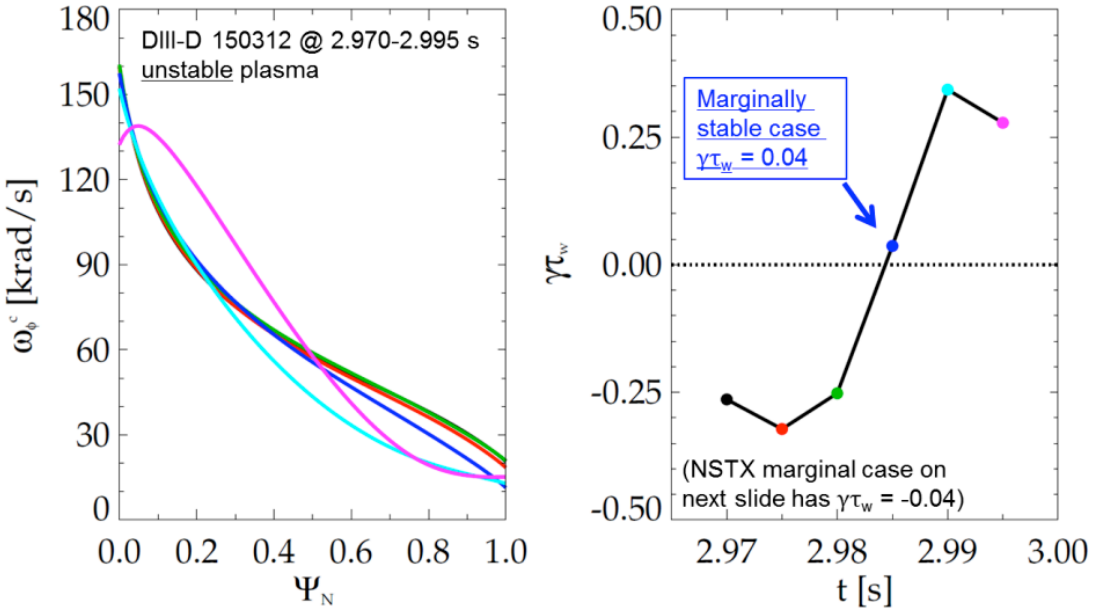

Fig. 4.8: (left) Plasma rotation profile evolution and (right) computed kinetic RWM stability using the MISK code for DIII-D high β_N, high q_{min} plasma suffering a major β_N collapse at t ~ 2.990s. RWM normalized growth rate $\gamma\tau_w > 0$ indicates instability.

The high β_N, high q_{min} target plasma used in the experiment was taken directly from DIII-D shot 150312, and that plasma has been analyzed for kinetic RWM stability. The results are summarized here, and are compared to RWM unstable plasmas in NSTX to determine the dominant physical stabilization mechanisms. The MISK code was used to compute the kinetic RWM stability for DIII-D shot 150312 at the observed experimental RWM marginal stability point with β_N=3.5, q_{min}=2.8. In this case, changes of the kinetic stabilization due to the peaking of the plasma toroidal rotation profile appear to be the dominant cause for the decrease in kinetic RWM stability. The rotation profile evolution and the computation of the crossing of the kinetic RWM marginal stability at the time of a rapid, 60% collapse in the experimental value of β_N is shown in Fig. 4.8.

In addition, the DIII-D experiment has found that reducing q_{min} below 2 experimentally increases the RWM stability of this plasma. The q_{min} variation was also examined for similar DIII-D plasmas in preparation for the present experiment, and the theoretical RWM stability analysis also shows increased stability, which is a combination of both an increase in the ideal and kinetic components of the stability functional δW.

The kinetic RWM stabilization physics of an NSTX plasma experimentally exhibiting an unstable RWM was compared to the equivalent analysis shown above for the recent DIII-D experiment. Many NSTX equilibria that have reached marginally stability have been analyzed for kinetic RWM stability. Here, we choose a plasma at “intermediate” levels of

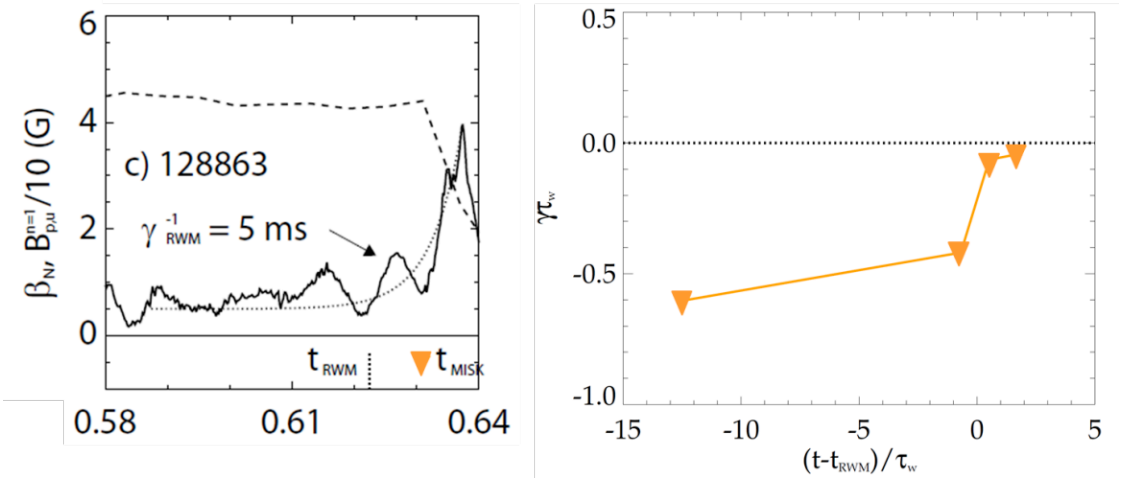

Fig. 4.9: (left) evolution of β_N and n = 1 RWM amplitude and (right) theoretically computed kinetic RWM growth rate for an NSTX high β_N plasma suffering a full current quench disruption.

plasma rotation in NSTX, and with moderately high β_N, which appears to be the least stable combination at relatively high rotation in NSTX [NSTXU-5], and most analogous to the DIII-D plasma. The evolution of β_N and n=1 RWM amplitude are shown in Fig. 4.9 for an NSTX plasma in these conditions that disrupts due to the RWM, along with the theoretically computed kinetic RWM growth rate. The reconstructed equilibria approaching the time of disruption are found to approach the theoretically computed kinetic RWM marginal stability point.

Analysis of the DIII-D and NSTX experimental results summarized above provides a unified understanding of kinetic RWM stability physics in tokamaks based on the kinetic RWM stabilization physics model. The unstable and/or marginally stable modes were found at significant levels of plasma rotation in both devices, and share common dynamics observed during mode growth and rotation. Kinetic RWM stabilization theory is broad enough to explain the observed RWM destabilization in both devices, and an important complementarity has been found in the analysis to date that are part of the underlying theory: stabilization can be dominated by bounce orbit resonance in DIII-D for higher rotation plasmas, but is dominated by ion precession drift resonance in NSTX. This is illustrated for stable plasmas in DIII-D and NSTX, as well as the RWM unstable plasmas shown above. Figure 4.10 shows a comparison of the MISK-calculated imaginary part of the kinetic component of the RWM stability functional δW_K for RWM stable plasmas in DIII-D and NSTX vs. scaled experimental rotation. Here, the abscissa value of $\omega_\varphi/\omega_\varphi^{exp}$=1 corresponds to rotation profile measured in the experiment, and values less than unity correspond to rotation profiles that are scaled self-similarly to lower speeds to extrapolate the analysis. Here, we focus on the experimentally accessed

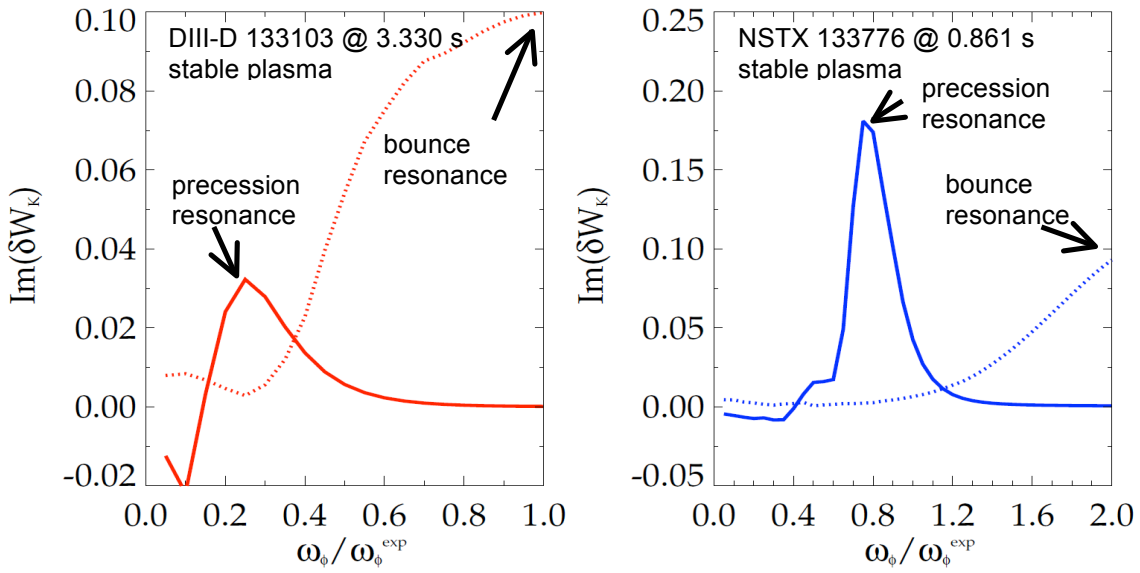

Fig. 4.10: Im(δW_K) vs. scaled experimental rotation DIII-D and NSTX, as calculated by MISK.

rotation profiles ($\omega_\varphi/\omega_\varphi^{exp}$=1). At this relatively high rotation in DIII-D, the stabilizing resonance between the bounce motion of the ions and the plasma rotation is dominant, whereas in comparison NSTX case, the kinetic stabilization due to the ion precession drift resonance is stronger than the bounce resonance stabilization.

A similar comparison of the physics components that create the kinetic stabilization in DIII-D and NSTX is shown in Fig. 4.11 for the unstable plasma described earlier in this section. It is again found that bounce resonance stabilization dominates the DIII-D

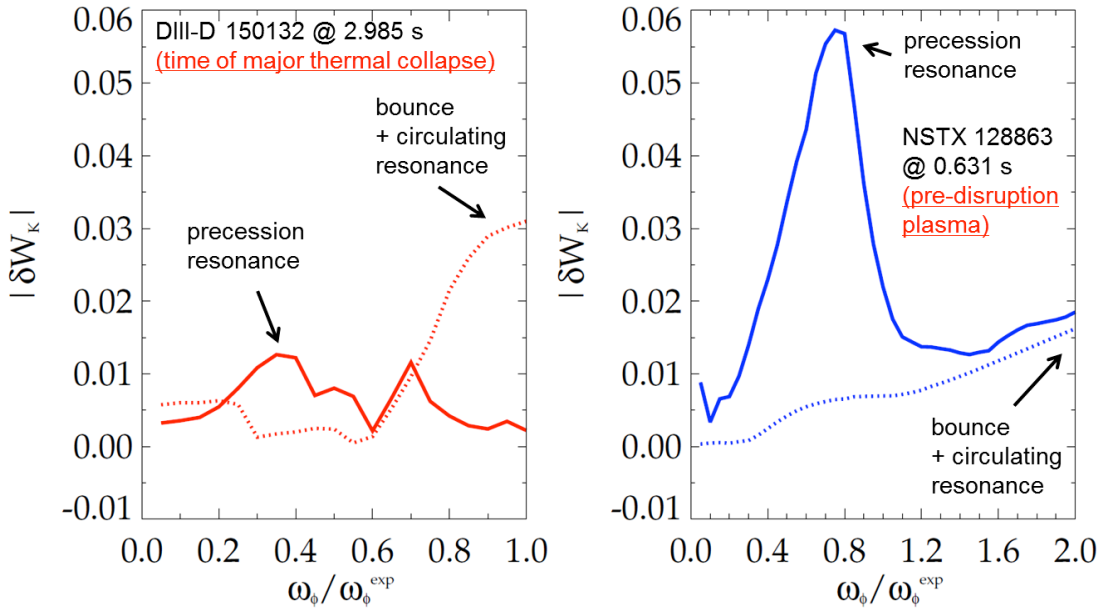

Fig. 4.11: Kinetic RWM stability functional |δW_K| vs. scaled experimental rotation in DIII-D and NSTX, as calculated by the MISK code.

plasma at the relatively high experimental rotation profile, while ion precession drift stabilization is stronger than the bounce resonance stabilization in NSTX.

4.1.3: Kinetic RWM marginal stability in NSTX and DIII-D – comparison of theoretical and experimental stability

The detailed experimental and analysis results above show a unified understanding of kinetic RWM stabilization physics between the devices. Common analysis tools, (e.g the MISK code), were used to analyze the experimental results on both devices. Quantitative agreement was found between theory and experiment of kinetic RWM marginal stability points over a wide range of plasma rotation profile and speed. A decrement was found in the predicted marginal stability point when significant portions of the plasma had zero rotation. Extensive kinetic stability runs were completed and compiled since the last report. The MISK kinetic RWM analysis of the reconstructed DIII-D equilibrium evolutions that reach the marginal RWM stability points in the experiment described above, as well as many NSTX plasmas that either become RWM unstable, or retain stability, are summarized in Fig. 4.12. This single diagram contains a wealth of information that shows for the first time the unification between DIII-D and NSTX high β plasmas regarding RWM stability and associated theoretical computations of kinetic RWM stability. First, we find that plasmas free of other MHD modes can reach linear kinetic RWM marginal stability, and also find that (as published from NSTX experiments for several years now) there is no simple "critical rotation speed" that ensures RWM stability – the plasma can become RWM unstable at high levels of plasma rotation. Trajectories of both DIII-D and NSTX plasma moving from stability to instability experimentally are indicated by the connected dots with arrows indicating the direction of the plasma evolution. Each point represents a unique, reconstructed equilibrium, with kinetic RWM growth rates computed by the MISK code. The computation includes the effects of fast particles on plasma stability. The quantitative level of agreement between experiment and theory regarding the RWM marginal stability points is remarkable. The error in the calculation is $\Delta\gamma\tau_w$~0.2–0.3. Figure 4.12 also shows that global bursting MHD modes can lead to non-linear destabilization before linear stability limits are reached, as described in detail above. This is shown, for example, for the lowest rotation DIII-D case. The plasma terminates in a full current quench disruption, but at the point of the experimental disruption, the calculations shows linear kinetic RWM stability. However, the actual disruption is observed to correlate with the onset of a global bursting MHD mode. It is hypothesized that the RWM is non-linearly destabilized by this bursting event. Note that based on variations of the input equilibrium for the kinetic RWM stability calculation, it is presently not thought that the linear calculation has an error bar

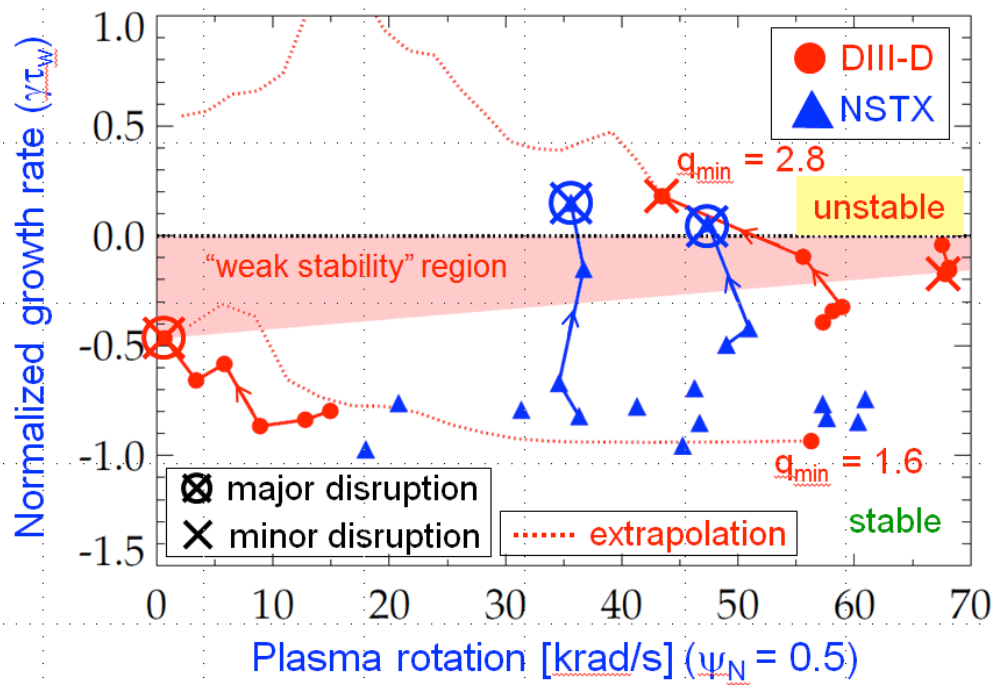

Fig. 4.12: Kinetic RWM growth rate (computed by the MISK code) normalized to the conducting wall eddy current decay time for NSTX and DIII-D plasmas suffering RWM instability, and also plasmas that are stable, as a function of plasma rotation speed.

large enough to allow the plasma to be linearly unstable. Therefore, the actual experimental point of destabilization below the linear marginal stability point defines a region of "weak stability", which has been reported in past experimental studies on DIII-D [NSTXU-10]. The present experiment quantifies for the first time the level of $\Delta\gamma\tau_w$ that defines this weak stability region below the computed linear RWM marginal stability point. Comparing DIII-D results at the extremes of rotation in Fig. 4.12, is appears that the magnitude of $\Delta\gamma\tau_w$ defining the weak stability region decreases as the plasma rotation increases. Finally, the dotted lines in Fig. 4.12 represent kinetic RWM stability calculations based on experimental DIII-D equilibrium reconstructions of the experimental high β_N, high q_{min} plasmas with the toroidal rotation profile self-similarly varied from high to low rotation. In this study, we find that these plasmas are less stable as q_{min} increases, and that marginal stability is bounded by $1.6<q_{min}<2.8$ over the full range of plasma rotation scanned. It is noteworthy to state that the extrapolation at q_{min}=1.6 remarkably connects up smoothly from the plasma at high rotation to the plasma at low rotation – a different plasma shot – but with nearly the same q_{min} (1.7 in the experimental plasma at low rotation).

4.2: Development of reduced models for fast ion transport

Several numerical tools have been improved and validated against NSTX and DIII-D data to provide a more accurate description of the fast ion evolution in NB-heated plasmas. Those models have been developed to provide quantitative predictions of fast ion evolution also for scenarios with instabilities causing enhanced fast ion transport. Instabilities range from toroidal Alfvén eigenmodes (TAEs) and other Alfvénic instabilities to lower frequency MHD and energetic particle-driven modes such as long-lived kink modes, fishbones and EPMs. To complement ongoing work on DIII-D and NSTX data, the improved modeling capabilities are ready for validation with data from dedicated NSTX-U experiments. Experimental plans have been finalized for the next NSTX-U experimental campaign after machine re-commissioning, see Sec. 4.8.

4.2.1: Critical Gradient Model (CGM)

A "critical gradient" model (CGM) is being validated against NSTX experiments in addition to its preliminary validations against DIII-D data [NSTXU-11][NSTXU-12]. Among the NSTX plasmas available for the analysis, discharge #141711 with reversed

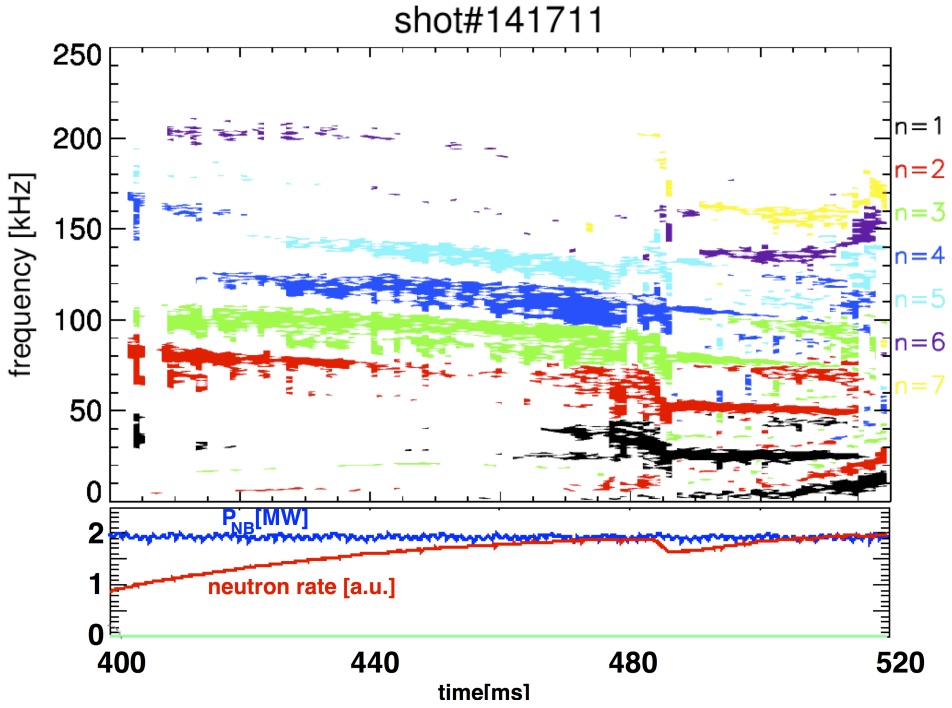

Fig. 4.13: Mirnov coil measured and analyzed magnetic field oscillations spectrum vs time in NSTX discharge #141711. Shown to the right is the color coding for toroidal mode numbers. Bottom insert depicts the NBI injected power (blue curve) and neutron flux evolution (red curve, in normalized units).

magnetic shear profile was chosen. It is characterized by the presence of several instabilities driven by beam ions in the TAE range of frequencies [NSTXU-13]. Instabilities have low to medium toroidal mode number ($2<n<6$) and feature characteristic frequency chirps on a millisecond time scale.

Figure 4.13 shows the evolution of different signals. Toroidal mode numbers are color coded in the figure as indicated. The observed modes are not virulent instabilities, despite the chirping behavior toward the end of the discharge when a TAE *avalanche* event occurs. The choice of this shot is made due to its relatively benign AE activity for NSTX, which transforms to the avalanche at t=480 ms. Note that the CGM is not applicable beyond t=480 ms, as the physics of EP transport in the avalanche is far more complicated than the model implies.

In the application of CGM to the NSTX data, a version of the model based on the normalization of the AE growth rates to NOVA-K [NSTXU-14] computed increments was used. The nomalization constants are derived using the TAE mode structures at four to five radial points, r/a ≃ 0.1, 0.3, 0.5, 0.7 and 0.9. They are chosen by finding the locations of the maximum values of the growth rates. Between those locations, a linear interpolation formula was used. An analytic expression for growth and damping rates is employed outside that range. Figure 4.14 presents the results of the model predictions

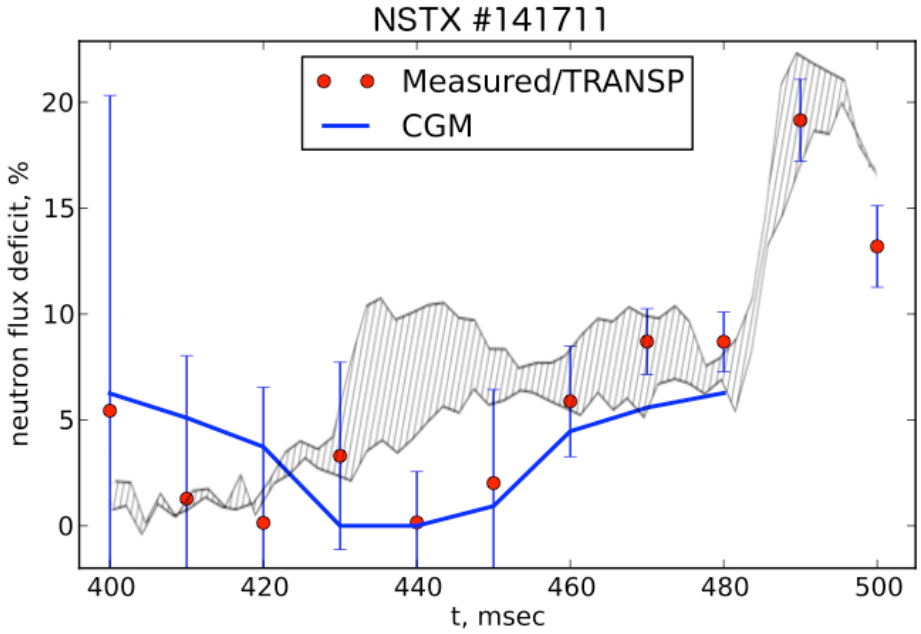

Fig. 4.14: Neutron deficit as computed by the TRANSP code for NSTX #141711 (red dots) and comparison with the predictions by the CGM (blue line). At t=480 ms, a TAE avalanche occurs (cf. Fig. 4.13) beyond which CGM could not be applied. The dashed region shows results from the "kick" model recently implemented in NUBEAM/TRANSP, see Sec. 4.2.3.

against the NSTX data. Considering experimental uncertainties in the absolute calibration of the neutron detectors, the CGM predictions are within the error bars of the measurements. Overall, the CGM validation exercise against the NSTX experimental data results looks promising and warrants a confidence in its possible predictions. The validating exercise ensures that the quasilinear approach targeted within PPPL is an appropriate method for future research in the EP area.

It is expected that CGM may not be confidently applicable to regimes for which a perturbative approach is not adequate. This is the case, for example, for a test DIII-D scenario with high q_{min} (discharge #153072), for which CGM underpredicts the neutron deficit by the factor of ~2. The question emerges whether the model is applicable, since earlier studies suggest that non-perturbative explanations should be brought [NSTXU-15]. A new version of CGM has been developed to account for the nonperturbative excitation of various modes - including TAEs - when their drive is strong and a perturbative approach would fail. The HINST code (HIgh-N STability code, [NSTXU-16][NSTXU-17]) is available for that purpose and was applied for the DIII-D case. The code solves the system of equations in the ballooning variable to find the mode structure and its net growth rate non-perturbatively. As an example, it is applied to a DIII-D plasma where the drive reaches $\gamma/\omega \sim 0.3$ locally and the application of the perturbative NOVA-K results is questionable. HINST computed net growth and damping rate are used for nCGM normalization where the linear interpolation was used again between the computed values of the growth rates. Here 20 radial points provided the growth and damping normalization points.

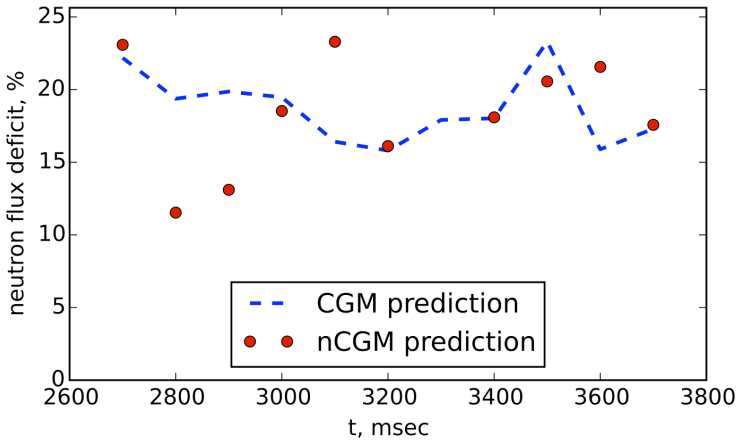

Fig. 4.15: Comparison of the CGM and nCGM predictions for DIII-D test case, discharge #153072. The deficit should be compared with the experimentally obtained deficit using classical computations by the TRANSP code.

The results of the DIII-D validation show that the predictions of both CGM and nCGM are close to each other, see Fig. 4.15. They are also close to the neutron flux deficit independently computed through a "kick" model (see Sec. 4.2.3 below) when the same type of modes (e.g. TAEs) are considered. Note that the non-perturbative CGM can not be used in NSTX though since nCGM normalization is based on HINST code results which is a high-n ballooning code and can not be justified for typical NSTX conditions.

4.2.2: Extension of the ORBIT code for mode saturation amplitude estimates

A combination of analytic models and the particle-following numerical simulation code ORBIT is being developed to find the saturation levels of unstable Alfvén modes and the resulting effect on beam and alpha particle distributions [NSTXU-18]. The initial unstable mode spectrum and eigenvalues are supplied by the NOVA code, then time evolution of these modes to saturation is computed with the guiding center code ORBIT. Solving the drift kinetic equation with a guiding center code in the presence of Alfvén modes driven unstable by a distribution of high energy particles requires the use of a δf formalism. The initial distribution, f_0, is assumed to be a steady state high energy particle distribution in the absence of the modes, and $f=f_0+\delta f$ describes the particle distribution in the presence of the modes. The Hamiltonian is written as $H=H_0+H_1$ with H_0 giving the unperturbed motion, conserving particle energy E, toroidal canonical momentum P_ζ, and magnetic moment μ. By writing the initial particle distribution in terms of these variables, a simple means of calculating mode-particle energy and momentum transfer results, providing a very accurate δf formalism. The numerical beam deposition code NUBEAM in TRANSP produces a list of particles, giving energy, pitch, and location, which can be used to find the unperturbed distribution $f_0(E,P_\zeta,\mu)$. The effect of unstable Alfvén modes on high-energy particle distributions is being examined for NSTX [NSTXU-18], and will then be extended to DIII-D and ITER scenarios.

4.2.3: "Kick" model implementation in TRANSP/NUBEAM

A reduced model for fast ion transport ("kick" model [NSTXU-19]) has been implemented in TRANSP [NSTXU-20] and tested against NSTX and DIII-D data [NSTXU-21]. Initial results compare well with experimental results and with predictions from the "critical gradient" model, cf. Fig. 4.14. Extensive validation is ongoing, suggesting further improvements to the model. One key issue to resolve is to improve the model implementation in the NUBEAM module of TRANSP. For instance, in its first implementation the model was applied in between macroscopic NUBEAM time steps

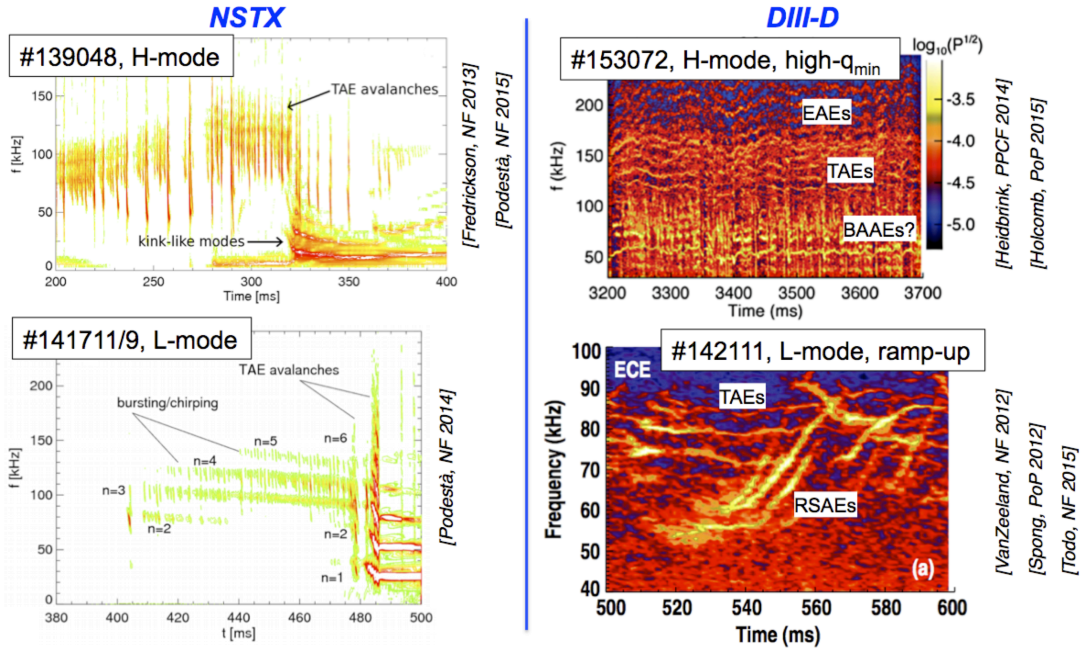

Fig. 4.16: Spectra of fluctuations as a function of time and frequency for the 5 cases selected for a combined NSTX/DIII-D study of fast ion evolution modifications by instabilities. Data from NSTX are obtained from magnetic sensors at he plasma edge. Data from DIII-D are obtained from a CO2 interferometer. All discharges feature Alfvénic activity in the toroidal Alfvén eigenmode range of frequency. Other MHD instabilities are also observed for some of the discharges.

[NSTXU-19]. This resulted in under-estimated losses for particles that are near a loss boundary. Work is in progress to merge the model in the "orbiting" section of NUBEAM, so that classical mechanisms (scattering, slowing down) and additional transport can be treated on similar time scales. Once validated, this model is expected to provide more accurate simulations of the fast ion phase space evolution, which enables more quantitative predictions of quantities such as NB current drive and power exchange between fast ions and thermal populations (cf. next Section).

4.3: Current drive and fast ion modeling in the presence of instabilities

Enhanced fast ion transport caused by instabilities can be detrimental for the operation of fusion devices such as ITER and a Fusion Nuclear Science Facility. Increase in fast ion losses reduces the fusion efficiency, affects the controllability (and predictability) of quantities such as Neutral Beam (NB) driven current and may cause harm to in-vessel structures. It is therefore important to develop and validate modeling tools that enable accurate predictions of fast ion transport in future devices. Examples of improved modeling tools have been discussed in the previous Sections. In this Section, the "kick

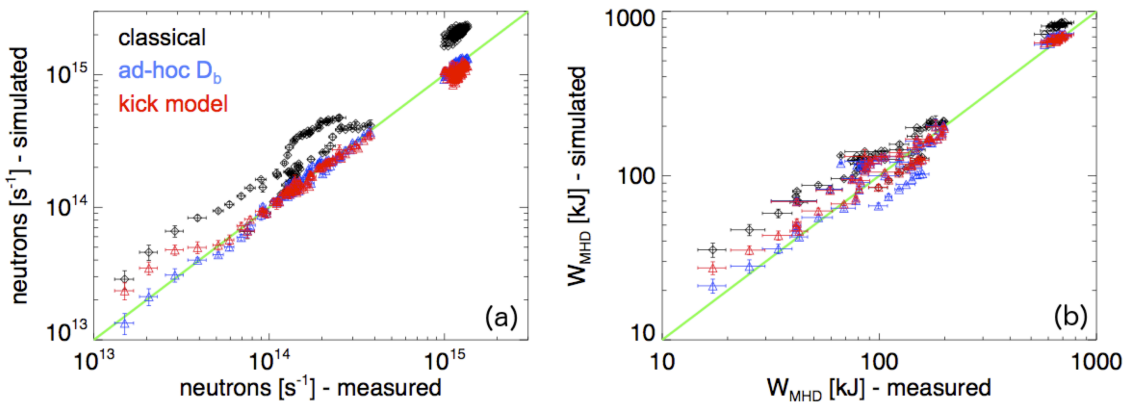

Fig. 4.17: Results from adjusting the time-varying diffusivity D_b (ad-hoc diffusive model) and the mode amplitude scaling factor (kick model) to match (a) the measured neutron rate and (b) the stored energy, W_{MHD}, computed by the EFIT equilibrium reconstruction code.

model" implemented in TRANSP is applied for a preliminary analysis of NB-heated NSTX and DIII-D discharges [NSTXU-21]. The two main goals are (i) to compare predictions of the model for a variety of plasma scenarios and (ii) to compare results from the kick model with those obtained from a simpler (purely diffusive) model. The latter assumes the radial fast ion density gradient as the only drive for fast ion transport, therefore it lacks of the capability to resolve phase space modifications of the fast ion distribution function.

4.3.1: Experimental scenarios and analysis procedure

The discharges analyzed in this study have been selected to encompass a variety of NB-heated plasma scenarios, including L- and H-mode plasmas, ramp-up scenarios and a high-q_{min}, nearly steady-state discharge (Fig. 4.16). All discharges feature robust Alfvénic activity. Other MHD instabilities (kink-like modes and NTMs) are also present in some cases. For each discharge, three TRANSP runs are performed to compile a database with relevant quantities such as neutron rate, stored energy, NB driven current, fast ion density. The three runs refer to "classical" analysis without any additional fast ion transport included; analysis with a time-dependent, spatially uniform fast ion diffusivity (called "ad-hoc model" in the following and in the figures); analysis with the phase space resolved "kick model" to simulate fast ion transport.
For the ad-hoc model, the diffusivity D_b is adjusted as a function of time to give a good match between simulated and measured neutron rate and stored energy (W_{MHD}, reconstructed through the EFIT code for equilibrium reconstruction) cf. Fig. 4.17. A similar procedure is here adopted to adjust the amplitude scaling factor for each mode included in the kick model. Starting from the experimental mode amplitude - when available -, corrections are applied iteratively to optimize the match with neutrons and

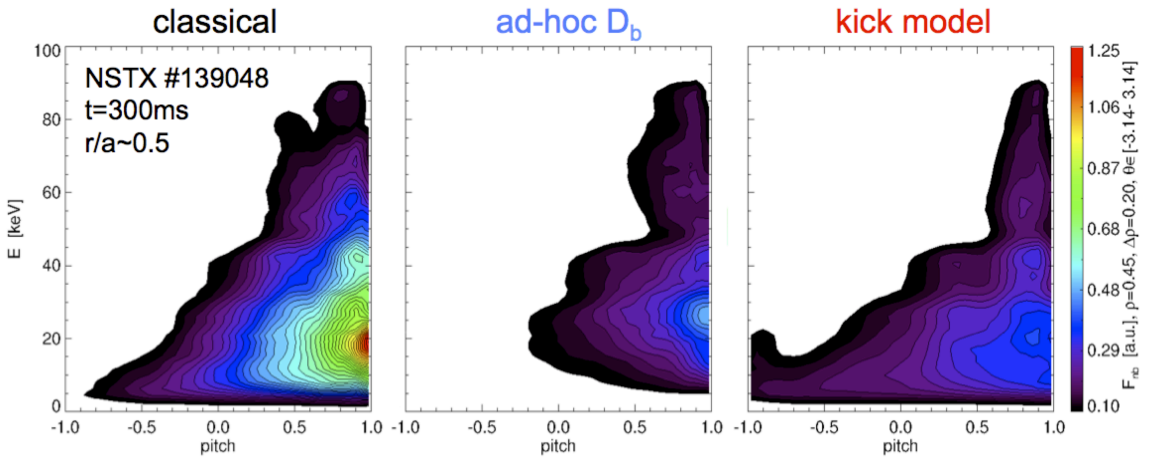

Fig. 4.18: Fast ion distribution function computed through TRANSP/NUBEAM for NSTX #139048 at t=300ms. The three cases refer to simulations assuming "classical" fast ion physics, a simple diffusive model for fast ion transport and the new kick model.

W_{MHD}. Results of this procedure are also shown in Fig. 4.17, which compares the measured neutron rate and W_{MHD} with the results for the three TRANSP runs for all discharges. As it can be seen from the figure, "classical" runs tend to overestimate neutrons and stored energy. This is an indication that fast ion transport is enhanced by instabilities, resulting in decreased fast ion confinement. Overall, both the "ad-hoc" and "kick" models are capable to recover the drop in the measured quantities within the experimental uncertainties.

4.3.2: Modifications of the fast ion distribution

A first indicator of the effects of instabilities on the fast ion population is provided by the fast ion distribution function computed by TRANSP. Figure 4.18 shows an example from a NSTX discharge with unstable TAEs that develop into so-called *avalanches*, i.e. large amplitude bursts of the modes followed by drops in the measured neutron rate and enhanced losses. Effects of the instabilities are clearly not taken into account in the "classical" TRANSP run, which serves as reference for the analysis with the two other models.
Consistently with the decrease in neutron rate and stored energy, additional fast ion transport causes a reduction in the core fast ion content. However, significant differences are observed when the simple diffusive model or the kick model are used. In the first case, the entire distribution is reduced by a similar amount, regardless of energy or pitch of the fast particles. For the kick model, some regions of the distribution suffer a larger depletion than others. More specifically, higher energy co-passing particles are transported more efficiently, whereas the lower energy part of the distribution appears almost unaffected. This is consistent with the fact that co-passing particles are the ones

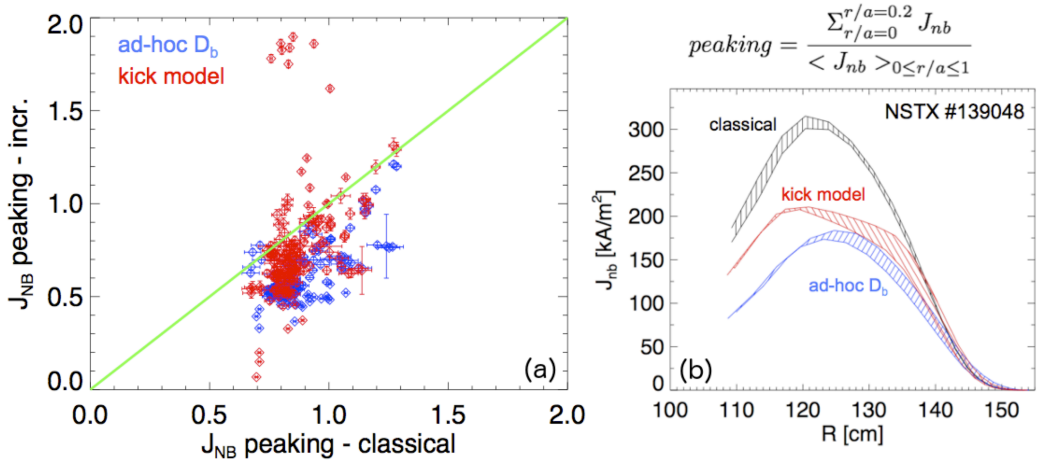

Fig. 4.19: (a) NB driven current peaking with respect to "classical" TRANSP simulations for the entire NSTX/DIII-D database. (b) Example of radial profiles of J_{NB} for a NSTX scenario with TAE avalanches.

driving the instabilities, and therefore are more prone to be affected by the modes. These observations can be expected to imply differences for other quantities that result from integrals of the fast ion distribution over energy.

4.3.3: Broadening of fast ion density and NB-driven current profiles

Experimentally, Alfvénic instabilities are known to cause flattening and reduction in the fast ion density, n_b. Information on the radial profile of the NB driven current is much more difficult to obtain directly from the experiments, and analysis through codes such as TRANSP is required. Figure 4.19 shows a comparison of the peaking factor computed for the NB driven current, J_{NB}, based on the three assumptions for fast ion transport. The peaking is computed as the ratio between central current to its average over the entire

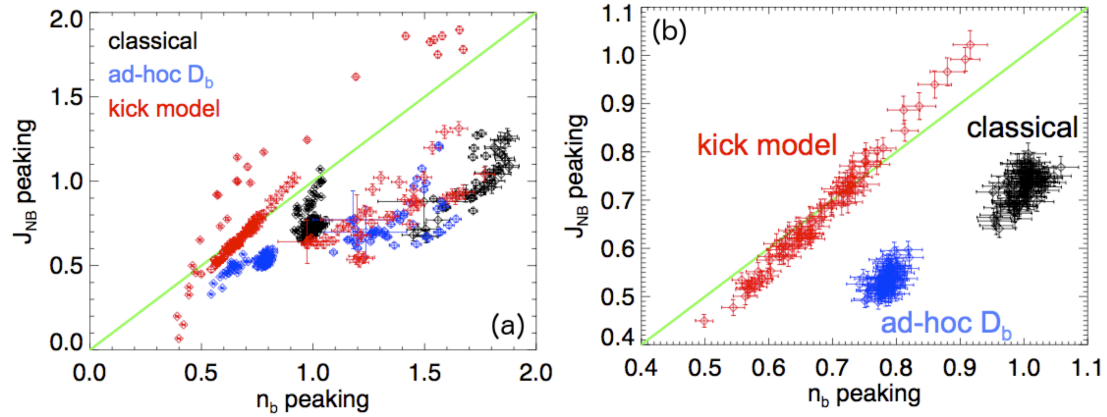

Fig. 4.20: (a) Analysis of the combined fast ion density and J_{NB} evolution through correlation of the peaking factor of current and fast ion density. (b) Details for DIII-D discharge #153072, showing the correlation that emerges from simulations with the kick model.

minor radius. As a general result from the NSTX/DIII-D database, the peaking is reduced by up to a factor 2 with respect to "classical" simulations without additional fast ion transport. The two transport models predict a comparable broadening of the J_{NB} profile. However, as expected from the differences observed in the fast ion distribution functions, the radial profiles obtained with the two models can be different (Fig. 4.19b). This results from the phase space selectivity of the kick model, not present in the ad-hoc model. Further differences in the TRANSP results are observed from a combined analysis of the evolution of fast ion density and NB driven current profiles, see Fig. 4.20. A broadening is predicted in both quantities, with significant reduction of the fast ion density peaking. A main difference for the two transport model is the correlation between J_{NB} and fast ion density evolution predicted by the kick model. Figure 4.20b shows an example from a high-q_{min}, nearly steady-state DIII-D discharge, for which J_{NB} and n_b peaking align along a straight line. More analysis is required to assess the generality of these results. However, they suggest that the correlation between energy and canonical angular momentum changes induced by resonant instabilities, which is included in the kick model, is important for quantitative predictions of scenarios with NB current drive.

4.3.4: Implications for the assessment of NB current drive efficiency and power balance

A summary of the results from the combined NSTX/DIII-D analysis is presented in Fig. 4.21. The NB current drive efficiency with respect to "classical" simulations is shown as a function of the computed deficit in neutron rate. (Since the deficit is roughly proportional to the amount of Alfvénic activity, the x-axis can be taken as an indicator of the severity of the instabilities). For the cases considered here, up to 60% neutron rate

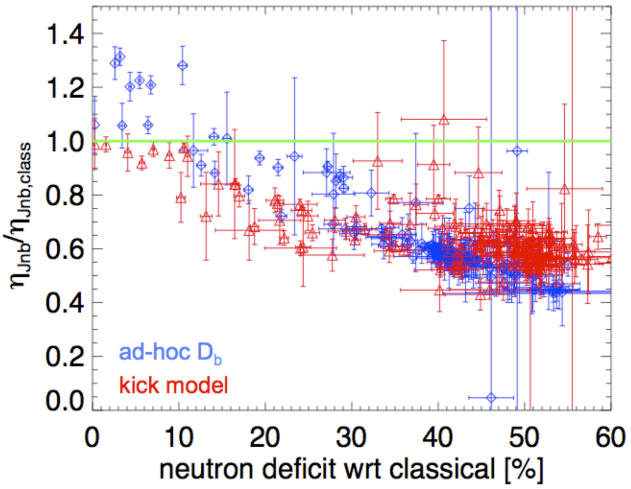

Fig. 4.21: Summary plot of NB current drive efficiency with respect to "classical" simulation, shown here as a function of the computed neutron rate deficit. The latter is taken as a proxy for the level of mode activity.

deficit is observed, which translates in an overall reduction of NB current drive efficiency by 20-60%. The large reduction indicates that these effects must be taken into account for accurate modeling and interpretation of the experimental data. Furthermore, the material presented in the previous Sections also suggests that a correct treatment of the fast ion evolution is required, possibly including phase space effects when resonant instabilities are observed.

These conclusions do not only apply to the study of fast ion dynamics and their effects on NB-CD efficiency, but are also of broader interest for integrated modeling. For instance, Fig. 4.22 reports the results for the computed power transferred from the NB ions to the thermal electron population through thermalization for the same database discussed above. When additional fast ion transport is included in the simulation, a reduction of ~2 in the power with respect to "classical" simulations is computed. Similarly to the results for NB driven current profiles, the overall reduction is comparable for the two transport models compared here, but the radial profiles can be substantially different. This large difference in source terms can lead to even more profound differences in a power balance analysis, e.g. to estimate the local thermal diffusivities.

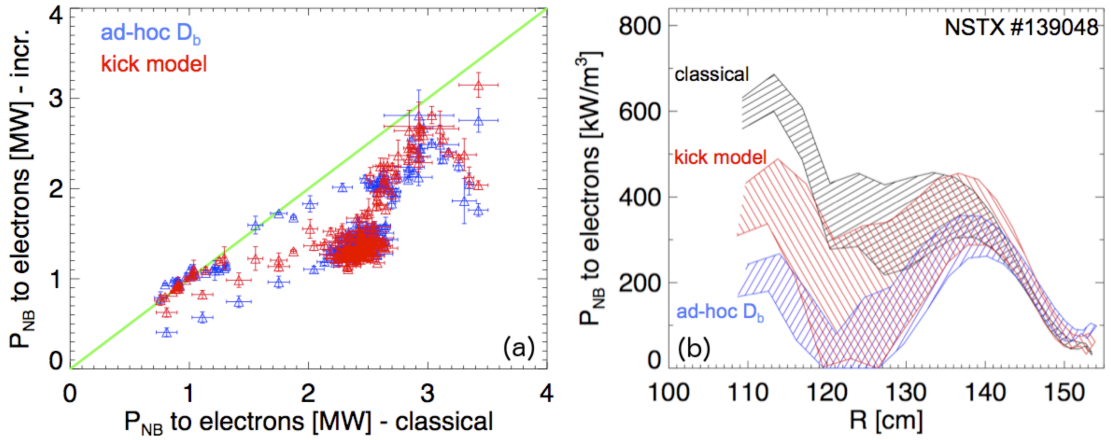

Fig. 4.22: (a) Total NB power transferred to the electrons through thermalization with respect to "classical" predictions. (b) Detail of the radial profile of power to electrons for NSTX discharge #139048, showing the differences in the profiles inferred using the different models.

4.4: Validation of LH-CD modeling through time-dependent simulations

4.4.1: C-Mod target scenario, diagnostics and modeling assumptions

Validation of Lower Hybrid Current Drive calculations through time-dependent simulations has several advantages. The evolution in time of simulated quantities, like the free-boundary current profile, the surface voltage and the Hard X Ray (HXR) emissivity profile from a synthetic diagnostic in the CQL3D code, can be compared with the measured V_{loop}, HXR profile and the plasma current reconstructed from MSE pitch angle measurements for an extended set of conditions. This integrated approach can unravel inconsistencies between measurements and calculations and identify where improvements to either modeling tools or measurements are needed [NSTXU-22]. For this LH-CD validation study, the analysis indicates a complex interplay between diagnostic uncertainties and modeling approximations. Initial results of the validation exercise suggest that no strong claims can be made on the agreement (or disagreement) between measured and calculated quantities, mainly because of the many sources of uncertainties in the data analysis and simulation process.

Time traces of a C-Mod plasma discharge selected to illustrate the validation procedure are shown in Fig. 4.23. This discharge has 0.6 MW of absorbed LH power between 0.9 s and 1.8 s. The phasing of the antenna is changed to decrease the launched $n_{//}$ from 2.5 down to 1.6 in four steps, as reported in the figure's caption.

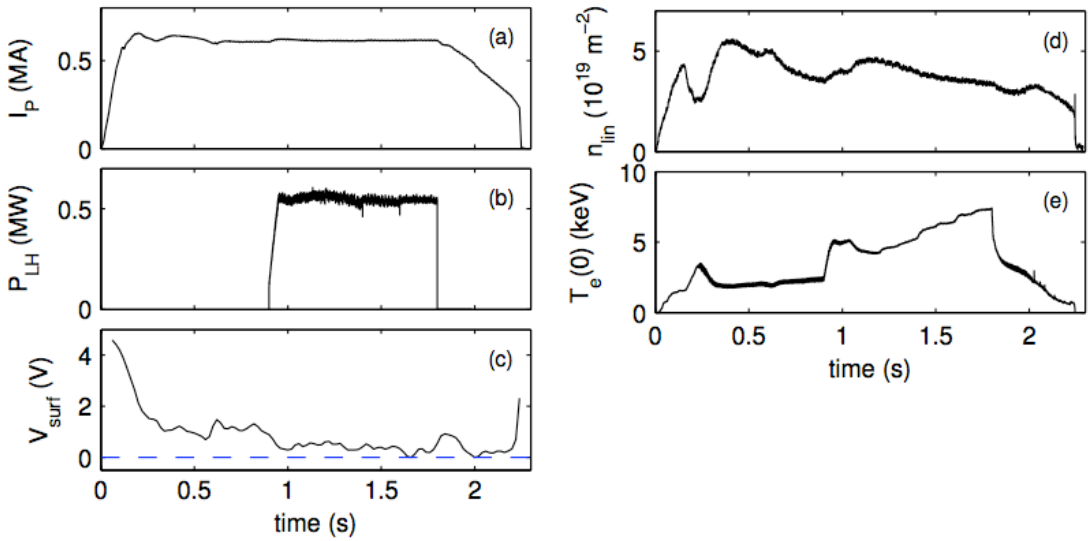

Fig. 4.23: Waveforms for discharge 1120912028. (a) plasma current, (b) LH input power, (c) surface voltage, (d) line averaged density, (e) central electron temperature from the GPC diagnostic. The LH injection period is divided in four phases depending on the injected spectrum: phase I, 0.9<t<1.2s, has $n_{//}$=2.5; phase II, 1.2<t<1.4s, has $n_{//}$=2.2; phase III, 1.4<t<1.6s, has $n_{//}$=1.9; phase IV, 1.4<t<1.6s, has $n_{//}$=1.6.

Several modeling tools have recently become available in the TRANSP code for validating LH-CD studies. The ray-tracing code GENRAY has been coupled with the 2D Fokker-Planck code CQL3D for high-fidelity calculation of LH heating and current drive. GENRAY is a generalized 3D optical ray tracing code that traces the LH waves as they propagate into the plasma. It is coupled with an adjoint calculation for the LH current drive efficiency. GENRAY includes a description for poloidally distributed LH waveguide grids by distributing rays along the full vertical extent of the launcher. This is crucial for accurate simulation of the LH wave propagation and absorption, since the parallel wavenumber evolution of LH ray trajectories is sensitive to their initial poloidal launch point. CQL3D is a bounce-averaged Fokker-Planck code. It takes the flux- surface averaged quasi-linear diffusion coefficient from GENRAY as an input and calculates the electron distribution function depending on input LH wave fields, toroidal electric field, collisional slowing-down and pitch angle scattering. The distribution function is solved for in three dimensions, i.e. radius, velocity and pitch angle. At each time step, the ray paths calculated by GENRAY are used as input for CQL3D to re-calculate the quasi-linear diffusion coefficient based on the most recent CQL3D calculated electron distribution function, and to advance the distribution function in time.

4.4.2: Validation of LH-CD models against experiments

Time-dependent simulations of LH current drive have been run with TRANSP. The total current is used as a boundary condition in the fix-boundary and in the free-boundary evolution of the poloidal field diffusion equation. The simulation uses measured coil currents and a feedback control on the radial and vertical position. The last closed flux surface is used as a reference for the convergence of the free-boundary solution. The measured loop voltage, V_{loop}, is assumed to be a 'trusted' measurement that is compared with the calculated V_{loop}.

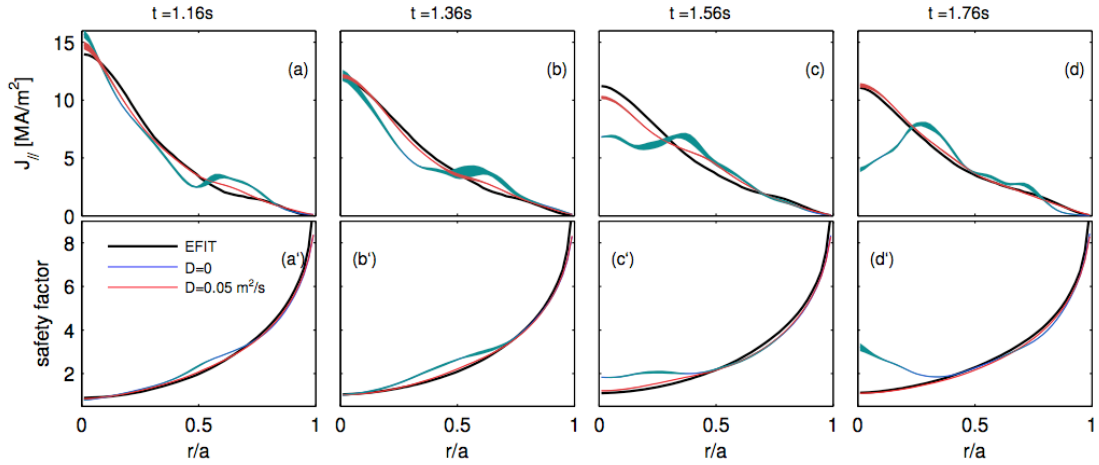

Fig. 4.24: Top row: plasma current profiles. Bottom row: safety factor profiles. From left to right, profiles are calculated at (a) 1.16s (b) 1.36s (c) 1.56s (d) 1.76s. Different curves refer to the constrained profiles from MSE-EFIT (black), calculations with no radial diffusion (blue) with D=0.01 m^2/s (green) and with D=0.05m^2/s (red).

Since ion temperature measurements are not available, ion temperature is calculated under the assumption of neoclassical ion thermal transport. Ion temperature profiles are then rescaled to satisfy the total (measured) neutron rate. For electrons, the experimental electron density and temperature profiles are prescribed as a function of time. The deuterium background ion density is calculated from quasi-neutrality based on two different measurements of Z_{eff}. Since direct, calibrated measurements of the plasma Z_{eff} are not available for this discharge, Z_{eff} is inferred from measured radiation profiles. Since the LH current efficiency is inversely proportional to Z_{eff}, the effect of different Z_{eff} assumptions on the calculations has been assessed. Simulation results suggest that (i) Z_{eff} has minor effect in the calculation of the LH current (except perhaps at low values of $n_{//}$); (ii) matching the measured V_{loop} is not a sufficient criterion to discriminate between different assumptions on Z_{eff}. Finally, no kinetic profiles are available outside the last closed flux surface, which introduces further uncertainties related to LH wave propagation in the SOL.

As an example of the results obtainable from this analysis, Figure 4.24 compares the profiles of total parallel current and of the safety factor calculated in free-boundary calculations, with profiles from EFIT reconstructions constrained by the MSE diagnostic (black, thick curve). Two cases are shown for the free-boundary calculations, one with no radial diffusion in CQL3D and one with a radial diffusion of D=0.05 m^2/s. The latter is the value needed to reproduce the current profile at all times in the simulation, in particular to reproduce the monotonic q-profiles during phase III and IV (corresponding time intervals are given in the caption of Fig. 4.23). This value is close to the range of

D=0.01−0.04 m^2/s previously inferred from experiments with LH power modulation [LH-2, LH-3] and to the value of D = 0.04 m^2/s inferred from a comparison with HXR emission and with the total current in experiments with fully non-inductive current drive [NSTXU-25]. Note that a radial diffusion coefficient of D=0.01 m^2/s would still predict a hollow current profile and a reversed-shear q-profile. However, the best agreement with the current profile does not provide the best agreement with the HXR profiles. These are better reproduced by choosing a radial diffusion coefficient of D=0.01 m^2/s, at least during phase I-II. A value of D=0.05 m^2/s would predict profiles too peaked at all times. It is interesting to note that the HXR profiles during phase III-IV cannot be reproduced under any assumption on the radial diffusion coefficient. In all cases, even without radial diffusion, an excess of photon counts is predicted by the synthetic diagnostic in CQL3D on the central channel and a depletion of counts on the peripheral channels.
The surface voltage is overestimated in all cases with finite radial diffusion. Since it is reasonable to assume a finite level of radial diffusion based on previous experiments [LH-2, LH-3], four main questions arise to improve the confidence in the available simulation tools and their use for analysis of experimental scenarios:

1. What causes the over-peaking of the HXR synthetic diagnostic?
2. What causes the overestimate of the surface voltage?
3. What are the uncertainties in the reconstructed equilibrium and current profile from the MSE diagnostic?
4. What are the uncertainties in the free-boundary equilibrium calculations in TRANSP?

Overall, the simulations indicate evidence of a complex interplay between many different elements. Uncertainties in the input plasma parameters, in the LH model and in the transport solver combine to - and in some cases compensate - each other. The correct answer should be derived from a comparison among all available quantities (from the experimentally available data and from the simulations) to identify inconsistencies and to address limitations of the model. Although the LH current drive efficiency explicitly depends on the plasma composition Z_{eff}, it is found that this parameter has a minor effect on the HXR profiles calculated in CQL3D. Small differences are found for flat or peaked profiles, as well as for a 50% difference in the amplitude. The largest effect in the LH calculations is due to the magnetic field (equilibrium) topology. Small differences in the plasma boundary can have a large effect on the HXR profile. The other largest effect is due to the plasma edge. These results indicate a need for a more accurate treatment of the SOL plasma in the simulations, which should take into account 2D variations of the density and temperature in the SOL.

Results also indicate that ray tracing, being an initial value problem, might be insufficient for model validation. Full wave codes, which take into account the wave propagation between the antenna and the plasma, are instead free from these problems and represent a more appropriate tool. Because they are computationally intensive, however, these codes are not yet available for time-dependent calculations of LH waves.

4.5 Characterization of impurity profiles and transport

Accurate measurements of impurity profiles and transport are required for a quantitative assessment of power balance (through the radiated power) and effective plasma composition, Z_{eff}. The latter is used in the interpretation of non-inductive current profiles through the neoclassical diffusivity. Recent upgrades to the NSTX-U diagnostics providing 1D and 2D measurements of radiated power are presented in Sec. 4.5.1, and their interpretation discussed in Sec. 4.5.2. Those sections are largely based on the material discussed in Refs. [NSTXU-26]-[NSTXU-27]. Section 4.5.3 summarizes an example of interplay between non-inductive current and impurity profiles from LHCD scenarios on C-Mod. These studies are planned on both NSTX-U and C-Mod to assess the role of impurities on plasma performance, focusing on non-inductive current drive scenarios. Preliminary results from impurity transport studies through laser blow-off [NSTXU-28] for C-Mod scenarios with LHCD are presented in Sec. 2.3.

4.5.1 Upgraded radiated power measurements on NSTX-U

The bolometric diagnostic in NSTX-U has been upgraded to enhance the midplane coverage and radial resolution with two tangential views. The addition of a new set of poloidally-viewing arrays is being also considered to measure the 2D radiation distribution.
A compact diagnostic [NSTXU-26] has been installed at the equatorial midplane of a tangential port. It will measure the 1D radial structure of the photon emissivity profile in

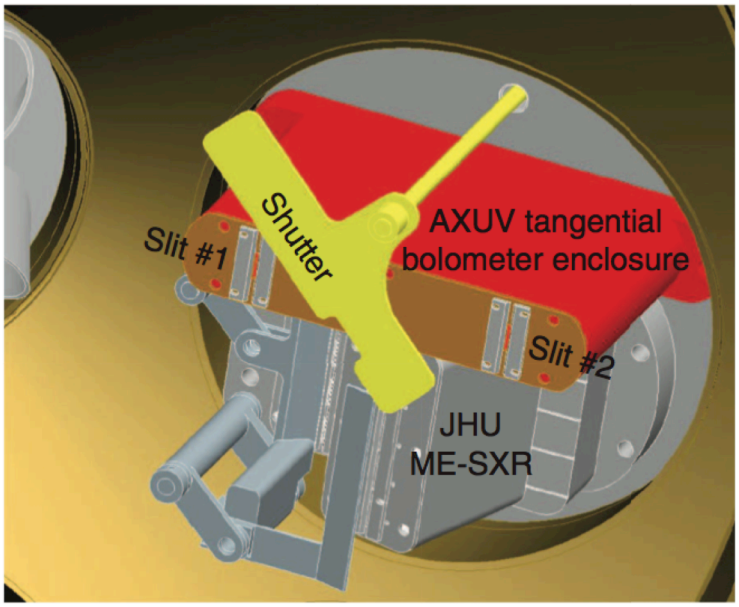

Fig. 4.25: Top view of the high-resolution tangential AXUV diode array designed for NSTX-U (from Ref. [NSTXU-26]).

order to infer edge and core power balance, as well as impurity transport and MHD studies. A schematic of the diagnostic is shown in Fig. 4.25.
The new arrays will measure line and continuum emission from the plasma with photon energies of few eV up to 10 keV, therefore the signal to noise ratio will depend strongly on the local electron and impurity density as well as the plasma temperature.
In addition to the tangential system, a new two-dimensional set of pinhole cameras are being developed to tomographically reconstruct the radiated power on a single poloidal plane [NSTXU-27]. The proposed system consists of three cameras utilizing photodiodes to image the plasma from separate locations. Each camera is designed utilizing one AXUV diode array composed of 20 vacuum-ultraviolet measuring silicon diodes. The diodes provide fast time response, robustness in tokamak environments, and wide spectral sensitivity.

4.5.2 Interpretation of impurity measurements including poloidal asymmetries

A synthetic diagnostic capability has been developed to estimate the response of both the 1D tangential AXUV diode array and the 2D poloidally viewing system described in Sec. 4.5.1. The local radiated power density profiles are modeled using hydrogenic Bremsstrahlung and cooling rates for the intrinsic impurities of choice (for example, C and Fe). Profiles of electron, ion and impurity densities measured at the midplane are remapped in 2D based on EFIT reconstructed equilibrium. Poloidal asymmetries are computed based on the effects of centrifugal forces. The diagnostic response is then simulated based on amplifiers' gain and diode response, in addition to the actual geometry and lines of sight of the array. Combining the information on profiles and

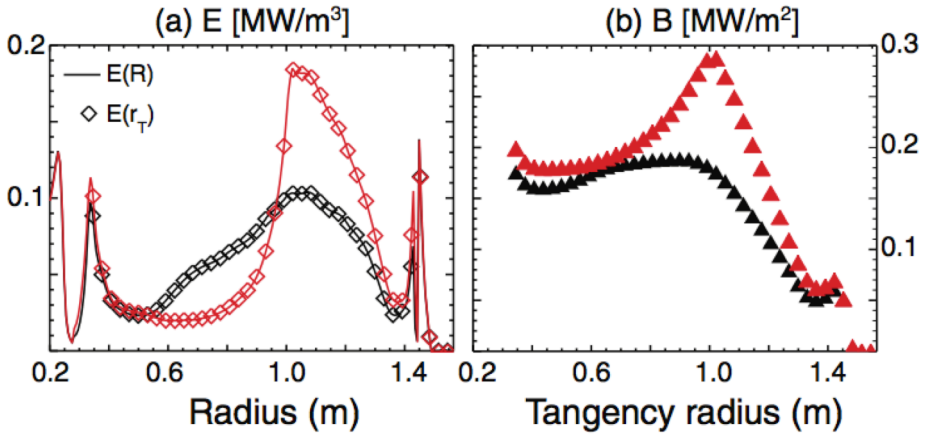

Fig. 4.26: (a) Midplane emissivity and (b) integrated brightness from Fe emission computed for the same background profiles without (black) and with (red) centrifugal effects included (from Ref. [NSTXU-26]).

system response, the integrated brightness is calculated from the local emissivity. Corrections are included for the highly non-linear AXUV diodes response for energies 1-100eV. This correction is important to account for radial variations of the impurity profiles, e.g. due to edge localization of carbon emission. When applied to NSTX scenarios with large plasma rotation, the method shows that taking into account centrifugal effects - leading to poloidal asymmetries in the impurity profiles - is indeed important for a correct interpretation of the experimental data, see Fig. 4.26 [NSTXU-26]. A similar approach will be tested on NSTX-U to interpret the experimental data for radiated power measurements, assuming an analytical form for the poloidal impurity distribution that includes centrifugal effects from plasma rotation.

4.6: Characterization of the fast ion distribution function

4.6.1: FIDAsim modeling

Key diagnostics for the experimental characterization of the fast ion distribution function on NSTX-U are fast-ion D-alpha (FIDA) systems and arrays of solid-state neutral particle analyzers (ssNPA). Analysis and interpretation of FIDA and ssNPA data is challenging, since the systems sample only a portion of the entire distribution. The FIDAsim code [NSTXU-29] is used for forward-modeling of experimental data to infer the actual distribution function based on predictions from the TRANSP/NUBEAM code and comparison to experimental data. Recent development of a FIDA analysis technique will enable accurate interpretation of data from the upgraded FIDA and ssNPA systems available on NSTX-U (see below for details on the diagnostics). To test the technique, FIDA data from an extensive NSTX database have been compared to "classical" predictions that neglect transport by instabilities [NSTXU-30]. Even in the absence of detectable MHD, in virtually all cases the profile peaks at smaller major radius and the profile is broader than the predictions. Abrupt large-amplitude MHD events flatten the FIDA profile, as do most toroidal Alfven eigenmode (TAE) *avalanche* events. Generally, the onset of a long-lived mode also flattens the FIDA profile. There is a shortfall of high-energy ions at large major radius in discharges with repetitive TAE bursts.

4.6.2: Implementation of a new "3D Halo" model in TRANSP/NUBEAM

To improve the interpretation of both FIDA and ssNPA data, a new 3D "halo" model previously implemented in TRANSP has undergone extensive verification for NSTX and projected NSTX-U scenarios [NSTXU-31]. The 3D halo neutral code uses a "beam-in-a-box" model that envelopes both injected beam neutrals and resulting halo neutrals. Upon deposition by charge exchange, a subset of the beam energy components produces first generation halo neutrals that are tracked through successive generations until an ionization event occurs or the descendant halos exit the box. The 3D halo neutral model and Neutral Particle Analyzer (NPA) simulator in the TRANSP code have been benchmarked with the Fast-Ion D-Alpha simulation (FIDAsim) code. When using the same atomic physics database, TRANSP and FIDAsim simulations get excellent agreement on the spatial profile and magnitude of beam and halo neutral densities, as well as the NPA energy spectrum. The simulations show that halo neutrals remain in the vicinity of the neutral beam footprint as expected and that halo neutral density can be comparable with beam neutral density. Future comparisons between measurements, FIDAsim and TRANSP modeling will benefit from this important improvement for NSTX-U scenarios with complex NB injection patterns.

4.7: Diagnostics improvements on NSTX-U

4.7.1: Fast Ion D-Alpha and Neutral Particle Analyzers

In preparation for the upcoming NSTX-U Run, both vertical and tangential FIDA diagnostics have been reinstalled, aligned and calibrated. Improvements have been made in the control modules and stray-light blocking to help make the measurements more accurate and reliable. Both FIDA systems are ready for plasma experiments on NSTX-U. A new and innovative ssNPA system, which uses stacks arrays of silicon diodes with different foil thickness to get spatial profile measurements and some energy information, has been installed. Arrays mounted at different ports around the NSTX-U vessel provide both radial and tangential views to enable measurements of the fast ion distribution at different values of radius, energy and pitch. The electronics have been successfully tested on bench and they are able to measure fluctuations up to 150 kHz, which is suitable to study fast ion driven instabilities and transport. The final integration test of ssNPA detectors and electronics is currently underway. Other fast ion diagnostics that were previously available on NSTX have also been reinstalled and tested. This includes neutron counters and a scintillator-based lost-ion probe (sFLIP) which measured lost fast ions reaching the vessel wall.

4.7.2: Charged Fusion Product array

An important addition to the NSTX-U set of fast ion diagnostics is an array of fusion product detectors, recently tested on MAST [NSTXU-32]. Professor Werner Boeglin, of the Physics Department of Florida International University (FIU) in Miami, Florida, has been collaborating with the NSTX-U group to implement an array of surface barrier diode detectors to measure the emission rate and radial profile of the 3 MeV protons and 1 MeV tritons produced by DD fusion reactions in NSTX-U plasmas [NSTXU-33]. These particles' gyro orbits are unconfined even at maximum magnetic field in NSTX-U. Consequently, this diagnostic can provide details of the spatial extent of the NB ion population through tomographic reconstruction of the fusion reaction rate profile along the curved orbits that reach each detector in the array. The result aids in determining the profile of the neutral beam driven current. The instrument is also capable of measuring the effects of MHD activity on the beam ion density profile. In the past year, Prof. Boeglin and co-workers analyzed an extensive set of data from a prototype of this system that had been fielded on MAST in 2013. The data confirmed the feasibility of the measurement and preliminary results are similar to those of the MAST neutron camera,

which measures the DD fusion reactivity profile by means of the neutrons emitted from the reaction. Prof. Boeglin's student, Ramona Perez, successfully defended her Ph.D. dissertation, entitled "A Charged Fusion Product Diagnostic for a Spherical Tokamak", on this instrument and data in April 2015 [NSTXU-34]. Another Ph.D. student has joined Prof. Boeglin's research group and has completed the design of the detector array for NSTX-U, based upon the results from MAST. This design has passed its Final Design Review at PPPL and is under construction, for use in forthcoming NSTX-U campaigns.

4.7.3: Internal measurements of fast ion driven instabilities

UCLA collaborators will be installing a 96 GHz Doppler backscattering system before the end of the calendar year. It recently underwent and passed a design review. Fabrication of the antenna mounting structure is proceeding (the electronics are already finished). It will probe density fluctuations with k_θ~10–15 cm^{-1}. It can penetrate to equilibrium densities as high as ~$1.1x10^{20}$ m^{-3}. (There is a tradeoff between penetration and achievable k_θ. Penetrating to high equilibrium density reduces k_θ). The system can also function as a reflectometer, in which chase it will reflect at $1.1x10^{20}$ m^{-3}. A four channel 81-87 GHz system is currently being fabricated and is expected to replace the 96 GHz system early next year. As a reflectometer, it will extend the existing capability for measuring MHD or fast-ion mode amplitude in the core to higher density (the current reflectometer array penetrates to $7x10^{19}$ m^{-3}). As a DBS system, it will measure the Doppler shift of the turbulent fluctuations, which can be used to determine plasma equilibrium and fluctuation **E**x**B** velocity. That may allow direct determination of the **E** fluctuation associated with fast- ion driven modes. Currently, only the density perturbation associated with fast ion driven modes can be directly measured.

4.8: Experimental plans after machine re-commissioning

The improved modeling capabilities are expected to be ready for validation with data from dedicated NSTX-U experiments. Experimental plans have been finalized to cover the most important aspects of NSTX-U re-commissioning, with emphasis on the new, 2nd NB injection line, see Table 1. The initial characterization will start with an asssessment of fast ion confinment and dynamic for "MHD-quiescent" scenarios for which classical fast ion physics applies. Data from those experiments will be compared to predictions from numerical tools such as the NUBEAM module in TRANSP. Experiments will then be extended to higher-performance, H-mode plasma cenarios with a variety of NB injection mixes. Under these conditions, with injected NB power exceeding 2-4MW, Alfvénic and other MHD instabilities are likely to be excited. This will provide the opportunity to test and validate the fast ion transport models described above, in order to obtain accurate modeling of the fast ion distribution function and of its temporal evolution. Finally, planned experiments for the coming Run include dedicated sessions to explore scenarios which maximize the non-inductive NB-driven current fraction, up to fully non-inductive scenarios, and to explore the range of validity of "critical gradient" models for fast ion transport and profile evolution.

XP/XMP	***Title***	***Goals***
110	FIDA/ssNPA/sFLIP checkout	Commissioning of fast ion diagnostics. Test background subtraction techniques for FIDA. Compare phase space response of different systems. Test sFLIP diagnostic.
107	Neutron diagnostic calibration	Obtain low-NB-power plasmas with low neutron count rate. Transfer calibration from pulse-counting to current-counting mode for fission chamber counter. Transfer calibration to scintillators.
1522	Beam ion confinement of 2nd NB line	Checkout confinement properties of fast ions from 2nd NB line in quiescent conditions. Investigate confinement vs. beam source, injection energy, plasma current, toroidal field. Compare with classical predictions from NUBEAM/TRANSP.
1523	Characterization of 2nd NB line	Perform assessment of operating regimes achievable with 1st + 2nd NB lines. First characterization of NB-CD with 2nd NB line. Dedicated section to study pressure profile modifications vs. NB source mix. Complement Ip/Bt scan XP by Kaye et al.
1524	AE critical gradient	Explore validity of "critical gradient" approximation for fast ion profile in the presence of instabilities. Validate numerical models. Characterize EP transport vs. NB power, fast ion pressure with unstable AE modes.
1507	Maximize non-inductive current fraction in H-mode	Develop high non-inductive fraction H-mode scenario, ideally achieving full non-inductivity. Optimize NB mix for high non-inductive scenarios.

Table 4.1: List of approved XMP/XPs (Sept. 2015) that directly address JRT-15 related topics.

References

[NSTXU-1] S. A. Sabbagh et al., Nucl. Fusion **50**, 025020 (2010)
[NSTXU-2] J. W. Berkery et al., Phys. Rev. Lett. **104**, 035003 (2010)
[NSTXU-3] J. W. Berkery et al., Phys. Plasmas **17**, 082504 (2010)
[NSTXU-4] S. A. Sabbagh et al., Nucl. Fusion **53**, 104007 (2013)
[NSTXU-5] J. W. Berkery et al., Phys. Plasmas **21**, 056112 (2014)
[NSTXU-6] A. Turnbull et al., Plasma Phys. Control. Fusion **45**, 1845 (2003)
[NSTXU-7] Y. Nagayama et al. Phys. Rev. Lett. **69**, 2376 (1992)
[NSTXU-8] A. H. Boozer, Phys. Plasmas **6**, 3180 (1999)
[NSTXU-9] J. Bagaipo et al., Phys. Plasmas **18**, 122103 (2011)
[NSTXU-10] E. J. Strait et al., Phys. Plasmas **14**, 056101 (2007)
[NSTXU-11] K. Ghantous et al., Phys. Plasmas **19**, 092511 (2012).
[NSTXU-12] W. W. Heidbrink et al., Nucl. Fusion **53**, 093006 (2013).
[NSTXU-13] M. Podestà et al., Nucl. Fusion **52**, 094001 (2012).
[NSTXU-14] N. N. Gorelenkov et al., Phys. Plasmas **6**, 2802 (1999).
[NSTXU-15] Z. Wang et al., Phys. Rev. Lett. **111**, 145003 (2013).
[NSTXU-16] C. Z. Cheng et al., Nucl. Fusion **35**, 1639 (1995).
[NSTXU-17] C. Z. Cheng and N. N. Gorelenkov, Phys. Plasmas **11**, 4784 (2004).
[NSTXU-18] R. B. White et al., to be presented at 57th APS-DPP Meeting, Savannah GA (2015)
[NSTXU-19] M. Podestà et al., Plasma Phys. Control. Fusion **56** (2014) 055003
[NSTXU-20] M. Podestà et al., Nucl. Fusion **55**, 053018 (2015)
[NSTXU-21] M. Podestà et al., paper O-01, IAEA-TM on Energetic Particles, Vienna - Austria (Sep. 2015)
[NSTXU-22] F. M. Poli et al., submitted to Plasma Phys. Control. Fusion (2015)
[NSTXU-23] A. E. Schmidt, PhD Thesis, Massachusetts Institute of Technology
[NSTXU-24] A. E. Schmidt al., Phys. Plasmas **18** (2011) 056122
[NSTXU-25] P. T. Bonoli al., Phys. Plasmas **15** (2008) 056117
[NSTXU-26] L. Delgado-Aparicio et al., Rev. Sci. Instrum. **85** (2014) 11D859
[NSTXU-27] I. Faust et al., Rev. Sci. Instrum. **85** (2014) 11D856
[NSTXU-28] N. T. Howard et al., Rev. Sci. Instrum. **82** (2011) 033512
[NSTXU-29] W. W. Heidbrink et al., Commun. Comput. Phys. **10**, 716 (2011)
[NSTXU-30] W. W. Heidbrink et al., in preparation (2015)
[NSTXU-31] S. S. Medley et al., submitted to Plasma Phys. Control. Fusion (2015)
[NSTXU-32] M. Cecconello et al., Plasma Phys. Control. Fusion **57**, 014006 (2015)
[NSTXU-33] W. U. Boeglin et al., Rev. Sci. Instrum. **81**, 10D301 (2010)
[NSTXU-34] R. Perez et al., Rev. Sci. Instrum. **85**, 11D701 (2014)